

**HYDRODYNAMIC STUDY OF A SIDEWALL NOZZLE
ASSISTED GAS-SOLID FLUIDIZED BED**

A thesis

*submitted in partial fulfillment of the
requirements for the degree of*

DOCTOR OF PHILOSOPHY

by

JITENDRA SINGH RAWAT

(136107001)



**DEPARTMENT OF CHEMICAL ENGINEERING
INDIAN INSTITUTE OF TECHNOLOGY GUWAHATI
ASSAM-781039, INDIA**

November, 2022

DEDICATION

I would like to dedicate my thesis

to my beloved parents



STATEMENT

It do hereby declare that the contents in the current thesis entitled “**Hydrodynamic Study of a Sidewall Nozzle Assisted Gas-Solid Fluidized Bed**” is the results of the thesis work carried out by me, as a research scholar in the Department of Chemical Engineering, **Indian Institute of Technology Guwahati**, Assam, India, under the supervision of **Dr. Rajesh Kumar Upadhyay** and **Dr. Pankaj Tiwari**.

In keeping with the general practice of reporting scientific observations, due acknowledgments have been made wherever the work described is based on the finding of other researchers.

November, 2022



JITENDRA SINGH RAWAT

(136107001)



CERTIFICATE

It is certified that the work presented in the thesis entitled “**Hydrodynamic Study of a Sidewall Nozzle Assisted Gas-Solid Fluidized Bed**” by **Jitendra Singh Rawat**, a student in the Department of Chemical Engineering, Indian Institute of Technology Guwahati, Assam, India, for the award of the degree of **Doctor of Philosophy** has been carried out under our supervision.

The report and content of this thesis have not been submitted , in part or full, to any other University or Institute for the award of any degree or diploma.



Dr. Pankaj Tiwari

(Supervisor)

Associate Professor

Department of Chemical Engineering

Indian Institute of Technology Guwahati

Guwahti-781039, Assam, India



Dr. Rajesh Kumar Upadhyay

(Local Supervisor from External Institute)

Associate Professor

Department of Chemical Engineering and Technology

Indian Institute of Technology (BHU)
Varanasi

Varanasi-221005, U.P., India

ACKNOWLEDGMENTS

I would like to express my deep gratitude to *Dr. Rajesh Kumar Upadhyay* and *Dr. Pankaj Tiwari*, my thesis supervisors, for their kind support, suggestions, guidance and invaluable critiques of this research. I appreciate the Foreign examiner *Prof. Miryan C. Cassanello* (Universidad de Buenos Aires) and the Indian examiner *Prof. Vimal Kumar* (Faculty of Chemical Engineering, IIT Roorkee) for their insightful remarks and suggestions on the thesis. I would also like to offer my thanks to the supervisory committee including *Prof. Anugrah Singh* (The Chairman), *Prof. Tapas Kumar Mandal* (Internal Member), *Prof. Saumya Ji* (Ex. External Member, resigned midway) and *Prof. V. Kulkarni* (External Member) for their valuable feedback and comments. I also offered my thanks to all faculty members of our department including *Prof. V. S. Moholkar*, *Prof. B. P. Mandal* for their support. I would also like to highlight the special support from *Prof. G. Pugazhenti*.

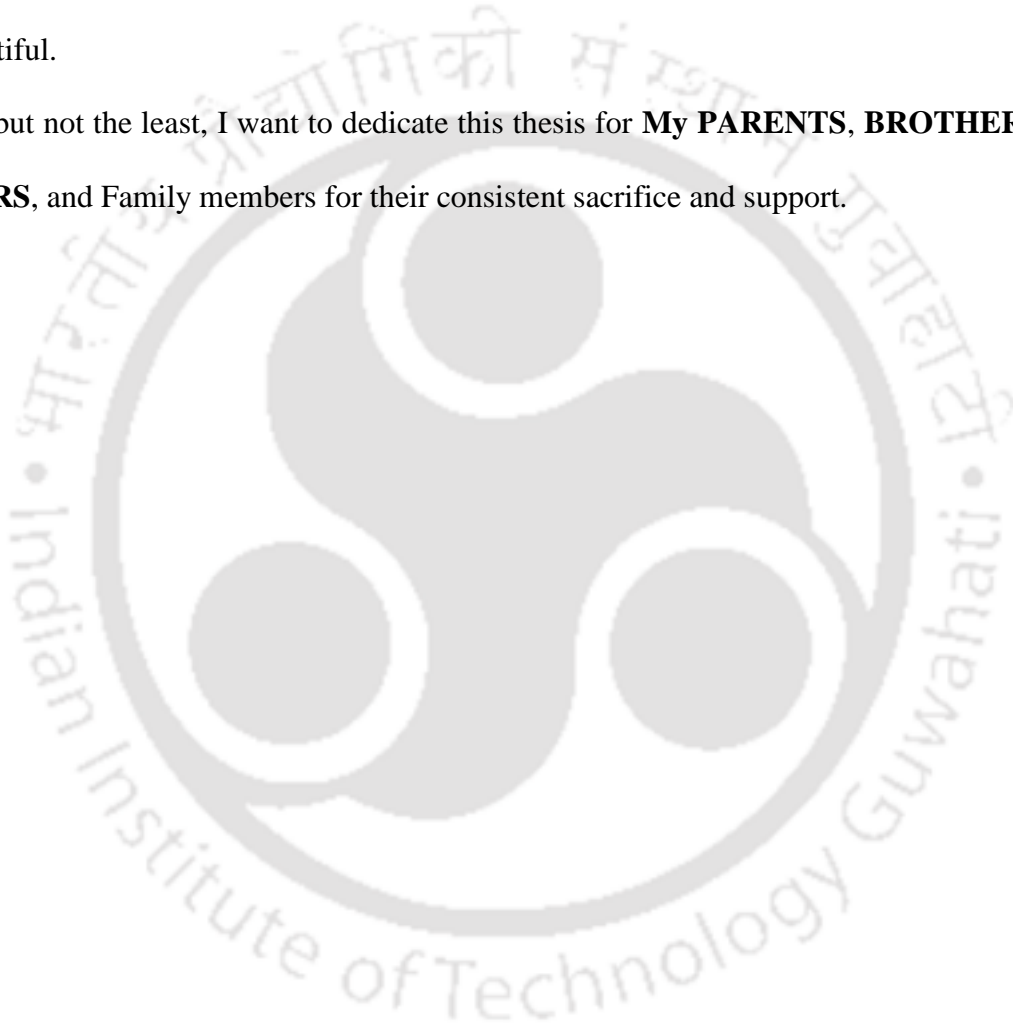
This work was made possible by a scholarship provided by the *Ministry of Human Resource Development, Government of India*. In addition, it was able to complete by the support of the *Board of Research in Nuclear Science (BRNS)*, under the sponsor organization for the current project. I wish to convey my special thanks to *Dr. H. J. Pant & Dr. K. T. Shenoy* for making their efforts to provide the Radioactive Particle in time and providing their support during my stay in **Bhabha Atomic Research Center (BARC)** for Radioactive Safety Officers training. Financial assistance from the **BRNS** and **Department of Energy (DAE)** during this research period was highly appreciated. A special thank is also due to our labmates, including **Dr. Prem Kumar, Dr. Shilpi Verma, Dr. Richa Sharma, Dr. Lipika Kalo, Dr. Rahul Saha, Dr. Pallab Das**, Karan, Sonit, Trilok, Prem Sagar, Roushni, Punampriya, Keshav Kumar.

I wish to extend my thanks to all the staff members of the Chemical Engineering department, Mr. Deep Sinha, Bhagya da, Shailen Das, Jayanta, Ariful etc. for their help at the difficult time.

I wish to acknowledge the help given by all members of Academics, Central Computer Center, and Library etc.

I also want to mention every bit of help, support, gestures of every individual during this journey at IITG campus. I feel honored to have such beautiful peoples around me. I extend my due thanks to Dr. **Ram Kumar**, Dr. **Sharbani**, Dr. **Babul**, Dr. **Anil**, Dr. **Robin**, Dr. **Kedar**, Dr. **Rahul Kesharwani**, Pawan Krishna Kanchi, Rahul Jain, Kishor for making this journey so beautiful.

At last but not the least, I want to dedicate this thesis for **My PARENTS, BROTHER AND SISTERS**, and Family members for their consistent sacrifice and support.



ABSTRACT

The progress of new chemical technologies is moving faster in the design of the unconventional reactor system to upgrade the old technologies and to solve new tasks. There are several tasks that need to be addressed for enhancement of the selectivity of the product in a distributed feeding of reactants along with the reactor height. One of such reaction is, thermal denitration of ammonium di-uranate (ADU), which thermally decompose the ammonium nitrate into nitrogen and water vapor. The reaction is carried out in a fluidized bed maintained at 350 °C. In this reactor, the side streams of ADU (reactants) are injected at higher velocity through multiple pneumatic nozzles. At the surface of the hot solid ammonium nitrate decomposes into nitrogen and water vapor. It is observed that fraction of ammonium nitrate bypasses the reactor without any decomposition. This affect the performance of the reactor and overall process. The extent of bypassing depends on nozzle diameter, flowrate, nozzle configuration, solid flow field and solid distribution. Therefore, it is vital to study the effect of above mentioned parameters on the behavior of sidewall nozzle injected fluidized bed reactor.

The solid flow field parameters, characterizing the hydrodynamics of the solid phase (glass beads or Geldart B type powder), are measured via a non-invasive, radioactive particle tracking (RPT) technique. The investigation is conducted in a laboratory-scale cold flow model setup of 0.21 m diameter and 2.25 m height cylindrical column by studying: single nozzle injection with two different sizes (6 mm and 1 mm) at same planes, and multiple injections of 6 mm diameter nozzle at same planes. All RPT experiments with multiple sidewall injections has been performed in a 6 mm diameter nozzle under fixed fluidization conditions. The experimental results show that the symmetric arrangement of injection at the sidewall of the

bed does not only reduce the axial mean velocity of the solid but also bring the system in a condition similar to the normal fluidization.

In the subsequent chapter of this thesis, gamma-ray densitometry measurement technique (GDT) has been used to study the solid distribution in the same experimental setup and for different configuration of nozzles. Single/multiple sidewall horizontal injection(s) through 6 mm diameter nozzle(s), operating at same plane are used at fixed fluidization condition and the solid hold up are measured using chordal scans. This work has been conducted at different nozzle flow rates. The results show that the solid hold up is lowest (~15%) at lower plane in the case of three nozzles. Similar study has been performed at same injection flowrates through two nozzles of same size (6 mm or 1 mm) operated at different plane. Thus, such result provides useful information on the effect of different configurations of nozzles for optimizing the design consideration of the reactor.

Finally, computational fluid dynamics (CFD) simulations are performed by using commercial software ANSYS 14.5 and compared with experimental findings. The outcome of this work will be important in optimization, designing and troubleshooting of sidewall nozzle assisted fluidized bed.

TABLE OF CONTENT

DEDICATION	i
STATEMENT	iii
CERTIFICATE	v
ACKNOWLEDGMENTS	vii
ABSTRACT	ix
TABLE OF CONTENT	xi
LIST OF FIGURES	xvi
LIST OF TABLES	xxiii
Chapter 1 Introduction	1
Scope	1
1.1. Introduction	1
1.1.1. Gas-Solids Fluidization and their Flow Patterns.....	2
1.1.2. Theoretical Prediction of U_{mf}	4
1.1.3. Types of particles	6
1.2. Pneumatic Nozzles Assisted Fluidized Beds	7
1.2.1. Injection through Vertical Nozzle.....	8
1.2.2. Injection through Horizontal Nozzle.....	13
1.2.3. Applications of Secondary Injection through Nozzles	25
1.2. Motivation	31
1.3. The objective of the Thesis	32
1.4. Layout of Thesis	33
Notations	34
Greek symbols	35
Subscript	35
Abbreviation	36
References	36
Chapter 2 Experimental Setup and Measurement Techniques	42
	xi

Scope	42
2.1. Introduction	42
2.1.1. Void Fraction Measurements Techniques.....	43
Pressure Gradient Method	43
Electrical Capacitance Tomography.....	44
Gamma-ray and X-ray Based Techniques.....	45
2.1.2. Velocity Measurement Techniques.....	46
Laser Doppler Velocimetry (LDV)	46
Particle Image Velocimetry	48
Radioactive Particle Tracking (RPT)	49
Positron Emission Particle Tracking (PEPT)	49
2.2. Gamma-Ray Densitometry Techniques (GDT)	50
2.2.1. Implementation of GDT: Current Work	52
2.3. Radioactive Particle Tracking Method	56
2.3.1. Development History of RPT	58
2.3.2. Implementation of RPT Experimental setup.....	69
2.3.3. Post-processing of RPT data	72
2.3.4. Resolution and Sensitivity	78
2.4. Summary	82
Notations	82
Greek Symbols	82
Subscript	83
Abbreviations	83
References	83
Chapter 3 Investigation of Gas-Solid Fluidized Bed with a Single Sidewall Injection	
Using RPT	90
Scope	90
3.1. Introduction	90

3.2. Experimental Setup and Operating Conditions	93
3.3. Results and Discussion	99
3.3.1. RPT Measurements for a Single 6 mm ID Sidewall Nozzle Injection	99
Probability Density Function (PDF) of instantaneous velocities of solid ...	99
Mean velocity of solid	102
Fluctuation velocities.....	108
Granular temperature.....	111
Axial dispersion coefficient.....	113
3.3.2. RPT measurement with a single injection through 1 mm ID nozzle	114
Mean axial velocity	114
Mean radial velocity.....	117
Axial rms velocity	120
Granular temperature.....	124
Axial dispersion coefficients	126
3.3.3. Effect of nozzle diameter	127
The instantaneous axial velocity.....	127
Effect on mean axial velocity	132
Effect on mean radial velocity.....	140
Effect on dispersion coefficient.....	146
3.3.4. Two sidewall injections operating at same planes ($z=0.20$ m)	148
3.4. Summary	157
Notation	159
Greek Symbols	160
Superscript	160
Abbreviation	160
References	160
Chapter 4 Solid Holdup Measurements in Gas-Solid Fluidized Bed with Sidewall Injections via GDT Experiment	165

Scope	165
4.1. Introduction	165
4.2. Experimental setup	167
4.3. Result and Discussion	171
4.3.1. Without Sidewall Injection	172
Effect of Aspect ratio.....	173
4.3.2. Horizontal Sidewall Injection ($\alpha = 0^\circ$) with a Single Nozzle at Plane AA'	177
GDT Data with 6 mm Nozzle.....	177
GDT Data with 1 mm Nozzle.....	181
Effect of the Nozzle Diameter	181
4.3.3. Multiple sidewall injections with 6 mm diameter nozzles at the same plane ($z=0.20$ m)	185
Effect of two sidewall injections on the same plane	185
Effect of three sidewall Injections at the same plane	185
Comparison of solid holdup data with single, two and three sidewall injection(s) through 6 mm ID nozzle(s) at the same plane.....	188
4.3.4. Multiple sidewall injections operating at a different plane.....	190
Solid distribution with two side injection through large diameter nozzles (6 mm ID)	190
Solid distribution with two side injection through small diameter nozzles (1 mm ID)	194
Comparison between GDT data of same size nozzles injections operating at the different planes	196
4.3.5. Inclined sidewall injection ($\alpha = -45^\circ$) with a single nozzle at plane AA'	196
4.4. Summary	201
Notations	204
Greek Symbols	204

Subscript	205
Abbreviations	205
References	205
Chapter 5 Conclusions and Future Work	208
Scope	208
5.1. Summary	208
5.2. Future Work	212
Appendix A. CFD Modelling of Gas-Solid Fluidized Beds with Single Side Injection	214
Scope	214
A. 1. Introduction	214
A.1.1. Constitutive Equations	216
A. 2. Case Set Up	230
A. 3. Results and Discussion	233
A.1.1. Grid Independency Test	233
A.1.2. Effect of Restitution Coefficients.....	237
A.1.3. Effect of Specularity Coefficients	241
A.1.4. Effect of Drag Models.....	242
A. 4. Summary	246
Notations	247
Greek Symbols	248
Subscript	248
Abbreviation	248
References	249

LIST OF FIGURES

Figure 1.1 (i) Gas-solid fluidization flow regimes, including (a) Fixed bed, (b) Fluidized bed, (c) Bubbling bed, (d) Slugging bed, (e) Turbulent bed, (f) Fast fluidized bed, and (g) Pneumatic conveying (Adapted from Grace, 1997); and (ii) the qualitative nature of the pressure drop vs gas inlet velocity curve for the gas-solid fluidized bed	3
Figure 1.2 Different groups of particles for air at ambient conditions (Adapted from Geldart, 1973)	6
Figure 1.3 Schematic of (a) spouted bed coater, (b) top spray and (c) bottom spray coater (Wurster, 1953)	9
Figure 1.4 Schematic representation of jet penetration length (L_j) in horizontal gas injection into a gas fluidized bed (Adapted from Chen and Weinstein, 1993)	14
Figure 2.1 Schematic of LDV system in forward scattering mode (Adapted from Durst et al. (1981))	47
Figure 2.2 Description of PIV techniques (Adapted from Dantec Dynamics)	48
Figure 2.3 Schematic diagram of (a) experimental set up and (b) γ -ray densitometry set up	53
Figure 2.4 Schematic representation of source and detector assembly during column scanning in a horizontal plane. (b) Photograph of GDT setup	55
Figure 2.5 Schematic diagrams of (a) experimental setup and (b) RPT setup	70
Figure 2.6 Schematic of (a) experimental column with detector arrangements surrounding it, (b) top view of detectors arrangements, (c) side view of the detectors arrangements, (d) dimensions of nozzle, and (e) photograph of RPT setup	71
Figure 2.7 Description of principle of RPT methodology	73
Figure 2.8 Comparison of experimental and simulated counts from a distance-count map for detector 10	76
Figure 2.9 Resolution and sensitivity distribution at different planes with one nozzle side injection. Each column represents the angular position (θ) of the vertical plane with reference to the axis of side injection. (a) $\theta = 0^\circ$, (b) $\theta = 90^\circ$ and (c) $\theta = 45^\circ$	80

Figure 2.10 Resolution and sensitivity distribution for (a) one nozzle injection, (b) two nozzle injections, and (c) three nozzle injections	81
Figure 3.1 Schematic of nozzle locations in the two sidewall nozzle fluidized bed: (a) front view (b) top view	94
Figure 3.2 Evaluation of the coordinates of detector position	94
Figure 3.3 Schematic of (a) detector arrangements outside the bed column, (b) top view of the setup, and (c) view of observation plane representing the position of multiple axial heights	98
Figure 3.4 Photographs of twin fluid type nozzles with (a) $d_j = 6$ mm and (b) $d_j = 1$ mm ...	98
Figure 3.5 PDF of instantaneous axial velocity of solid particle at different r/R and z locations inside the bed	101
Figure 3.6 Visual of bubble migrations in 2D experimental set up (a) primary bubble formed at the bottom of bed, (b) interaction of primary and secondary bubble and (c) rising of bubble from nozzle wall to center of the bed	102
Figure 3.7 Contour plots of mean axial velocity of solid at different axial planes (a) $z = 3$ cm, (b) $z = 15$ cm, (c) $z = 21$ cm, and (d) $z = 25$ cm	104
Figure 3.8 Contour plots of mean radial velocity of solid at different axial planes (a) $z = 3$ cm, (b) $z = 15$ cm, (c) $z = 21$ cm, and (d) $z = 25$ cm	105
Figure 3.9 Time average mean axial velocity profiles of solid at fixed $Q_1=120$ LPM (a) injection plane ($y=0$), and (b) azimuthal averaged	107
Figure 3.10 Radial Variation of mean radial velocity of solid at fixed $Q_1=120$ LPM (a) injection plane ($y=0$), and (b) azimuthal averaged	108
Figure 3.11 Radial variation of axial rms velocity of particle at fixed $Q_1=120$ LPM (a) injection plane ($y=0$), and (b) azimuthal averaged	110
Figure 3.12 Radial variation of radial rms velocity of particle at fixed $Q_1=120$ LPM (a) injection plane ($y=0$), and (b) azimuthal averaged	111
Figure 3.13 Radial variation of granular temperature of solid at fixed $Q_1=120$ LPM (a) injection plane ($y=0$), and (b) azimuthal averaged	112
Figure 3.14 Radial variation of the solid axial dispersion coefficient at fixed $Q_1=120$ LPM (a) injection plane ($y=0$), and (b) azimuthal averaged	114

Figure 3.15 Lateral distribution of mean axial velocity of solids for fixed Q_1 (a) 20 LPM, (b) 30 LPM, (c) 40 LPM, (d) 60 LPM, (e) 80 LPM and (f) 100 LPM.....	116
Figure 3.16 Azimuthal averaged mean axial velocity for different axial planes at fixed Q_1 (a) 20 LPM, (b) 30 LPM, (c) 40 LPM, (d) 60 LPM, (e) 80 LPM and (f) 100 LPM.....	117
Figure 3.17 Lateral distribution of mean radial velocity of solids for fixed Q_1 (a) 20 LPM, (b) 30 LPM, (c) 40 LPM, (d) 60 LPM, (e) 80 LPM and (f) 100 LPM.....	118
Figure 3.18 Azimuthal averaged mean radial velocity for different axial planes at fixed Q_1 (a) 20 LPM, (b) 30 LPM, (c) 40 LPM, (d) 60 LPM, (e) 80 LPM and (f) 100 LPM.....	119
Figure 3.19 Lateral distribution of axial rms velocity of solids for fixed Q_1 (a) 20 LPM, (b) 30 LPM, (c) 40 LPM, (d) 60 LPM, (e) 80 LPM and (f) 100 LPM	122
Figure 3.20 Azimuthal averaged axial rms velocity for different axial planes at fixed Q_1 (a) 20 LPM, (b) 30 LPM, (c) 40 LPM, (d) 60 LPM, (e) 80 LPM and (f) 100 LPM	123
Figure 3.21 Lateral distribution of granular temperature of solids for fixed Q_1 (a) 20 LPM, (b) 30 LPM, (c) 40 LPM, (d) 60 LPM, (e) 80 LPM and (f) 100 LPM.....	124
Figure 3.22 Azimuthal averaged granular temperature for different axial planes at fixed Q_1 (a) 20 LPM, (b) 30 LPM, (c) 40 LPM, (d) 60 LPM, (e) 80 LPM and (f) 100 LPM.....	125
Figure 3.23 Lateral distribution of dispersion coefficient of solids for fixed Q_1 (a) 20 LPM, (b) 30 LPM, (c) 40 LPM, (d) 60 LPM, (e) 80 LPM and (f) 100 LPM.....	126
Figure 3.24 PDF of instantaneous velocity at different z-planes (a) $z=0.15$ m, (b) $z=0.21$ m and (c) $z=0.25$ m	131
Figure 3.25 Contour of axial mean velocity for different size nozzles at (a) $z = 0.03$ m, (b) $z = 0.15$ m, (c) $z = 0.21$ m, and (d) $z = 0.25$	135
Figure 3.26 Contour of radial mean velocity for different size nozzles at (a) $z = 0.03$ m, (b) $z = 0.15$ m, (c) $z = 0.21$ m, and (d) $z = 0.25$ m	137
Figure 3.27 Effect of nozzle diameter on the mean axial velocity of solids.....	138
Figure 3.28 Effect of nozzle diameter on the azimuthal averaged axial velocity of solids	139
Figure 3.29 Effect of nozzle diameter on the mean radial velocity of solids	140
Figure 3.30 Effect of nozzle diameter on azimuthal averaged radial velocity of solids.....	141
Figure 3.31 Effect of nozzle diameter on the axial rms velocity of solids	142

Figure 3.32 Effect of nozzle diameter on azimuthal averaged axial rms velocity of solids	143
Figure 3.33 Effect of nozzle diameter on the granular temperature of solids.....	145
Figure 3.34 Effect of nozzle diameter on the azimuthal averaged granular temperature of solids	146
Figure 3.35 Effect of nozzle diameter on the solids dispersion coefficient	147
Figure 3.36 Effect of nozzle diameter on azimuthal averaged axial dispersion coefficient of solids	148
Figure 3.37 Lateral distribution of axial solid velocity for two secondary air flowrates at (a) 60 LPM, (b) 70 LPM, (c) 80 LPM and (d) 100 LPM	149
Figure 3.38 Azimuthal averaged and time-averaged axial solid velocity for two secondary air flowrates at (a) 60 LPM, (b) 70 LPM, (c) 80 LPM and (d) 100 LPM.....	150
Figure 3.39 Axial RMS solid velocity for two secondary air flowrates at (a) 60 LPM, (b) 70 LPM, (c) 80 LPM and (d) 100 LPM	152
Figure 3.40 Azimuthal averaged axial RMS solid velocity for two secondary air flowrates at (a) 60 LPM, (b) 70 LPM, (c) 80 LPM and (d) 100 LPM	153
Figure 3.41 Lateral distribution of solid granular temperature for two secondary air flowrates at (a) 60 LPM, (b) 70 LPM, (c) 80 LPM and (d) 100 LPM.....	154
Figure 3.42 Azimuthal averaged and time-averaged solid granular temperature for two secondary air flowrates at (a) 60 LPM, (b) 70 LPM, (c) 80 LPM and (d) 100 LPM.....	155
Figure 3.43 Lateral distribution of axial dispersion coefficients of solid for two secondary air flowrates at (a) 60 LPM, (b) 70 LPM, (c) 80 LPM and (d) 100 LPM.....	156
Figure 4.1 GDT setup (a) photographs of cold model setup and (b) top view representation of GDT process at nozzle plane AA'	169
Figure 4.2 Cold flow model (a) schematic of GDT experiment setup, (b) top view of nozzle arrangements and (c) side view of nozzle arrangements.; α is the angle between injection line and x-axis.....	170
Figure 4.3 Determination of U_{mf} from pressure drop curve.....	171
Figure 4.4 Time-averaged profiles of solid hold-up as a function of dimensionless lateral position (x/R) without sidewall injection at $H/D_t=3.10$ for (a) $z = 0.15$ m, (b) $z = 0.20$ m, (c) $z = 0.25$ m and (d) $z = 0.60$ m.....	175

Figure 4.5 Time-averaged profiles of solid hold-up as a function of dimensionless lateral position (x/R) without sidewall injection at $U/U_{mf}=3.12$ for (a) $z = 0.15$ m, (b) $z = 0.20$ m, (c) $z = 0.25$ m and (d) $z = 0.60$ m..... 176

Figure 4.6 Time-averaged profiles of solid hold-up as a function of dimensionless lateral position (x/R) with single nozzle injection (6 mm ID) at different z -planes for (a) $Q_1=80$ LPM, (b) $Q_1=100$ LPM and (c) $Q_1=120$ LPM ($H/D_t = 3.57$; $U/U_{mf}=3.12$, $d_p=709 \mu\text{m}$) ... 178

Figure 4.7 Time-averaged profiles of solid hold-up as a function of dimensionless lateral position (x/R) with large diameter (6 mm ID) single nozzle injection at different injection flowrates for (a) $z=0.15$ m, (b) $z = 0.20$ m and (c) $z = 0.25$ m ($H/D_t = 3.57$, $U/U_{mf}=3.12$, $d_p=709 \mu\text{m}$) 180

Figure 4.8 Time-averaged profiles of solid hold-up as a function of dimensionless lateral position (x/R) with small diameter (1 mm ID) single nozzle injection at different z -planes for (a) $Q_1=80$ LPM, (b) $Q_1=100$ LPM and (c) $Q_1=120$ LPM ($H/D_t = 3.57$, $U/U_{mf}=3.12$, $d_p=709 \mu\text{m}$) 182

Figure 4.9 Comparison of solids hold-up with single injection of two different size nozzle and in the absence of nozzle at $Q_1 = 80$ LPM for (a) $z=0.15$ m, (b) $z = 0.20$ m and (c) $z = 0.25$ m ($H/D_t = 3.57$, $U/U_{mf}=3.12$, $d_p=709 \mu\text{m}$) 183

Figure 4.10 Comparison of solids hold-up with single injection of two different size nozzle and in the absence of nozzle at $Q_1 = 120$ LPM for (a) $z=0.15$ m, (b) $z = 0.20$ m and (c) $z = 0.25$ m ($H/D_t = 3.57$, $U/U_{mf}=3.12$, $d_p=709 \mu\text{m}$) 184

Figure 4.11 Time-averaged profiles of solid hold-up as a function of dimensionless lateral position (x/R) with two nozzle injections (6 mm ID) at different z -planes for (a) $Q_{1,2}=80$ LPM, (b) $Q_{1,2}=100$ LPM and (c) $Q_{1,2}=120$ LPM ($H/D_t = 3.57$, $U/U_{mf}=3.12$, $d_p=709 \mu\text{m}$) 187

Figure 4.12 Time-averaged profiles of solid hold-up as a function of dimensionless lateral position (x/R) with three nozzle injections (6 mm ID) at different z -planes for (a) $Q_{1,2,3}=80$ LPM and (b) $Q_{1,2,3}=100$ LPM ($H/D_t = 3.57$, $U/U_{mf}=3.12$, $d_p=709 \mu\text{m}$)..... 188

Figure 4.13 Comparison of solid holdup data with sidewall injection(s) operating at (a) $z = 0.15$ m, (b) $z = 0.20$ m, and (c) $z = 0.25$ m ($H/D_t = 3.57$, $U/U_{mf}=3.12$, $d_p=709 \mu\text{m}$)..... 189

Figure 4.14 GDT data for solids holdup at different axial heights with sidewall injection(s) of large size nozzles, N1 and N4 ($d_j = 6$ mm) operating at (a) $Q_{1,4} = 80$ LPM, (b) $Q_{1,4} = 100$ LPM, and (c) $Q_{1,4} = 120$ LPM ($H/D_t = 3.57$, $U/U_{mf}=3.12$, $d_p=709 \mu\text{m}$) 191

Figure 4.15 GDT data for solids holdup at different axial heights with sidewall injection(s) of large size nozzles, N1 and N5 ($d_j = 6 \text{ mm}$) operating at (a) $Q_{1,5} = 80 \text{ LPM}$, (b) $Q_{1,5} = 100 \text{ LPM}$, and (c) $Q_{1,5} = 120 \text{ LPM}$ ($H/D_t = 3.57$, $U/U_{mf} = 3.12$, $d_p = 709 \mu\text{m}$)	192
Figure 4.16 GDT data for solids holdup at different axial heights with sidewall injection(s) of large size nozzles, N1 and N6 ($d_j = 6 \text{ mm}$) operating at (a) $Q_{1,6} = 80 \text{ LPM}$, (b) $Q_{1,6} = 100 \text{ LPM}$, and (c) $Q_{1,6} = 120 \text{ LPM}$ ($H/D_t = 3.57$, $U/U_{mf} = 3.12$, $d_p = 709 \mu\text{m}$)	193
Figure 4.17 GDT data for solids holdup at different axial heights with sidewall injection(s) of small size nozzles ($d_j = 1 \text{ mm}$) operating at (a) $Q_{1,4} = 80 \text{ LPM}$, (b) $Q_{1,4} = 100 \text{ LPM}$, and (c) $Q_{1,4} = 120 \text{ LPM}$ ($H/D_t = 3.57$, $U/U_{mf} = 3.12$, $d_p = 709 \mu\text{m}$)	195
Figure 4.18 Comparison of GDT data for solids holdup for different sizes sidewall injection(s) operating at (a) $z = 0.15 \text{ m}$, (b) $z = 0.20 \text{ m}$ and (c) $z = 0.25 \text{ m}$ ($H/D_t = 3.57$, $U/U_{mf} = 3.12$, $d_p = 709 \mu\text{m}$)	197
Figure 4.19 GDT data of solids holdup for inclined sidewall injection with single injection operating at (a) $z = 0.15 \text{ m}$, (b) $z = 0.20 \text{ m}$ and (c) $z = 0.25 \text{ m}$ ($H/D_t = 3.57$, $U/U_{mf} = 3.12$, $d_p = 709 \mu\text{m}$, $d_j = 6 \text{ mm}$)	198
Figure A.1 Schematic of 3-D simulation model (a) fluidized bed geometry, (b) side view, (c) top view and (d) bottom section of fluidized bed system	231
Figure A.2 Effect of grid size on the time-averaged solid volume fraction (<i>Drag model=Hulin Gidaspow</i> , $H/D_t = 3.57$, $U/U_{mf} = 3.12$, $U_{mf} = 0.36 \text{ m/s}$, $d_p = 709 \mu\text{m}$; $\phi = 0.003$, $e = 0.95$, $u_j = 72 \text{ m/s}$)	235
Figure A.3 Solid velocity for different grids used in TFM simulations (<i>Drag model=Hulin Gidaspow</i> , $H/D_t = 3.57$, $U/U_{mf} = 3.12$, $U_{mf} = 0.36 \text{ m/s}$, $d_p = 709 \mu\text{m}$; $\phi = 0.003$, $e = 0.95$, $u_j = 72 \text{ m/s}$)	236
Figure A.4 Contour of (a) solid volume fractions and (b) time-averaged solid axial velocity	238
Figure A.5 Effect of restitution coefficient on time-averaged solid axial velocity	239
Figure A.6 Effect of restitution coefficient on time-averaged solid axial RMS velocity ...	240
Figure A.7 Effect of specularity coefficient on time-averaged solid axial	241
Figure A.8 Comparison of mean axial velocity of solids obtained from RPT and CFD simulation with different drag models	243

Figure A.9 Contour of mean axial velocity of solids obtained through CFD simulation with different drag models (a) Gibilaro model, (b) Hill-Koch-Ladd model and (c) Gidaspow (d) Syamlal and (e) RPT experiment for fixed operating condition ($H/D_t=3.57$, $U/U_{mf}=3.12$, $U_{mf}=0.36$ m/s, $d_p=709$ μ m; $\phi = 0.01$, $e = 0.95$, $u_j = 72$ m/s)245

Figure A.10 Contours of time-averaged axial velocity of solids on xz-plane for fixed operating condition ($H/D_t=3.57$, $U/U_{mf}=3.12$, $U_{mf}=0.36$ m/s, $d_p=709$ μ m; $\phi = 0.01$, $e = 0.95$, $u_j = 72$ m/s)246



LIST OF TABLES

Table 1.1 Reported data sets of C1 and C2 in the literature	5
Table 1.2 Summary of the correlations developed for jet penetration length (L_j) with vertical gas injection in fluidized bed	12
Table 1.3 Literature summary of horizontal sidewall injection in gas-solid fluidized beds	18
Table 1.4 Summary of correlation for predicting penetration length (L_j) in horizontal gas-injection into gas-fluidized bed.....	24
Table 2.1 Review of RPT works conducted in different multiphase flow systems	60
Table 2.2 Equation used in RPT for evaluation of key parameters (Roy et al. 2000)	78
Table 3.1 Operating conditions of RPT measurement with one/two sidewall horizontal injection ($d_p=709 \mu\text{m}$; $\rho_p=2500 \text{ kg/m}^3$; $H/D_t = 3.57$; $U/U_{mf} = 3.12$)	96
Table 3.2 The coordinates of detector for RPT experiments with 6 mm nozzle diameter ...	96
Table 4.1 Properties and flow conditions of air-glass beads fluidized bed system	168
Table 4.2 Details nozzle injection flowrates and configuration used for GDT setup ($\alpha=0^\circ$)	172
Table 4.3 Measured chordal solid holdup with sidewall injection of large size nozzle operated at different flowrates ($H/D_t = 3.57$; $U/U_{mf}=3.12$; $d_p=709 \mu\text{m}$).....	199
Table 4.4 Measured chordal solid holdup with sidewall injection of small size nozzle operated at different flowrates ($H/D_t = 3.57$; $U/U_{mf}=3.12$; $d_p=709 \mu\text{m}$).....	200
Table 4.5 Measured chordal solid holdup with inclined sidewall injection of small size nozzle operated at different flowrates ($H/D_t = 3.57$; $U/U_{mf}=3.12$; $d_p=709 \mu\text{m}$)	200
Table A-1 Summary of the models used in the gas-solid fluidized bed	217
Table A-2 Constitutive equations used in momentum equations	223
Table A.3 Summary of literature available on horizontal nozzle injection in the gas-solid fluidized bed.....	223
Table A.4 Summary of properties and parameters used in simulation of fluidized bed	229
Table A.5 Details of grids used for CFD-TFM simulation.....	231

Chapter 1 Introduction

Scope

In this chapter, the background of the fluidization process is presented. Thereafter, a summary on the fluidized bed and sidewall nozzle assisted fluidized bed is highlighted. Hydrodynamics of the sidewall nozzle assisted fluidized bed is also described along with key applications of such reactors. The key literature citing the previous work on these systems are also briefly presented. Thereafter the motivation for the current thesis work along with thesis objectives are discussed.

1.1. Introduction

History was made on December 16, 1921 with an introduction of a new chapter in the energy and power sector. Fritz Winkler of Germany was the first person who supplied the gaseous products of combustion into the bottom of the reactor containing the coke particles and successfully demonstrated the gasification of coal in a fluidized bed. Winkler observed that the coke particles were lifted by the drag force of the gas to act like fluid (Winkler, 1922). Thereafter, a new terminology called “fluidization” was initiated for this kind of experiment (Squires, 1983). Later, Winkler built a commercial bubbling fluidized bed of 12 m² cross-section for gasification, monitored the process, measured the process variables and filed patents. In 1938, Warren Lewis and Edwin Gilliland invented a suitable gas-solid contacting process known as fast fluidized bed at the Massachusetts Institute of Technology (MIT) for fluid catalytic cracking (FCC) process. Douglas Elliott in 1960 recognized the advantage of burning instead of gasifying the coal in bubbling fluidized bed (BFB) and promoted the process to generate steam with immersion of boiler tubes in it. Based on the gas-solid contacting different types of gas-solid reactors/contactors (bubbling bed, slug bed, conical bed, riser,

downer, pneumatic conveying bed, rotary bed, vortex type bed etc.) were investigated and commercialized in last few decades. Further, it has been established that the efficiency of these gas-solid reactors/contactors is a function of the flow patterns of participatory reactants/phases, their contact with the catalyst/particle present in the bed and the reaction kinetics (Kunii and Levenspiel, 1991). Therefore, for better design and scale-up of any gas-solid bed it is critical to understand the flow physics and contacting pattern. Further, in most of the commercially used gas-solid reactors, multi-reactant/feed are used in the same bed (like FCC unit, denitration system, coater etc.). Mostly, in such system the secondary reactant/feed is injected in the bed through array of nozzles mounted at the sidewall of the reactor while primary reactant/feed is injected from the bottom of the reactor. The contacting of these phases (fluid-fluid-solid) and flow physics governs the performance of such system. The design of the secondary feed/reactant injection system critically affects the interaction and flow patterns of the overall beds. Therefore, understanding the hydrodynamics of such system, design of the geometry and the feed injection assembly become an area of research for efficient performance of gas-solid systems (Kunii and Levenspiel, 1991).

1.1.1. Gas-Solids Fluidization and their Flow Patterns

The fluidized bed reactor is one of the best system for gas-solid contacting because of its better heat and mass transfer characteristics due to enhanced surface area. Therefore, fluidized bed systems are widely used in industry. A fluidized bed is an upgrade version of fixed bed reactor. A fixed bed is the starting state of fluidization process as shown in Figure 1.1 (a). Initially, a vertical vessel is filled with some solid particles up to a certain height (H). This state is known as the “*fixed bed*”. The fluid stream is allowed to flow in upward direction through the bottom of the vessel. The stationary solid particle experiences the drag force by the fluid motion. The drag force depends on the relative velocity of the phases. At low fluid velocity, the drag force is not enough to lift the solid particles against its gravity. Hence it remains in the packed bed

state. At a fluid velocity when the drag force is equal to the weight of the particles in the bed, these particles start moving up. The velocity at which this happens is known as minimum fluidization velocity (U_{mf}) and at this velocity the bed becomes fluidized. At minimum fluidization velocity bed height is higher than the packed bed reactor and denoted by H_{mf} in Figure 1.1(i)b. Further, increase in the velocity of the fluid increases the height of the bed keeping the overall pressure drop constant and the bubble starts forming at minimum bubbling velocity (U_{mb}). The minimum fluidization velocity is generally found experimentally by plotting the bed pressure drop, (ΔP_{bed}) against the gas superficial velocity as shown in Figure 1.1(ii) (Grace, 1997).

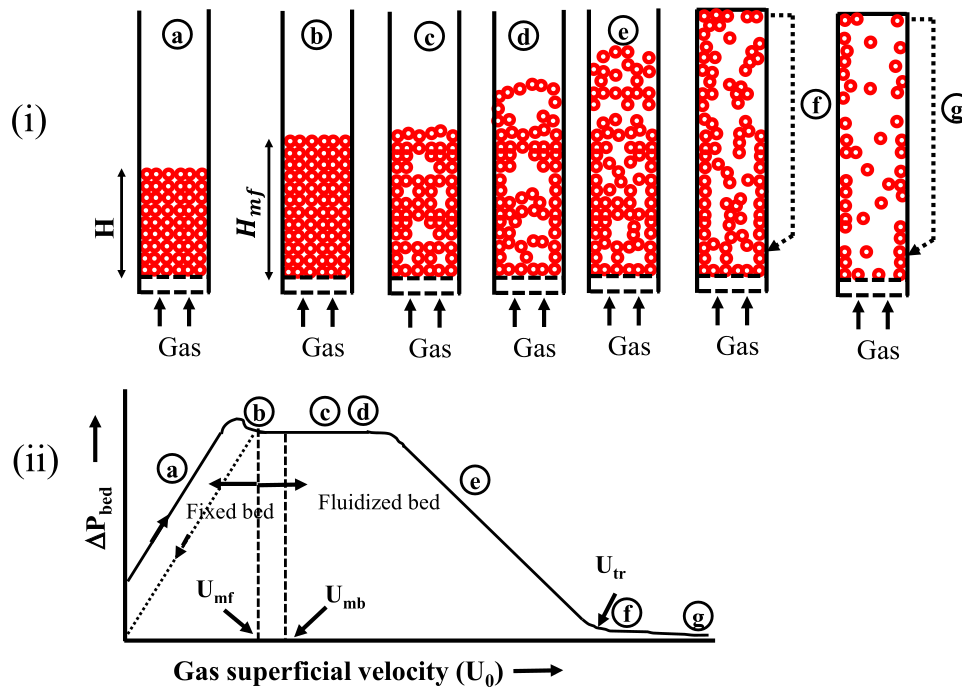


Figure 1.1 (i) Gas-solid fluidization flow regimes, including (a) Fixed bed, (b) Fluidized bed, (c) Bubbling bed, (d) Slugging bed, (e) Turbulent bed, (f) Fast fluidized bed, and (g) Pneumatic conveying (Adapted from Grace, 1997); and (ii) the qualitative nature of the pressure drop vs gas inlet velocity curve for the gas-solid fluidized bed

Fluidization regimes are different for liquid and gas systems and are classified into two major categories: (1) particulate or smooth and (2) aggregative or bubbling (Harrison et al., 1961). Most of liquid solid fluidized beds fall under first category in which, no bubbles are formed in the system. Hence, particulate fluidization is also known as homogeneous fluidization. In the second category, the voids generations, its growth, and rapid motion provide the bed heterogeneity environment which is commonly found in gas-solids fluidized beds for all class of particles. However, Geldart's group A particle also shows particulate fluidization behaviour at low gas velocity. Several criteria to distinguish between particulate and aggregative fluidization have been set by many researchers (Wilhelm and Kwauk, 1948; Harrison et al. 1961; Rowe 1962; Verloop and Johanson, 1974). The voids are also referred as the bubble. In the current thesis, only gas-solid system is discussed until mentioned anywhere. In a gas-solid system, several regimes are obtained based on gas velocity and particle classification. The commonly observed flow regimes are (a) fixed beds, (b) particulate fluidization, (c) bubbling fluidization, (d) slugging fluidization and (e) turbulent fluidization as shown in Figure 1.1. If the gas velocity exceeds the terminal velocity of the solids, other flow regimes can be observed such as fast fluidization, circulating fluidized bed and pneumatic conveying (Figure 1.1). In these cases, particles are entrained out of the system and then recycled back into the system to maintain the solids inventory (Bi and Grace, 1995b).

1.1.2. Theoretical Prediction of U_{mf}

It is known that at the onset of minimum fluidization point, pressure drop across the beds becomes equal to the weight of the solids media present in the gas-solid fluidized bed. The pressure drop in a fluidized bed can be written as:

$$\left. \frac{dP}{dz} \right|_b = (\rho_s \varepsilon_s + \rho_g \varepsilon_g)g \quad \text{or} \quad \Delta P_{bed} = (\rho_s - \rho_g)(1 - \varepsilon_{mf})gH_{mf} \quad (1.1)$$

Where ρ_s and ρ_g are the density of solids and gas present in the beds respectively. ε_{mf} and H_{mf} are the voidage and height of the bed respectively at the minimum fluidization condition.

Similarly, the pressure drop across the fixed beds can be expressed as (Ergun, 1957):

$$\Delta P_{bed} = \frac{150\mu_g U_{mf} (1 - \varepsilon_{mf})^2}{\phi^2 d_s^2 \varepsilon_{mf}^3} + \frac{1.75\rho_g U_{mf}^2 (1 - \varepsilon_{mf})}{\phi d_s \varepsilon_{mf}^3} \quad (1.2)$$

Using $Re_{mf} = d_s U_{mf} \rho_g / \mu_g$ and $Ar = \rho_g (\rho_s - \rho_g) g d_s^3 / \mu_g^2$, with equation (1.1) and (1.2),

one can get a quadratic equation as:

$$Re_{mf}^2 + \frac{150 (1 - \varepsilon_{mf})}{1.75 \phi} Re_{mf} - \frac{\phi \varepsilon_{mf}^3 Ar}{1.75} = 0 \quad (1.3)$$

$$Re_{mf} = \frac{\rho_g d_p U_{mf}}{\mu_g} = \sqrt{C_1^2 + C_2 Ar} - C_1 \quad (1.4)$$

The equation (1.4), the simplified version of Ergun equation (Equation 1.2), involves two dimensionless numbers, Reynolds number (R_{mf}) and Archimedes number (Ar). Table 1.1 is presented for different sets of values for C_1 and C_2 available in the literature.

Table 1.1 Reported data sets of C_1 and C_2 in the literature

C_1	C_2	Reference
33.7	0.0408	Wen and Yu (1966a)
25.7	0.0365	Richardson (1971)
25.3	0.0571	Saxena and Vogel (1977)
25.25	0.0651	Babu et al. (1978)
27.2	0.0408	Grace (1982)
28.7	0.0494	Chitester et al. (1984)

1.1.3. Types of particles

The type of fluidization regime observed in gas-solids fluidized bed is strongly dependent on the type of particles (size and density) used. Geldart (1973) classified the powder into four different groups and these are C, A, B, and D as shown in Figure 1.2. Group C particles are very fine in nature with strong inter-particles forces. Therefore, these particles are unable to fluidize at normal operating conditions. During fluidization process, they rise as plug of solids in low diameter beds but form channelling in large diameter beds.

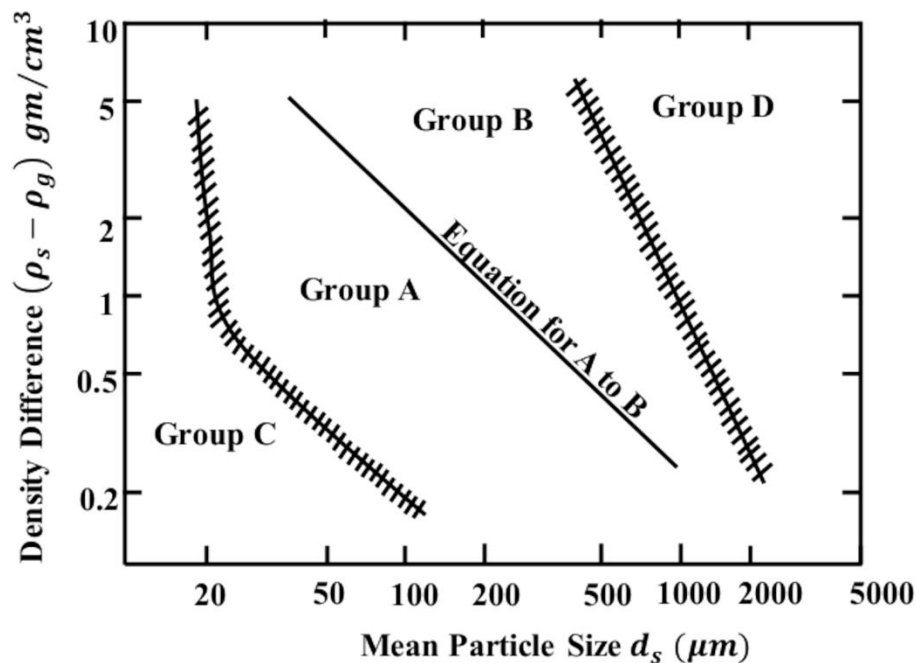


Figure 1.2 Different groups of particles for air at ambient conditions (Adapted from Geldart, 1973)

Group A particles have weak inter-particle forces during fluidization and therefore, easily fluidize at low velocity. The smooth fluidization is observed at low operating velocity. Further, increase in the velocity shifts the smooth regime into the bubbling regime ($U_{mb} > U_{mf}$). These particles belong to small size particle diameter and/or low density ($< 1400 \text{ kg/m}^3$). Group B

particles are fluidizable in nature and start with bubbling regime at low operating velocity. The bubbles are formed as soon as fluidization occur ($U_{mb} = U_{mf}$) and grow to large size. The mean particle size varies in the range of $40 \mu\text{m} < d_s < 500 \mu\text{m}$ while particle density is in the range of $1400 < \rho_s < 4000 \text{ kg/m}^3$. Group D particles are generally large in size, high dense, and spoutable in nature.

1.2. Pneumatic Nozzles Assisted Fluidized Beds

The conventional fluidized beds have many drawbacks. One of the critical drawback is the formation of the bigger bubble at high flow rates. The large size bubbles reduce the gas-solid contacting which may cause bypassing of the reactant without any conversion. This reduces the overall process efficiency of the system and increases the load on the bed as exit gases need to be recycled to achieve the desirable conversion. Another drawback of the conventional fluidized bed is non uniform solid mixing. The solid velocity is high near the center of the column due to the influence of the bubbles and lower near the wall due to the no-slip condition. This becomes more severe in high throughput gas-solid fluidized bed where larger bubbles are formed and results into non-uniform bed temperature and mass transfer in the bed. This rigorous solids movement also leads to solid's attrition and entrainment. Further, the contacting of different reactants in multi-reactant gas-solid fluidized bed is also a critical issue.

Therefore, several modifications have been implemented in conventional fluidized beds to overcome the above-mentioned disadvantages particularly for high throughput and multicomponent system. One of the possible solution of above mentioned problems is to inject one or more reactant through the pneumatic nozzles at different section of the bed. This arrangement reduces the gas flow rate from the bottom of the column and hence minimizes the bubble size and theoretically also provides better contacting. In general, the nozzles are placed in two orientation (i) vertical and (ii) horizontal. Further, in literature, studies have been reported on injection of both gas and/or gas-liquid reactant through these nozzle orientations

in the fluidized bed. However, most of the reported studies are on gas injection through vertical nozzles (Merry., 1975; Yang and Keairns., 1979; Filla et al., 1983; Grace and Lim., 1987; Cleaver et al., 1995; Vaccaro., 1997; Musmarra., 2000; Hong et al., 2003; Zhang et al., 2004).

1.2.1. Injection through Vertical Nozzle

The vertical nozzle injections are often used in different processes such as drying, coating , etc. Figure 1.3a shows the conventional spouted bed coater in which four different sections including air inlet, process chamber, expansion and segregation zones, are observed. In the process chamber, the material to be coated is fed and fluidized with the primary air inlet (or process air as shown in Figure 1.3a). The coating agent/solvent is supplied through bottom as coating solvents. The coated particles can be withdrawn from the discharge pipe. There are two categories of coaters used in the different industries: first, the top spray or vertically downward spray while the second is bottom spraying or upward jet system. Top spray and bottom spray coaters are shown in Figure 1.3b and Figure 1.3c.

The top spray coater is well applied in the food industry due to large batch size, high versatile and simple to use (Dewettinck and Huyghebaert, 1999). However, this can be used in different process such as coating and agglomeration. In this type of system, the fluidized air is supplied through distributor in vertical upward direction, and the coating solvent is sprayed from the top so that the suspended particles can be coated (Figure 1.3b). The coated particles moves up from the process chamber to the expansion region, and finally return back into the process chamber. Hence, it can be easily seen that both the fluids work counter-currently. The second type of coaters as shown in Figure 1.3c, usually known as the Wurster coaters (Wurster, 1953), are mostly used in pharmaceutical industry for coating of pellets. In Wurster coater, the coating agent and the fluidized medium are both supplied from the bottom co-currently. The nozzle is used for spraying the coating agent. In addition, an insert (or draft tube) is used in Wurster coater to improve the design and operational flexibility. The accurate control of particle and

gas residence time can be accomplished through the use of a draft tube that separates the annulus and spout region. In Wurster coater, injected coating agent's atomized droplets migrate co-currently with the suspended particles in the Wurster tube. It thus provides enhanced heat and mass transfer and helps to induce uniform coating (Aulton et al., 1995).

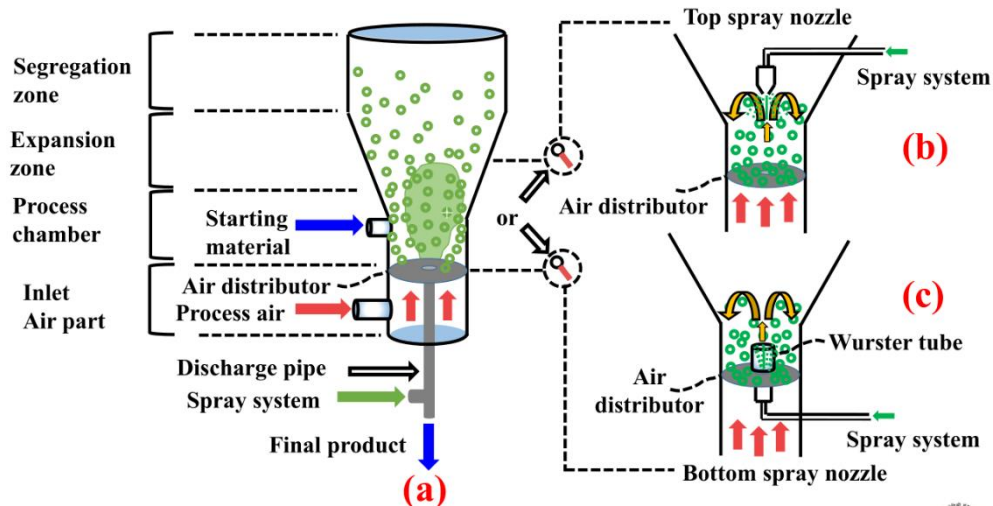


Figure 1.3 Schematic of (a) spouted bed coater, (b) top spray and (c) bottom spray coater (Wurster, 1953)

There is ample literature on the vertical injection of gas jets into fluidized beds (Shakhova, 1968; Zenz, 1968; Basov et al., 1969; Merry, 1975; Wen et al., 1977; Filla et al., 1983; Vaccaro et al., 1997; Zhang et al., 2012; Materazzi et al., 2017). A brief summary of these work is presented in Table 1.2.

Merry (1975) proposed a correlation to predict the jet penetration length (L_j) and jet angle (θ_j) in a 2D column with rectangular base. The dimension of base was 0.2 m wide and 0.012 m depth. The set up was made of plexiglass, and single nozzle of diameter 19.1 mm was centrally located at the bottom. The nozzle was directed in vertical direction, and the water was injected through nozzle into a bed of lead shots (with $d_p=1, 2$ mm) fluidized bed. The correlation for L_j is only valid to the low viscosity fluid or in case of aggregative fluidization, and also applicable for narrow range of particle size.

Wen et al. (1977) conducted experiments in a 2D bed of glass beads ($d_p = 280 \mu\text{m}$; $\rho_p = 2410 \text{ kg/m}^3$) for a single jet ($d_j = 8 \text{ mm}$). In addition, they carried out similar experiments with three jets (each nozzle with $d_j = 3.2 \text{ mm}$) using different bed materials, i.e. ,0.28 mm glass beads, 0.45 mm P.V.C. beads, and 0.83 mm sand. For all these data, the normalized penetration length (L_j / d_j) were measured and plotted against the two-phase Froude number. The correlation was developed using these data which is shown in Table 1.2.

Wen et al. (1982) proposed a criterion to differentiate the jet from the bubbles, formed due to inject of gas (air) vertically upward, in a gas-fluidized bed via an optical probe. The sand particles of size 133, and 250 μm , and spherical glass particles of 500 μm were used in the experiment. The mechanism of jet and bubble formation was dealt with on the basis of the presence of dead zones around the orifice at the distribution level. The discussion showed that the presence of defluidized particle around the orifice was responsible for the jet formation.

Fila et al. (1983) conducted experiments to study the influence of particle diameter (d_p), density and shape on jet characteristics in fluidized bed. Experiments were performed in a transparent column with $390 \times 16 \text{ mm}^2$ rectangular base. A vertical jet of $6 \times 16 \text{ mm}^2$ was used to inject the air, on the vertical axis of setup. Six type of solid materials with density in range of 1200 to 2500 kg/m^3 and size in the range of 0.7-3.0 mm were used in the experiments. The experiments were conducted at three bed heights (8, 10 and 11 cm) and the bed materials were operated at three fluidization velocities (78, 125 and 260 cm/s) of fluidization air. The jet velocity was kept fixed and maintained at 60 m/s for all cases. High speed videography (1000-5000 frames/sec.) was used to measure jet angle and axial velocity of solid particles in the bed. Similarly, the jet axial velocity was also determined by 0.7 mm outer diameter (OD) pitot tube measurement. Finally, it has been concluded that gas velocity decayed faster for spherical particles than the non-spherical particles of same density and size; for heavier than lighter particles; for coarser than finer particles of same density and size. Larger jet angle was observed

for spherical particles than non-spherical particles of same size and density. Jet angle also increased with material of large size and high density.

Vaccaro et al. (1997) investigated the interaction of a vertical gas injection on a bed of fluidized material and measured the jet penetration length (L_j) via simultaneous measurement of static pressure at two different positions, one at the wall and second at the bed axis, located 0.06 m above the distributor level. The experiments were conducted in two cylindrical columns, made of perspex, of I.D. 0.35 and 0.20 m respectively. Two separate air feeding system were employed, one passed through a perforated type distributor (0.6 mm hole with 2 mm square pitch) and second was used to inject the air at high velocity along the axis of bed through different nozzle. Four nozzle diameter ($d_j = 6, 10, 19$ and 25 mm) were used. Glass beads of size (d_s) 0.8-1.2 mm and density (ρ_s) of 2600 kg/m^3 were used as packing material. The experiment were performed with the bed height (H_b) of 0.1-0.8 m, injection velocity (u_j) of 35-95 m/s and fluidization number (U/U_{mf}) of 1.1-2.3. They reported that L_j increases as u_j and d_j increases. Similarly, it was also observed that L_j decreases with increasing U/U_{mf} (1.1 to 2.3) for large nozzle diameter and slightly increases in case of small diameter nozzles.

Zhang et al. (2012) made a 2D fluidized bed of plexiglass with 0.3 m width, 2.0 m height and 0.025 m depth. A rectangular slit of width 0.01m was made at the central position of the plate distributor. The ballotini particle ($d_p = 275 \text{ }\mu\text{m}$; $\rho_p = 2550 \text{ kg/m}^3$) was used as a fluidized material. The jet velocity, fluidization velocity and packed bed height were fixed at 7.07 m/s (or $100 U_{mf}$), 0.07 m/s (U_{mf}), and 0.50 m respectively. A video camera was used to capture the photograph through the transparent wall. Finally, a numerical model based on two fluid model using ANSYS CFX solver was used to predict the jet penetration length (L_j) and compared with experimental data. They reported the existence of three flow regimes (isolated, merged, and transitional jet) in the beds in case of double jets operating with same and different flow rates. For double jets with equal jet velocity, the jet penetration length (L_j) decreased with

increasing the distance between nozzles. It was concluded that the jet penetration length (L_j) decreased by more than 30 % when two nozzles replaced one nozzle and operated at equal velocity.

Table 1.2 Summary of the correlations developed for jet penetration length (L_j) with vertical gas injection in fluidized bed

Authors	Correlations for L_j ,	Range of application
Shakhova (1968)	$\frac{L_j}{d_j} + \frac{1}{2} \cot \theta = 13 \left[\frac{\rho_f U_j}{\rho_p \sqrt{g d_p}} \right]$	-
Basov et al. (1969)	$\frac{L_j}{d_j} = \left(\frac{0.919 d_p}{0.0007 + 0.566 d_p} \right) \cdot \frac{U_j^{0.35}}{d_j^{0.3}}$	-
Zenz (1968)	$0.0144 \frac{L_j}{d_j} + 1.3 = 0.51 \log(\rho_j U_j^2)$	-
Merry (1975)	$\frac{L_j}{d_j} = 5.2 \left(\frac{\rho_j d_j}{\rho_p d_p} \right)^{0.3} \left[1.3 \left(\frac{U_j^2}{g d_j} \right)^{0.2} - 1.0 \right]$	Aggregative fluidization and 3D beds
Wen et al. (1977)	$\frac{L_j}{d_j} = 814.2 \left(\frac{\rho_p d_p}{\rho_f d_j} \right)^{-0.585} \left(\frac{\rho_f d_j U_j}{\mu} \right)^{-0.654} \left(\frac{U_j^2}{g d_j} \right)^{0.47}$	-
Wen et al. (1977)	$\frac{L_j}{d_j} = 15.0 \left(\frac{\rho_f U_j^2}{(\rho_p - \rho_f) g d_j} \right)^{0.187}$	-

L_j : Penetration length; θ_j : Jet angle; d_j : Jet diameter; ρ_j : Secondary fluid density; U_j : Injected fluid velocity; ρ_f : Primary fluid density; d_p : Particle diameter; ρ_p : Particle density; V : Vertical

Materazzi et al. (2017) conducted experiments in a 0.15 m diameter fluidized bed, fabricated with Perspex, with a flexible nozzle installed at the center of the distributor. X-ray imaging tool was used to measure the void fraction for different set of nozzle configurations such as centrally upward single (type C), one sided multiple jets placed horizontally (type B), and multiple jets fixed horizontally (type A). Geldart A type sand particles of diameter 0.265 mm and density 2650 kg/m^3 were fluidized with air. They reported that the new design configuration improved the performance over the single injection jet to minimize the erosion.

1.2.2. Injection through Horizontal Nozzle

Figure 1.4 shows the schematic of horizontal gas injection into gas fluidized bed. In such beds pneumatic nozzles are placed on the side wall and reactant(s)/gas are injected in the normal direction of the primary fluid injection from the bottom of the column. Such injections can help in maintaining the uniform temperature and concentration profile throughout the bed if designed properly. This can also help in controlling the rate of reaction and can also provide good mixing.

In case of liquid reactant, mostly twin fluid nozzles are used which reduces the liquid reactant into small droplets and helps in maintain the bed temperature. It also provide uniform mixing and concentration profile. However, if nozzle assemblies are not designed properly for both gaseous and liquid reactant injections, these beds can lead to severe bypassing of the reactant (Figure 1.4). The gases injected through the side nozzles can interact with the bubbles formed at the bottom of the column (near the distributor) due to primary gas injection. In some cases, it is found that such interaction leads to the formation of bigger bubbles which can also migrate towards the injection wall. Reactant(s), which are injected in the vicinity of these bigger bubbles, moves with these bubbles (in the wake of the bubble in case of liquid reactant or in the emulsion zone of the bubble). This significantly reduces the residence time of reactant in the bed and leads to severe bypassing and reduced conversion. Therefore, the proper design of

the nozzle assembly system and understanding the underline physics of the bed is key to the successful design of such fluidized beds. Though such beds are widely used in industry, the studies reported on these beds are limited which are summarised in Table 1.3 and given below.

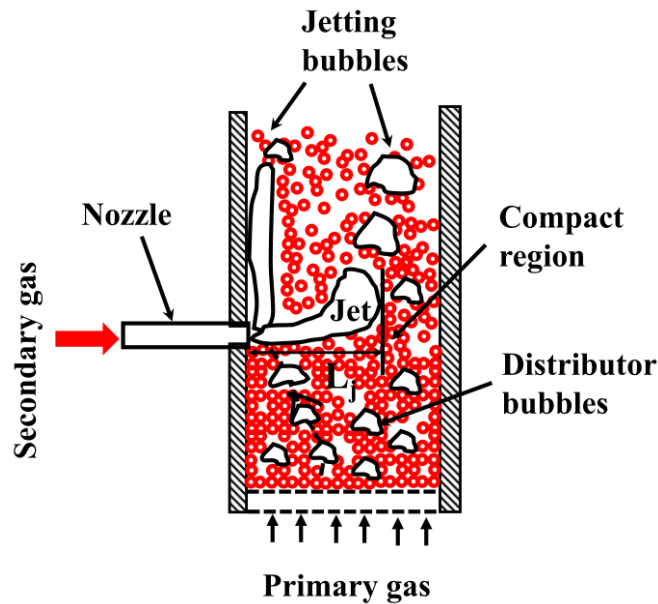


Figure 1.4 Schematic representation of jet penetration length (L_j) in horizontal gas injection into a gas fluidized bed (Adapted from Chen and Weinstein, 1993)

Merry (1971) carried out experiments in 3D column fluidized bed of different particles (steel shot, kale seed and sand). Nozzle with different diameters (2.54 to 14.3 mm) and injection velocities (40-300 m/s) were used. A correlation for measuring the penetration length (L_j) was developed. They measured the jet penetration length and jet angle for varying jet velocities. Finally, the correlations were developed as shown in Table 1.3.

Xuereb et al. (1991a) performed a test to measure penetration length (L_j) and jet angle (θ_j) with a horizontal or inclined injection and local gas velocity in 2D fluidized bed. The polystyrene particles, with different size and density, were used as bed materials. The jet velocity vary between 35-125 m/s. They showed that the gas velocity profile became asymmetric in radial direction.

Chyang et al. (1997) performed an experiment in a 2D fluidized bed of cross section $0.38 \text{ m} \times 0.015 \text{ m}$, made of acrylics with a single sidewall nozzle of different exit diameter ($d_j = 3, 4.5, 6, 7.5$ and 9 mm) mounted at an axial height of 0.1 m . Glass beads of different sizes ($d_p = 0.214, 0.0545, 0.775$ and 0.920 mm) were used as the solid media. The initial bed height (H_b) was maintained at 0.214 m . The nozzle velocity was varying in the range of 1 to 130 m/s . The gas fluidization number (U/U_{mf}) value was maintained between 0 to 4 . The high speed videography technique was implemented to measure jet penetration length, L_j , by capturing the photograph under dynamic condition of beds. Effect of jet velocity (U_j), nozzle diameter (d_j), particle diameter (d_p), and bed height (H_b) were observed on the penetration length (L_j). They reported that jet penetration length increased with increasing jet velocity (U_j) and nozzle diameter (d_j) while decreases with larger d_p and H_b . In addition, the effect of gas superficial velocity (U) on jet penetration length (L_j) was also observed and maximum value of L_j was observed in $0.6 < U/U_{mf} < 1$. A phase diagram, based on modified Froude number (Fr^*) and ratio of nozzle diameter to particle diameter (d_j/d_p), was drawn. In this diagram, it is shown that the low Fr^* favors bubbling regime and high Fr^* favors jetting regime.

Copan (1999) demonstrated a test to see the motion of bubbles in a 2D fluidized bed in the presence of horizontal jets and found that fluidizing bubbles always travel toward the injected jet. Finally, these bubbles were entrained by jets after interaction and the height of interaction plane depends on the injection velocities. Copan reported that the horizontal jets in such fluidized beds partially shields the upper region from the turbulence in the bubbling regime.

Al Sherehy (2002) conducted an experiment to measure L_j in a cylindrical column with diameter (D_c) 0.152 m using FCC particles (Geldart A). The bed was maintained at $H_b = 1.15 \text{ m}$. The nozzle was placed at an axial height, $H_j = 0.56 \text{ m}$ from the distributor level. The operating conditions were set to $U_j = 0.2 - 226 \text{ m/s}$ and $U/U_{mf} = 1.7$ ($U = 0.0051 \text{ m/s}$; $U_{mb} = 0.007 \text{ m/s}$). However, the results were reported based on visual observations.

Wang et al. (2015) tried to validate the data of L_j obtained from the work of Al Sherehy (2002), with the simulation data predicted in similar condition using Multiphase Flow with Interphase eXchange (MFIx) computational fluid dynamics (CFD) package developed by Syamlal (Syamlal et al., 1993). The filtered model, developed by Sundaresan's group in Princeton, was used for drag model and solid viscosity. The predicted data of L_j were in good agreement with the experiments. They have also reported the solid fraction and solid velocity profile of their simulated work. However, the experimental validation of such profiles were missing.

Bhowmick et al. (2015) visualized the interaction between the horizontal jet and fluidized bubbles in a 3D transparent fluidized bed. Glass beads ($d_p = 385 \mu\text{m}$; $\rho_p = 2500 \text{ kg/m}^3$) were used as solid media and air was used both as primary gas and secondary (or injected) gas. They observed that the location of interaction plane between the jetting bubbles and distributor bubbles (originated from primary gas) was greatly affected by primary gas velocity. At low velocity ($U/U_{mf} = 1.5$), it was located above the nozzle plane but came down when the velocity was reached to $2.0 U_{mf}$. In addition, the gas volume fraction was also measured with a non-invasive i.e. gamma ray densitometry techniques at different flow rates of primary gas, and injected gas velocity and bed heights.

Recently, Koeninger et al. (2017) employed the particle image velocimetry (PIV) technique to measure the particle velocity in a 3D bed with a horizontal gas injection. The glass beads was used as packing material. They observed that particle velocity was increased with the primary gas pressure. However, as PIV worked in visual range the data accuracy was limited near the wall only. A detailed literature review of other works carried out on horizontal nozzle injection through side wall is presented in Table 1.3.

Table 1.4 shows experimental correlations for the length of penetration of horizontal gas jets in fluid beds. It has been reported that the length of penetration increases with velocity and density of the injected gas. However, all these correlations are valid for subsonic velocities. It

has been observed that the flow field measurement of different phase in the gas-fluidized bed along with the sidewall injection, is a challenging task to perform due to high injection velocity gradients in dense bed condition. The photographic techniques (such as PIV, videography) and invasive techniques (optical probe, pitot tube etc.) has their limitation as they do disturb the flow. To overcome with these limitations, radioactive particle based measurement techniques (GDT and RPT) are preferred to infer the flow behavior of the gas-fluidized bed in the presence of several configuration of sidewall nozzles.



Table 1.3 Literature summary of horizontal sidewall injection in gas-solid fluidized beds

Technique	Investigators	Experiment details	Remarks
Photography	Shakhova (1968)	Experiment was conducted in a 2D setup with copolymer material (diameter=4 mm, 1000 kg/m ³). The bed material was fluidized with air. A secondary gas (air) was injected at an injection velocity in the range of 52-303 m/s through a horizontal injection with various nozzles (4-6 mm).	A correlation was developed for the jet penetration length (L_j). prediction
Photography	Merry (1971)	Sand particles of diameter 0.18 and 0.33 mm were used in 2D and 3D setup as the fluidized bed materials. The injection velocities of air in the range of 5-20 m/s and 40-300 m/s were used through different size nozzles (2.54 – 14.3 mm). In addition, experiments were also conducted with steel shot (0.28 mm) and Kale seeds (2 mm) in 2D set up.	Two different regimes (jetting and bubbling) was observed. In the jetting regime, jet penetration length (L_j) was proportional to the jet velocity (U_j) and in the bubbling regime, it was found that $L_j \propto (U_j)^{2/5}$.

Photography	Roach (1993)	Set up made of Perspex column with a base of 400 mm × 300 mm and height of 1100 mm. Nozzles with different diameters (1, 2, 3, 5.5 and 8 mm) were used. Polystyrene beads (diameter=4.1 mm; density=20 kg/m ³) were filled upto 1.0 m height. Primary air velocity was varied upto 3 U _{mf} (U _{mf} =0.095 m/s). The injection velocities were used in range of 0.15-180 m/s.	Bed velocity had first order dependency on the jet penetration was observed.
Photography	Chyang et al. (1997)	2D bed of rectangular base with cross section of 0.38 m × 0.015 m, made of acrylics sheets, was used in the experiment. Nozzles with different diameter (d _j = 3, 4.5, 6, 7.5 and 9 mm) was operated at 0.1 m height at the injection velocity of 1-130 m/s. Different size glass beads (0.214, 0.0545, 0.775 and 0.920 mm) were used and filled upto 0.214 m.	The phase diagram consisted of bubbling, transition and jetting were drawn based on modified Froude number, Fr* and d_j/d_p . Low Fr* favoured bubbling phenomenon while high Fr* favoured jetting phenomenon. It was observed that jetting

Photography	Al-Sherehy (2002)	3-D cylindrical bed with diameter 0.152 m and 2.056 m was used for experimental work. FCC particles (diameter 61 μm and 1460 kg/m^3) was filled upto a fixed height 1.15 m. The compressed air was supplied through distributor at 0.0051 m/s. A tube of ID 4.3 mm, mounted on the wall 0.56 m above the distributor, was used for spraying the secondary gas into the bed at three different velocities (50,78.5 and 156 m/s).	Non uniform distribution of injected gas was found at the injection plane for low injection flowrate. At the upper levels, the injected gas distribution was reduced. The higher jet penetration length (L_j) was reported at higher jet velocity (U_j).
Triboelectric probes	Dawe et al. (2008)	Fluidized bed of 0.3 m wide, 1.0 m long and 3.2 m height was used for experiment. The bed was operated at an excess velocity, U_{ex} ($=U-U_{mf}$) of 0.39 m/s. Three different particles (fluid coke, sand, glass beads) were used and the bed height was maintained at 0.3 m. Three type of nozzles with four different nozzle diameter were utilized to inject the secondary	New correlation of L_j was developed for sonic jets involving diameter of nozzle, equivalent speed of sound of the gas, gas-density, and two coefficients. Jet angle (θ_j) was found proportional to the gas mass flow rate, and was decreased with

		gas (air, Argon, Helium) into the bed. The jet penetration length (L_j) and jet angle (θ_j) were measured, and a correlation was developed for the same.	increasing nozzle diameter/density of injected gas.
X-ray computer tomography (CT) Two Fluid Model with MFI	Deza et al. (2011)	Fluidized bed column with internal diameter (ID) of 102 mm was used for X-ray CT measurement. A tube of ID 11 mm was attached to the bed for secondary injection (of air). Grount nut shell of 500-600 μm was used.	Investigation showed that 2D simulations prediction was higher than 3D simulations. Upto 20 % Q_{mf} (minimum fluidization flow rate) increase in injection flowrate did not affect the behaviour of bed. It was reported that second injection, placed in opposite to each other, enhanced the mixing and overall homogeneity.
γ -ray densitometry	Bhowmick et al. (2015)	A pilot-scale cylindrical column with diameter 250 mm and height 1650 mm was used for experiment. Primary gas (air) was supplied through distributor at the bottom. Secondary air injection was sprayed into	In the absence of side injection, at low fluidization velicity (U), the voidage fraction was higher at wall end and lower at the central region, and at high U the voidage profile reversed.

		<p>the bed through a twin fluid type nozzle (diameter 1.3 mm). Glass bead (Geldart B type) of diameter 385 μm and density 2500 kg/m^3 was used as bed material and was filled inside the bed upto a height of 645 mm. A radioactive source (Cs-137) and NaI (Tl) were used for scan purpose.</p>	<p>In the presence of side injection, at $U=1.5 U_{mf}$ ($U_{mf}=0.156 \text{ m/s}$), the jetting bubble and distributor bubble interacted above the distributor plane and moved from wall to core region. At $U=2.0 U_{mf}$, the two bubbles interacted at the nozzle plane.</p>
<p>Particle Image Velocimetry (PIV), capacitance probe, X-ray computer tomography (CT)</p>	<p>Koeninger et al. (2017)</p>	<p>Semi-circular base (diameter=0.19 m) cylindrical column with glass plate on the front side was used in the experiment. Compressed air was used as a primary/ secondary gas. The secondary gas was injected through a nozzle diameter of 3 mm which was placed at 75 mm. Glass beads ($d_p=0.092 \text{ mm}$; $\rho_p=2500 \text{ kg/m}^3$) was used as bed (solid) material.</p>	<p>Higher the injected gas pressure (or velocity), higher the mean solid velocity and lower the solid mixing.</p> <p>At single gas injection, higher mean particle velocity observed at non-fluidized case ($U=0$) than the fluidized case ($U=U_{mf}$).</p>

X-ray computer tomography	Koeninger et al. (2018)	Cylindrical fluidized bed (diameter=0.094 m) equipped with three nozzles in confocal arrangement (120°) at an axial height of 75 mm from distributor, was used for experiment. The solid loading of 1.2 kg was used to ensure the bed height 130 mm. Primary air velocity (U) was varied between 0-0.026 m/s. Secondary air velocity (U _j) was adjusted between 50 to 300 m/s.	<p>Lower the U_j, higher the bending of jet in upward direction due to low axial momentum.</p> <p>High U_j, more the penetration length (L_j).</p> <p>Higher the U, wider the jet and broader the jet boundary.</p> <p>Smaller particle led to the increase in the fluctuation at the jet boundary and hence, more turbulent mixing was observed.</p>
---------------------------	-------------------------	--	---

ϵ_g : Gas voidage; D_b : Bed diameter; H_b : Packed bed height; d_p : Particle diameter; ρ_p : Particle density; d_j : Jet diameter; U_j : Jet velocity; U : fluidization velocity; U_{mf} : Minimum fluidization velocity; L_j : Penetration length;

Table 1.4 Summary of correlation for predicting penetration length (L_j) in horizontal gas-injection into gas-fluidized bed

Authors	Correlations for L_j ,	Range / Recommendation
Shakhova (1968)	$\frac{L_j}{d_j} = 7.8 \frac{\rho_l}{\rho_p} \frac{U_j}{\sqrt{gd_p}}$	$1 < \frac{d_j}{d_p} < 1.5$ $83 < U_j (m/s) < 192$ Underpredicts at higher injection velocities
Zenz (1968)	$0.044 \frac{L_j}{d_j} + 1.57 = 0.5 \log(\rho_f U_j^2)$	$32 < U_j (m/s) < 64$ Underpredicts at higher injection velocities
Merry (1971)	$\frac{L_j}{d_j} + 4.5 = 5.25 \left(\frac{\rho_f U_j^2}{(1-\varepsilon)\rho_p g d_p} \right)^{0.4} \left(\frac{\rho_f}{\rho_p} \right)^{0.2} \left(\frac{d_p}{d_j} \right)^{0.2}$	$1.5 < \frac{d_j}{d_p} < 80$ $1.6 \times 10^{-4} < \frac{\rho_f}{\rho_p} < 12 \times 10^{-4}$ $40 < U_j (m/s) < 200$ Best fit for $50 \leq U_j (m/s) \leq 155$

Benjalloun et al. (1995)	$\frac{L_j}{d_j} = 5.52 \left(\frac{\rho_f U_j^2}{(\rho_p - \rho_f) g d_j} \right)^{0.27}$	$1 < Fr < 380$
Hong et al. (1997)	$\frac{L_j}{d_j} + 3.8 = 1.64 \times 10^{-6} \left(\frac{\rho_j U_j^2}{(1-\varepsilon)\rho_p g d_p} \right)^{0.327} \left(\frac{\rho_g}{\rho_p} \right)^{0.1974} \left(\frac{d_p}{d_j} \right)^{-0.04}$	$2.2 < \frac{d_j}{d_p} < 7$ $7.5 \times 10^{-4} < \frac{\rho_f}{\rho_p} < 8 \times 10^{-4}$ $6 < U_j (m/s) < 190$ overpredicts at higher injection velocities

L_j : Penetration length; d_j : Jet diameter; U_j : Jet velocity; d_p : Particle diameter; ρ_p : Particle density; ρ_g, ρ_f : Gas density; H: Horizontal;

Most of the studies reported on such beds are limited to develop the model to find the jet penetration depth (Shakhova, 1968; Zenz, 1968; Merry, 1971; Benjalloun et al., 1995; Chyang et al., 1997; Hong et al., 1997; Al-Sherehy, 2002, 2004). Some limited experimental studies are also performed however, these studies are mostly limited to the rectangular beds and most of these measurements were either based on visual observations or photographic technique. In a dense gas-solids fluidized bed such measurements have limited accuracy.

1.2.3. Applications of Secondary Injection through Nozzles

As mentioned, there are numerous industrial applications of conventional fluidized beds. In many of these applications, like spouted bed coating (Walzel, 1993), fluid catalytic cracking (Avidan, 1992), combustion of liquid fuels (Anthony and Lu, 2001; Barker and Beacham, 1980; Okasha et al., 2003), thermal denitration (Bjorklund and Offutt, 1973; Fane et al., 1974), and metal nitrate waste (Sridhar, 1986) etc., reactant/promoters are injected in the bed through

pneumatic nozzles placed at sidewall. The injection of secondary fluids along with reactant severely affects the performance of the fluidized bed due to change in the flow field. Therefore, over the many decades, researchers are trying to investigate the effect of nozzles on the fluidized bed. Some of the key industrial applications are presented below.

Fluid catalytic cracking

The fluid catalytic cracking (FCC) unit is the second major industrial application in hydrocarbon processing after coal gasification. It is the largest industrial application of fluidization over the period of last 60 years. It has 400 units worldwide (Chen, 2011) and already surpassed by coal combustion (the leading industry) in last 10 years. In FCC, the cracking of long chain of the vaporized heavy hydrocarbon or residues from the crude is occurred in the presence of hot catalyst. The final products are light hydrocarbons such as gasoline, kerosene, diesel and light olefins. The gasoline contents present in the raw crude oil is usually less than 10 %. Thus, FCC becomes so critical operation to generate the high gasoline product (>50 %) with high octane value and sometimes, it is referred as “heart of refinery” (Avindan, 1992; Murphy, 1992; Reichle, 1992). Figure 1.5 shows the schematic of the FCC unit. The feed or crude oil is fed to the riser through nozzles as shown in Figure 1.5. The feed vaporizes during the upward motion of hot catalyst in the riser. The hot catalyst acts as a heat carrier in the process and helps in the vaporization of crude oil. The reaction takes place inside the reactor at the moderate temperature (500-550 °C), with producing lights product in the gaseous phase, which leave the reactor from the top. The deactivated catalyst are then passed through stripper section, acting as gentle fluidized beds with the help of steam, and regenerated by burning of coke accumulated on the catalyst surface.

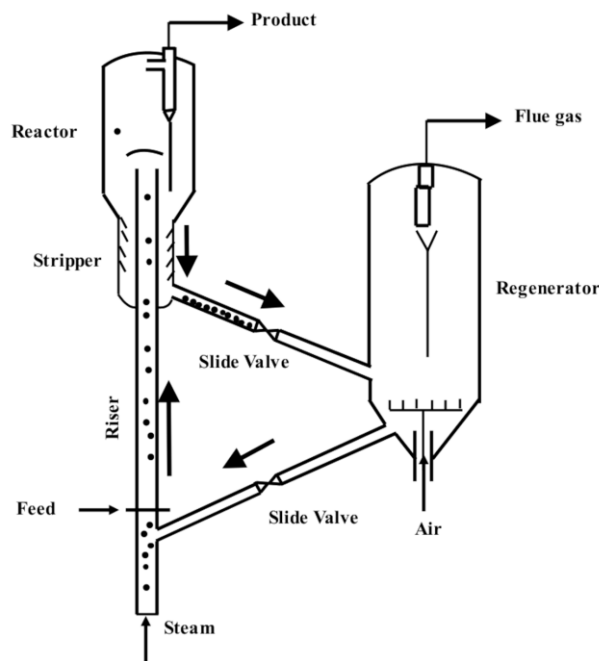


Figure 1.5 Schematic of shell riser FCC unit (Adapted from Kunni and Levenspiel, 1991)

After recirculating the regenerated catalyst into regenerator, which is operated in bubbling fluidization condition by air, the catalyst particles are continuously transported between the riser and regenerator. There are only two disadvantages of dense FCC units: (1) the residence time of gas phase is uncontrolled, and (2) residence time distribution of solids are not uniform. Depending on the applications and type of reactions, the design of FCC unit is still improving.

Coking Process

Another typical example or industrial application of nozzle assisted injection is coking process. It is very often found in petroleum industry. The typical fluid coking process as similar to that operating at Syncrude is shown in Figure 1.6 (Syncrude, 2012). The heavy residual petroleum stocks is injected into reactor part through a set of nozzles placed at the wall of the reactor (Figure 1.6). Long chain hydrocarbons are thermally broken into smaller hydrocarbons by breaking carbon-carbon bonds in the coking process. The parent molecule has the insufficient number of hydrogen atom to produce the corresponding aliphatic hydrocarbons. Hence, the

parent molecule lose the some carbon atoms to produce the lighter product without loss of any hydrogen atoms. Therefore, this is also known as “carbon-rejection process”.

There are two coking processes available in petroleum industry, utilizing the fluidized beds technology, such as the fluid coking process and the flexi coking process. The reactor works at high temperature (480-550 °C) in the bubbling fluidization regime of coke material using the steam at the bottom. The coke particles are Geldart B type. Hence, it is suitable for bubbling fluidization. The atmospheric topped bitumen (ATB), vacuum topped bitumen (VTB), and residue are injected through side nozzles into the reactor. Due to contact with the hot coke particles, the residue is converted into smaller carbon chain products. Some fraction of coke particles is again sent to the burner, heated up (at 590-700 °C), and then supplied to the reactor to carry on coking process. In design perspective, it is always preferred to favour the formation of large bubbles in the fluidized reactor in such process as they can carry the vaporized products at the top of the reactor to minimize the residence time of gaseous products. The large bubbles are also suitable for vigorous mixing of wetted coke particles and dried coke particles to ensure uniform distribution of these particles. In flexi coking, an Exxon technology was implemented. It is an addition of coke gasifier at the end of the line to yield boiler fuel, after sulfur removal (Yerushalmi, 1982).

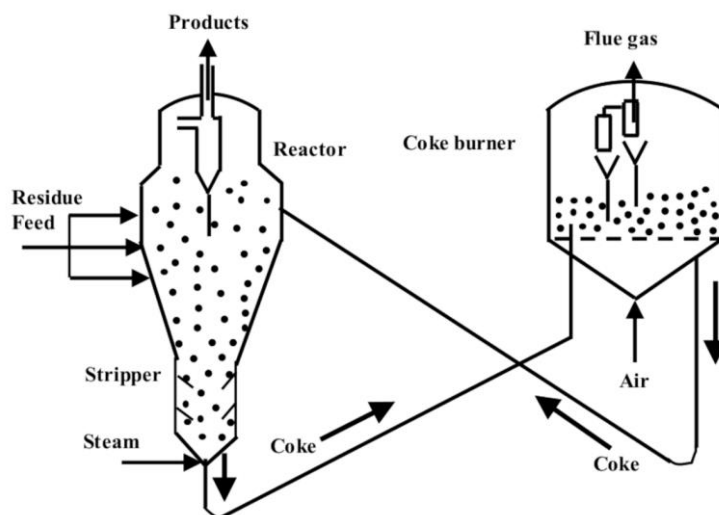


Figure 1.6 Schematic of fluid coking unit (adapted from Syncrude., 2012)

Thermal denitration

Thermal denitration process of ammonium di-uranate (ADU) residue, which is a hazardous waste produced during the processing of uranium, is a suitable way to expose this waste into the surrounding. The ADU residue contains certain amount of nitrate (80-100 g/L) with the radioactive waste. The typical thermal denitrator is shown in Figure 1.7. The thermal denitrator is a bed of silica, which is Geldart B type material, operated under bubbling regime. The ADU residue, containing the ammonium nitrate solution, is supplied to the reactor through the sidewall pneumatic type nozzle systems. The pneumatic type nozzle is useful for atomization process (Lefebvre, 1989). The atomization process helps in the conversion of the feed solution into smaller sized droplets by shearing of high velocity of gas. Thus, the mixture of atomizing gas and liquid droplets leaves the nozzle as a jet, which has enough kinetic energy to penetrate the bed of fluidized silica particles.

After leaving the nozzle, the atomizing gas separates from the jet as a void or bubble. Simultaneously, the particles in the vicinity of the jet regions are coated with the liquid solution, and droplets are deposited on the solid surface. The reactor is operated at high temperature (~350 °C) to proceed the thermal denitration process, which is very low to carry out fuel

combustion process. The sublimation point of nitrate solution is 210 °C. The vaporization of nitrate droplets is not possible to occur because short residence time of droplets. Hence, evaporation takes place within the jet zone. The bed temperature is important for this process. It is reported that the reaction zone length depend on the bed temperature and decreases as the bed temperature increases. Therefore, better heat transfer is most favourable condition to achieve higher conversion.

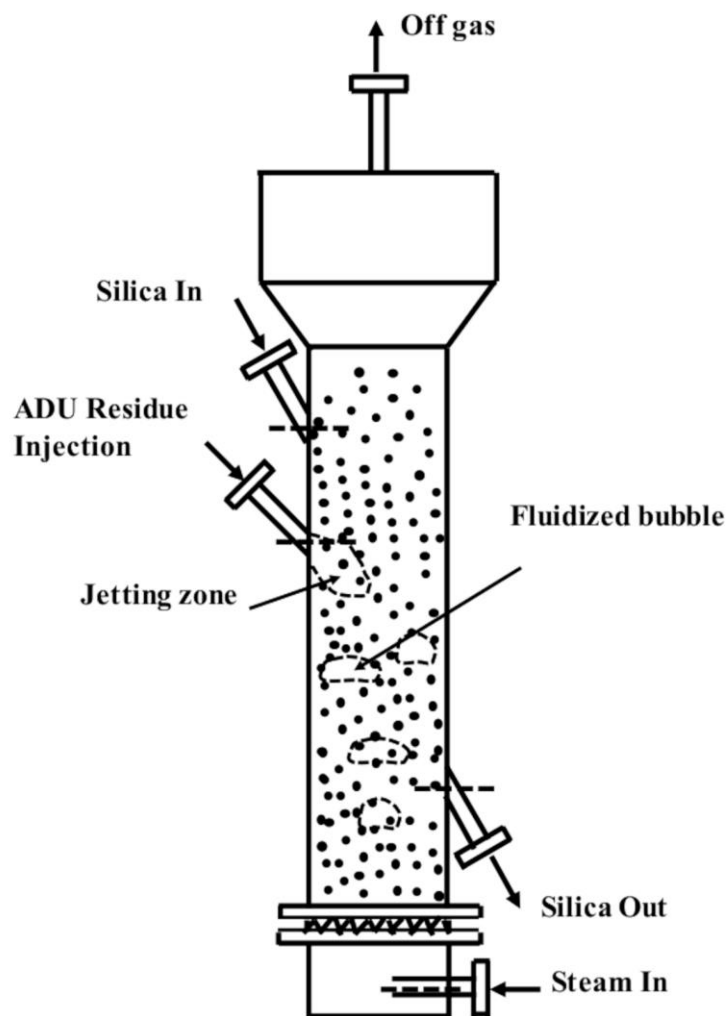


Figure 1.7 Schematic diagram of thermal denitration of ADU unit (Adapted from Bhowmick et al., 2012)

1.2. Motivation

The fluidized bed with pneumatic nozzle injection has wide applications in different industrial processes. However, even after their extensive applications, very few studies are reported on nozzle assisted fluidized bed. Most of these studies are reported for vertical nozzle injections (downward or upward direction). Few studies are available in literature for horizontal nozzle injection into fluidized bed system. Further, most of the studies reported on horizontal nozzle injection systems are based on only visual or photographic observations. The main aim of reported studies has been to find the nozzle injected fluid penetration depth and its dependence on different operating conditions. Further, most of these studies are reported on rectangular columns. Though such columns give an edge for visual observation, the generated data are severely affected by the presence of walls. Limited investigations are reported on single and multiple sidewall nozzle injections system to measure the solid distribution and effect of operating conditions on solid distribution (Koeninger et al., 2017; Koeninger et al., 2018). However, again the main aim of those studies was to find the nozzle penetration depth and solid fraction. The detailed studies on such column to find the velocity profiles of the solids and solid distributions inside the reactor are largely missing. Further, the effect of different operating parameters on behaviour of the such bed particularly in terms of velocity profile and higher order moment of the velocity is also missing. It is also found that limited studies are reported with multiple nozzle injections on the same and different axial plane which is of the great industrial importance. Further, no studies are reported on measurement/calculation of turbulent quantities and find the local bed dynamics of the bed. Further, the effect of different operating parameters on turbulent quantities like fluctuation velocities, rms velocities, granular temperature, solid dispersion etc. are also missing. These parameters are very critical for all the industrial applications discussed above where such beds are used. The effect of different nozzle type and injection assemblies on overall solid flow dynamics are also missing in the

literature. Therefore, the current thesis targets a systematic approach to decipher the flow physics of horizontal nozzle assisted gas-solid fluidized bed. A state of the art non-invasive velocity measurement technique, radioactive particle tracking (RPT) is used to track the motion of the solids. The effect of different operating parameters like primary gas velocity, injected gas velocity are investigated. Further, the effect of different nozzle diameters on solid flow dynamics and solid distribution are deciphered. Finally, the effect of number of nozzle(s) injection on same and different plane and their effect on solid flow field, turbulent quantities and solid distributions are studied. A computational model based on commercially available CFD approach is also developed for the same column and data is validated against the experimental findings.

1.3. The objective of the Thesis

The global aim of the current work is to explore the understanding of the local hydrodynamics of sidewall nozzle assisted gas-solid fluidized beds and optimization of nozzle assembly for such bed. To accomplish these objectives, a state-of-the-art experimentation approach is used to generate the experimental data. The key objectives of the work are as follows:

- Measurements of solid flow field in a single sidewall nozzle assisted gas-solids fluidized bed to investigate
 - Effect of nozzle flow rates
 - Effect of nozzle diameters
- Measurements of solid flow field in a multiple nozzle injection system
 - Effect of nozzle assembly
 - Effect of injection flowrates
- Measurement of solid volume fraction in the sidewall nozzle assisted gas-solid fluidized bed
 - Effect of nozzle flow rates

- Effect of single nozzle or multiple nozzles operating at same/different planes
- Effect of nozzle diameters

1.4. Layout of Thesis

The structure of the thesis is organized as follows. The thesis contains five chapters. The background, applications, motivation and objectives of the thesis are demonstrated in Chapter 1. A brief introduction of the relevant literature available on the nozzle assisted fluidized bed has also been highlighted. In Chapter 2, details of experimental measurement techniques, radioactive particle tracking (RPT) and gamma ray densitometry (GDT), used in current work is discussed. The working principle of these technique, post processing of data and measurement issues for current system is also highlighted in this chapter. Chapter 3, presents the experimental data for one and two sidewall nozzle assisted fluidized bed. RPT experiments are performed to measure the local and mean solid velocity field. The effect of sidewall nozzle injection on the instantaneous, mean and fluctuating velocity profiles of solids are investigated. Further, various turbulent quantities like rms velocities, granular temperature, diffusivity, anisotropic coefficient etc. are calculated. Effect of nozzle injection velocity and nozzle diameter on solid velocity fields are also investigated.

In Chapter 4, experimental data for solid distribution, obtained through GDT measurement, for single and multiple nozzle assemblies are presented. Effect of nozzle diameter and gas injection flowrates on both axial and radial solid distribution are investigated to characterize the behaviour of nozzle assisted fluidized bed. Chapter 5 concludes the overall findings of the current research work with recommendation and future work.

Further, an experimental data with single nozzle injection has been validated using numerical simulation in Appendix. Appendix A, presents the results of Euler-Euler computational fluid dynamics (CFD) simulations based models for single sidewall nozzle assisted fluidized bed. Effect of different drag models and boundary conditions (restitution coefficients and

specularity coefficients) on prediction of flow physics of such beds are presented. Finally, CFD simulation results are validated using RPT and GDT data.

Notations

$Ar = \frac{g\rho_f d_p^3 (\rho_p - \rho_f)}{\mu^2}$	Archimedes number	[-]
C_1, C_2	Empirical constants	[-]
d_j	Nozzle diameter	[m]
d_p	Particle diameter	[m]
D_c	Column diameter	[m]
$Fr^* = \frac{2\rho_g d_j^2 U_j^2}{3\rho_p d_p^3 g}$	Modified Froude number	[-]
g	Gravity	[m s ⁻²]
H	Bed height	[m]
H_j	Axial height of jet injection	[m]
H_{mf}	Bed height at minimum fluidization velocity	[m]
L_j	Jet penetration length	[m]
ΔP_{bed}	Pressure drop of bed	[Pa]
$\left. \frac{dP}{dz} \right _b$	Axial gradient of pressure drop across the bed	[kg m ⁻² s ⁻²]
Re_{mf}	Reynold number at minimum fluidization	[-]

u_j	Nozzle injection or jet velocity	[m s ⁻¹]
U	Gas superficial velocity or fluidization velocity	[m s ⁻¹]
U_{mb}	Minimum bubbling velocity	[m s ⁻¹]
U_{mf}	Minimum fluidization velocity	[m s ⁻¹]
U_{tr}	Transport velocity	[m s ⁻¹]
U/U_{mf}	Fluidization number	[-]

Greek symbols

$\varepsilon_g, \varepsilon_s$	Volume fraction of gas, solids respectively	[-]
ε_{mf}	Volume fraction of gas at minimum fluidization	[-]
μ_g	Dynamic viscosity of gas	[Pa s]
ϕ	Sphericity of particles	[-]
ρ_g	Density of gas	[kg m ⁻³]
ρ_s, ρ_p	Density of solid particle	[kg m ⁻³]
θ_j	Jet angle	[degree, °]

Subscript

mb	Minimum bubbling
mf	Minimum fluidization
s	Solid phase
g	Gas phase

Abbreviation

ADU	Ammonium diuranate
BFB	Bubbling fluidized bed
CFD	Computational fluid dynamics
FCC	Fluid catalytic cracking
GDT	Gamma ray densitometry technique
MFIX	Multiphase Flow with Interphase eXchange
PIV	Particle image velocimetry
RPT	Radioactive particle technique

References

- Al Sherehy, F., 2002. Distributed addition of gaseous reactants in fluidized beds. PhD Thesis. University of British Columbia. BC, Vancouver, BC, Canada.
- Avindan, A. , 1992. FCC is far from being a mature technology. Oil Gas J. 90, 59.
- Babu, S. P., Shah, B., Talwalkar, A., 1978. Fluidization correlations for coal gasification materials-minimum fluidization velocity and fluidized bed expansion ratio. AIChE Symp. Ser. 74 (176), 176-186.
- Basov, V, A., Markhevka, V. I., Melik-Akhnazanov, T. Kh., Orochko, D. I., 1969. Investigation of the structure of a non-uniform fluidized bed. Int. Chem. Eng. 9 (2), 263.
- Bi, H. T., Grace, J. R., 1995b. Effect of measurement method on velocities used to demarcate the onset of turbulent fluidization. Chem. Eng. J. 57, 261-271.
- Bjorklund, W.J., Offutt, G.F., 1973. Fluidized bed denitration of uranyl nitrate. AIChE Symp. 69 (128), 123.
- Bhowmick, S., Rao, H., Sathiyamoorthy, D., 2012. Thermal denitration of ammonium nitrate solution in a fluidized bed reactor. Ind. Eng. Chem. Res. 51, 8394-8403.

Bhowmick, S., Sharma, V.K., Samantray, J.S., Pant, H.J., Shenoy, K.T., Dash, A., Roy, S.B., 2015. Experimental Investigation on Interaction of Side Gas Injection with Gas Fluidized Bed Using γ -ray Transmission Technique. *Ind. Eng. Chem. Res.* 54, 11653–11660.

Chen, Y. M., 2011. Evolution of FCC-Past present and Future-and the challenges of operating a high-temperature CFB system, in Proceedings of 10th conference on fluidized bed technology, Beijing, China, May, p.68.

Chen, L., Weinstein, H., 1993. Shape and extent of the void formed by a horizontal jet in a fluidized bed. *AIChE J.* 39, 1901-1909.

Chitester, D. C., Kornosky, R. M., Fan, L. S., Danko, J. P., 1984. Characteristics of fluidization at high pressure. *Chem. Eng. Sci.* 39, 253-261.

Chyang, C.S., Chang, C.H., Chang, J.H., 1997. Gas discharge modes at a single horizontal nozzle in a two-dimensional fluidized bed. *Powder Technol.* 90, 71–77.

Copan, J. G., 1999. Macroscopic modelling of a fluid bed coker and experimental studies of one and two phase jets. University of Saskatchewan, Saskatoon.

Cleaver, J. A. S., Ghadiri, M., Tuponogov, V. G., Yates, J. G., and Cheesman, D. J. 1995. Measurement of jet angles in fluidized-beds. *Powder Technol.* 85 (3), 221-226.

Dawe, M., Briens, C., Berruti, F., 2008. Study of horizontal sonic gas jets in gas-solid fluidized beds. *Can. J. Che. Eng.* 86, 506-513.

Dewettinck, K., and Huyghebaert, A., 1999. Fluidized bed coating in food technology. *Trends in Food Science & Technology*, 10, (4-5) 163-168.

Deza, M., Heindel, T. J., Battaglia, F. 2011. Effect of mixing using a side port air injection on biomass fluidized bed. *J. Fluids Eng.* 133(11), 111302-(1-9).

Ergun, S., 1952. Fluid flow through packed columns. *Chem. Eng. Prog.* 48, 89-94.

- Filla, M., Massimilla, L., and Vaccaro, S., 1983. Gas jets in fluidized beds-the influence of particle-size, shape and density on gas and solids entrainment. *Int. J. Mult. Flow.* 9 (3), 259-267.
- Geldart, D., 1973. Types of gas fluidization. *Powder Technol.* 7, 285-292.
- Grace, J. R., 1997. *Circulating Fluidized Beds.* 1997th ed. Chapman and Hall.
- Grace, J. R., Lim, C. J., 1987. Permanent jet formation in beds of particulate solids. *Can. J. Chem. Eng.* 65 (1), 160-162.
- Grace, J. R., 1982. Fluidized-bed hydrodynamics. In: *Handbook of Multiphase Systems.* (Hetsroni G, ed.) Washington: Hemisphere, pp 8-5-8-64.
- Harrison D., Davidson J. F., de Kock J. W., 1961. On the nature of fluidized bed. *Trans Inst Chem Eng* 39, 202-211.
- Hong, R. Y., Guo, Q. J., Luo, G. H., Zhang, J. Y., and Ding, J., 2003. On the jet penetration height in fluidized beds with two vertical jets. *Powder Technol.* 133 (1-3), 216-227.
- Hong, R., Li, H., Wang, Y., 1997. Studies on the inclined jet penetration length in a gas-solid fluidized bed. *Powder Technol.* 92, 205-212.
- Koeninger, B., Hensler, T., Schug, S., Artl, W., Wirth, K. E., 2017. Horizontal secondary gas injection in fluidized beds: Solid concentration and velocity in multiphase jets. *Powder Technol.* 316, 49-58.
- Koeninger, B., Koegl, T., Hensler, T., Artl, W., Wirth, K. E., 2018. Solid distribution in fluidized beds with horizontal high speed gas jets. *Powder Technol.* 336, 57-69.
- Kunni, D., Levenspiel, O., 1991. *Fluidization Engineering.* 2nd ed. Boston: Butterworth-Heinemann.
- Lefebvre, A. H., 1989. *Atomization and Sprays.* Hemisphere Publishing Corp. New York.
- Materazzi, M., Lettieri, P., Dodds, J. M., Milliken, A., 2017. X-ray imaging for design of gas nozzles in large scale fluidized bed reactors. *Powder Technol.* 316, 41-48.

Merry, J. M. D., 1971. Penetration of a horizontal gas jet into a fluidized bed. *Trans. Inst. Chem. Eng.* 49, 189-195.

Merry, J. M. D., 1975. Penetration of vertical jets into fluidized beds. *AIChE J.* 21 (3), 507-510.

Murphy, J. R., 1992. Evolutionary design challenge mark FCC process. *Oil Gas J.* 90, 49.

Musmarra, D., 2000. Influence of particle size and density on the jet penetration length in gas fluidized beds. *Ind. Eng. Chem. Res.* 39 (7), 2612-2617.

Reichle, A. D., 1992. Fluid catalytic cracking hits 50 year mark on the run. *Oil Gas J.* 90, 41.

Richardson, J. F., 1971. Incipient fluidization and particulate system. In: *Fluidization*. (Davidson, J. F., Harrison, D., eds.) New York: Academic Press, pp 28-64.

Roach, P. E. 1993. The penetration of jets into fluidized beds. *Fluid Dyna. Res.* 11, 197-216.

Rowe, P. N., 1962. The effect of bubbles on gas-solids contacting in fluidized beds. *Chem. Eng. Prog. Symp. Ser.* 58 (38), 42-56.

Saxena and Vogel., 1977. The measurement of incipient fluidization velocities in a bed of coarse dolomite at temperature and pressure. *Trans. Inst. Chem. Eng.* 55, 184-189.

Shakhova, N. A., 1968. Discharge of turbulent jets into a fluidized bed. *J. Eng. Phys. Thermophy.* 14 (1), 32-36.

Squires, A. M., 1983. *Fluidized Bed Combustion and Application*, Howard, J. R., Applied Science Publishers Barking, p. 278.

Syamlal, M., Rogers, W., O'Brien, T. J., 1993. *MFIX Documentation: Theory Guide*, Technical Note, U.S. Department of Energy. National Energy Technology Laboratory.

Syncrude., 2012. Website of Syncrude, www.syncrude.ca.

Vaccaro, S., 1997. Analysis of the variables controlling gas jet expansion angles in fluidized beds. *Powder Technol.* 92 (3), 213-222.

- Verloop, J., Heerjes, P. M., 1974. On the origin of bubbles in gas-fluidized beds. *Chem. Eng. Sci.* 29, 1101-1107.
- Walzel, P. 1993. Liquid atomization. *Int. Chem. Eng.* 33 (1), 46-60.s
- Wang, S., Yang, Q., Shao, B., Zhao, J., Liu, L., Liu, Y., 2015. Numerical simulation of horizontal jet penetration using filtered fluid model in gas-solid fluidized bed. *Powder Technol.* 276, 1-9.
- Wen, C.Y., Chen, L.H. 1982. Fluidized bed freeboard phenomena: Entrainment and elutriation. *AIChE J.*, 28: 117-128.
- Wen, C.Y., Horio, M., Kirshnan, R., Khosravi, R., Rengarajan, P., 1977. Jetting Phenomena and Dead Zone Formation on Fluidized Bed Distributors. in *Proc. 2nd Pacific Chem. Eng. Cong. Nagoya, Japan.*
- Wen, C. Y., Yu, Y. H., 1966a. A generalized method for predicting the minimum fluidization velocity. *AIChE J.* 12, 610-612.
- Winkler, F., 1922. Verfahren zum Herstellen Wassergas. Patent DE437970C.
- Wilhelm, R. H., Kwauk M. 1948. Fluidization of solids particles. *Chem. Eng. Prog.* 44, 201-217.
- Wurster, D. E., 1953. Method of applying coatings onto edible tablets or like. USA Patent No. 2 648, 609.
- Xuereb, C., Laguérie, C., Baron, T., 1991. Etude du comportement de jets continus horizontaux ou inclinés introduits dans un lit fluidisé par un gaz I: Morphologie des jets. *Powder Technol.* 67, 43–56.
- Yang, W. C., Keairns, D. L., 1979. Estimating the jet penetration depth of multiple vertical grid jets. *Ind. Eng. Chem. Fund.* 18 (4), 317-320.
- Yerushalmi, J., 1982. Applications of fluidized bed, Chapter 8.3 in *Handbooks of Multiphase Systems*, Hetsroni, G. (Ed.), Hemisphere Publishing Co., Washington, DC.

Zenz, F. A., 1968. Bubble formation and grid design. *Inst. Chem. Symp. Ser.* 30, 136-139.

Zhang, K., Pei, P., Brandani, S., 2012. CFD simulation of flow pattern and jet penetration depth in gas-fluidized beds with with single and double jets. *Chem. Eng. Sci.* 68, 108-119.

Zhang, K., Zhang, J. Y., and Zhang, B. J., 2004. CFD simulation of jet behaviour and voidage profile in a gas-solid fluidized bed. *Int. J. Energy. Res.* 28 (12), 1065-1074.



Chapter 2 Experimental Setup and Measurement Techniques

Scope

This chapter summarizes a brief review of the key measurement techniques used for the measurements of flow quantities like phase fraction, phase velocities and other turbulent quantities to decipher the flow field in detail. Initially, a brief overview of the contemporary techniques is presented. The techniques used in this work, gamma-ray densitometry and radioactive particle tracking (RPT), are explored in detail later. Finally, the experimental setup used in the current work is discussed along with implementation strategy of gamma-ray densitometry and RPT technique.

2.1. Introduction

It has been realized in recent decades that a proper investigation of the gas-solids fluidized bed reactors demands the use of sophisticated measuring techniques with capability to provide the required information over the entire flow field, as well as time, at multiple scales (Chaouki et al., 1997; Upadhyay, 2010; Kamalanathan et al. 2017). Aside from the mean velocities and volume fractions, information about the flow fluctuations or dynamics (quantified in terms of cross-correlations and auto-correlations) is also desirable. In addition, it is preferable if such techniques are amenable to automation to reduce extensive human involvement in the data collection process. While such data are “stand-alone” sets of information which would direct design and scale-up strategies, it also provides information that is crucial to establish the validity of conventional models like phenomenological flow models describing Residence Time Distribution (RTD), as well as more recent and sophisticated models like those based on Computational Fluid Dynamics (CFD). In fact, it almost seems imprudent to validate CFD predictions on overall holdup and flow rates, because for CFD

model, the later are only integrals based on local information (both in time and space), that are computed with fidelity. Thus, fair validation must involve at multiple scales, for which one needs experimental information also at multiple scales.

Several experimental techniques have been reported in literature to quantify the flow field in gas-solids fluidized bed reactors, with each technique having its own advantages and disadvantages (Chaouki et al., 1997; Upadhyay, 2010; Kamalanathan, 2017). Mainly information regarding phase distribution and velocity fields along with the turbulent quantities are required to decipher the complete flow field of any gas-solid reactor. Different invasive and non-invasive techniques are used to measure these quantities in gas-solid reactors. The details of some key techniques which are widely used to measure phase fraction and velocity fields along with turbulent quantities are given below.

2.1.1. Void Fraction Measurements Techniques

There are several techniques that are continuously being used for measurements of phase fraction in the gas-solid reactors. These are:

Pressure Gradient Method

The most commonly used technique to measure the phase fraction at industrial level is pressure gradient method. In this method pressure difference is measured between two planes in which solid/gas phase fraction needs to be measured. The pressure difference is measured through manometer or differential pressure transducers. Once the pressure difference is recorded the volume fraction of solid in fluidized bed is measured by using equation 2.1.

$$\frac{\Delta P}{L} = (\rho_g - \rho_s)(1 - \varepsilon_s)g \quad (2.1)$$

Where, ΔP is the pressure drop measured across the bed; L is the distance between the two pressure probe; ρ_s and ρ_g are the solid and gas density, respectively; ε_s is the solid fraction in

the system. However, large fluctuations are observed in pressure drop reading due to continuous coalescence and breakage of the bubble in the bed which leads to uncertainty in phase fraction data calculated through pressure drop measurement. Further, it provides volumetric average phase fraction data instead of local or cross sectional average solid/gas fraction.

Electrical Capacitance Tomography

Electrical capacitance tomography (ECT) is a non-invasive measurement technique. It utilizes the basic facts that the dielectric constant of solids and gas used in gas-solid system is quite different. In ECT, several electrodes are used to cover the entire cross-section of the bed to provide full three dimensional pixel wise distribution of dielectric constants of solids and gas in the gas-solid system (Weber and Mei, 2013). Generally, 8 to 16 electrodes are used based on column diameter and resolution required. The electrodes are excited one by one by providing a voltage to one particular electrode and maintaining other electrode at reference potential. The capacitance value between the excited electrode and other electrodes are collected. Similarly, other electrodes are excited and capacitance values are noted down. Hence, a total $n(n-1)/2$ measurements are performed for n number of electrodes used in the experiment. The permeability distribution in the bed is calculated by using these measured capacitance values. The governing equations which are solved to measure the permittivity distribution are:

$$\nabla \alpha(x, y) \nabla \varphi = 0 \quad (2.2)$$

$$C_{ij} = \frac{1}{\Delta V_{ij}} \oint \alpha(x, y) \nabla \varphi dA \quad (2.3)$$

Here, $\alpha(x, y)$ is the permittivity distribution in the measuring plane; φ is the electric potential field; C_{ij} is the measured capacitance between electrodes i and j , and ΔV_{ij} is the applied voltage difference between the excited electrode and other electrode over the pair ij , and A is the surface

area of the electrode. The phase distribution is directly related with the permeability distribution.

Image reconstruction based on 'so-called' inverse problem (determining the permittivity distribution from capacitance measurement) possesses the major challenge and limits the accuracy of the measurement. Further, the temporal resolution of the technique is very high but spatial resolution is relatively poor (Upadhyay, 2010; Kamalanathan, 2016).

Gamma-ray and X-ray Based Techniques

Gamma-ray and X-ray tomography have been used for investigation of gas-solid systems for the past three decades. The continuous development of gamma and X-ray technique is mainly due to the medical imaging. Basically, Gamma ray and X-ray tomography are based on the transmission tomography principle which uses the fundamental property of matter to attenuate the light. Both X-ray and gamma ray are the electromagnetic radiation, when it is passed through the attenuating medium; the intensity of emitted beam reduces. The reduction in the intensity of emitted beam can be found by using Beer Lambert law. Effective mass attenuation coefficient can be calculated from both emitted and detected intensities if the length of the transmission is known. However, this effective mass attenuation coefficient calculated gives the line averaged values and not the point values. For measurements of solid fraction in gas-solid system, these kinds of line-averaged values are used by several authors (Upadhyay and Roy, 2010; Bhowmick et al., 2015; Yadav et al., 2016) as it is non-invasive and simple to measure and usually called as densitometry (first generation tomography).

In densitometry technique, detector and collimated source are placed in line in such a way that the detector centre and source centre are collinear. The investigation system is placed in between the source and detector. To obtain the mass attenuation coefficient, the individual attenuation coefficients of the phases (Gas and solid, it should be noted that attenuation coefficient of most of the gases are negligible) are obtained by measuring the intensity of the

transmission at the empty bed, packed bed and at actual operating conditions in gas-solid system. From, the mass attenuation coefficients, chordal average volume fraction can be computed. This technique provides good spatial resolution however the temporal resolution is low. The use of X-ray system for densitometry experiment is difficult as in such system one need to move the column as X-ray production system is very bulky and it is almost impossible to move it. Hence, in the current thesis gamma-ray densitometry method is used to measure the phase fraction in fluidized bed. The details of gamma-ray technique is explained later.

2.1.2. Velocity Measurement Techniques

In this section, the key techniques used to measure the solid velocity fields in gas-solid fluidized bed system are reviewed. Similar to the volume fraction measurement technique, velocity measurement techniques can also be classified as invasive and non-invasive. The invasive technique used intrusive probes to measure the velocity fields which mostly disturb the flow field. Further, due to high solid fraction, the intrusive probes are damaged frequently. Hence, in gas-solid systems, mostly non-invasive techniques are used. Some of the key non-invasive techniques used in gas-solid fluidized bed systems are discussed below:

Laser Doppler Velocimetry (LDV)

Laser Doppler velocimetry is well established, non-intrusive measurement technique for point measurement of local velocity fields. LDV was invented by Yeh and Cummins (1964). In LDV, velocity of a moving object is found by illuminating it using laser light and measuring the Doppler shift in the frequency of the light scattered by the moving element. Figure 2.1 describes the principle of LDV. For the light source, particle acts as a moving observer and which in turn acts as a moving source for the detector / receiver. Light scattered by the seeded particles is proportional to the velocity of the particle (Roy et al., 1997).

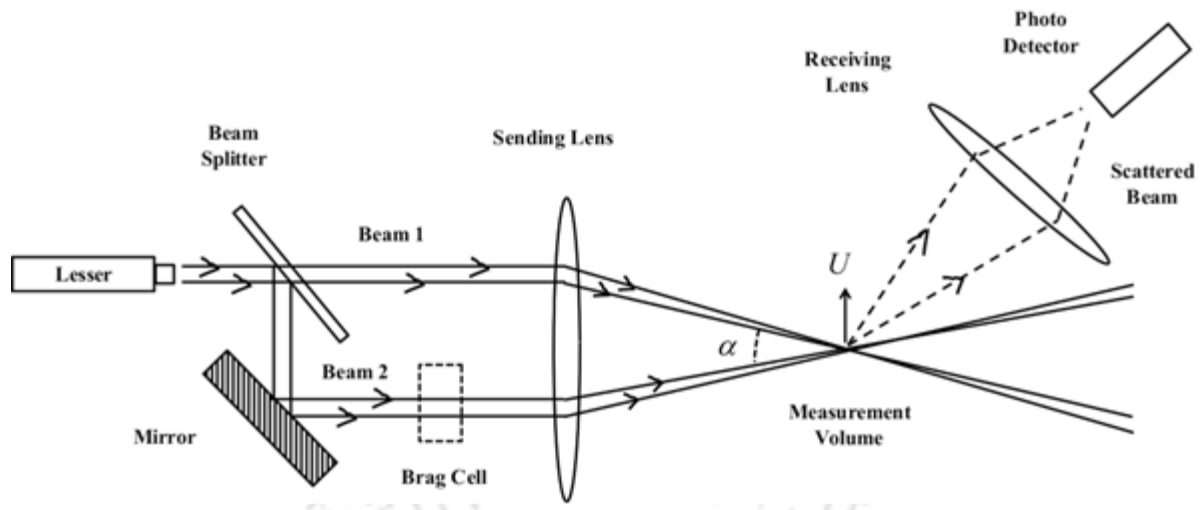


Figure 2.1 Schematic of LDV system in forward scattering mode (Adapted from Durst et al. (1981))

In case of gas-solid fluidized bed mostly solids present in the bed are used as seed particles. The scattered beam of light results into a modulated signal, also called Doppler burst, of the frequency, f as given by the following expression:

$$f = \frac{u}{d} = \frac{u\lambda}{2 \sin(\alpha / 2)} \quad (2.4)$$

Where, d is the fringe width. LDV spatial and temporal resolution is very high and unlike most of the velocity measurement technique, it does not require any tedious calibration. However, the major issue with LDV implementation in gas-solid system is scattering of the light due to presence of discrete phase (solid in case of gas-solid system). The scattering becomes more critical when solids of different sizes are present in the system and/or when solid fraction inside the bed is more than 5-10%. These two are the most common feature of any gas-solid systems. Hence, with LDV one can get the information only near the wall and not at entire volume for gas-solid fluidized bed (Upadhyay, 2010).

Particle Image Velocimetry

Particle image velocimetry (PIV) is a non-intrusive, optical based technique like LDV. Unlike LDV, PIV provides the full field instantaneous velocity information. Figure 2.2 shows the schematic of the PIV measurement technique which is adopted from Dantec Dynamics.

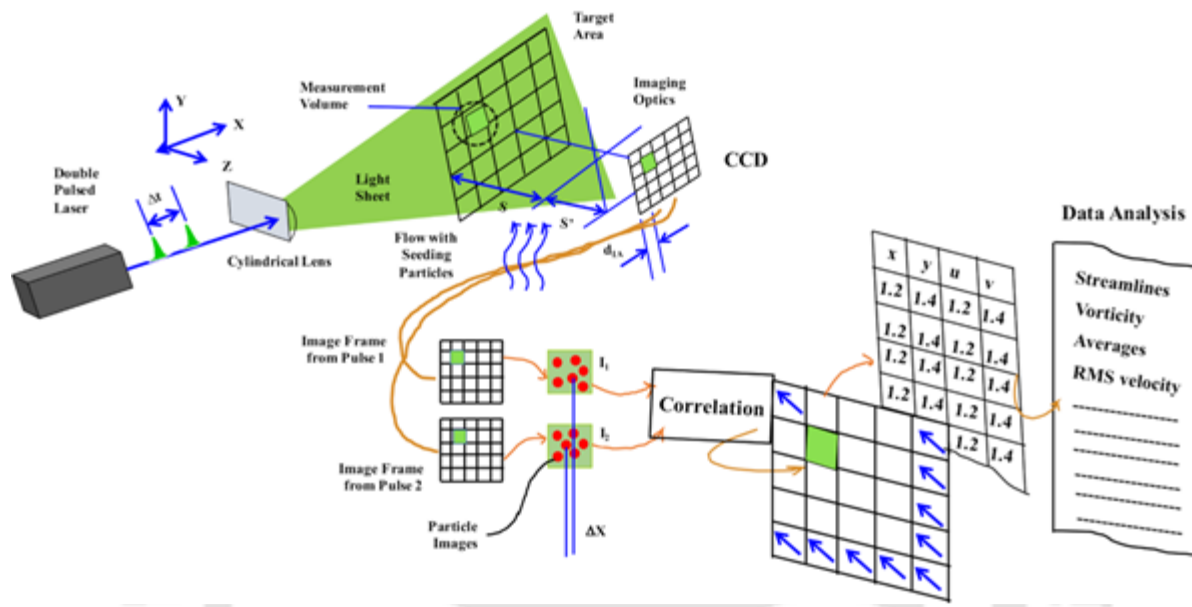


Figure 2.2 Description of PIV techniques (Adapted from Dantec Dynamics)

In PIV, a laser sheet is used to illuminate the flow system and the image of solid particles (or seeded particles) is captured at a successive time interval (Adrian, 1991). To measure the complete flow field several seed/solid particles are tracked. However, it is not possible to measure the displacement of each seed particle. Therefore, each image is divided into a small cell area called as interrogation cell. A cross-correlation algorithm is used to analyze the image and to find the displacement in the cell. The velocity is calculated by using $\Delta x/\Delta t$, where Δx shows the displacement of the cell and Δt is the time between two successive images. Similarly, all the components of the velocity can be obtained with the use of a stereoscopic arrangement. However, similar to LDV, PIV can also not be used for high solid fraction system due to large scattering of the light beam (Bokkers et al., 2004). Hence, the application of PIV for gas-solid bed is mostly limited to fast fluidized bed where solid fraction is generally less than 10%.

Radioactive Particle Tracking (RPT)

Radioactive particle tracking (RPT) is a gamma-ray based non-invasive flow measurement technique that provides the complete instantaneous field information. In RPT, the motion of a 'single' radioactive particle which is the marker of the phase, is tracked. In case of gas-solid system the tracer (radioactive) particle size, shape and density is kept same as of the other solids present in the bed (Lin et al., 1985, Roy et al., 2005; Limtrakul et al., 2005; Upadhyay et al., 2010; Kalo et al., 2019). The motion of this single tracer particle is tracked by using several specially designed scintillation detectors which are strategically placed around the vessel of interest. All the detectors simultaneously acquire the photons emitted by the tracer particle. This photon count time series acquired for each detector is used to reconstruct the position of the tracer particle by using suitable reconstruction algorithm. Thereafter, the local velocity fields is calculated from time differencing of the two successive particle locations (Devanathan et al., 1991; Larachi et al., 1994; Kiared et al., 1997; Chen et al., 1999; Cassanello et al., 2001; Roy et al., 2005; Upadhyay et al., 2013; Kalo et al., 2019) . From this local velocity time series several flow quantities like mean velocities, fluctuation velocities, rms velocities, granular temperature, and other turbulent quantities are calculated by using suitable post processing algorithm (Cassanello et al., 1995; Roy et al., 2002; Roy et al., 2005; Upadhyay et al., 2013; Kalo et al., 2018). Due to the high penetration ability of gamma-ray, this technique is preferred for gas-solid system compared to others. Hence, in current thesis RPT is used to map the solid velocity fields and other turbulent quantities in gas-solid fluidized bed. The details of the technique, reconstruction algorithm and post processing methods to calculate the flow quantities are explained in section 2.3.

Positron Emission Particle Tracking (PEPT)

Positron emission particle tracking (PEPT) is also a radiation based technique similar to RPT. However, in case of PEPT instead of gamma-ray source a positron source (mostly F-18, Na-

22, Cu-61) is used. In PEPT, a single tracer particle (positron source) is introduced into the system. The size, shape and density of this positron source is same as of the solids present in the flow. The positron emitted by tracer particle annihilates with the electron present in the material surrounding the tracer which produces two back to back gamma rays of 512 KeV energy. These gamma-ray is detected by a specially designed detector which covers the entire column, representing the line passing through the tracer particle. Several such lines are detected simultaneously which are used to find the position of the tracer particle. It is important to note that in PEPT only simultaneously detected back to back gamma-rays are counted. The position time series obtained from the experiment is used to calculate the local velocity fields and other flow quantities. The hardware used (detector system) used in PEPT is very costly. Hence, it is available in only University of Birmingham, UK, with Professor Parker's research group (Parker et al., 1993, 1996; Laverman et al., 2012; Medrano et al., 2017). Further, due to the limited energy, PEPT cannot be used for large system.

2.2. Gamma-Ray Densitometry Techniques (GDT)

The application of a non-invasive gamma-ray technique, based on the attenuation principle of radiation, has been started in the 1950s and has a wide impact on different industrial sectors especially in petrochemical. This measurement technique is most versatile due to non-intrusive in nature, relatively inexpensive, reliable, portable, and feasibility to measure in one-shot. If the intensity of a beam of radiation incident on a body is I_0 , and the intensity after the radiation passes through the body is I , then the attenuation function is defined as the ratio I/I_0 . Since each photon is an independent entity, the attenuation function also reflects the “probability” that a photon entering the object of interest eventually leaves the object of interest and continues on its path, without any interaction with the material of the medium. The measurement I/I_0 is referred to as a **projection** measurement. The attenuation of any beam of radiation depends on the property called “total attenuation coefficient” (product of the linear attenuation coefficient,

(m^{-1}) and density (kg/m^3)), and is a function of the distance the beam travels in the medium. The intensity of any energetic beam passing through a medium follows Beer-Lambert's law, as given by the following equation 2.5.

$$\frac{I}{I_0} = \exp(-\mu\rho l) \quad (2.5)$$

Where I and I_0 are the count rates measured in the presence of an attenuating medium and in the vacuum, respectively; ρ and μ are the density and linear attenuation coefficient of the intervening medium; and l is the total length of the path travelled across the medium by radiation. Thus, a denser medium (such as a solid) attenuates more radiation (hence leads to a higher decrease of photon counts) while a lighter medium (such as a gas) causes less attenuation. Therefore, if the attenuation of a controlled beam of radiation by an intervening medium can be quantified or measured, then this information can be used to back-calculate the density of the medium.

In tomography, many projections are taken in a cross-sectional plane and the entire set of projections are used to reconstruct the density distribution in a cross-sectional plane (two-dimensional transmission tomography), or more recently, the density distribution in a three-dimensional volume (three-dimensional transmission tomography). In order to make the data acquisition faster, in a typical tomography setup, many detectors are used together for simultaneous acquisition of projections (such as in a medical CT scanner). However, without any loss in theoretical error, the same process can be undertaken by measuring *one projection at a time*, and this can be done in a densitometry (as done commonly in medical diagnostics in bone densitometry). Thus, conceptually there is no difference between the two measurement methods, and the difference lies only in the way the data are acquired.

In the densitometry setup, a single detector and a single collimated source are aligned together on a moving carriage. At one end of the carriage, a scintillation detector (NaI(Tl)) is fixed, and at the other end a lead-collimated gamma ray source is positioned. The column of interest (such as fluidized bed) is suitably positioned between detector and source. There is an arrangement to move this carriage both in horizontal and in vertical directions, step-wise. As indicated earlier, by using Beer-Lambert's law, the phase holdup can be calculated along the chord along which the attenuation in the radiation is measured and from that the time-averaged chordal averaged phase volume fractions of any two-component system (ε_1 and ε_2) may be deciphered (Roy et al., 2001; Upadhyay et al., 2009; Upadhyay, 2010) :

$$\mu = \mu_1 \varepsilon_1 + \mu_2 \varepsilon_2 \quad (2.6)$$

$$\varepsilon_1 + \varepsilon_2 = 1 \quad (2.7)$$

Where, μ is the average mass attenuation coefficient of medium and μ_1 and μ_2 are the individual (single medium or single material) mass attenuation coefficients of phases 1 and 2, respectively.

2.2.1. Implementation of GDT: Current Work

In order to investigate the solid distribution in the present work, experiments are performed in a laboratory scale setup via GDT measurements. To serve the purpose, an experimental setup integrated with multiple nozzles is designed and fabricated in such a way so that GDT can be implemented. The designed setup has customized functionality such as integration of one or more secondary injections at one/different planes as per the requirements. In addition, several uniform size ports (ID=2 mm) were made to perform pressure measurements (or calibration in velocity measurements).

Figure 2.3a shows the schematic diagram of experimental setup. A mild steel cylindrical column of 21 cm internal diameter and 2250 cm height is used as fluidized bed in this case. The setup has three different sections. The bottom section is used as a plenum and provides uniform distribution of primary gas (such as air) as shown in Figure 2.3a. The middle section is occupied with solid particles which can be fluidized with the up flow of primary gas (or air) through the air distributor. The air-distributor is made of a circular mild steel plate with a several number of uniform size holes (2 mm). The top section (with large internal diameter of 31 cm and height of 750 mm) is used to avoid the entrainment of the solids at high gas velocity.

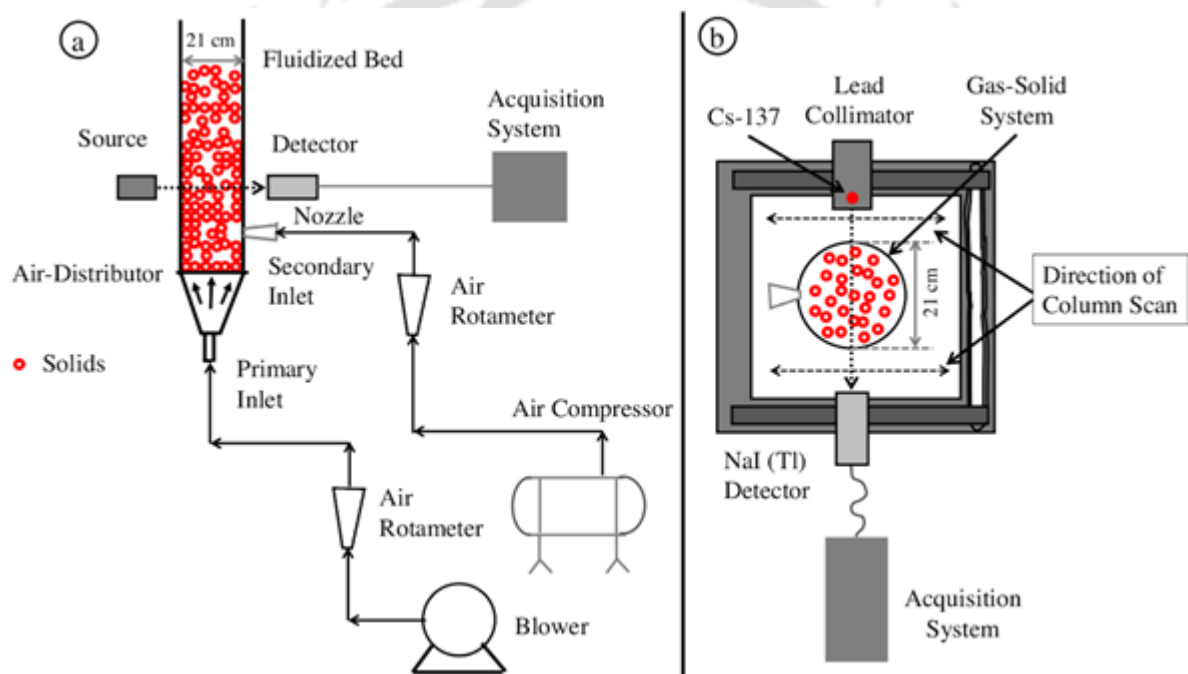


Figure 2.3 Schematic diagram of (a) experimental set up and (b) γ -ray densitometry set up

Three layers of multiple secondary inlets (three inlets per layer) are provided at the periphery of the middle section at fixed axial location. These layers are located at 20 cm, 40 cm and 60 cm distance from the distributor level. These inlets at the column wall can be used as the side injection. The side injection is provided through a nozzle which has flexibility to inject the secondary gas at different angles. The secondary gas is supplied to the bed from an air

compressor which is reciprocating type compressor. The primary air is supplied from a twin lobe blower. Blower and compressor can be operated upto 12000 LPM at 7000 mm WG (water guage) pressure and 1000 LPM at 12 bar pressure, respectively.

Experiments are performed with glass beads (Geldart B type) of mean diameter of 709 μm and particle density of 2500 kg/m^3 . The fixed amount of solids is fed into the column and bed height is maintained (at 75 cm in this case). The bed occupied with solid particles is operated under a finite range of primary gas superficial velocities (0 - 1.25 m/s) without any side gas injection and the bed pressure drop is measured by acquiring the pressure fluctuation with two pressure transducers. The minimum fluidization (U_{mf}) velocity of particles were measured and found to be 0.36 m/s.

For conducting the experiments at a fixed operating condition, an in-house GDT setup has been installed in the laboratory. For this purpose, a rectangular platform is designed in such a way so that the multiphase system can be placed inside the scanner and easily accessible in two dimensional movement. This platform is required to support the detector and the radioactive source as shown in Figure 2.3b. As mentioned above, detector and source are collinearly aligned and placed across the scanning system. The axial movement of the platform allow the user to scan the system at a fixed height. Similarly, the radial movement of detector and source (as both are connected and aligned) provide finite number of projections (S_i) during the scan of the system (refer Figure 2.4a) at any vertical height. The single chord S_1 in Figure 2.4a represents the path of the transmitted ray which passes through scanning medium. Thus, chord S_1 is a single projection formed during the radial scan of the system. Therefore, a finite number of projections are available at any horizontal plane which can be further used to infer the phase distribution (such as solid fraction $\epsilon_s(x_i)$). For extracting $\epsilon_s(x_i)$, at any point x_i , three scans are conducted at different bed conditions: column filled with solids (packed bed), column filled

with only gas phase (empty bed), and required operating condition (two-phase present). Figure 2.4b shows the photograph of GDT setup.

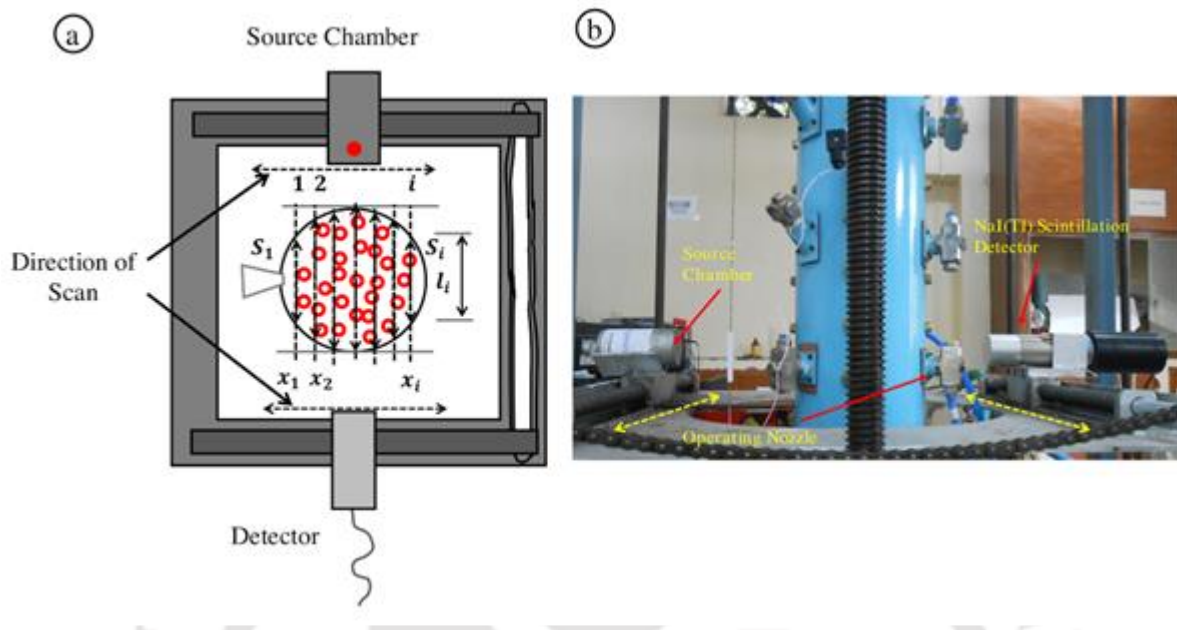


Figure 2.4 Schematic representation of source and detector assembly during column scanning in a horizontal plane. (b) Photograph of GDT setup

The detail of the components or hardware used in the implementation, are summarised as follows:

Nozzles

For the secondary air injection at the sidewall, twin fluid (TF) type nozzles are used. The TF type nozzles are usually used in the atomization process in which liquid is allowed to flow at the annular space and gas at the axis with high velocity. In the current work, two different sizes (or diameter) nozzles are employed to investigate its effect on fluidization. The nozzles (Type 1/2 J BSPT AIR ATOM) are purchased from S. S. Co. R. The set-up has a total nine ports at three axial locations to mount the nozzles. Three nozzles can be operated simultaneously, with 120° apart from each other at a fixed axial position (z). In GDT experiments, two different size nozzles (ID = 1 mm and 6 mm) are used for secondary gas injection. The secondary gas

injection can be horizontal (or perpendicular to the primary gas injections), inclined downward (at 45° to the column wall) and incline upward (at 45° to the wall) as shown in Figure 2.4b.

Caesium-137

The caesium-137 (**Cs-137**) radioactive particle (of activity 7 mCi and half-life 30 years) was used in GDT experiments. It is a gamma-ray emitting source. The mechanism involved in the emission of gamma-ray is available in literature. The Cs-137 particle was supplied from the Bhabha Atomic Research Center (BARC) and licensed by the Board of Radiation and Isotope Technology (BRIT). The source was kept inside a lead chamber to avoid the unwanted radiation falling on the detector surface when it is passed through the test section. A single narrow beam was allowed to pass through the lead chamber from a small opening.

NaI (Tl) Detectors

In GDT experiment, the scintillation detector are used for detection of gamma ray which passes through the multiphase system. It is notable that the detector and source are always placed co-linearly across the column as shown in Figure 2.4b. In current experiments, a NaI (Tl) (2 in x 2 in crystal size) based scintillation detectors is used. This detector has three main components: an inorganic crystal such as NaI (Tl), photo multiplier tube (PMT) and dynodes. The function, structure and applications of these component are available in literature (Upadhyay, 2010; Kamalanathan, 2016).

2.3. Radioactive Particle Tracking Method

Radioactive particle tracking (RPT) is a novel non-invasive flow mapping technique that holds promise for probing multiphase systems. In radioactive particle tracking technique, a tracer particle which encapsulates a high energy gamma ray source is used as the marker of the phase whose velocity is to be mapped. The underlying idea is that a suitably designed tracer particle should be able to hermitically follow the phase it is designed to trace. For example, if the phase of interest is a liquid, the particle is designed to be neutrally buoyant with that phase. If the

phase of interest is a granular solid, then the tracer particle is designed to have the same shape, size and density as a typical entity of that granular phase.

The path of tracer particle is tracked with the help of scintillation detectors, which are strategically placed around the vessel of interest. During the actual experiments the tracer particle is allowed to move freely inside the vessel. The position of the tracer particle is determined by an array of scintillation detectors that monitor the γ -rays emitted by the tracer particle. The intensity of radiation recorded at each detector decreases exponentially as the distance between the particle and detector increases. In order to estimate the position of the tracer particle from the measured radiation intensities, a calibration step needs to be performed prior to a RPT experiment by placing the tracer particle at various known locations and monitoring the radiation recorded by each detector (Roy et al., 2005; Upadhyay, 2010; Kalo et al., 2019). Using this information calibration curves are established that relate the intensity received at a detector to the distance between the tracer particle and detector. Further, appropriate reconstruction algorithm is used to reconstruct the position of the tracer particle at a given sampling time. Thereby, a sequence of instantaneous position data is acquired that yields the position of the tracer particle at successive sampling instant. It may be recognized that this instantaneous position time series of tracer particle has Lagrangian character. Time differencing between two successive particle positions yields the instantaneous velocities as a function of time and position (Lagrangian velocities), which is averaged at each spatial location. Over the whole time span, this yields the ensemble averaged velocity flow map. The difference between the time averaged velocity and instantaneous velocity yields the instantaneous fluctuation velocity. Various turbulent parameters can be calculated with the help of these velocities.

Beside these quantities several other parameters like dispersion coefficient, autocorrelation coefficient, Hurst exponents, time of flight and residence time distribution can also be

calculated by using RPT experimental data (Roy et al., 2005; Kalo et al., 2018, 2019). In some instances, dynamic time series analysis of RPT data has been presented as a potential method to distinguish flow regimes in multiphase reactors (Cassanello et al., 1995; Fraguio et al., 2006; Kalo et al., 2018, 2019). The RPT is not a new technique and is being used from decades. Every researchers have contributed some part to improve the RPT technique and its implementation on multiphase flow reactors. The development history of the RPT is given below.

2.3.1. Development History of RPT

The first application of RPT was started in the 1960s to measure the full flow field map of solid-phase on gas-solid fluidized beds (FBs) and spouted beds by Kondukov et al. (1964), Borlai et al. (1967) and van Velzen et al. (1974). The lack of instrumental and computational facility were observed in their work and hence, an updated version of RPT facility was developed to study solid dynamics in the gas-solid FBs at the University of Illinois at Urbana Champaign (Chen et al., 1983; Lin et al., 1985; Sun et al., 1988; Moslemian et al., 1989). Thereafter, two more upgraded model of RPT came up. These set up were installed at Florida Atlantic University (FAU) and Chemical Reaction Engineering Laboratory (CREL) at Washington University. The FAU-CREL facility was utilized to quantify the velocity fields associated with liquid phase (Devanathan et al., 1990; Dudukovic et al., 1991; Yang et al., 1992; Moslemian et al., 1992), the Reynolds stresses and dispersion coefficients (Moslemian et al., 1992; Yang et al., 1993), the mixing in bubble columns (Kumar et al., 1994). Further, the RPT was also employed in gas/liquid-solids FBs (Roy et al., 1994; Cassanello et al., 1995; Godfroy et al., 1997; Larachi et al., 1996). Thereafter, RPT was established in IIT Delhi, India and the same was applied to study gas-solid binary fluidized bed, bubble column and gas-liquid-solids reactors (Upadhyay, 2010, Yadav et al., 2019)). In year 2012, another RPT setup was installed in IIT Guwahati and applied to investigate flow physics in conical fluidized bed, circulating fluidized bed and bubble columns (Kamalanathan, 2016; Kalo et al., 2018, 2019).

A RPT facility has also been implemented in Argentina, in the National Commission of Atomic Energy, and experiments in liquid-solid fluidization have been performed (Fraguio, 2010; Salierno, 2016; Salierno et al, 2018; Maestri et al., 2019).

Prominent findings measured with RPT in various multiphase reactors are reviewed briefly in Table 2.1. The implementation of RPT in the present work is discussed in detail in the next section. Further, the working principle of RPT and post-processing of RPT data are also briefly discussed thereafter.



Table 2.1 Review of RPT works conducted in different multiphase flow systems

Researchers/ Group of researchers	System type/ size	Bed media	Measurement Methods	Remarks
Solid Flow Measurement in Gas Fluidized Beds				
Lin 1985	FB; GS system; Plexi-glass column; $D_C = 13.83$ cm;	Two size GB with 0.6-0.8 mm & 0.42-0.6 mm (2500 kg/m^3);	RPT experiments were conducted with $32 < U < 89$ cm/s by using the Sc- 46 tracer particle to identify the solid circulation cell in the bed. In addition, the mean velocities in axial and radial direction were also evaluated.	The bed exhibited a toroidal vortex consist of an upward solid motion near the wall and downward motion at the wall region for the low gas velocity. Similarly, the pattern was reversed at high velocity..
Roy et al., 1994	GS system; SB; Plexiglas column; $D_C = 0.152$ m; With conical base 60°	GB particles with different sizes; $1.25 < U_{\text{air}} < 1.92$ m/s	RPT was used to evaluate the cycle time distribution, spout shape, the solid mixing time and velocity fields of particle. The mean axial and radial	The time-averaged angular velocities found to be negligible (or close to zero). At the spout region ($z=375$ mm), the mean axial velocity of a particle was positive at the core while

			velocities were plotted at three different axial levels	negative near the wall region. At the same level, mean radial velocity increased to attain the maximum value as for $0 < r < R$ region but again began to decelerate as r close to the wall (or R) due to particle wall collision.
Godfroy et al., 1996b	CFB; GS system; $D_C = 82$ mm; $H_C = 7$ m;	150 μ m sand particle (2500 kg/m^3); circulation rate of 25 kg/m^2 by $U_{\text{air}} = 4$ m/s .	RPT was performed in the fully developed zone ($4 \text{ m} < z < 5 \text{ m}$) to measure the velocity fields of solid particles by using 500 μ m Au-198 radioactive tracer (2000 kg/m^3).	The parabolic shape of the mean axial velocity of particles was observed in the experiment. The axial motion of the particle was upward at the core region and downward at the wall region.
Kamalanathan (2016)	GS-system, CFB1: $D_C = 0.052$ m; $H_C = 3.2$ m; CFB2: $D_C = 0.1$ m;	500 μ m glass beads (2500 kg/m^3); For CFB1: $U_g = 6.7, 7.0, 7.3,$ 7.8, 8.8 and 9.6 m/s .	RPT was performed in CFB1 at 1.2 m to 2.2 m from the bottom. RPT was performed in CFB2 at 3.5 m to 4.3 m from the bottom. In both the cases, Residence Time Distribution (RTD) was employed to	Different size and shape of clusters were observed in CFB1 for all cases. Negative velocities were observed near the wall. Mean axial velocity of solids were high at the axis and low at the wall. For all operating conditions, plug flow behaviour was observed.

	<p>$H_C = 6.0$ m;</p>	<p>$G_S = 85, 95$ and 110 kg/m².s .</p> <p>For CFB2:</p> <p>$U_g = 8.6, 9.6$ and 10.5 m/s;</p> <p>$G_S = 70, 90, 110$ and 126 kg/m².s</p>	<p>investigate the solid mixing behaviour.</p>	<p>Similarly, for CFB2, the motion is predominant in axial direction with low fluctuation in radial and azimuthal direction. Negative velocities were observed near the wall.</p> <p>For same operating condition, high mean axial solid velocity was found with larger column.</p>
<p>Efthima and Al-Dahhan (2017)</p>	<p>Gas-Solid system;</p> <p>For FB1:</p> <p>$H_C = 1.68$ m;</p> <p>$D_c = 0.14$ m;</p> <p>For FB2:</p> <p>$H_C = 1.68$ m;</p> <p>$D_c = 0.44$ m;</p>	<p>210 μm glass beads (2500 kg/m³);</p> <p>Bed height:</p> <p>H/D = 0.1-2.2 for FB1</p> <p>H/D = 0.05-2.5 for FB2</p> <p>$U_g / U_{mf} = 1.5, 2.0$ and 3.0 ($U_{mf} = 0.10$</p>	<p>RPT was conducted to measure the velocity fields and turbulence parameters of solid in two different columns. Cobalt-60 (500 μCi activity and 600 μm diameter with half-life of 5.28 years and two photo peaks) was used as a tracer.</p>	<p>High axial solid velocity was observed in the larger column at high gas velocity. In both the column, upward motion of solids was observed at the central region and downward flow near the wall for all operating conditions. The shear stress were higher in the larger column than in the smaller one and increased with the gas velocity. Radial solids velocity were also higher in larger column due to coalesce of bubbles in</p>

		m/s for FB2 and 0.12 m/s for FB1)		radial direction. High solid mixing and diffusion were observed in larger column, due to the wall effect.
--	--	-----------------------------------	--	---

Solid Flow Measurement in Liquid Fluidized Beds

Bascoul et al., 1993	3D-LSFB; Two-bed height: $H_{bed}=0.6$ and 0.75 m;	10 mm plastic sphere and 0.65 mm GB	The recirculation pattern was observed with the use of RPT for two different bed expansion.	The relative solid-liquid velocity was increased with increasing bed height or liquid velocities. The particle dispersion coefficient increased with increasing liquid velocity. They observed that tall beds represented by a single circulation loop while shallow beds were represented by a perfectly mixed reactor.
Kiared et al., 1997	LSFB; water-GB/PVC system; glass column;	3 mm GB (1300 kg/m^3); 5.5 mm PVC (1300 kg/m^3)	Particle dispersion coefficients, mean solid velocities were measured by using RPT method with a radioactive	Higher shear stress observed for PVC particles than GB particles. The D_x , D_y were found to be independent of ρ_p and d_p . For GB particle, U_z

	$H_C = 1.5$ m; $D_c = 0.1$ m;		source, Sc-46. A total 8 number of (3 in by 3 in) <i>NaI (Tl)</i> detectors were used.	is positive at the core and negative near the wall.
Roy and Dudukovic, 2001	Liquid-Solid Riser, Plexiglass column: $H_C = 10$ feet; $D_c = 6$ inch;	Spherical glass beads of 2.5 mm with density of 2500 kg/m ³ , Total inventory-110 lb. $U_L = 0.15, 0.20, 0.23$ m/s Solids-to-Liquid flow ratio (S/L): 0.10, 0.15, 0.20	In house, Computed tomography (CT) and radioactive particle technique (RPT) were used in estimating the time-averaged solid volume fractions and solid velocities under all operating conditions, respectively.	The correlation for solids fraction and axial solid velocity as a function of radial position were developed from the CT and RPT experiments, respectively. The upflow solids flow at the center and downflow near the wall were observed from experiments. Finally, computational fluid dynamics (CFD) with FLUENTS solver was implemented to validate the experimental findings.
Kalo et al., 2019	Liquid-Solid System, Conical Fluidized Bed with $D_{bottom} = 0.05$ m to	Spherical glass beads of 0.6 and	RPT was conducted in the experimental setup using two different size of tracers (0.6 and 1.0 mm Sc-46)	Segregation index of greater than 0.97 were observed which showed good mixing at all operating liquid velocities. The liquid-solid

	$D_{top}=0.2$ m and cone angle of 5.4 degree.	1.0 mm (2500 kg/m ³); $U_L/u_{mpf(1\text{ mm})} = 2.0, 3.0$ and 4.0 ($U_L = 0.07, 0.1$ and 0.14 m/s, respectively)	at all operating conditions. The solids flow fields with fluctuations were calculated under all operating conditions. From time series analysis, various parameters such as Hurst exponent (H), Kolmogorov entropy (KE) and correlation dimension (CD) were calculated.	systems operating under the mentioned conditions was persistent/super dispersive in nature (as $H>0.5$). They observe that the system was a chaotic in nature for all conditions (as $KE>0$) and binary beds were more chaotic than mono beds. A regime change was observed at 0.1 m/s liquid velocity.
--	---	--	---	---

Solid Flow Measurement in Gas-Liquid-Solids Fluidized Beds

Cassanello et al., 1996	Air-water-solids; GLS FB; Plexi-glass column bed; $H_C = 1.0$ m; $D_c = 0.1$ m;	GB: 0.9, 3 & 5 mm (2500 kg/m ³); PVC: 5.5 mm (1320 kg/m ³)	The solid axial number distribution and mixing times were measured experimentally, and modelled as well	Mixing time model predicted higher value for mixing time than experiments. Mixing times were observed higher for lower solid velocities.
-------------------------	--	---	---	--

Liquid Flow Measurement in Gas-Liquid system

Devanathan et al., 1990	Air-water system; BC; $H_C = 1.0$ m; $D_c = 0.292$ m;	$U_{air} = 0.105$ m/s; $H_{water} = 0.584$ m;	RPT measurement was employed to measure liquid flow fields using an embedded Sc-46 in 2.4 mm polypropylene sphere (density 1.01 gm/cc)	A single recirculation cell was observed in the flow patterns of the bubble column. Reynold's stress profile gave similar trends as the single-phase flow but have a higher magnitude.
Moslemian et al., 1992	Air-water system; BC; $D_c = 0.190$ m	$2 < U_{air} < 14$ cm/s	RPT method was executed to measure the liquid velocity, Reynold's stresses, integral time scales etc. using Sc-46 as a tracer with 16 NaI(Tl) scintillator detectors	The integral time scales were reported independent of column diameter and gas velocities. It has been reported that Reynold's stresses increase with gas velocity.
Yang et al., 1993	Air-water system; BC; $H_C = 1.0$ m; $D_c = 0.114, 0.190, 0.292$ m		Experiments were carried out for varying gas velocities (0.02 to 0.184 m/s) in each column, covering all flow regimes from bubble to churn flow	The mean axial velocity at the low and high gas velocity was plotted. The plot corresponding to high gas velocity showed positive mean axial velocities at the core and negative at the wall for

			regime in BC. Mean velocity, Reynold's stress for liquid phase were computed using RPT.	all axial heights. This showed the presence of a single (clockwise) liquid circulation cell. Similarly, a clockwise cell was observed only in the upper height of the BC at low velocity with a second (anti-clockwise) cell, near the distributor.
Yadav et al. (2019)	Convective flow in Liquid Column: $D_C = 0.12$ m; $H_C = 1.0$ m;	$U_1 = 0.01$ cm/s at $T=50-70$ °C.; Sc-46 was used as tracer particle. The lightweight Expanded microspheres of density 25 kg/m ³ was used to match the density.	RPT experiments were conducted in a liquid column to study the vapour bubble dynamics with two heater rod configuration (ID=12 mm and length 1.0 m) powered by 2 kW heat source. LIBSVM MATLAB software tool was used for position reconstruction.	The void fraction at the heater wall region, axial liquid velocity and turbulent kinetic energy increases for both rod configuration with increasing T from 50 to 70 °C. The decrement in liquid velocity was observed at higher liquid flowrate as the inlet liquid velocity increases from 0.01 to 0.02 cm/s.

CFB: Circulating Fluidized Beds; BC: Bubble Column; FB: Fluidized Beds; SB: Spouted Beds; G/S: Gas-Solid; L/S: Liquid-Solid; GLS: Gas-Liquid-Solids; GB: Glass Beads; PVC: Poly Vinyl Chloride; D_x , D_y , and D_z : Dispersion coefficient in x-, y- and z-direction; U_x , U_y , and U_z : Mean solid velocity in x-, y- and z-direction;



2.3.2. Implementation of RPT Experimental setup

The laboratory scale cold flow model is set up and fabricated as per the design constraints and limitations of RPT measurements. A schematic diagram of laboratory scale experimental set up is shown in Figure 2.5. An experimental setup is a cylindrical vessel of 210 mm diameter and 1750 mm height as shown in Figure 2.5a. Beyond this height, the upper section of vessel is expanded upto 310 mm diameter and 500 mm in height to prevent the entrainment of solids. The experiments are performed with the one or multiple side horizontal injections through pneumatic nozzles of different diameters (6 mm / 1 mm) which operate at the same axial levels or different axial levels. The position and arrangement of nozzles are shown in Figure 2.6. With operating two different size nozzles, the system parameters and physical properties of two phases are kept same. In the present work, the bed was operated at $3 U_{mf}$ (or 1.12 m/s). Glass beads (diameter $709 \mu\text{m}$, density 2500 kg/m^3 and Geldart B type) is used as the bed material. The RPT setup for the measurement of velocity fields of solid phase is designed and fabricated in the laboratory. The schematic of the RPT setup is presented in Figure 2.5b.

In the RPT setup, a finite number of scintillator detectors (such as NaI (Tl)) are placed outside the column at four different axial planes as shown in Figure 2.6. As shown in Figure, these set of detectors are fixed on the four horizontal platforms which can move in z-direction. Thus, the axial position of detectors can be fixed as per requirement. Figure 2.6b shows the top view of the detectors arrangement in RPT setup where the nozzles location is also shown. These detectors are used to record the counts at different time intervals. These counts are also known as events. These counts are dependent on the intensity of the γ -rays of the tracer particles (or source) used in the experiment.

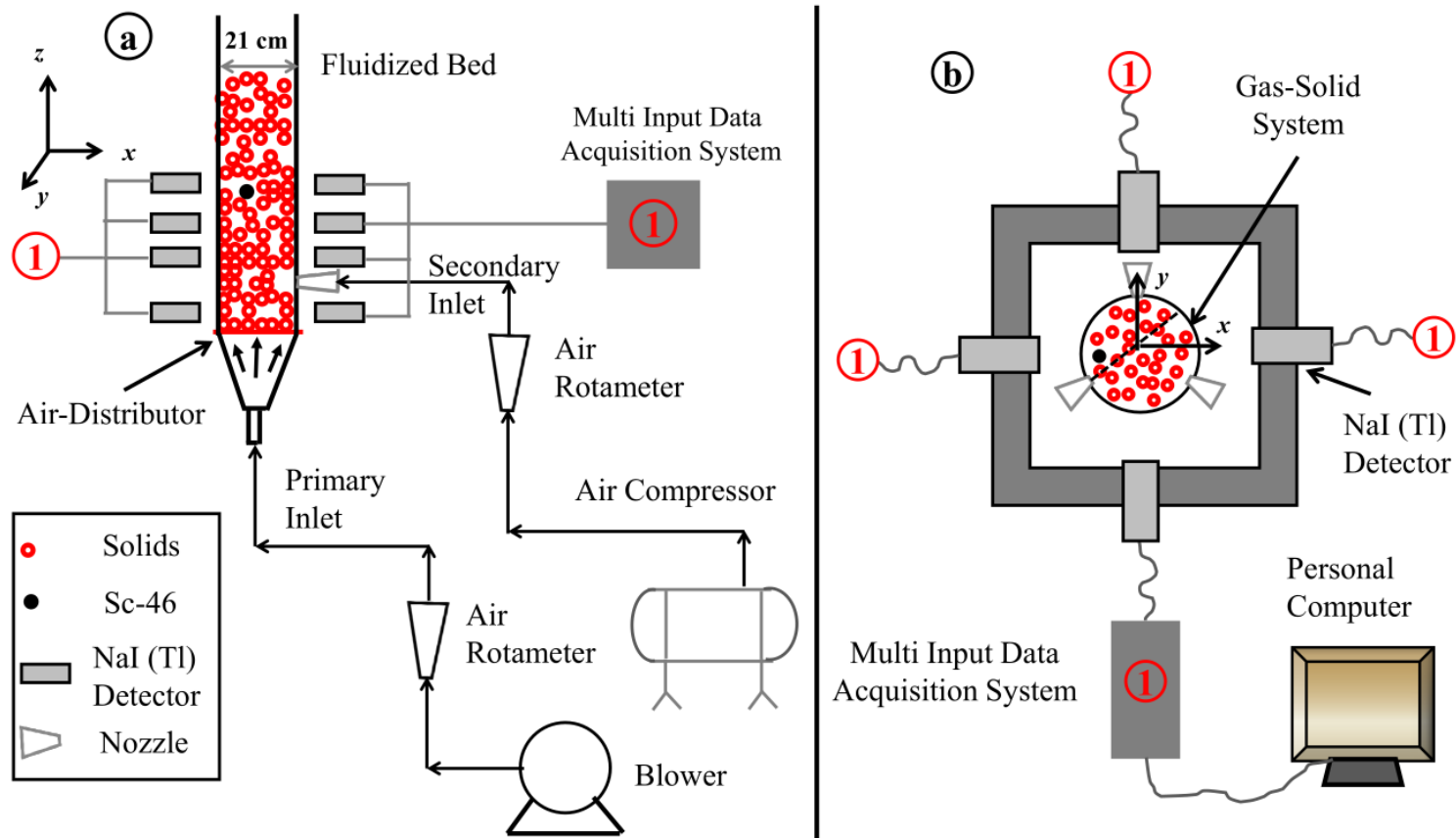


Figure 2.5 Schematic diagrams of (a) experimental setup and (b) RPT setup

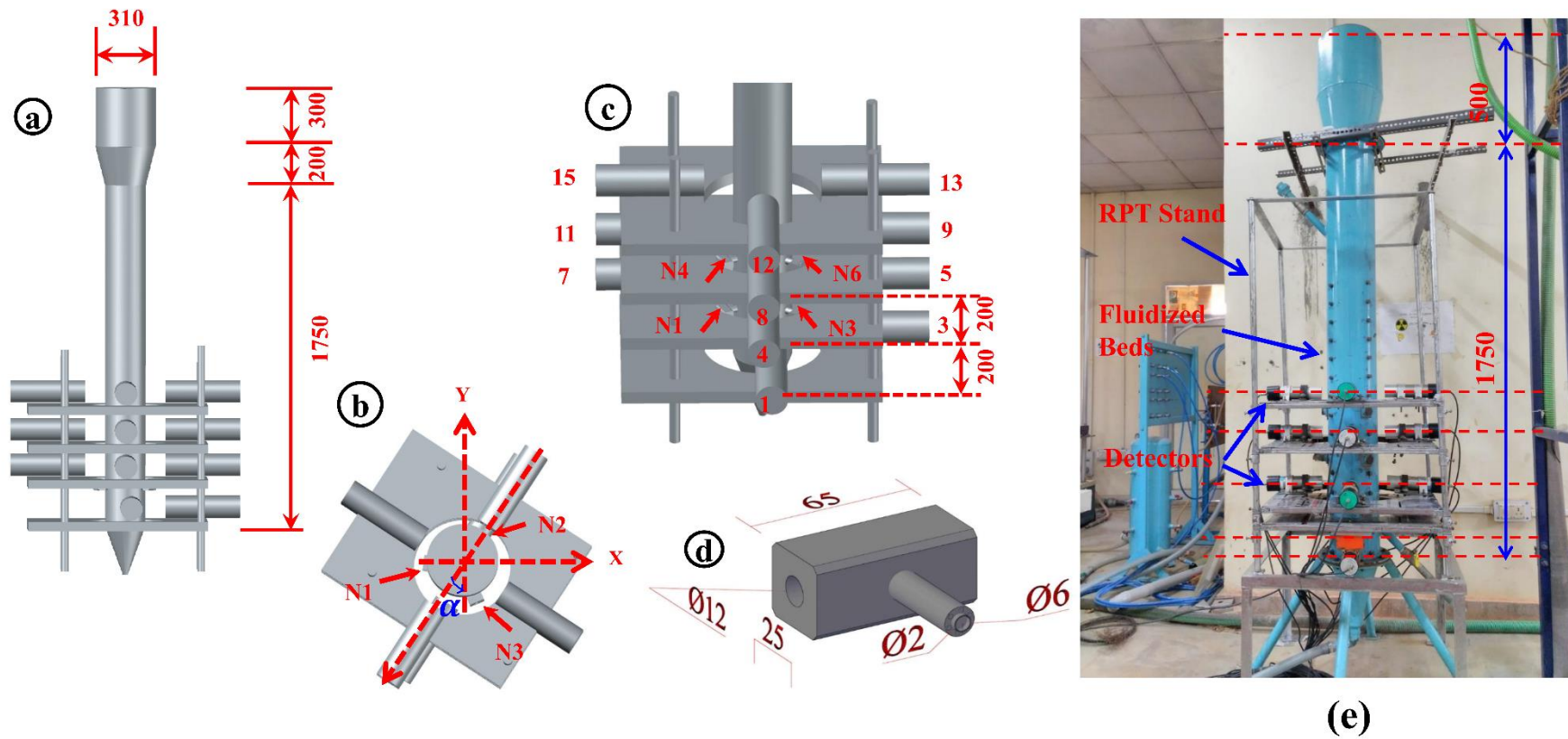


Figure 2.6 Schematic of (a) experimental column with detector arrangements surrounding it, (b) top view of detectors arrangements, (c) side view of the detectors arrangements, (d) dimensions of nozzle, and (e) photograph of RPT setup

The selection criteria of the tracer particle to track the position of the phase of interest is discussed in detail by Roy et al. (2002) and Upadhyay (2010). In the present case, a glass bead of similar physical properties doped with scandium-46 (Sc-46) is irradiated and used as a tracer particle. This tracer particle is encapsulated with the aluminium bead ensuring the density and size of the tracer particle match with the glass beads. The addition of gas using secondary inlet through multiple nozzles makes the implementation of RPT difficult which significantly affect the sensitivity and resolution of the measurements. Therefore, more attention should be given while positioning of the detectors around the experimental setup. Hence, calibration is performed carefully.

2.3.3. Post-processing of RPT data

Figure 2.7 shows the schematic of the acquisition process and post-processing of raw RPT data. In the RPT experiment, multiple NaI (Tl) scintillators detectors are placed outside the vessel of interest. The suitable tracer particle is selected as per the guidelines explained by Roy et al. (2002) and Upadhyay (2010). RPT is a two-step process. In first step tracer particle is placed at several known location inside the column of interest at in-situ condition. This is called calibration step in which for a known location of the tracer particle counts recorded in each detectors are noted down. In next step, actual experiment is performed in which tracer particle is free to move with the phase of interest. The counts recorded on each detector with the time is noted down during the actual experiment. The position of the tracer particle with the time is calculated thereafter by comparing the counts noted down during the calibration and counts recorded during the actual experiments (refer Figure 2.7).

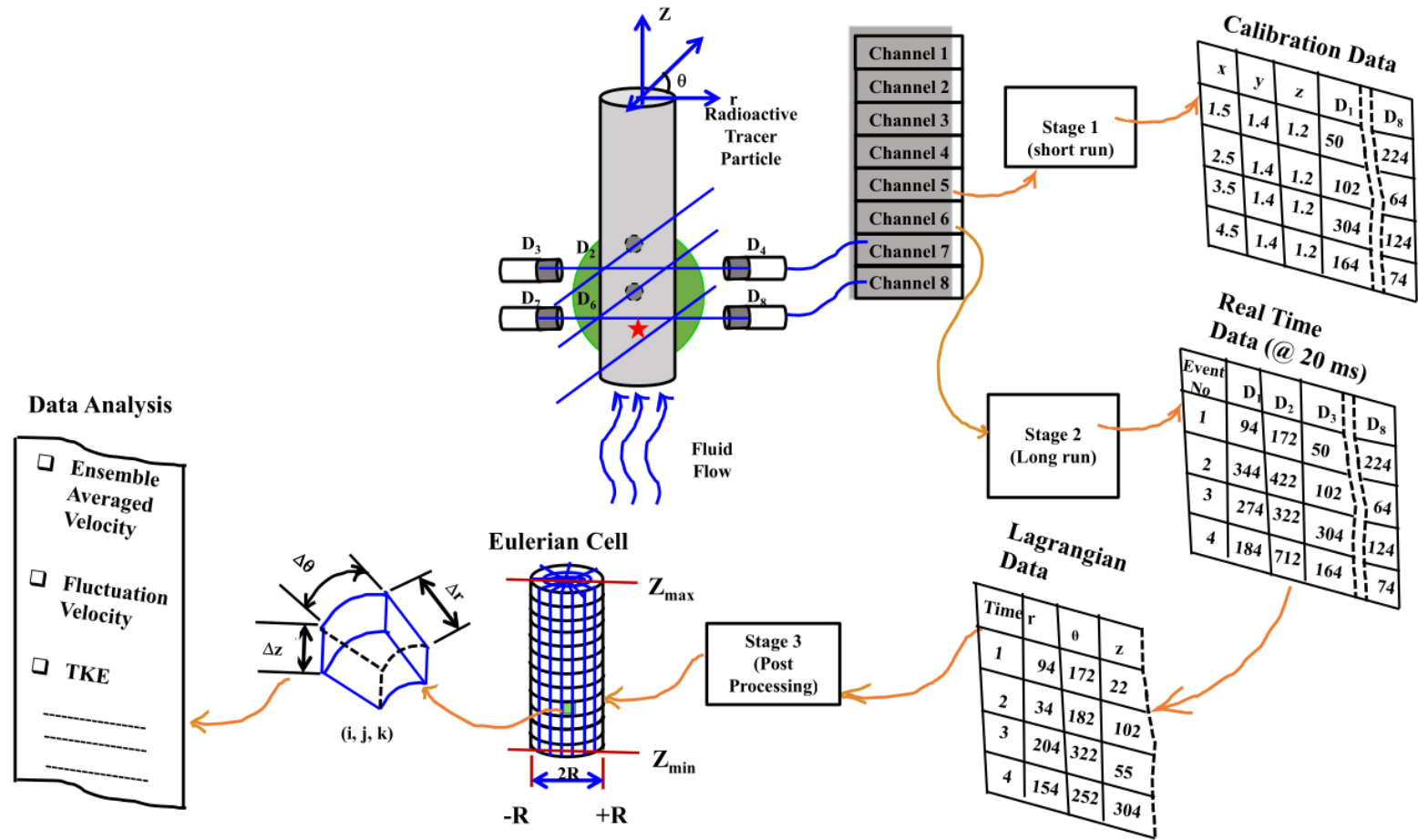


Figure 2.7 Description of principle of RPT methodology

In literature several reconstruction algorithms are used to reconstruct the tracer particle location with time. These are:

- Weighted Least Square Reconstruction Method
- Neural Network based Method
- Monte Carlo Method

Each method has its own advantage and disadvantage which re briefly discussed below.

Weighted Least Square Reconstruction Method

This method was used by Lin et al. (1985), Dudukovic et al. 1991 and Moslemian 1987. In this method, a polynomial relationship with higher orders is developed between calibration data (C_i) and distance (d_i) as follows:

$$d_i = \sum_{j=0}^m \frac{P_{ij}}{(C_i)^j} \quad (2.8)$$

The p_{ij} are polynomial coefficients and can be evaluated using the above equation. The m denotes the order of polynomial fit. A large number of calibration data points are required in this method to increase accuracy.

Neural Network-based Method

The use of 3-layer feedforward neural network (NNM) model is developed to relate the coordinates (x, y, z) as a function of recorded counts (C_i) as given below (Godfroy et al, 1997):

$$H_j = \frac{1}{1 + \exp(-\sum_{i=1}^{n+1} w_{ij} C_i)} \quad 1 \leq j \leq j-1 \text{ and } C_{n+1} = 1 \quad (2.9)$$

C_{n+1} and H_j are called bias and given the value of 1. Different layers of NNM are denoted as H , C and $(\bar{x}, \bar{y}, \bar{z})$ are defined as the hidden, input and output layer respectively. The output parameters $(\bar{x}, \bar{y}, \bar{z})$ are computed from the hidden layers as follows:

$$\bar{x} = \frac{1}{1 + \exp\left(-\sum_{j=1}^J w_{jx} H_j\right)} \quad (2.10)$$

$$\bar{y} = \frac{1}{1 + \exp\left(-\sum_{j=1}^J w_{jy} H_j\right)} \quad (2.11)$$

$$\bar{z} = \frac{1}{1 + \exp\left(-\sum_{j=1}^J w_{jz} H_j\right)} \quad (2.12)$$

The weighting coefficients w_{ij} , w_{jx} , w_{jy} and w_{jz} are known as fitting parameters of NNM and evaluating these coefficients is called training of the NNM.

Monte-Carlo Approach

This approach was developed by Beam et al. (1978) and later on modified by Larachi et al. (1994). The recorded counts (C) depend on different parameters including source activity (A), sampling time (T), dead time (τ), number of photo-peaks (ν) as per the following expression (Moens et al., 1981; Tsoufanidis, 1983):

$$C = \frac{T\nu A\phi\varepsilon}{1 + \tau\nu A\phi\varepsilon} \quad (2.13)$$

This is a widely used method and require less calibration points. However, detector optimization is always a concern for this method. In current work, this method is used for position reconstruction.

At the calibration stage, a datasheet comprises of the cylindrical coordinates of a finite number of calibration points and corresponding recorded counts for each detector are formed. In the current thesis, Monte-Carlo (MC) based approach is used to predict the counts for each detectors. A comparison between the calibration data and simulation-based data for a sample case are plotted and a typical distance versus count curve is shown in Figure 2.8. The three model parameters: source activity (A), dead time (τ) and effective attenuation coefficient (μ)

(or detector efficiency) are optimized for which the error is minimized. Similarly, a transient series of count data is recorded for each detector during the required operating condition at a fixed acquisition time (20 ms). In the second stage, the recording is done for a long time duration (16-20 hrs) and a time-count map is generated.

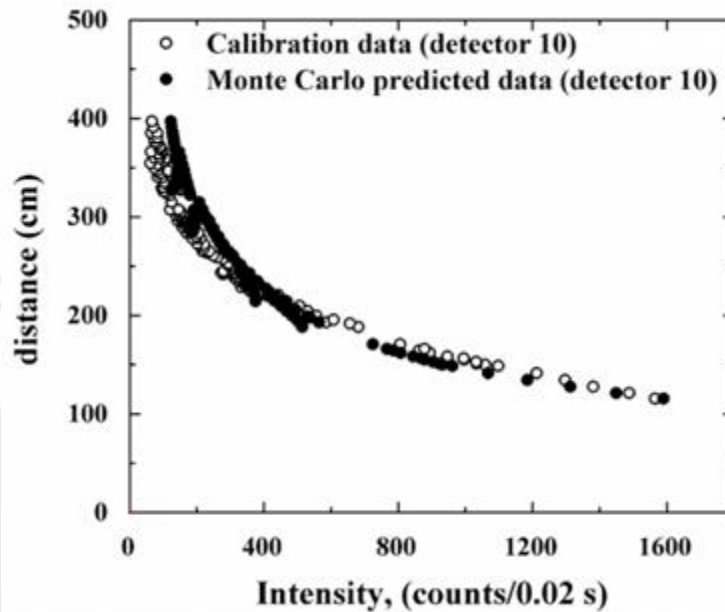


Figure 2.8 Comparison of experimental and simulated counts from a distance-count map for detector 10

For a third stage, the region of interest is discretized into smaller cell volume with a finite number of divisions in all three directions i.e. r , θ and z . The cell volume is kept constant with a known number of divisions in the radial direction (N_r) and axial direction (N_z) but the number of divisions in θ direction (N_θ) is changed. Using the optimal model parameters from MC, the counts are predicted at these cells within the domain. A parameter, χ^2 , is evaluated as given below:

$$\chi^2 = \sum_{i=1}^n \frac{(P_i - M_i)^2}{\sigma_i^2} \quad (2.14)$$

Where, P_i and M_i are the predicted count by MC and measured count for i -th detector. n denotes the number of detectors and σ_i is the uncertainty in counts. For a moving tracer particle, the best position is determined by cell centroid which minimizes χ^2 . Thus a transient data series of instantaneous positions is obtained for a set of experiments. The lagrangian instantaneous velocities are computed by dividing the difference of two successive instantaneous position of the tracer particle to the acquisition time.

The time (or ensemble) averaged velocities and other turbulence parameters like fluctuation velocities, root mean square velocities, granular temperature are calculated using the equations given in Table 2.2. Assuming Ergodicity, the ensemble-averaged velocities are evaluated at a particular Eulerian grid as the summation of instantaneous velocities divided by a total number of visits in that cell.

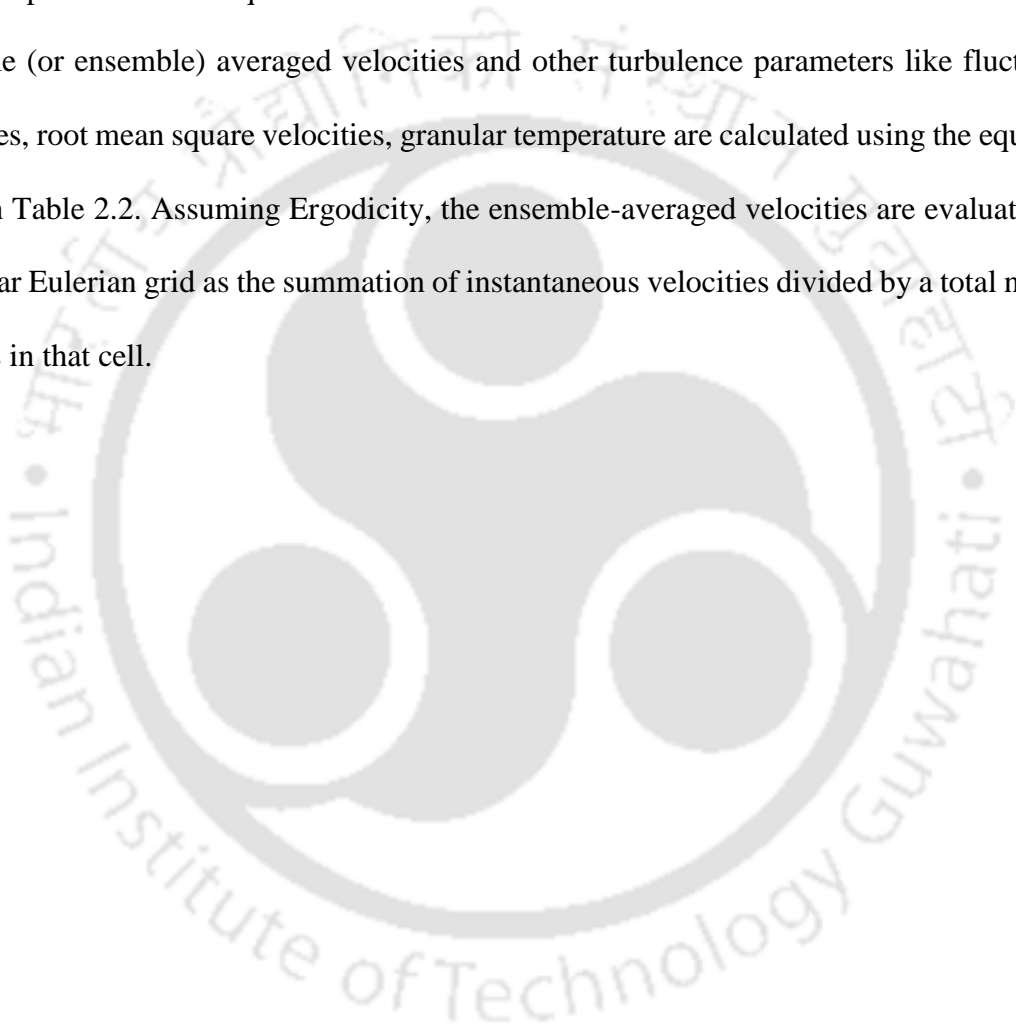


Table 2.2 Equation used in RPT for evaluation of key parameters (Roy et al. 2000)

Parameters	Equation
	$U_r = \frac{2}{\Delta T} [r_2 \cos(\theta_2 - \theta) - r]$
Instantaneous velocity (m/s)	$U_\theta = \frac{2}{\Delta T} [r_2 \sin(\theta_2 - \theta)]$
	$U_z = \frac{\Delta z}{\Delta T}$
Ensemble (time-averaged) velocity (m/s)	$\langle U_\alpha(i, j, k) \rangle = \frac{1}{N} \sum_{n=1}^N U_{\alpha,n}(i, j, k)$
Cross-sectional averaged mean velocity (m/s)	$\langle U_\alpha(k) \rangle^{CS} = \frac{\sum_{i=1}^{N_r} \sum_{j=1}^{N_\theta} \langle U_\alpha(i, j, k) \rangle N(i, j, k)}{\sum_{i=1}^{N_r} \sum_{j=1}^{N_\theta} N(i, j, k)}$
Root mean square velocity (m/s)	$U_{\alpha-rms} = \sqrt{\frac{1}{N} \sum_{j=1}^N U_\alpha^2}$
Granular temperature (m ² /s ²)	$\Theta_s = \frac{1}{3} \sum_{\alpha=r,\theta,z} U_\alpha^2$
Axial dispersion coefficient (m ² /s)	$D_{s,zz} = \frac{d}{2dt} \langle Z^2(E_0, t) \rangle$

Note: $\alpha = r, \theta, z$

2.3.4. Resolution and Sensitivity

Roy et al. (2002) applied the resolution and sensitivity in the liquid-solid system to measure the performance of the RPT setup. They have optimized the detector arrangement in RPT experiment based on the Monte Carlo approach which was used to obtain the count distribution

in one dimensional and two dimensional using Monte Carlo simulation. Later, Upadhyay (2010) had studied the effects of the activity of source particle, crystal size and material of the detector. He has concluded that this approach can be applied to optimize the detector arrangements before conducting RPT experiment and such arrangements are limited to the nature of experimental setup involved in the experiments. Considering one dimensional motion of tracer particle in Z direction, resolution and sensitivity are defined as the following mathematical expression (Roy, 2000).

$$R(z) = \sigma_c \frac{dz}{dC} \quad (2.15)$$

$$S(z) = \frac{1}{C} \frac{dC}{dz} = \frac{d \ln C}{dz} \quad (2.16)$$

Where, σ_c is the variance in counts recorded by each detector; C is the count registered in each detector, and z is the z-coordinate of the tracer position. In the case of multiple detectors, the resolution and sensitivity distribution in two dimensional space can be evaluated (Roy et al., 2002) for all detectors and it can be used to maximize the sensitivity and resolution (minimum R(z) and maximum S(z)). Therefore, in the current work, resolution and sensitivity are evaluated from the predicted counts in a 2-D space for one nozzle injection as shown in Figure 2.9. The resolution and sensitivity distribution are obtained at three different rz- planes sliced in three angular positions ($\theta=0^\circ$, 90° and 45° with respect to x-axis). Resolution is in the range of 2-2.5 mm at the axis of the column for all vertical planes. Similarly, the presence of more nozzles also affect the accuracy of RPT experiments drastically. Figure 2.10 shows the comparison of resolution and sensitivity with different nozzle configuration extracted at the same vertical plane ($\theta=0^\circ$). Resolution and sensitivity analysis is performed for the optimal positioning and arrangements of detectors to achieve maximum accuracy in the case of one nozzle side injection.

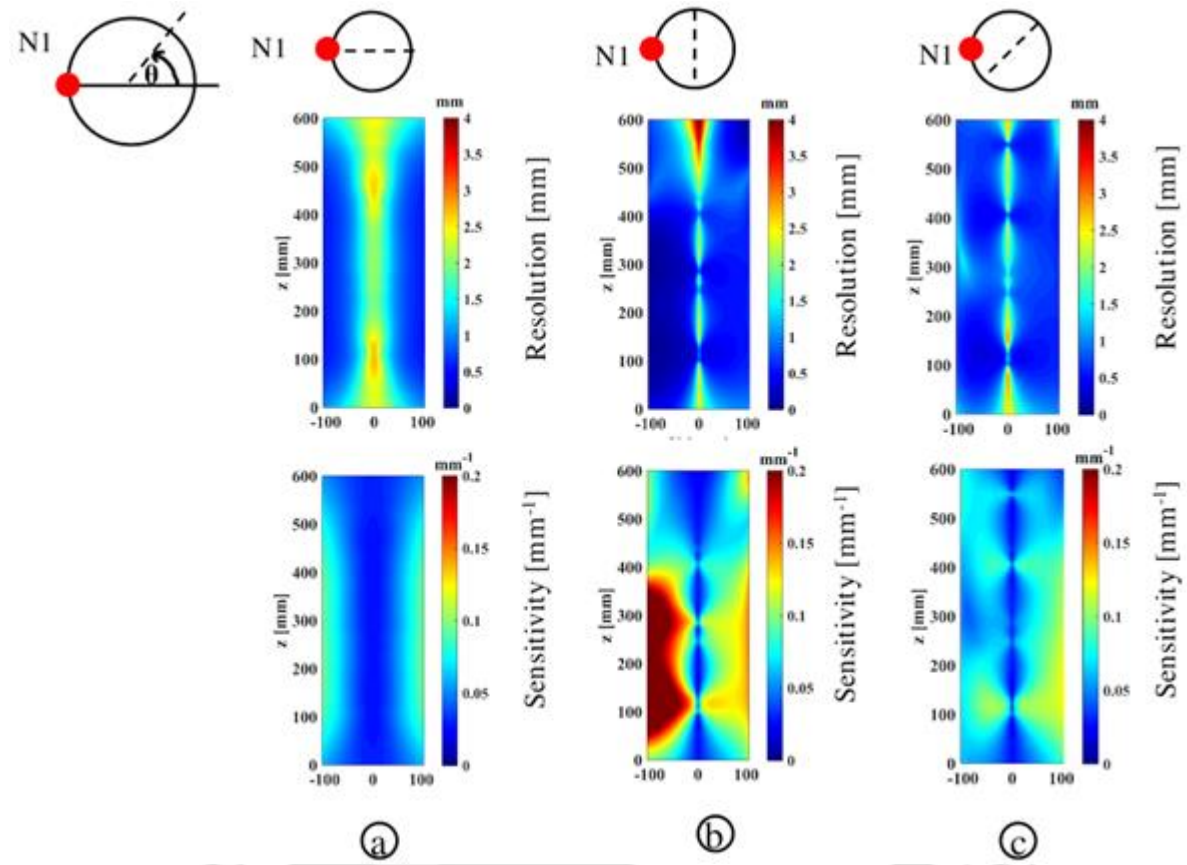


Figure 2.9 Resolution and sensitivity distribution at different planes with one nozzle side injection. Each column represents the angular position (θ) of the vertical plane with reference to the axis of side injection. (a) $\theta = 0^\circ$, (b) $\theta = 90^\circ$ and (c) $\theta = 45^\circ$

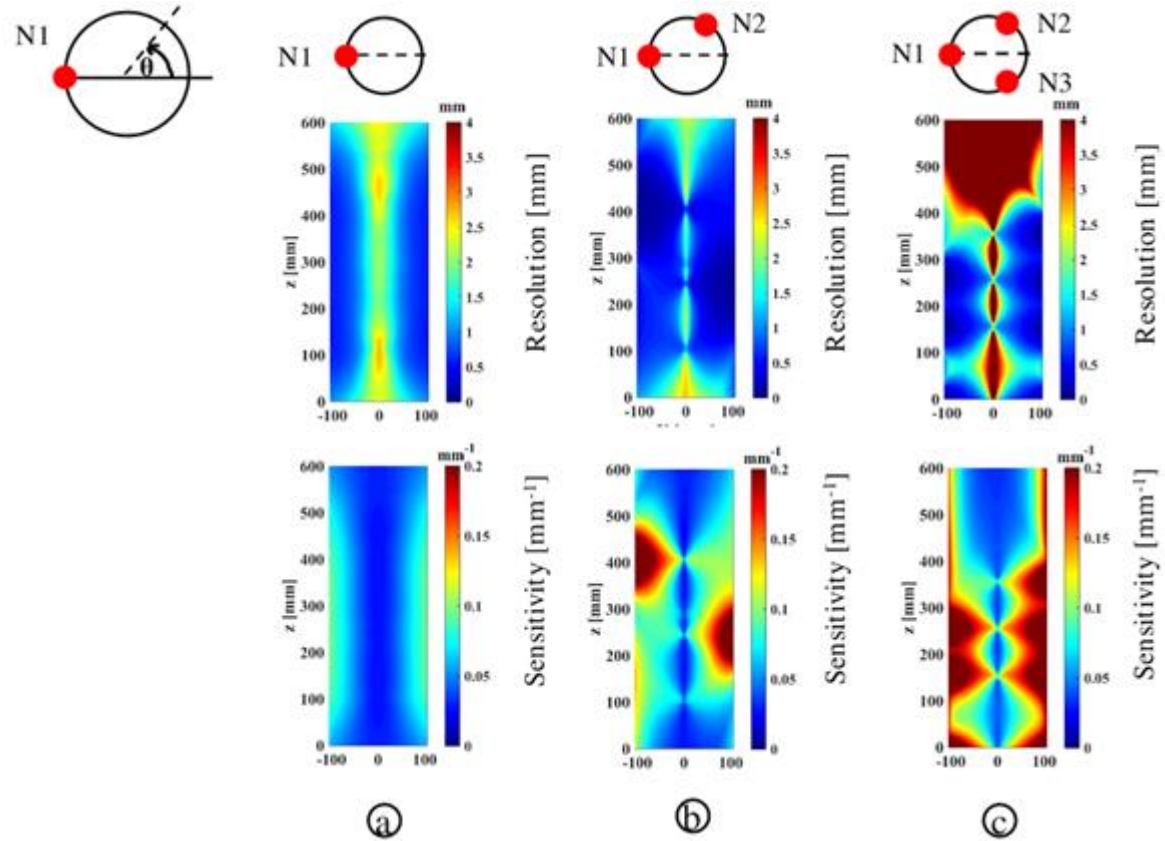


Figure 2.10 Resolution and sensitivity distribution for (a) one nozzle injection, (b) two nozzle injections, and (c) three nozzle injections

Institute of Technology

2.4. Summary

In summary, different measurement techniques available for the phase distribution and phase flow field measurements are discussed in detail. In general, two types of measurement methods are used for this purpose: invasive and non-invasive methods. Both measurements techniques have their limitations. However, in the present work to accomplish the objectives of the thesis, the non-invasive methods are implemented due to a high solid loading (or dense) system. The chordal averaged solid distribution and ensemble-averaged solid flow field parameters are measured using GDT and RPT methods respectively. Further, the accuracy of the measured data is improved by using source calibration, optimized electronics parameters (high voltage, gain, and low level discriminator (LLD)) for RPT, the optimized region of interest (ROI) for GDT, etc.

Notations

A_0	Activity of source at initial time ($t=0$)	[Ci]
$C(t)$	Source concentration	[-]
d_p	Particle diameter	[μm]
D_c	Diameter of column	[m]
I_0	Intensity of incident radiation	[photon. $\text{m}^{-2}\text{s}^{-1}$]
l	Distance between transmitter and receiver	[m]
P	Pressure	[Pa]
z	Axial coordiante	[m]

Greek Symbols

$\varepsilon_1, \varepsilon_2$	Void fraction of phase 1 and 2 respectively	[-]
ρ_p	density of particle	[kg/m^3]

μ_1, μ_2 Linear attenuation coefficients for phase 1 and 2 respectively [-]

Subscript

1, 2 phase 1 and 2 [-]

Abbreviations

ANN Artificial Neural Network

CFD Computational Fluid Dynamics

CREL Chemical Reaction Engineering Laboratory

CT Computed Tomography

FCC Fluid Catalytic Cracking

GDT Gamma Densitometry Technique

PMT Photomultiplier tube

RPT Radiative Particle Tracking

References

Adrian, R. J. 1991. Imaging technique for experimental fluid mechanics, Annual Reviews of Fluid Mechanics. 23, 261-304.

Bascoul, A., Couderc, J. P., Delmas, H., 1993. Mouvement des Particules Solides en Fluidisation Liquide Solide. Chem. Eng. J. 51, 135-150.

Beam, G. B., Wielopolski, L., Gardener, R. P., Verghese, K. 1978. Monte carlo calculation of efficiencies of right-circular cylindrical NaI detectors for arbitrarily located point sources. Nucl. Instrum. Meth. 154, 501-508.

Bhowmick, S., Sharma, V. K., Samantray, J. S., Pant, H. J., Shenoy, K. T., Dash, A., Roy, S.

B. 2015. Experimental investigation on interaction of side gas injection with gas-fluidized bed using γ -ray transmission technique. Ind. Eng. Chem. Res. 54 (46), 11653-11660.

- Bokkers, G.A., Van Sint Annaland, M., Kuipers, J.A.M., 2004. Mixing and segregation in a bidisperse gas-solid fluidised bed: a numerical and experimental study. *Powder Technol.* 140,176–186
- Borlai, O. L., Hodany, L., Blicke, T. 1967. Investigation into the Mixing in Fluidized Beds, *Proc. Int. Symp. Fluidization*, ed. Drinkenburg, A.A.H., Amsterdam, Netherlands University Press, 433-441.
- Cassanello, M., Larachi, F., Marie, M.-N., Guy, C., Chaouki, J., 1995. Experimental characterization of the solid phase chaotic dynamics in three-phase fluidization. *Ind. Eng. Chem. Res.* 34 (9), 2971–2980.
- Cassanello, M., Larachi, F., Kemoun, A., Al-Dahhan, M. H., Dudukovic, M. P. 2001. Inferring liquid chaotic dynamics in bubble columns using CARPT. *Chem. Eng. Sci.* 56, 6125-6134.
- Chen, M. M., Tchao, B. T., Liljegren, J. 1983. The effect of Bed Internals on the Solids Velocity Distribution in Gas Fluidized Beds. *Fluidization IV*, eds. D. Kunni and R. Toei, Engineering Foundation, New York, 203-210.
- Chen, J., Kemoun, A., Al-Dahhan, M. H., Dudukovic, M. P., Lee, D. J., Fan, L. S. 1999. Comparative hydrodynamics study in a bubble column using computer-automated radioactive particle tracking (CARPT)/computed tomography (CT) and particle image velocimetry (PIV). *Chem. Eng. Sci.* 54, 2199-2207.
- Chaouki, J., Larachi, F., Duduković, M.P. 1997. Non-invasive Tomographic and Velocimetric Monitoring of Multiphase Flows, *Ind. Eng. Chem. Res.* 36 (1997) 4476–4503.
- Devanathan, N., 1991. Investigation of liquid hydrodynamics in bubble columns via computer automated radioactive particle tracking (CARPT). D. Sc. Thesis. Washington University in St. Louis, USA.
- Devanathan N., Moslemian, D., Dudukovic, M. P. 1990. Flow Mapping in Bubble Columns using CARPT. *Chem. Eng. Sci.* 45, 2285-2291.

- Dudukovic, M. P., Devanathan, N., Holub, R. 1991. Multiphase Reactors: Models and Experimental Verification. Rev. Inst. Franc. Petr., 46, 439-464.
- Durst, F., Melling, A., Whitelaw, J. H. 1981. Principles and Practice of Laser Doppler Anemometry. 2nd Ed., Academic Press, London.
- Efthima, A., Al-Dahhan, M. H. 2017. Bed diameter effect on the hydrodynamics of gas-solid fluidized beds via radioactive particle tracking (RPT) technique. Can. J. Chem. Eng. 95, 744-756.
- Fraguío, M-S. 2010. Estudio Fluidodinámico De Reactores Multifásicos Mediante Técnicas De Análisis No – Invasivas. PhD Tesis; Universidad de Buenos Aires; área Química Industrial
- Fraguio, M. S., Cassanello, M. C., Larachi, F., Chaouki, J. 2006. Flow regime transition pointers in three-phase fluidized beds inferred from a solid tracer trajectory. Chem. Eng. Process. 45, 350-358.
- Godfroy, L., Larachi, F., Kennedy, G., Grandjean, B. P. A., Chaouki, J. 1997. On-Line Flow Visualization in Multiphase Reactors using Neural Networks. Appl. Radiat. Isotop. 48, 225-235.
- Godfroy, L., Larachi, F., Kennedy, G., Chaouki, J., 1996b. Simultaneous measurement of the 3-D position and velocity of a single radioactive particle in a CFB riser at high velocity. Proc. CFB V, Beijing, China.
- Kalo, L., Pant, H.J., Cassanello, M., Upadhyay, R.K. 2018. Time series analysis of a binary gas-solid conical fluidized bed using radioactive particle tracking (RPT) technique data. Chem. Eng. J., 377, 119807.
- Kalo, L., Kamalanathan, P., Pant, H. J., Cassanello, M. C., Upadhyay, R. K. 2019. Mixing and regime transition analysis of liquid-solid conical fluidized bed through RPT technique, Chem. Eng. Sci., 207, 702-712.

Kamalanathan, P. 2016. Investigation of gas-solid circulating fluidized bed at two scales using experimental and numerical techniques. PhD Thesis. IIT Guwahati, India.

Kamalanathan, P., Kalo, L., Pant, H. J., Upadhyay, R. K. 2017. Effect of dynamic bias on accuracy of radioactive particle tracking (RPT) technique at different data acquisition frequencies. *Applied Radiation and Isotopes*, 128, 13-21.

Kiared, K., Larachi, F., Cassanello, M., Chaouki, J., 1997. Flow structure of the solids in a three-dimensional liquid fluidized bed. *Ind. Eng. Chem. Res.* 36 (11), 4695–4704.

Kondukov, N. B., Kornilaev, A. N., Skachko, I. M., Akhromenkov, A. A., Kruglov, A. S. 1964. An Investigation of the Parameter of Moving Particles in a Fluidized Bed by a Radioisotopic Method. *Int. Chem. Eng.* 4, 43-47.

Kumar, S. B., Devanathan, N., Moslemian, D., Dudukovic, M. P. 1994. Effect of Scale on Liquid Recirculation in Bubble Columns. *Chem. Eng. Sci.* 49, 5637-5652.

Larachi, F., Kennedy, G., Chaouki, J. 1994. A γ -ray detection system for 3-D particle tracking in multiphase reactors. *Nucl. Instr. and Meth., A.* 338, 568-576.

Larachi, F., Kennedy, G., Chaouki, J. 1995. 3-D mapping of solids flow fields in multiphase reactors with RPT. *AIChE J.* 41(2), 439-442.

Larachi, F., Cassanello, M., Chaouki, J., Guy, C. 1996. Flow Structure of the Solids in a Three-Dimensional Gas-Liquid-Solid Fluidized Bed. *AIChE J.* 42(9), 2439-2453.

Laverman, J. A., Fan, X., Ingram, A., Annaland, M. S., Parker, D. J., Seville, J. P. K., Kuipers, J. A. M. 2012. Experimental study on the influence of bed material on the scaling of solids circulation patterns in 3D bubbling gas-solid fluidized beds of glass and polyethylene using positron emission particle tracking. *Powder Technol.* 224, 297-305.

Limtrakul, S., Chen, J., Ramachandran, P.A., Dudukovic, M. P. 2005. Solids motion and holdup profiles in liquid fluidized beds. *Chem. Engg. Sci.* 60, 1889-1900.

Lin, J. S., Chen, M. M., Chao, B. T. 1985. A novel radioactive particle tracking facility for measurement of solids motion in gas fluidized beds. *AIChE J.*, 31, 463-473.

Maestri, M., Salierno, G., Piovano, S., Cassanello, M., Cardona, M.A., Hojman, D., Somacal, H., 2019. CFD-DEM modeling of solid motion in a water-calcium alginate fluidized column and its comparison with results from radioactive particle tracking. *Chem. Eng. J.* 377, 120339.

Medrano, J. A., Tasdemir, F., Gallucci, F., Annaland, M. S. 2017. On the internal solid circulation rates in freely-bubbling gas-solid fluidized beds. *Chem. Eng. Sci.* 172 (23), 395-406.

Moens, L., De Donder, J., Lin, X. L., De Corte, F., De Wispelaere, A., Simonits, A., Hoste, J. 1981. Calculation of the absolute peak efficiency of gamma-ray detectors for different counting geometries. *Nucl. Instrm. and Meth.*, 187, 451-472.

Moslemian, D., 1987. Study of solids motion, mixing and heat transfer in gas-fluidized beds. PhD Thesis, University of Illinois, Urbana-Champaign, IL, USA.

Moslemian, D., Chen, M. M., Chao, B. T. 1989. Experimental and Numerical Investigations of Solids Mixing in a Gas-Solid Fluidized Bed. *Particulate Sci. Techn.*, 7, 335-355.

Moslemian, D., Devanathan, N., Dudukovic, M. P., 1992. Radioactive particle tracking for investigation of phase recirculation and turbulence in multiphase systems. *Rev. Scientif. Instrum.* 63, 4361-4372.

Parker, D. J., Broadbent, C. J., Fowles, P., Hawkesworth, M. R., McNiel, P. 1993. Positron emission particle tracking – A technique for studying flow within engineering equipment. *Nucl. Instr. and Meth.*, A. 326, 592.

Parker, D. J., McNeil, P. A. 1996. Positron emission tomography for process applications. *Meas. Sci. Tech.* 7 (3), 287-296.

Roy, D., Larachi, F., Legros, R., Chaouki, J. 1994. A study of Solids Behavior in Spouted Beds using 3-D Particle Tracking. *Can. J. Chem. Eng.* 72, 945-952.

- Roy, R. P., Velidandla, V., Kalra, S. P., 1997. Velocity field in turbulent subcooled boiling flow. *Trans-ASME: J Heat Trans.* 119, 754.
- Roy, S., Kemoun, A., Al-Dahhan, M.H., Dudukovic, M.P., 2005. Experimental investigation of the hydrodynamics in a liquid-solid riser. *AIChE J.* 51 (3), 802-835.
- Roy, S., Larachi, F., Al-Dahhan, M. H., Dudukovic, M. P., 2002. Optimal design of radioactive particle tracking experiments for flow mapping in opaque multiphase reactors. *Appl. Radiat. Isot.* 56, 485-503.
- Roy, S., Kemoun, A., Al-Dahhan, M.H., Dudukovic, M.P., 2001. A method for estimating the solids circulation rate in a closed-loop circulating fluidized bed. *Powder Technol.* 121, 213-222.
- Roy, S., Dudukovic, M. P., 2001. Flow mapping and Modelling of Liquid-Solid Risers. *Ind. Eng. Res.* 40, 5440-5454.
- Salierno, G.L., 2016. Tesis Doctoral Caracterización de equipos y medios multifásicos con métodos que emplean fuentes radiactivas Facultad de Ciencias Exactas y Naturales.
- Salierno, G., Maestri, M., Piovano, S., Cassanello, M., Cardona, M.A., Hojman, D., Somacal, H., 2018. Solid motion in a three-phase bubble column examined with Radioactive Particle Tracking. *Flow Meas. Instrum.* 62, 196–204.
- Sun, J., Chen, M. M., Chao, B. T. 1988. On the Fluctuation Motions due to Surface Waves in Gas Fluidized Beds. *Proc. 1st World Cong. Experim. Heat Transfer, Fluid Mechanics and Thermodynamics*, eds. R. K. Shah, E. N. Gani. And K. T. Yang, Elsevier Science Publishing, 1310-1318.
- Tsoufanidis, N, 1983. Measurement and detection of radiation, McGraw-Hill series in Nuclear Engineering.
- Upadhyay, R. K., Kaim, J., Roy, S. 2009. Investigation of downflow bubble columns: Experiments and Modeling. *JCEJ.* **42(1)**, s151-s161.

Upadhyay, R. K., 2010. Investigation of hydrodynamics multiphase reactors using radioactive particle tracking. PhD Thesis. IIT Delhi, India.

Upadhyay, R.K., Roy, S. 2010. Investigation of the hydrodynamics of binary fluidized beds via radioactive particle tracking and dual-source densitometry, *Can. J. Chem. Eng.* 88, 601–610.

Upadhyay, R. K., Pant, H. J., Roy, S. 2013. Liquid flow patterns in a rectangular air-water bubble column investigated with Radioactive Particle Tracking. *Chem. Eng. Sci.* 96, 152-164.

van Velzen, D., Flamm, H. J., Langenkamp, H., Casile, A. 1974. Motion of Solids in Spouted Beds. *Can. J. Chem. Eng.* 52, 156-161.

Weber, J.M., Mei, J.S., 2013. Bubbling fluidized bed characterization using electrical capacitance volume tomography (ECVT). *Powder Technol.* 242, 40–50

Yadav, A., Kushwaha, A., Roy, S. 2016. An algorithm for estimating radial gas holdup profiles in bubble columns from chordal densitometry measurements. *Can. J. Chem. Eng.* 94, 524-529.

Yadav, A., Pant, H. J., Roy, S. 2019. Velocity measurements in convective boiling flow using radioactive particle tracking technique. *AIChE J.* 66 (1), 1-11.

Yang, Y. B., Devanathan, N., Dudukovic, M. P. 1992. Liquid Backmixing in Bubble Columns via Computed Automated Particle Tracking (CARPT). *Chem. Eng. Sci.* 47, 2859-2864., also in *Experim. Fluids*, 16, 1-9 (1993).

Yang, Y. B., Devanathan, N., Dudukovic, M. P., 1993. Liquid backmixing in bubble columns via computer automated particle tracking (CARPT). *Experim. Fluids*, 16, 1-9.

Yeh, Y., Cummins, H. Z. 1964. Localized fluid flow measurements with an He-Ne laser spectrometer. *Appl. Phys. Lett.* 4, 176-178.

Chapter 3 Investigation of Gas-Solid Fluidized Bed with a Single Sidewall Injection Using RPT

Scope

In the present chapter, we measured the flow field of the solid phase in a 3-D cold flow model of a gas fluidized bed. A secondary fluid (air) is injected inside the bed under a fixed fluidization condition. Successful implementation of radioactive particle tracking (RPT) has been outlined. RPT provides a wide source of solid motion via Lagrangian trajectories. Further, hydrodynamics parameters such as ensemble-averaged velocities, fluctuation velocities, granular temperatures, and other variables are inferred from the Lagrangian trajectory for the solid phase. The effects of nozzle diameters and flowrates are presented. The axial dispersion coefficient of the solid is also measured for the same operating condition. Thus, the RPT data can be useful for the modeling, scale-up and designing of such type of fluidized bed for the commercial scale. It is noted that the experimental data in such types of the system are limited due to the availability of the radioactive source, safety concern and nature of the system.

3.1. Introduction

Gas-solid contacting is an important characteristic of a fluidized bed system that plays a significant role in defining the reactor performance for different industrial processes (Kunii et al., 1991). In many of these processes, like ethane oxidative dehydrogenation (Schmidt et al., 1994; Cavani and Trifiro, 1995), fluid cooking cracker (Wilson, J. W. 1997), liquid fuel combustion (Anthony and Lu, 2001; Okasha et al, 2003), thermal denitration (Bjorklund and Offutt, 1973; Fane et al., 1974), metal nitrate waste (Sridhar, 1986), granulation (Rizkalla and Lefebvre, 1975), and coating (Walzel, 1993) etc., reactant/promoters are injected in the bed

through pneumatic nozzles placed at the sidewall. Such injections have potential to change the flow field inside the bed and hence the performance of the reactor.

There are several factors that affect reactor performance in such cases. For example, in the ethane oxidative dehydrogenation, the O_2 -to- C_2H_6 ratio is a very critical parameter. Ethane lean feeds produce high ethane conversion and low ethylene selectivity. Ethane-rich feed produces low ethane conversion and high ethylene selectivity. The addition of O_2 along the reactor height causes a reduction in the partial pressure of O_2 at the inlet and any other location across the bed. It favors the desired reaction and results in higher conversion (Tonkovich et al., 1996). Another industrial process such as circulating fluidized bed (CFB) combustor, combustion utilizes the air in a staged manner with the addition of secondary or tertiary feeding streams to lower the NO_x emission. This type of staged feeding of reactant along the height is also used in bubbling bed combustors (Bramer, 1995). The other processes where injection of one of the reactant/promoters take place through sidewall nozzles are: denitration of ammonium diuranate in thermal denitrator $(NH_4)_2U_2O_7$ (Bhowmick et al., 2012), production of acrylonitrile in the Sohio process (Yates et al., 1987) and partial oxidation of butane to maleic anhydride in CFB (Contractor and Sleight, 1988) etc. In all these processes both high selectivity and conversion are required. According to Levenspiel (1999), reactant concentration does not affect the selectivity of the desired product for the reaction of the same order. However, the reactant concentration favors the high order reaction if it is higher, and similarly favors the low order reaction if it is lower. The yield of the desired product in above mentioned processes can be improved by either removing the undesired product continuously from the system or by using the reactant feed in distributed manner.

The later method is used commonly for these processes. However, the injection of reactant and/or promoters through sidewall pneumatic nozzles can change the flow field inside gas-solid fluidized bed. It should be noted that for the fast reactions local flow field and mixing is

more critical compared to the overall flow field. Hence, if not carefully designed such injection can adversely affect the conversion and selectivity. There are several design parameters which can affect the flow field inside such system. These are: nozzle injection flowrate/velocity, nozzle position, nozzle geometry, nozzle injection diameter, and nozzle assembly. Though these processes are widely used in industry, limited data on flow field is available in open literature for such column. This is mainly due to the limitation of measurement techniques. In most of these processes the column diameter is quite large so that the penetration depth of the nozzle injected fluid can be minimised. Very few techniques can provide the data in such a dense column of larger diameter. Therefore, mainly computational works are reported for such systems (Deza et al., 2011; Wang et al., 2015; Li et al., 2017). Bhowmick et al., 2015 have performed densitometry measurement in gas-solid bubbling fluidized bed with single side wall nozzle injection system. However, they have reported only the solid distribution for one nozzle injection velocity. Most of the other measurement is performed to find the penetration length of the nozzle injected fluid (Merry, 1971, 1975; Yang and Keairns, 1978, 1979; Yang, 1981; Ranjan and Christoff, 1982; Massimilla, 1985; Blake et al., 1990; Roach, 1993; Cleaver et al., 1995; Chyang et al., 1997; Hong et al., 1997; Vaccaro, 1997; Yang et al., 2015; Materazzi et al., 2017). Beside this, some work has been published to investigate the effect of a single nozzle injection of gas/spray which is perpendicular to the flow of primary gas, on the fluidization quality by computing the void fraction, particle velocity and jet penetration (Al-Sherehy, 2002; Al-Sherehy, 2004; Li, 2009, Deza et al., 2011; Wang et al., 2015; Bhowmick et al., 2015).

Bhowmick et al. (2015) reported that a large fraction of injected gas was bypassed as soon as it was injected into the system. They have used single nozzle system. This has been seen as a major problem to resolve in such type of system. Now if such system is operated for high throughput with single nozzle only then nozzle injection flowrate will be relatively high. Such system will be difficult to handle and may lead to severe bypassing. Therefore, for high

throughput system multiple nozzle should be used to avoid such bypassing. Koeninger et al. (2018) conducted an experiment with three side wall nozzle injections placed at the same plane in a gas-solid fluidized bed. They measured the solid distribution at different axial planes using a computed tomography (CT) experiment. They also observed that the focal point of the three injections is the most affected region where the solid fraction was least. The qualitative and quantitative understanding of hydrodynamic parameters (solid velocity, turbulent kinetic energy and shear stresses etc.) is still not available in the literature.

In current work, we have performed the radioactive particle tracking (RPT) experiments in a cold flow model of gas-solid bubbling fluidized bed. The experiments are performed with single and two side wall nozzle injection(s) system. The effect of sidewall nozzle injection flowrate/velocity on solid flow field is investigated. Further, the effect of nozzle inlet diameter on solid flow field are investigated. To the best of our knowledge such data is not available in open literature till now. Hence, the data can be used to develop both computational as well as phenomenological model and validation of the same.

3.2. Experimental Setup and Operating Conditions

The experimental setup described in previous chapter was used for RPT experiments also. Detailed information about the experimental setup, electronics hardware, and post-processing mechanism is already discussed (in section 2.3.2). Figure 3.1 shows the arrangements of two different nozzles N1 and N2 in the experimental setup. The location of the detector and an assessment of its coordinate are shown in Figure 3.2. The current RPT study has been employed for these two configurations: (i) single sidewall injection with 6 mm and 1 mm diameter nozzle, and (ii) two sidewall injections with 6 mm diameter nozzle.

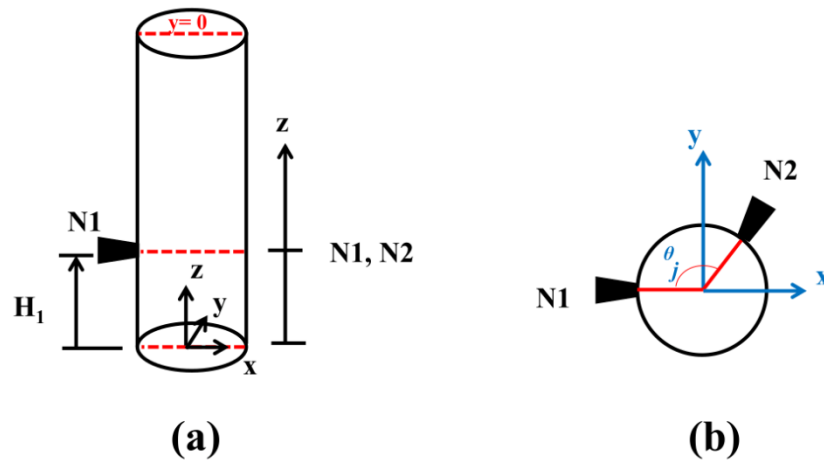


Figure 3.1 Schematic of nozzle locations in the two sidewall nozzle fluidized bed: (a) front view (b) top view

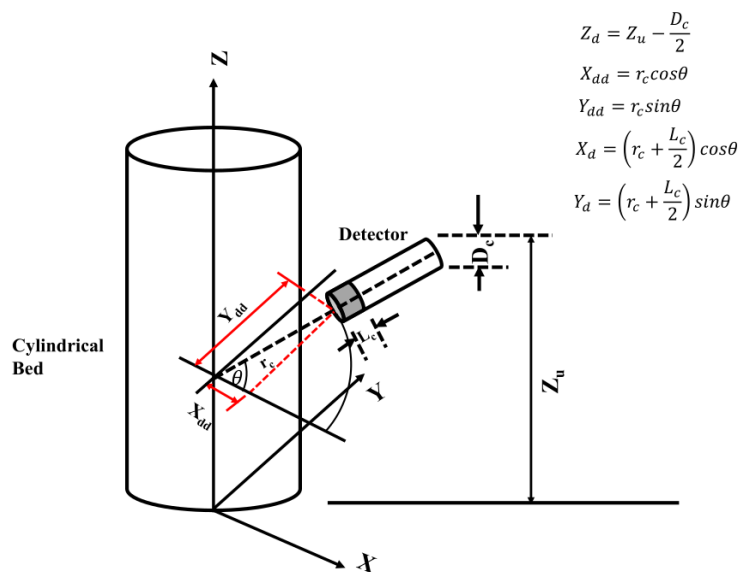


Figure 3.2 Evaluation of the coordinates of detector position

In first case, the detail of operating conditions and bed properties used for solids velocity measurement in the presence of a single nozzle injection are discussed. Figure 3.3 shows the schematic of the experimental setup along with the plane information at which data are plotted. Glass beads of 709-micron size and density 2500 kg/m^3 were used as a solid phase. Air was used as gas phase injected through the bottom of the column as a primary fluidizing gas and through side wall nozzles as a secondary injecting gas. Total 13 detectors are placed at 7 different axial locations to track the motion of the tracer particle. At each plane two detectors were placed which were 180° apart. The detectors at two successive planes were staged to achieve better resolution and sensitivity (Upadhyay, 2010; Upadhyay et al., 2019). Sc-46 doped inside the glass bead of same size and density was used as a tracer particle. The data for each condition was acquired at 50 Hz frequency for 10 hours. For each case, instantaneous velocity, mean velocity, rms velocities and granular temperature of solids are calculated by using post processing algorithm developed by previous researchers (Devenathan, 1991; Degalessan, 1997; Roy, 2000; Upadhyay, 2010; Kalo, 2019). For each case data are plotted at four different heights, 0.03 m, 0.15 m, 0.2 m, and 0.25 m, at nozzle injection plane to find the effect of side nozzle injections on solid flow field. To estimate the effect of nozzle injection on overall solid flow field azimuthal average values of above mentioned quantities are also plotted. Experiments were performed for two different nozzle inlet diameters, 1 mm and 6 mm. The photographs of both the nozzles are shown in Figure 3.4. Other than the nozzle injection diameter rest of the parameters like nozzle length, nozzle injection pressure and temperature were kept same.

Table 3.1 presents the detailed experimental conditions for which experiments were performed to study the effect of single side wall nozzle injection on solid flow profile. For all the experiments primary gas inlet velocity was kept constant at 1.12 m/s ($3 U_{mf}$) and H/D ratio was

maintained at 3.57 which corresponds to static bed height of 0.75 m. The coordinates of the detectors utilised in two alternative nozzle configurations are displayed in Table 3.2.

Table 3.1 Operating conditions of RPT measurement with one/two sidewall horizontal injection ($d_p=709 \mu\text{m}$; $\rho_p=2500 \text{ kg/m}^3$; $H/D_t = 3.57$; $U/U_{mf} = 3.12$)

Cases	Nozzle ID	d_j	θ_j	H_1	Q_1, Q_{12}
		[mm]	[in degree]	[m]	[LPM]
Single Nozzle	N1	6	0	0.20	40, 60, 100, 120
	N1	1	0	0.20	20, 30, 40, 60, 80, 100
Two Nozzle	N1, N2	6, 6	0, 120	0.20, 0.20	60, 70, 80, 100

Note: d_j = nozzle diameter; Q_1, Q_{12} = nozzle flowrates; H_1 = axial position of nozzle

Table 3.2 The coordinates of detector for RPT experiments with 6 mm nozzle diameter

Single Nozzle (N_1)					Two Nozzle (N_1, N_2)				
Xd	Xdd	Yd	Ydd	Zd	Xd	Xdd	Yd	Ydd	Zd
145.51	120.18	0	0	82.5	151.42	126.02	0	0	82.5
-145.9	-120.5	0	0	82.5	-144.4	-119	0	0	82.5
0	0	146.9	-121.5	75.5	0	0	-151.4	-126	75.5
145.9	120.5	0	0	278.5	155.42	130.02	0	0	278.5
0	0	147.86	122.47	294.5	0	0	150.42	125.02	294.5
-143.9	-118.5	0	0	284.5	-145.4	-120	0	0	284.5
0	0	-150.9	-125.5	285.5	0	0	-154.4	-129	285.5
145.9	120.5	0	0	397.5	153.42	128.02	0	0	397.5
0	0	145.86	120.47	415.5	0	0	149.42	124.02	415.5
-146.9	-121.5	0	0	402.5	-147.4	-122	0	0	402.5
0	0	-153.9	-128.5	396.5	0	0	-157.4	-132	396.5
145.9	120.5	0	0	513.5	154.42	129.02	0	0	513.5
-144.9	-119.5	0	0	513.5	-148.4	-123	0	0	513.5

In second case, the RPT study has been performed with two sidewall nozzles at same fluidization condition. More details about the position and alignments of these nozzles are shown in Table 3.1. This study has been conducted with four injections flowrates.



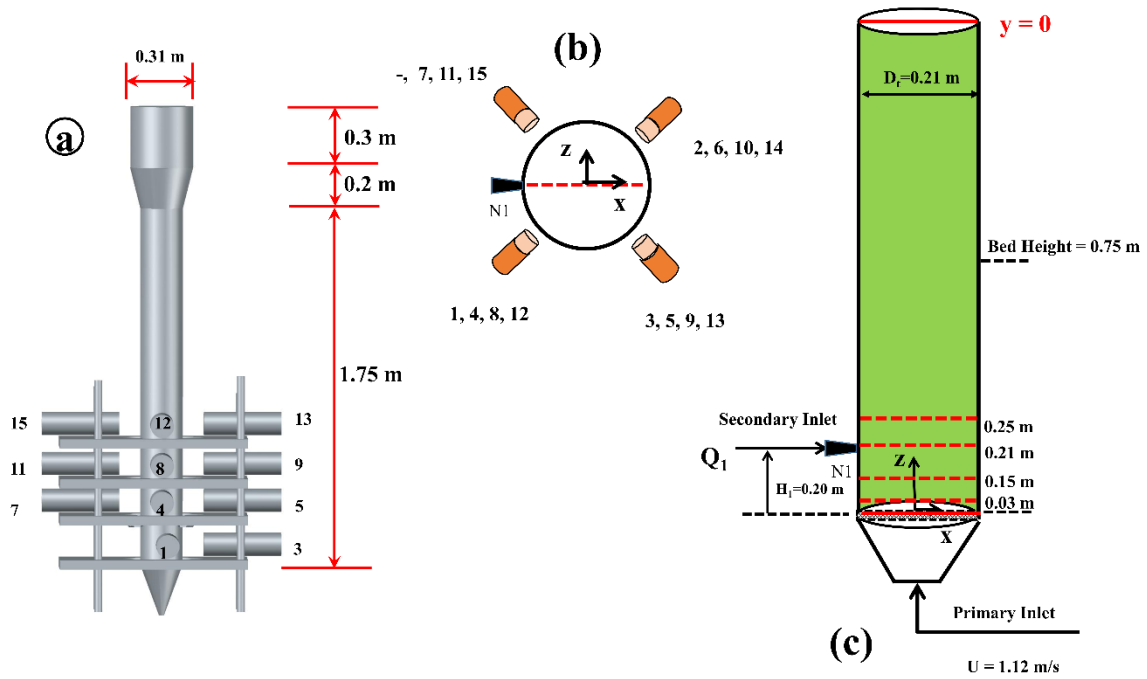


Figure 3.3 Schematic of (a) detector arrangements outside the bed column, (b) top view of the setup, and (c) view of observation plane representing the position of multiple axial heights

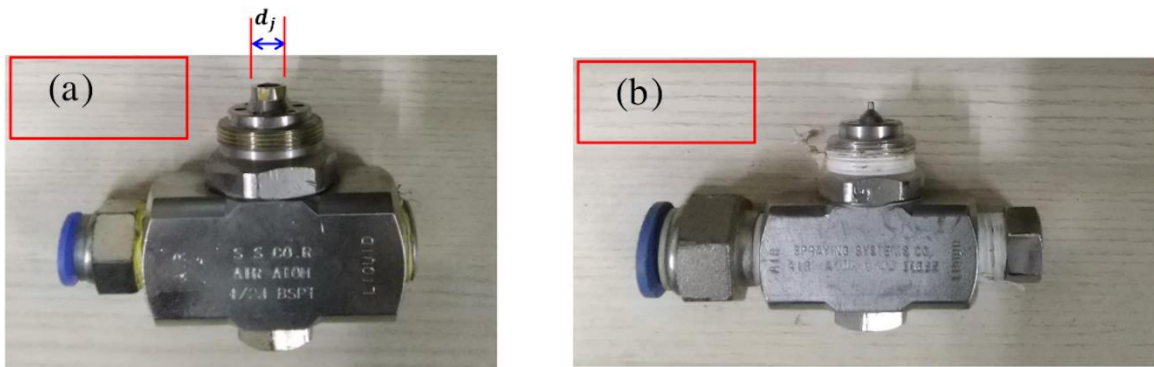


Figure 3.4 Photographs of twin fluid type nozzles with (a) $d_j = 6$ mm and (b) $d_j = 1$ mm

3.3. Results and Discussion

Experiments were performed in a fabricated experimental setup where the dynamics of the tracer particle were continuously monitored by recording the counts by using an array of scintillation detectors. The count-time series data obtained from each detector were used to find the position-time series of the tracer particle. The lagrangian track of the particle was further used to find the mean axial velocity, mean radial velocity, axial and radial rms velocities, granular temperature and solid diffusivity. The experiments were performed for two different diameter nozzles (6mm and 1mm) placed at same axial height ($z=20$ cm). It should be noted that at a time only one nozzle was placed. The other operating parameters i.e. injection flow rate (Q_1), exit nozzle diameter (d_j) are presented in Table 3.1.

3.3.1. RPT Measurements for a Single 6 mm ID Sidewall Nozzle Injection

RPT, experiments were performed for a single 6 mm ID nozzle which was placed at 20 cm height from the distributor plate on left side from centre (-R wall). The primary gas inlet velocity (passed through the bottom of the column) was kept constant at 1.12 m/s ($3 U_{mf}$). The secondary air (same as primary gas) was passed through the nozzle at 120 LPM flow rate. The H/D ratio of the initial bed (packed bed) was maintained at 3.57 for all the cases. The motion of a single radioactive particle, which was the marker for the solid present in the bed, was tracked for 10 hours continuously at 50 Hz frequency for all the conditions. The data acquired were post processed and presented below:

Probability Density Function (PDF) of instantaneous velocities of solid

The PDFs of radial and axial component of the instantaneous velocity of solid are calculated through RPT data. The PDF is calculated by approximation of the first derivative of the respective component of the instantaneous position with respect to the time using forward difference method as suggested by Roy et al. (2002).

Figure 3.5 shows PDFs of instantaneous axial velocity of the solid at three different radial positions and four different axial positions (as shown in Figure 3.3b). The left, ($r/R = -0.94$), centre ($r/R = 0$) and right ($r/R = 0.94$) sides of the column represents the injection wall, central zone and wall opposite to the injection side. The axial locations show planes below the nozzle injections ($z=3$ and 15 cm), and planes above the nozzle injection ($z=21$ and $z=25$ cm). The results show that PDF of axial velocity at all the locations is unimodal in nature. The red line shows the mean axial velocity of solid in that cell. In all the cells both positive and negative velocity of the solids are observed. This shows that at all locations solids moves both upward and downward directions, even near the sidewall nozzle injection points. However, the frequency of negative velocity is lower for left wall (nozzle side wall) compared to the right wall (opposite to the nozzle injection). A wide distribution is observed for axial instantaneous velocity at all the cells which confirms good axial mixing. This is possible only if the larger bubbles are formed near the nozzle injection wall. However, in literature it is established that bubbles in fluidized bed migrate towards the centre of the column (low resistance path) and avoid walls (Kunni and Levenspiel, 1991; Clift and Grace, 1985; Jackson, 1971; Davidson and Harrison, 1963). The current results show the opposite trend where the primary bubble generated at the distributor plate is migrating towards the injection wall and forms bigger bubble after having coalescence with the bubble generated at the nozzle injection point. To confirm this a 2D setup made of Perspex (transparent material) is build. Figure 3.6 shows the snapshot of the video recorded at same operating condition with the single nozzle. The results show the formation of the bigger bubble at and above the nozzle injection point and hence confirm the migration of the primary bubble towards the nozzle injection point. This may be due to the low pressure region created at the nozzle

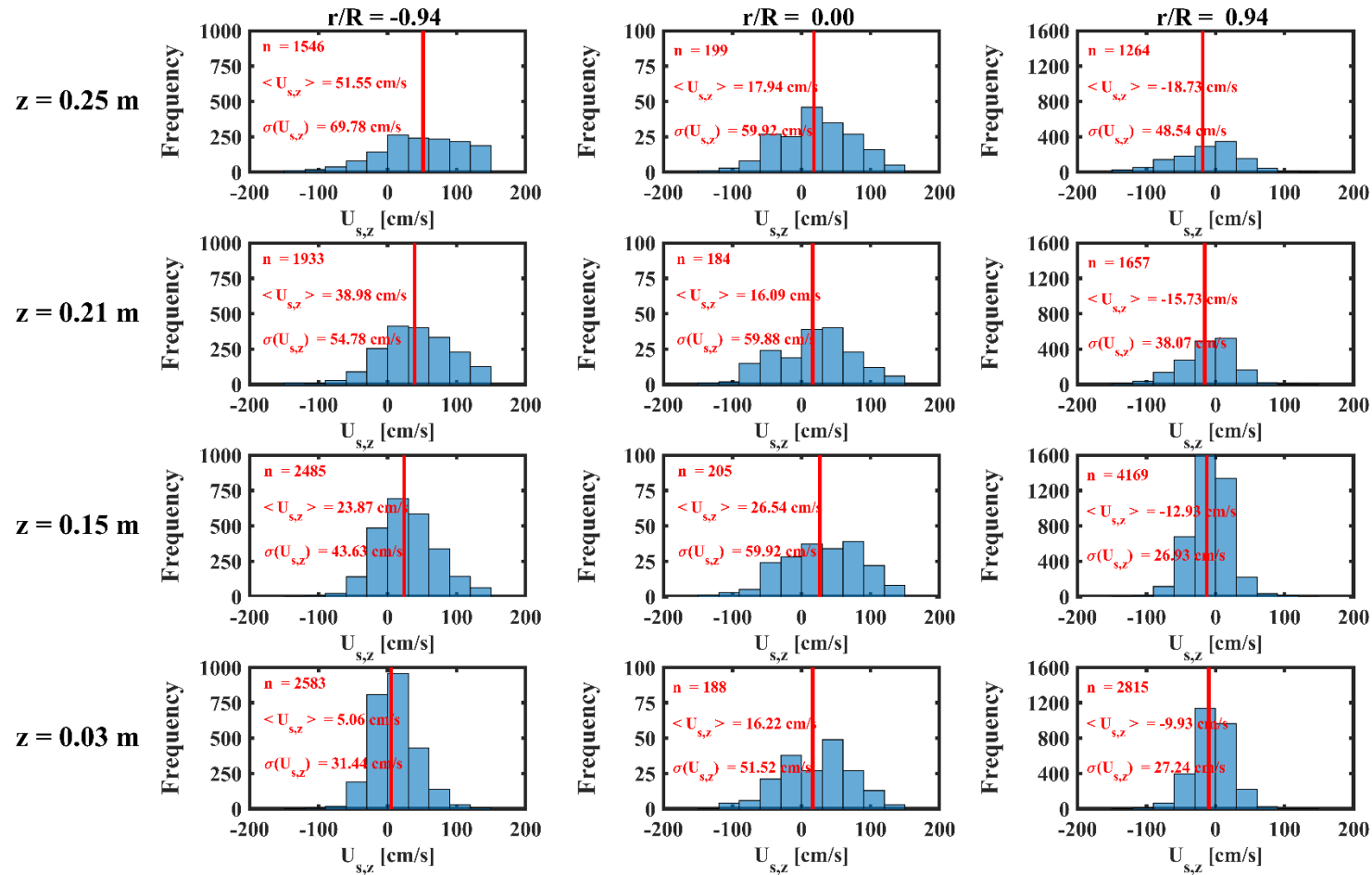


Figure 3.5 PDF of instantaneous axial velocity of solid particle at different r/R and z locations inside the bed

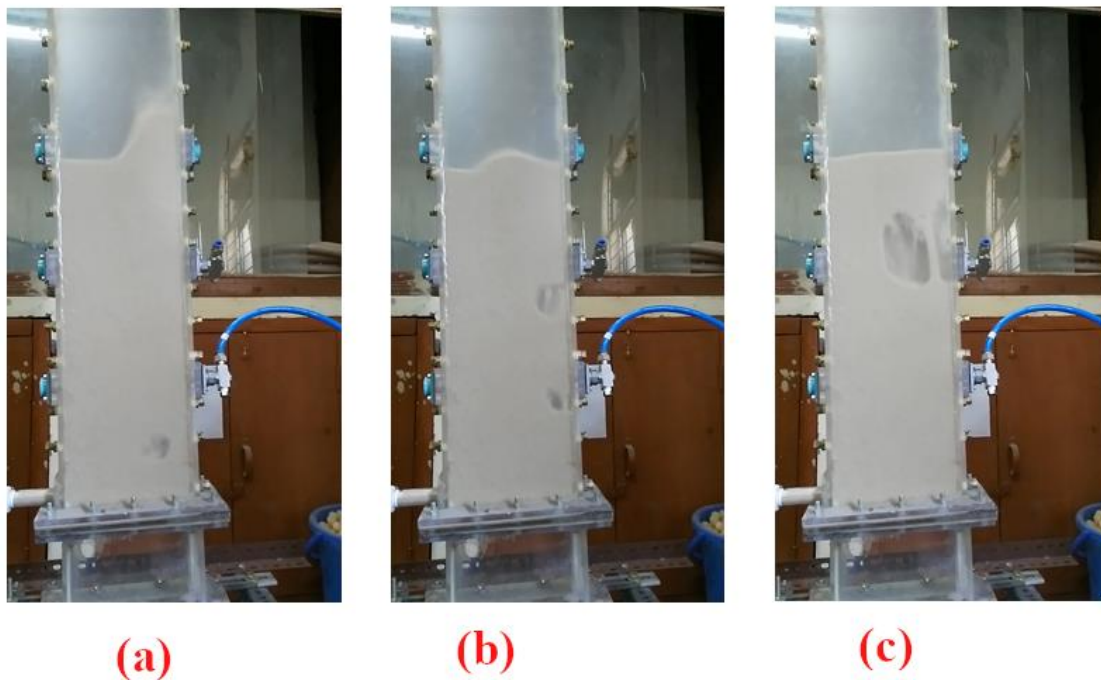


Figure 3.6 Visual of bubble migrations in 2D experimental set up (a) primary bubble formed at the bottom of bed, (b) interaction of primary and secondary bubble and (c) rising of bubble from nozzle wall to center of the bed

injection point due to high velocity injection of the secondary gas. The similar phenomena are also reported by Bhowmick et al. (2015).

Mean velocity of solid

Figure 3.7 shows the contour plot of mean axial velocity of solids at different heights (r - θ coordinates) for primary air inlet velocity of 1.12 m/s and nozzle injection (secondary air) flow rate of 120 LPM. The contour plots show that the solid velocity is positive towards the nozzle injection wall and negative on the other side. It is interesting to note that solid migration towards to nozzle injection wall start from the bottom of the column itself. This observation is contrary to the normal gas-solid fluidized bed (without nozzle injection). In which solids move

upward at the centre of the column and downward near the wall (Upadhyay, 2010). Therefore, these results show that the behaviour of sidewall nozzle injected fluidized bed is quite different from the traditional gas-solid fluidized bed. Results show that as we move up in the column, the red colour path is becoming more dark and moving towards the nozzle injection wall. This further establishes the migration of the solids towards the injection wall. The higher velocity indicates the formation of the bigger bubble at nozzle injection wall due to the bubble coalescence. The velocity of the solid further increases as we move up in the column. This shows the presence of larger bubble above the nozzle injection plane which drags the solids along with it.

Figure 3.8 shows the contour plots of radial solid velocity at different axial locations. Higher radial velocity is observed in case of sidewall nozzle assisted gas-solid fluidized bed compared to the traditional gas-solid fluidized beds (without nozzle injection). These results further confirm that the behaviour of sidewall nozzle injected gas-solid fluidized bed is significantly different. The higher radial solid velocity is observed due to the migration of the bubbles towards the nozzle injection wall which generate radial mean solid velocity. The results show that with moving up in the bed the radial mean solid velocity increases which signifies higher solid migration towards the wall due to the formation of bigger bubbles. The maximum mean radial solid velocity is observed above the nozzle injection plane this signifies that the coalescence of nozzle injected bubble and bubble generated at the distributor plate (bottom of the column) take place above the nozzle injection plane.

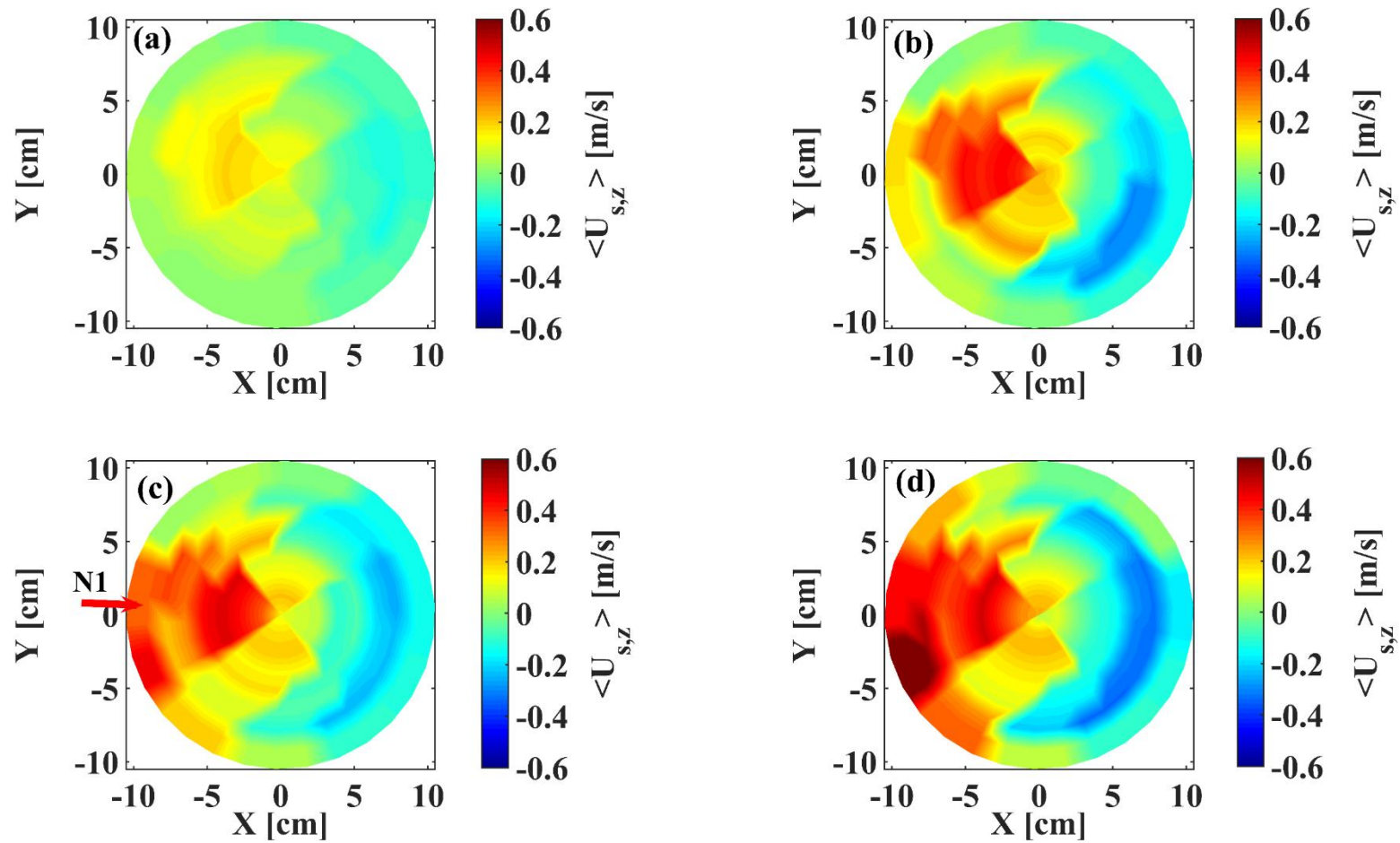


Figure 3.7 Contour plots of mean axial velocity of solid at different axial planes (a) $z = 3$ cm, (b) $z = 15$ cm, (c) $z = 21$ cm, and (d) $z = 25$ cm

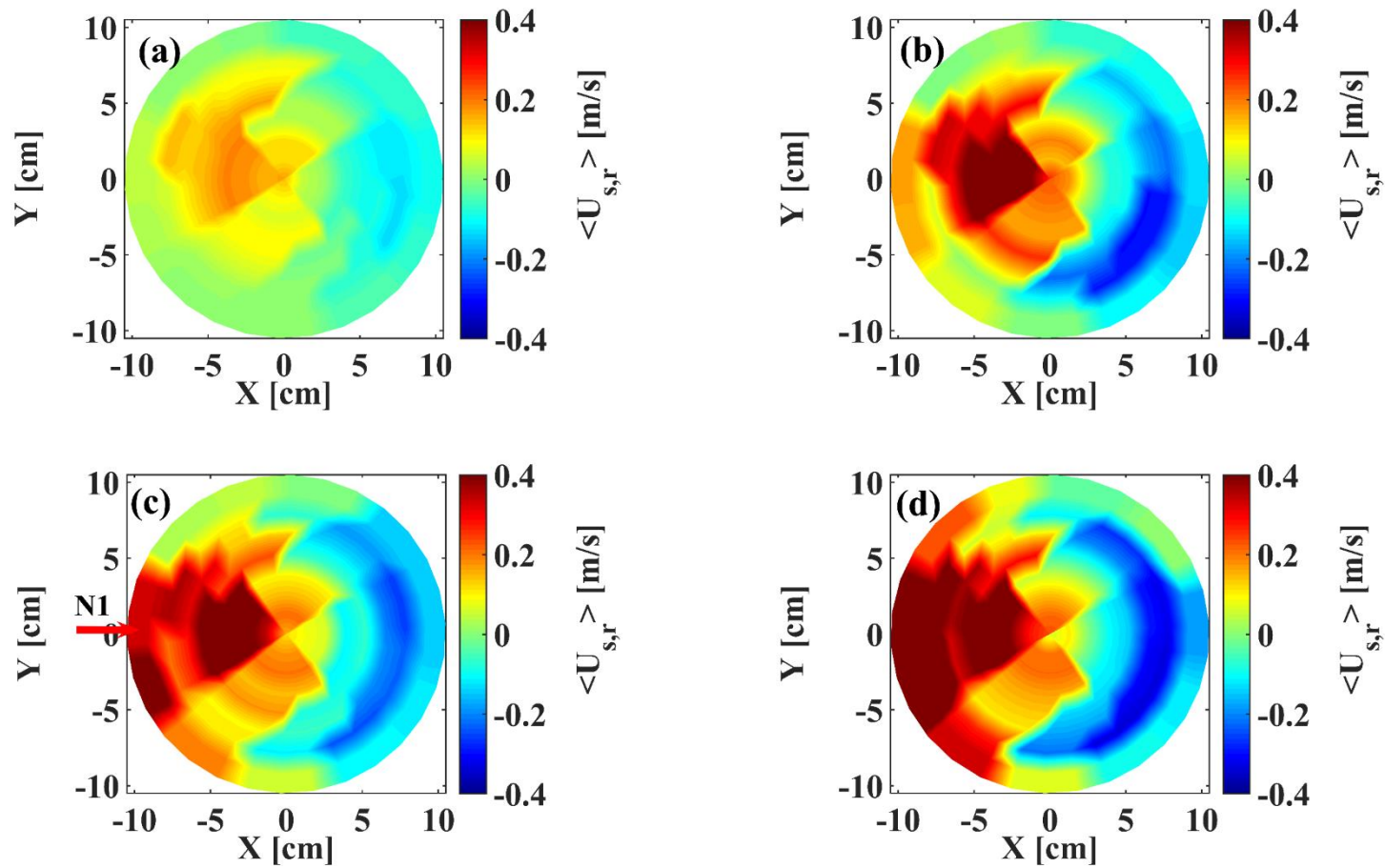


Figure 3.8 Contour plots of mean radial velocity of solid at different axial planes (a) $z = 3$ cm, (b) $z = 15$ cm, (c) $z = 21$ cm, and (d) $z = 25$ cm

Figure 3.9 shows the radial variation of mean axial velocity of solid at four different heights. Figure 3.9a shows the mean axial solid velocity at a central vertical plane ($y=0$). Please note that $x/R = -1$ indicates nozzle injection wall. Results indicate that solids move upward towards the nozzle injection wall and downward through the opposite wall at all the heights. This shows that bubble generated at the distributor plate start migrating from the bottom itself that results in single circulation cell for the solids in nozzle assisted fluidized bed compared to two circulation cells in traditional gas-solid fluidized bed (Upadhyay, 2010). The mean axial velocity of solid increases as we move upward. This indicates formation of the bigger bubbles. Similar observation has been reported by Wang et al. (2015). A sharp increase in upward solid axial velocity is observed above the nozzle injection plane, which may be due to the coalescence of nozzle injected bubble and bubble formed in the bed. These results further establish that the behaviour of nozzle assisted gas-solid fluidized bed is quite different from traditional gas-solid fluidized bed at least at injection plane. To find the overall effect of nozzle injection of nozzle assisted fluidized bed, azimuthal average axial velocity of solid is plotted at different heights as shown in Figure 3.9b. The azimuthal averaged mean axial velocity is positive at the centre and negative at the wall except at a height of 0.25m. Further, the azimuthal average solid axial velocity increases as we move up in the bed. This indicates formation of bigger bubble with the height due to the coalescence. These findings describe that the overall axial velocity distribution in nozzle assisted fluidized bed is similar to the traditional gas-solid fluidized bed. This may be due to the smaller flow rate (120 LPM) of secondary air injection as compared to large flowrate of primary air (2350 LPM). It also indicates that the column has no axis symmetry, which is evident, and the motion in different slices compensate themselves and result in a mild mean upward solid motion in the center and downward in the wall.

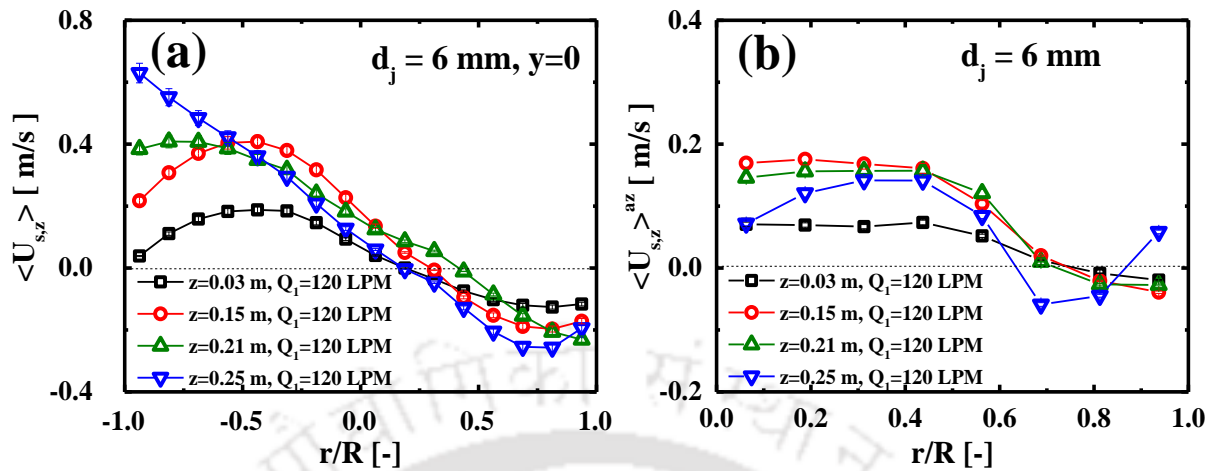


Figure 3.9 Time average mean axial velocity profiles of solid at fixed $Q_1=120$ LPM (a) injection plane ($y=0$), and (b) azimuthal averaged

Figure 3.10a shows the mean radial velocity profiles of the solids at xz -plane along the dimensionless length (r/R). Results show that the radial velocity is low compared to the axial velocity, however, they are not negligible. In conventional cylindrical fluidized bed with no sidewall nozzle injections several authors have reported low/negligible radial mean velocity compared to the axial mean velocity (Upadhyay, 2010; Kalo et al., 2020). The positive mean radial velocity is observed near the injection wall and negative mean radial velocity is found towards opposite wall. This further confirms the migration of primary gas bubbles towards the nozzle injection wall which leads to the positive radial velocity of the solids. Similar to the conventional fluidized bed (without nozzle injection), the azimuthal averaged radial solid velocity is negligible in this case also (shown in Figure 3.10b), except at the bottom section (near the distributor) where solids which are falling down through wall is moving towards the centre. These findings further confirm that overall behaviour of the ‘single’ nozzle assisted

fluidized bed is similar to the conventional gas-solid fluidized bed. However, the local dynamics of the both the beds are quite different which is more critical in case of fast or instantaneous reactions.

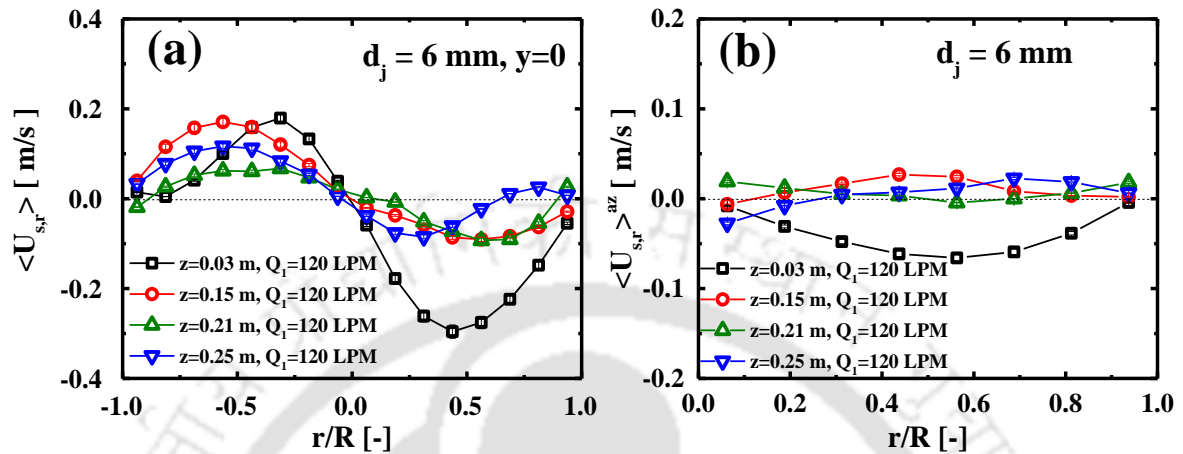


Figure 3.10 Radial Variation of mean radial velocity of solid at fixed $Q_1=120\text{ LPM}$ (a) injection plane ($y=0$), and (b) azimuthal averaged

Fluctuation velocities

Fluctuation velocity is an important feature to characterize the turbulence in the system. The spatial correlation $\langle U_i'U_j' \rangle$ or second order moments of the fluctuation velocity are very useful to compute the “Reynolds’ stresses” (Tennekes and Lumley, 1972; Monin and Yaglom, 1965; Frisch, 1995). It has significant role to define the transportation of momentum in j -direction due to fluctuation in the i -th component of velocity and vice versa. Since RPT provides an information of fluctuating behaviour in the multiphase system as discussed in the literature (Devanathan, 1991; Degalessan, 1997; Roy, 2000; Upadhyay, 2010). Using similar approach, the axial fluctuation and axial root mean square (rms) velocities are calculated as follows:

$$U_z' = u_z - \langle U_z \rangle \quad (3.1)$$

$$U_{z-rms} = \sqrt{\langle U_z'^2 \rangle} \quad (3.2)$$

The radial components of fluctuation and rms velocities can be calculated in similar manner as given by above Equation 3.1 to 3.2. The rms velocities in the axial and radial direction, and granular temperature per unit density are discussed in following subsection.

Axial rms velocity

Figure 3.11a shows a plot of the axial rms velocities for the solids as a function of bed height along the dimensionless position (x/R). Results show that the axial rms velocity profiles are symmetric at the lower bed heights (below the side injection) with higher value in the center and minimum at the wall. For $z=0.21$ m, axial rms velocity of solids becomes higher at left wall compared to the right wall. Therefore, an asymmetric distribution of axial rms velocity is obtained. This is to be anticipated since with a secondary air injection through nozzle there is more air supply (or energy input) to the system. Hence, the increase in system energy is gradually dissipated by the fluctuation of solid velocity. In Figure 3.11a, it is noticed that the fluctuation of solid velocity gradually increases along the height near injection zone. On the opposite wall, maximum fluctuation of axial velocity is observed at $z = 0.15$ m as bubble directs its movements towards the injection wall and finally merge with the jetting bubble (Figure 3.6b). Therefore, more solids get accumulated at opposite wall which results into the reduction of fluctuation velocity at $z = 0.21$ m. Further, the fluctuation of axial velocity increases as the bubble migrates from injection wall to the axis of bed (Figure 3.6c).

In Figure 3.11b, the azimuthal averaged axial rms velocity of solids along the dimensionless radius (r/R) is presented. For the upper height ($z=0.25$ m), the maximum axial rms velocity is present in the core region ($r/R \approx 0.7$). The effect of secondary air injection can be seen as the significant increment in the axial rms velocities close to the wall. The shifting of the maximum value of axial fluctuation is observed due to random motion of bubbles from center region to

the wall (Figure 3.11b). In Figure 3.11b, the axial rms continuously decreases with increasing radial position for all the lower heights except $z = 0.25$ m which is similar to previous study (Lin, 1981). In general, the axial rms increases with increasing height due to unidirectional motion of bubbles in the central region (Lin, 1981). In this case, the bubble follows bi-directional movement in axial as well as in radial direction.

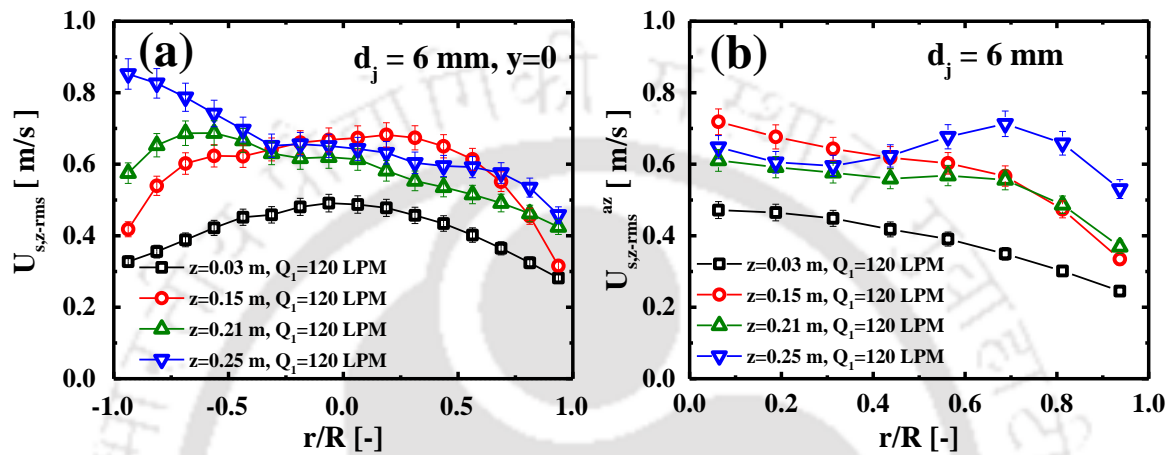


Figure 3.11 Radial variation of axial rms velocity of particle at fixed $Q_1=120$ LPM (a) injection plane ($y=0$), and (b) azimuthal averaged

Radial rms velocity

Figure 3.12a shows the radial rms velocity of solids at different bed heights along the dimensionless distance (r/R). In the lateral direction, the maximum radial rms velocity is obtained at the center and minimum at the wall as shown in Figure 3.12a. The azimuthal averaged radial rms velocity in dimensionless radial position (r/R) is also shown in Figure 3.12b. Further, the decrease in azimuthal averaged radial rms velocity is observed with the bed height. It is noticed that the radial component of azimuthal averaged rms velocity for the solids is 60% of the axial rms velocity at the same radial position. Therefore, in the primary flow direction, that is, in the axial direction, the fluctuations of solid velocity are dominant and there is an anisotropic flow in the system.

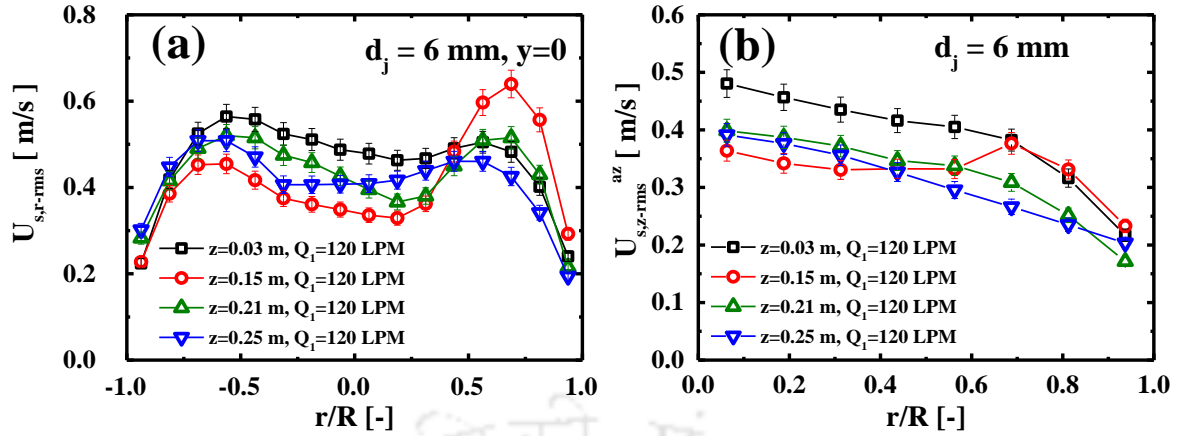


Figure 3.12 Radial variation of radial rms velocity of particle at fixed $Q_1=120$ LPM (a) injection plane ($y=0$), and (b) azimuthal averaged

Granular temperature

The turbulent kinetic energy (TKE) of the fluctuations is directly related to the normal stresses and is computed as follows:

$$TKE = \frac{1}{2} \rho_p \sum_{\alpha=r,\theta,z} \langle U_\alpha'^2 \rangle \quad (3.3)$$

The granular temperature (Θ_s) is an important parameter which is analogous to the absolute temperature of the system of gas molecules in the kinetic theory of gases. It is directly related to the fluctuations of the solid velocity and can be given by the kinetic theory of granular flow (KTGF). The detail information on KTGF is available in literature (Tartan and Gidaspow, 1994). The granular temperature is given as:

$$\Theta_s = \frac{1}{3} \sum_{\alpha=r,\theta,z} \langle U_\alpha'^2 \rangle \quad (3.4)$$

Figure 3.13a illustrates the distribution of granular temperature of solids as a function of bed height along the dimensionless distance (r/R) for the operating condition of $Q_1 = 120$ LPM, $U=1.12$ m/s and $H=0.75$ m. The granular temperature profiles are similar to axial rms velocity. Above the nozzle injection height, the granular temperature is higher towards the nozzle injection wall. This shows higher solid fluctuations due to the secondary injection of gas through sidewall nozzle. In Figure 3.13b, the azimuthal averaged granular temperature distribution of solids is plotted against dimensionless radial position for same operating condition. Results shows that the order of granular temperature are same as the rms velocities and the distribution trends are similar to the axial rms velocities. This shows that the axial fluctuation is dominating. Further, for azimuthal averaged granular temperature profile is similar to conventional gas-solid cylindrical fluidized bed without sidewall nozzle injections. The granular temperature profiles of solids are similar to the axial rms velocity.

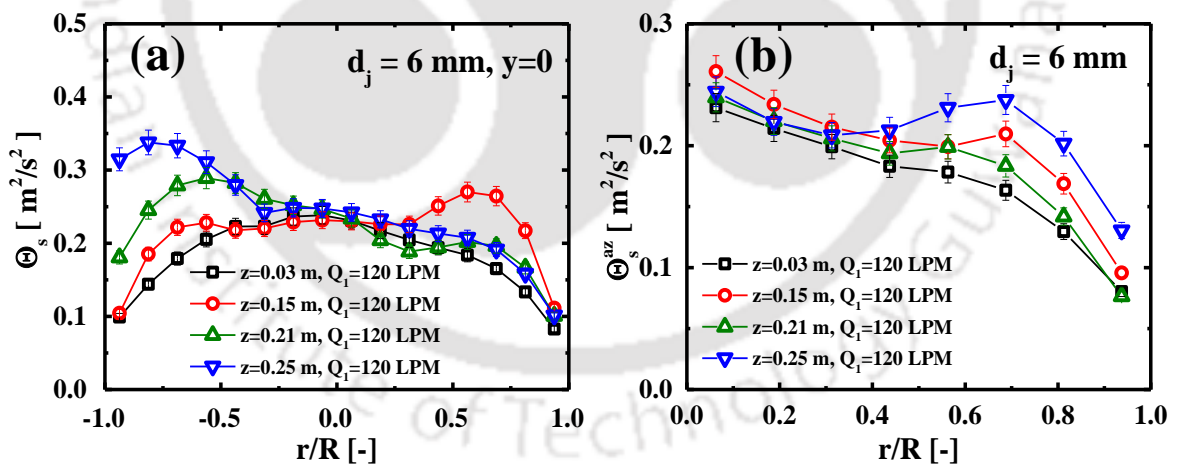


Figure 3.13 Radial variation of granular temperature of solid at fixed $Q_1=120$ LPM (a) injection plane ($y=0$), and (b) azimuthal averaged

Axial dispersion coefficient

The Lagrangian trajectory of instantaneous position data provides a wide source of information tools to measure the mixing time (Cassanello et al., 1996), circulation time distribution and particle dispersion coefficients (Limtrakul, 1996; Kiared et al., 1997; Degaleesan, 1997; Degaleesan et al., 1997). The axial dispersion coefficient is computed as the time derivative of the Lagrangian mean –square displacements as reported by Monin and Yaglom (1971). In the present case, it is measured in a similar way as explained by Kiared et al. (1997). The axial dispersion coefficients ($D_{s,zz}$) are computed with the assumption of homogeneous turbulence and gradient less flow (Limtrakul, 1996). To determine $D_{s,zz}$, first the excess displacement of z-component, $Z(E_0, t)$ is calculated by subtracting z- coordinate of the reference cell (x_0, y_0, z_0) or z_0 from the corresponding instantaneous axial position-time series data, $z(t)$.

The ensemble-averaged axial displacement $\langle Z(E_0, t) \rangle$ and mean squared displacement $\langle Z^2(E_0, t) \rangle$, are computed as:

$$\langle Z(E_0, t) \rangle = \frac{1}{N} \sum_{n=1}^N Z_n(E_0, t) \quad (3.5)$$

$$\langle Z(E_0, t) \rangle = \frac{1}{N} \sum_{n=1}^N Z_n(E_0, t) \quad (3.6)$$

$$\langle Z^2(E_0, t) \rangle = \frac{1}{N} \sum_{n=1}^N \left(Z_n(E_0, t) - \langle Z(E_0, t) \rangle \right)^2 \quad (3.7)$$

Finally, $D_{s,zz}$ is determined from the slope of axial mean square displacement curve and can be expressed as:

$$D_{s,zz}(E_0, t) = \frac{1}{2} \frac{d}{dt} \langle Z^2(E_0, t) \rangle \quad (3.8)$$

Figure 3.14a and 3.14b show the planer and azimuthal averaged axial dispersion coefficient of solids at different bed height (z) for the operating condition of $Q_1 = 120$ LPM, $U=1.12$ m/s and

$H=0.75$ m. The planer and azimuthal average value of dispersion coefficient of the solid is same across the cross-section at all the height though the solid mean velocity is same. Further, the value of dispersion coefficient is reducing with the bed height. This shows that bottom and top of the column behaves differently. The bottom section behaves like a mixed bed while top of the of the column behaves more like a plug flow reactor. This may be due to the bigger bubble generated at the top section. Hence, if one wants to model such beds, a multi-physics model needs to be used which will be the function of the bed height.

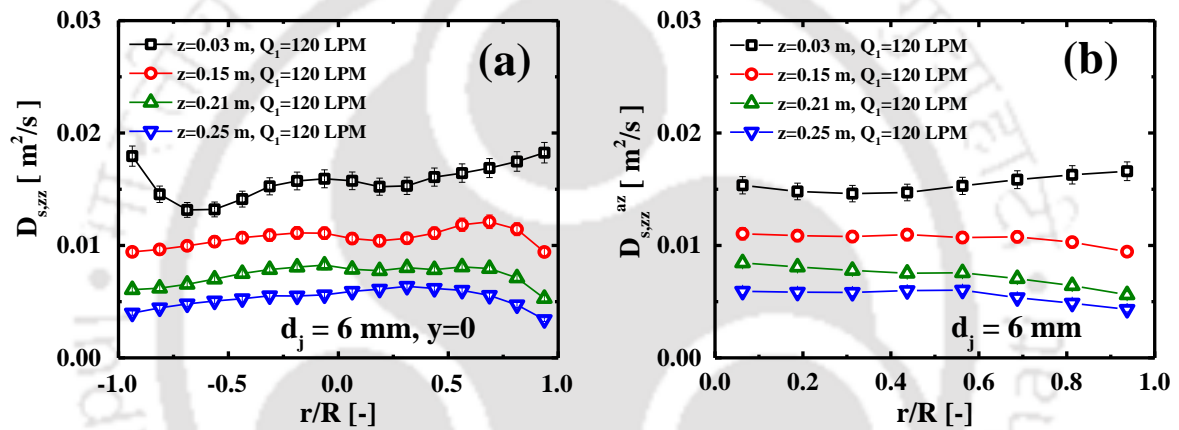


Figure 3.14 Radial variation of the solid axial dispersion coefficient at fixed $Q_i=120$ LPM (a) injection plane ($y=0$), and (b) azimuthal averaged

3.3.2. RPT measurement with a single injection through 1 mm ID nozzle

Mean axial velocity

The ensemble-averaged mean axial velocity of solid is determined for 4 different axial positions of the bed ($z=0.03, 0.15, 0.21$ and 0.25 m) at five different injection flowrates (20, 30, 40, 60, 80 and 100 LPM) through a single nozzle of 1 mm ID in gas-fluidized bed of 0.21

m diameter. Figure 3.15 shows the axial mean velocity profiles along the x-axis (or injection line of N1) with different injection flowrates (Q_1). This figure also shows the migration of fluidized bubbles towards the injection zone as it travels along with the height. This can be confirmed by the shift in the maxima of axial mean velocity at each height. The two separate zones can be observed by analysing these plots: 1) the left half region ($-1.0 < x/R < 0.4$), and 2) the right half region ($0.4 < x/R < 1.0$). In the left half region, the particles move upward while in the right half region, the particles move down along the right wall ($x/R = 1.0$). Therefore, one solid circulation cell can be observed for all the nozzle injection flowrates. In all the cases the solid migration towards the nozzle injection wall starts from the bottom itself and solid velocity becomes more asymmetric. Further, the velocity of the solids increases with height for all nozzle injection flowrates. This indicates that the sidewall nozzle-injected bubbles are merging with the bubbles originated at distributor to form a larger bubble, which is increasing the velocity of the solids. It is observed that with increase in nozzle injection flowrate marginal change in solid velocity is observed. This shows that solid motion is primarily dominated by the bottom gas flowrate. The sidewall nozzle injection affects the flow in nozzle injection plane and leads to migration of bubbles towards the nozzle injection wall due to the low pressure at the injection plane. The azimuthal averaged mean axial velocities are computed for all injection velocities (Q_1) and are compared for 4 axial heights as shown in Figure 3.16. The figures show that the maximum axial averaged (positive) velocity is found at the central region of the bed which continuously decreases until approach closer to the wall ($r/R=1.0$). At the wall, the negative velocities are noticed which is probably due to the downward motion of solids. This shows that average profile of nozzle assisted fluidized bed is similar to the conventional fluidized bed without any sidewall nozzle injection. However, the planar profile at nozzle injection plane is different due to the low pressure zone created because of nozzle injection. It is interesting to note that compared to conventional fluidized bed in sidewall nozzle injection

fluidized bed, maximum velocity is observed just below the injection plane. This is common in planar as well as azimuthal average profile. This indicate that the actual interaction of sidewall nozzle injected bubble and bubble generated at the distributor plate takes just below the nozzle injection plane. This phenomenon is more significant for 1 mm diameter nozzle compared to 0.6 mm diameter nozzle due to wider injection zone.

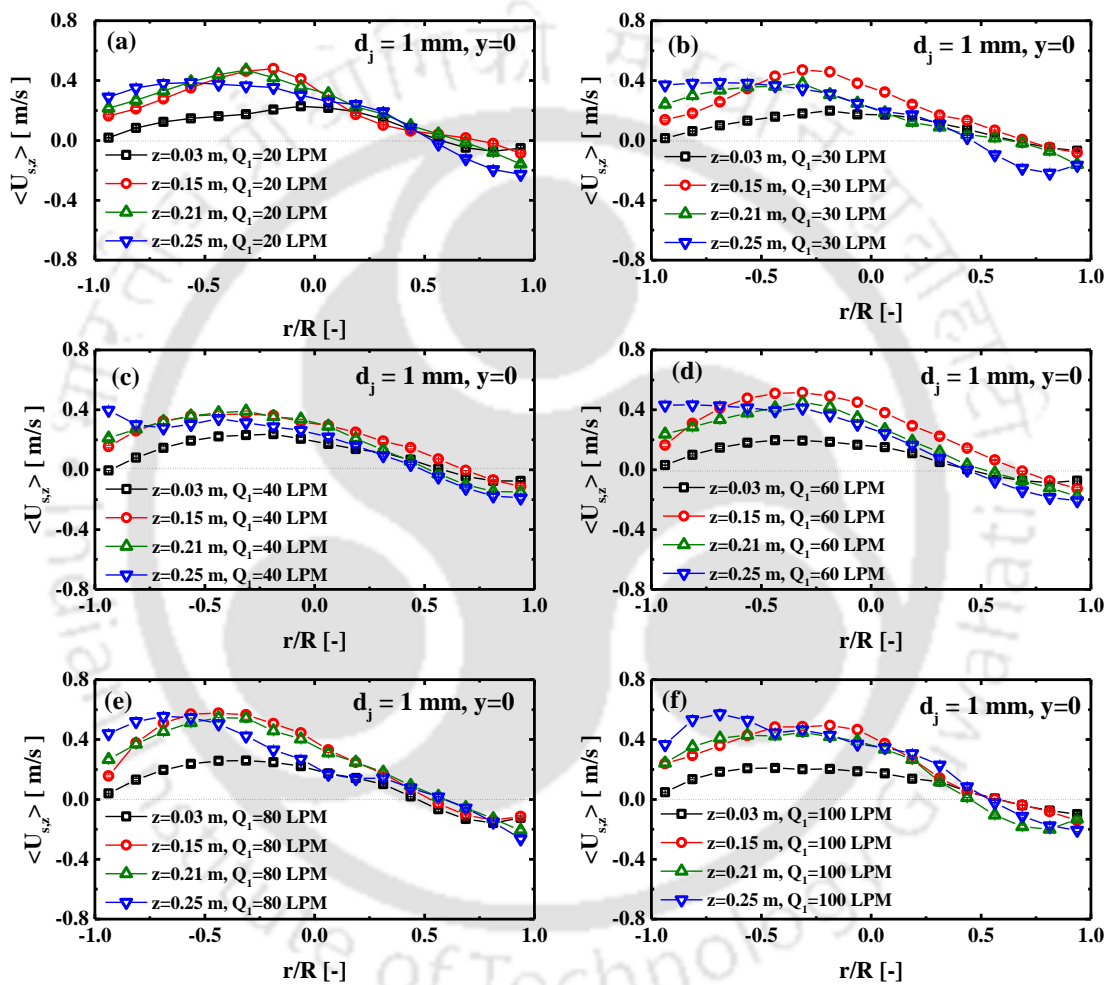


Figure 3.15 Lateral distribution of mean axial velocity of solids for fixed Q_1 (a) 20 LPM, (b) 30 LPM, (c) 40 LPM, (d) 60 LPM, (e) 80 LPM and (f) 100 LPM

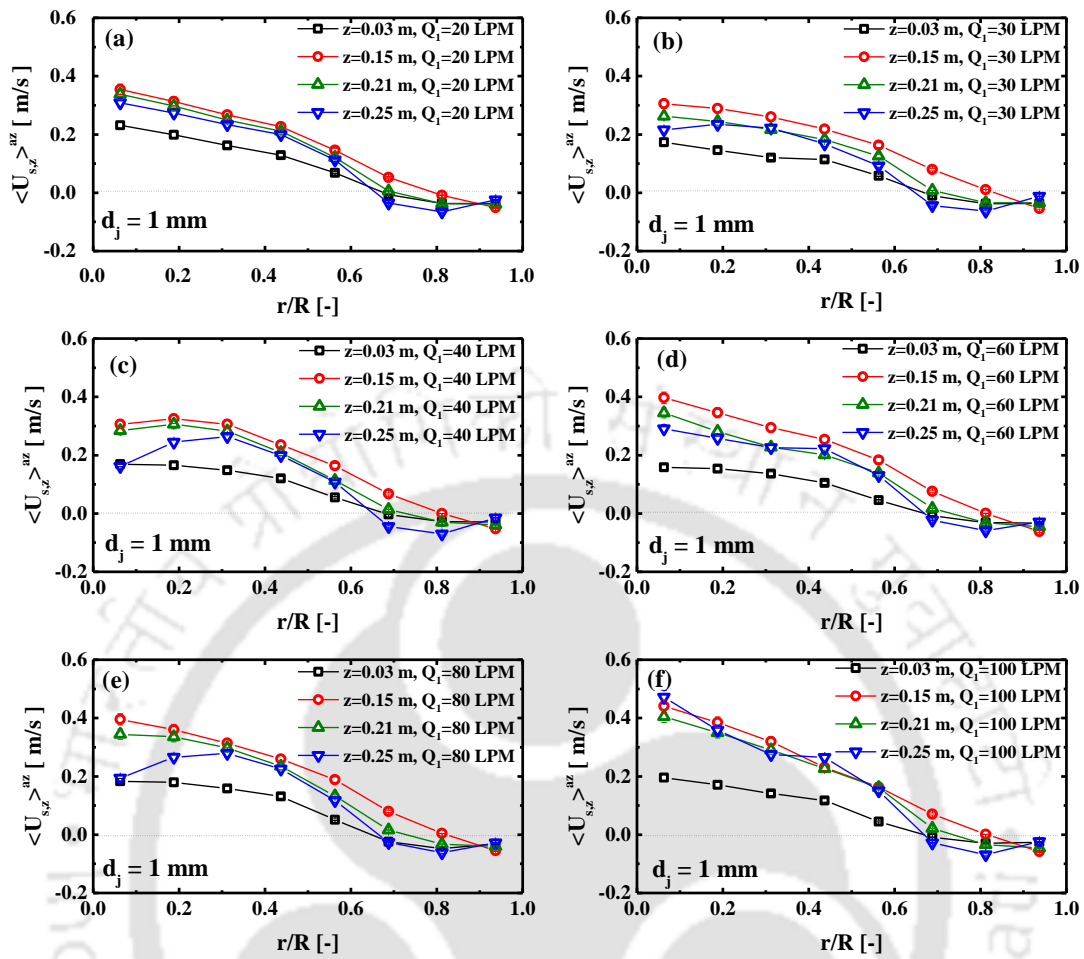


Figure 3.16 Azimuthal averaged mean axial velocity for different axial planes at fixed Q_1 (a) 20 LPM, (b) 30 LPM, (c) 40 LPM, (d) 60 LPM, (e) 80 LPM and (f) 100 LPM

Mean radial velocity

RPT allows us to measure the instantaneous positions of tracer in all three directions, hence, the radial component of the instantaneous velocity was also evaluated from the experimental data. The ensemble-averaged mean radial velocity was also computed with a single nozzle injection of 1 mm ID in the bed. Figure 3.17 shows the mean radial velocity along the injection

path of N1. In this case (with 1 mm ID), the mean radial velocities follow similar trends as previously shown by a 6 mm ID nozzle (Figure 3.9). It is worth to notice that positive radial velocities are observed near the injection wall ($x/R=-1.0$). At $z=0.15$ m, on approaching the opposite wall ($x/R=1.0$), a slight increase has been observed in the curve before crossing the point $x/R=-0.5$. Thereafter, the mean radial velocity continuously decreases and crosses the x -axis at $x/R=0$ which can be displayed in Figure 3.17. Afterward, negative velocities are observed closer to the other wall ($x/R=1.0$).

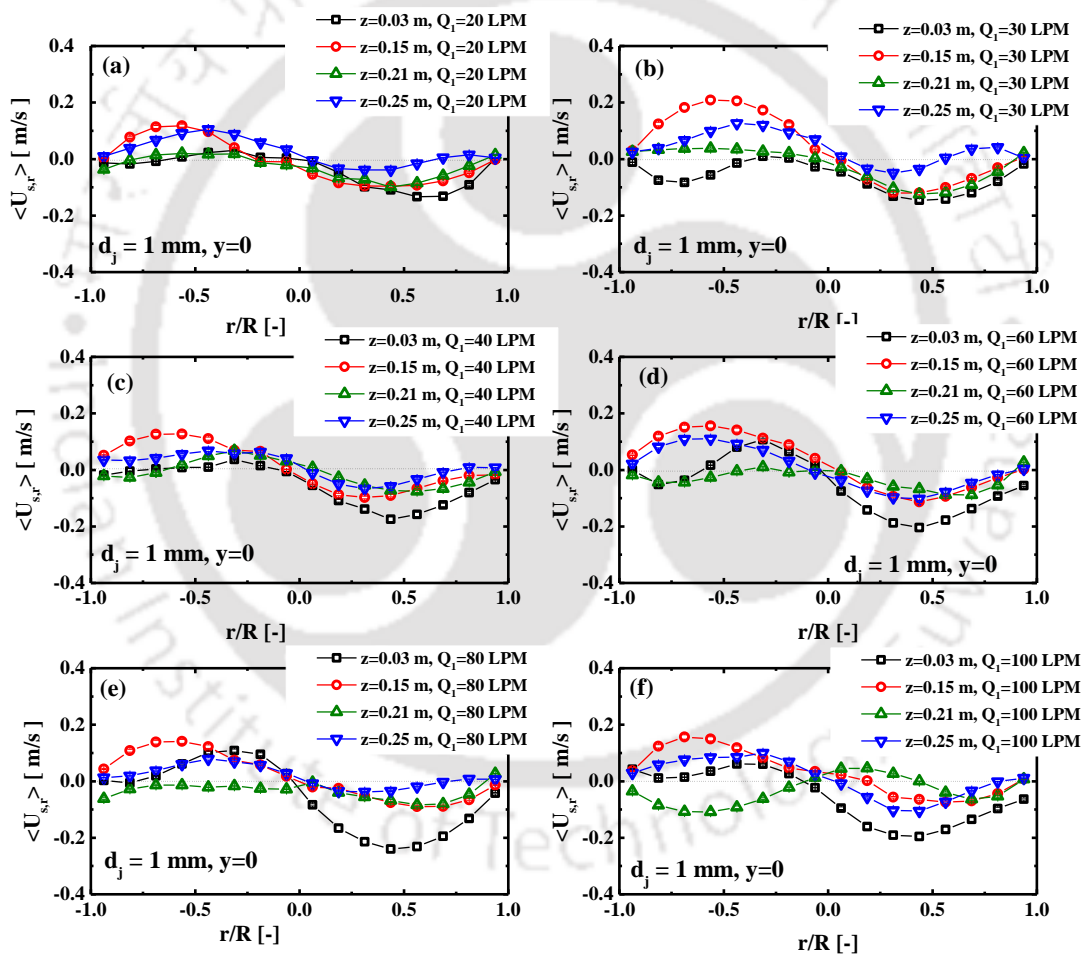


Figure 3.17 Lateral distribution of mean radial velocity of solids for fixed Q_1 (a) 20 LPM, (b) 30 LPM, (c) 40 LPM, (d) 60 LPM, (e) 80 LPM and (f) 100 LPM

Just above the injection level ($z=0.21$ m), the positive mean radial velocity near the injection wall has been observed at the lower value of Q_1 which becomes negative for high injection flowrates (Q_1). Figure 3.18 shows the azimuthal radial mean velocity of the particle, and the negative radial velocity with low magnitude are found at the lowest bed height ($z=0.03$ m). As being closer to the distributor ($z=0$ m), the solid particle moves towards the axis of the bed from the wall.

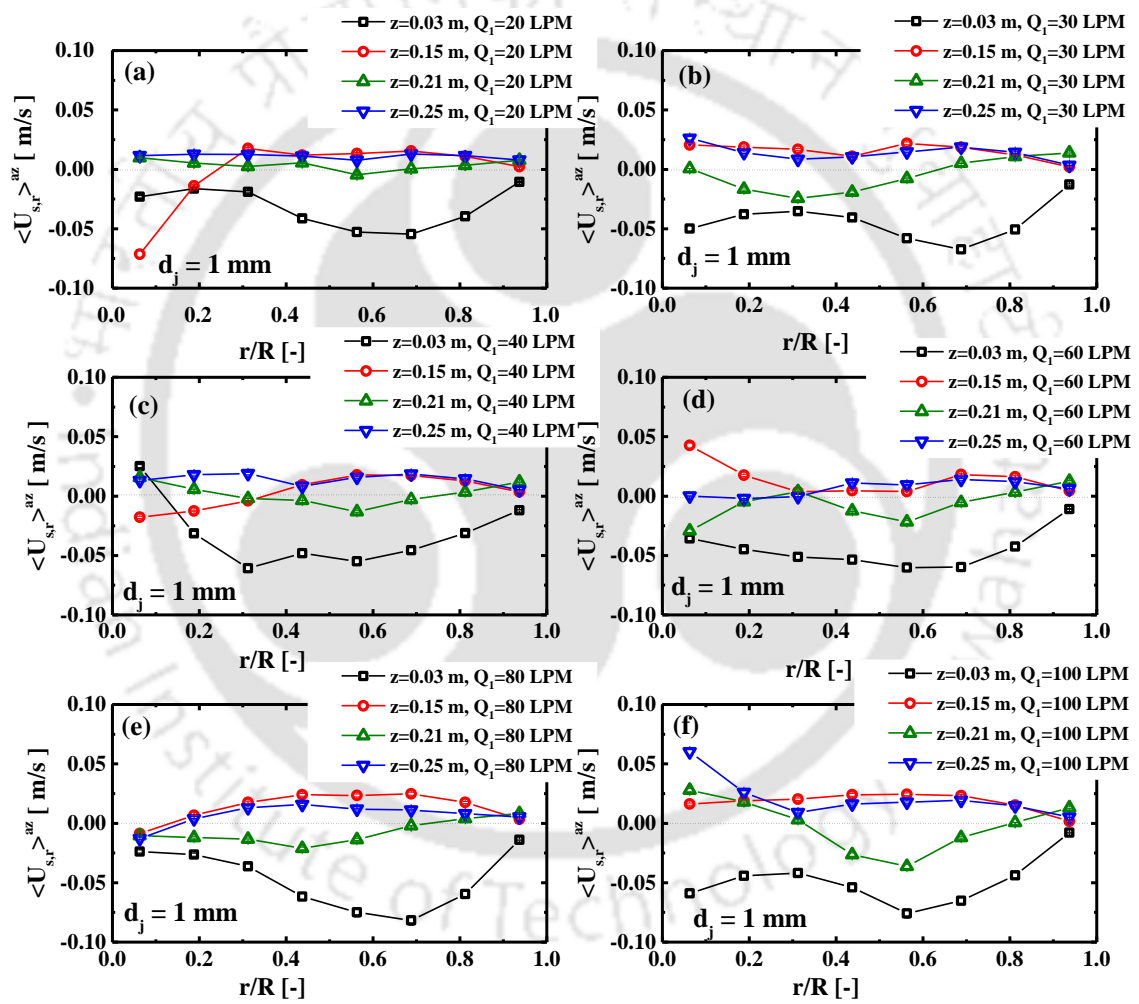


Figure 3.18 Azimuthal averaged mean radial velocity for different axial planes at fixed Q_1 (a) 20 LPM, (b) 30 LPM, (c) 40 LPM, (d) 60 LPM, (e) 80 LPM and (f) 100 LPM

Axial rms velocity

In this section, the comparison of axial rms velocities, measured at 4 different axial heights via RPT has been made and is shown in Figure 3.19. These radial distributions are plotted in the lateral direction along the x-axis for 6 different injection flowrates under a constant fluidization condition which is illustrated in Figure 3.19a-f. The axial rms velocity increases with the height. This shows that bed becomes more violent as we move up in the bed. This is due to the formation of the bigger bubbles with the height. Further, it is observed that with increase in nozzle injection gas flowrate, marginal increase in axial rms velocity is observed and overall pattern remains same for all the velocities.

This shows that the solid flow behaviour is dominated by the primary gas injected from the bottom of the column. The marginal increase in axial rms velocity is a result of the system's higher energy intake, which dissipates as improved solid fluctuations. For a higher injection velocity, the axial rms velocities are found to be high at $z = 0.25$ m. (Figure 3.19a-f). As a result of the bubble moving from the wall to the centre of the bed, there may be a significant accumulation of solids close to the injection wall and above the injection plane. Hence, both the high axial velocity of the solids and their high solid content close to the injection zone contribute to the axial rms velocity of the solids.

The axial rms velocities are found maximum close to injection zone for $z=0.25$ m and for all the injection velocities (Figure 3.19a-f). This shows that the interaction between jetting bubble and the fluidized bubble depends on the injection flowrates. In addition, the circumferentially averaged ensemble-averaged axial rms velocity is also evaluated for the same injections flowrates. These data are shown in Figure 3.20a-f. According to Figure 3.20, the maximum values of the azimuthally averaged axial fluctuating velocities are observed mainly in $r/R \sim 0.8$; close to the wall values generally decreases for planes farther from the secondary injection. These observations are shown at $z=0.03$ and $z=0.25$ m. Also, it can be shown that as the planes

approach the secondary injection, the azimuthally averaged axial fluctuation velocities increase radially and reach their maximum at the center.



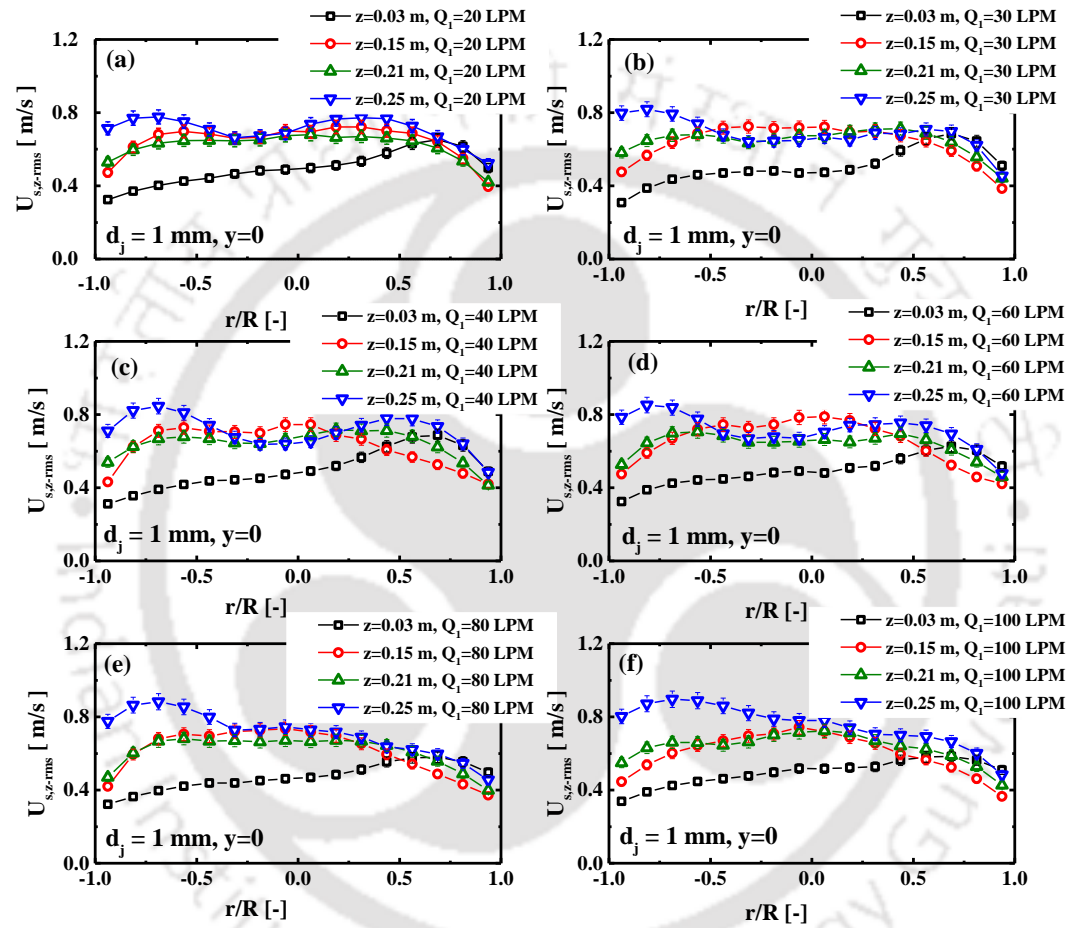


Figure 3.19 Lateral distribution of axial rms velocity of solids for fixed Q_1 (a) 20 LPM, (b) 30 LPM, (c) 40 LPM, (d) 60 LPM, (e) 80 LPM and (f)

100 LPM

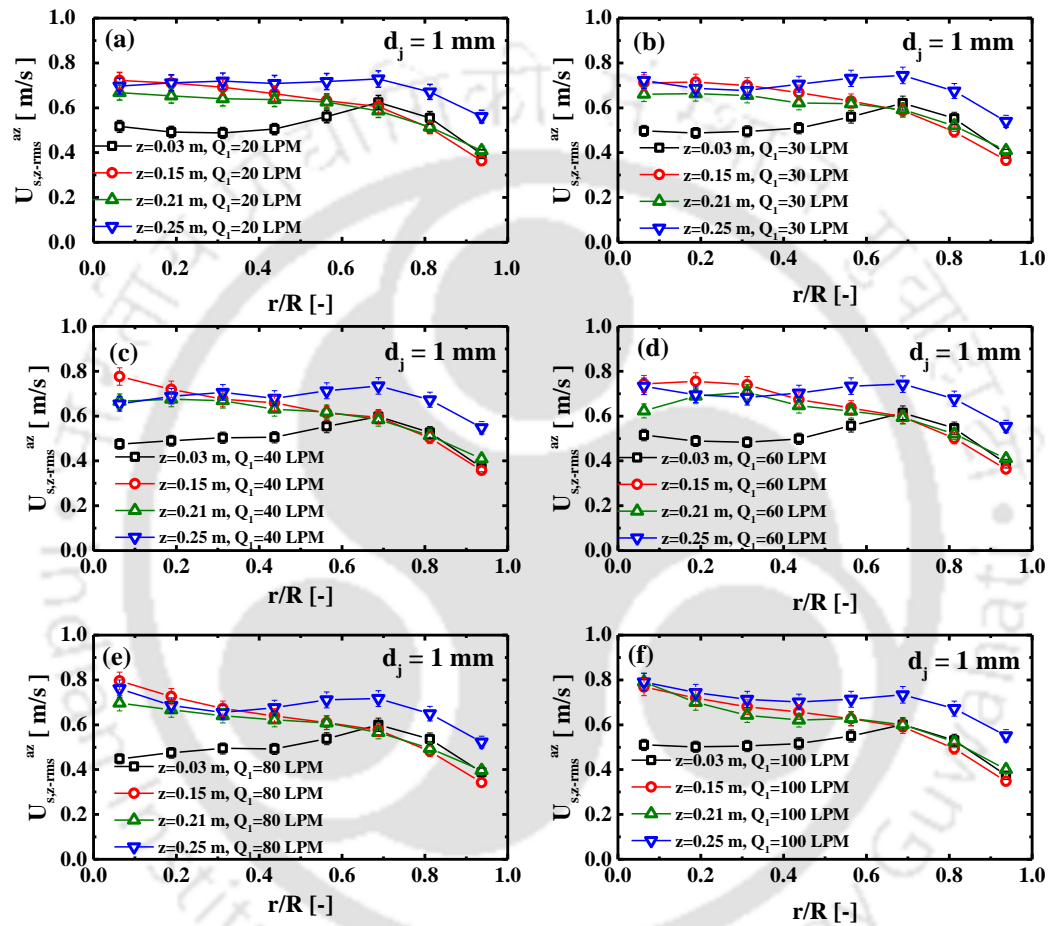


Figure 3.20 Azimuthal averaged axial rms velocity for different axial planes at fixed Q_1 (a) 20 LPM, (b) 30 LPM, (c) 40 LPM, (d) 60 LPM, (e) 80 LPM and (f) 100 LPM

Granular temperature

Figure 3.21a-f shows the lateral profiles of granular temperature evaluated at four z-planes under the experimental conditions presented in Table 3.1. At $z=0.03$ m, the granular temperature is asymmetric in nature due to the high disturbance near the distributor.

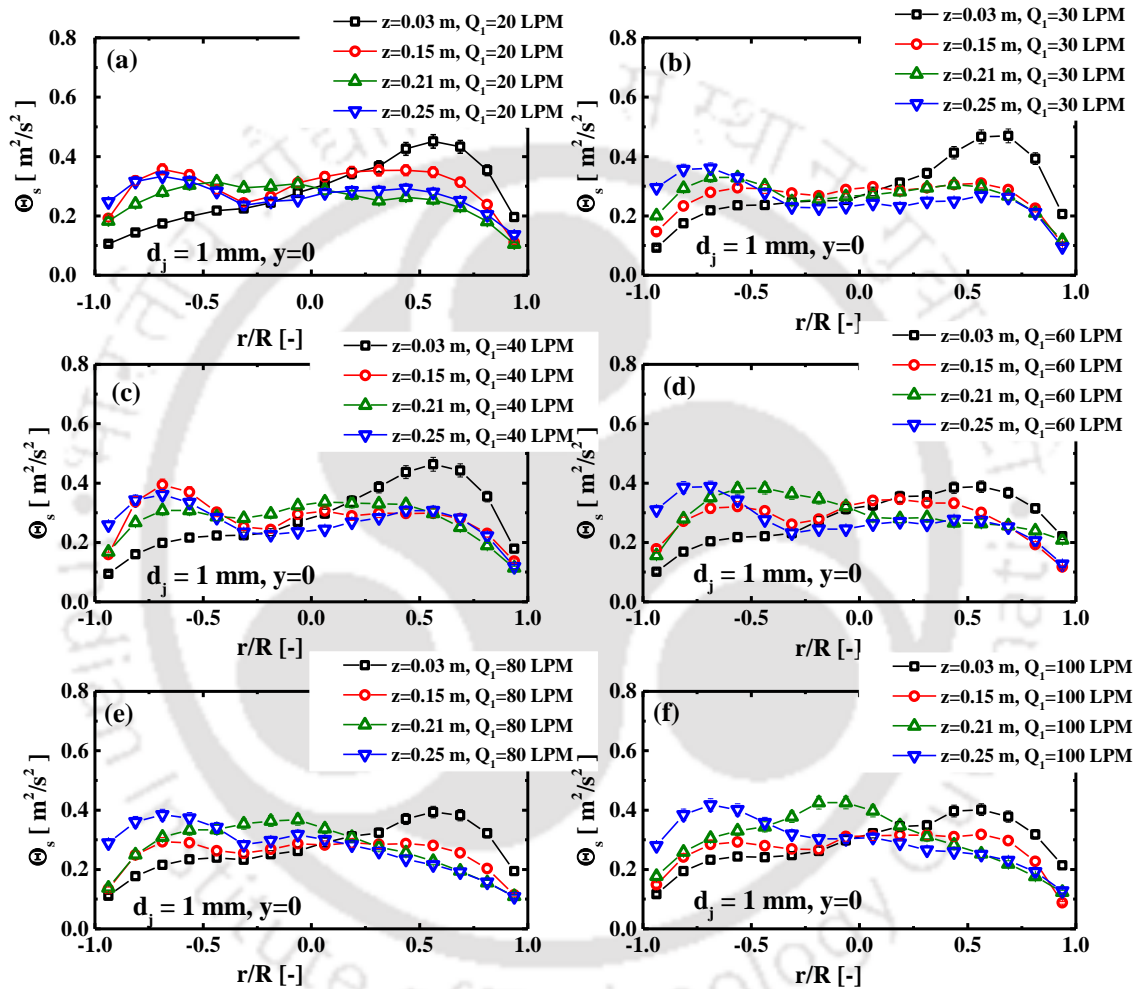


Figure 3.21 Lateral distribution of granular temperature of solids for fixed Q_1 (a) 20 LPM, (b) 30 LPM, (c) 40 LPM, (d) 60 LPM, (e) 80 LPM and (f) 100 LPM

At the highest z-plane ($z=0.25$ m), the maximum granular temperature is noticed near the injection wall. The local maximum value is varied from 0.3 to 0.4 m^2/s^2 as the injection flow rate is increased from 20 to 100 LPM. Figure 3.22a-f displays the circumferentially averaged and time-averaged granular temperature values. It approaches a maximum value at core and minimum at closer to the wall ($r/R=1.0$).

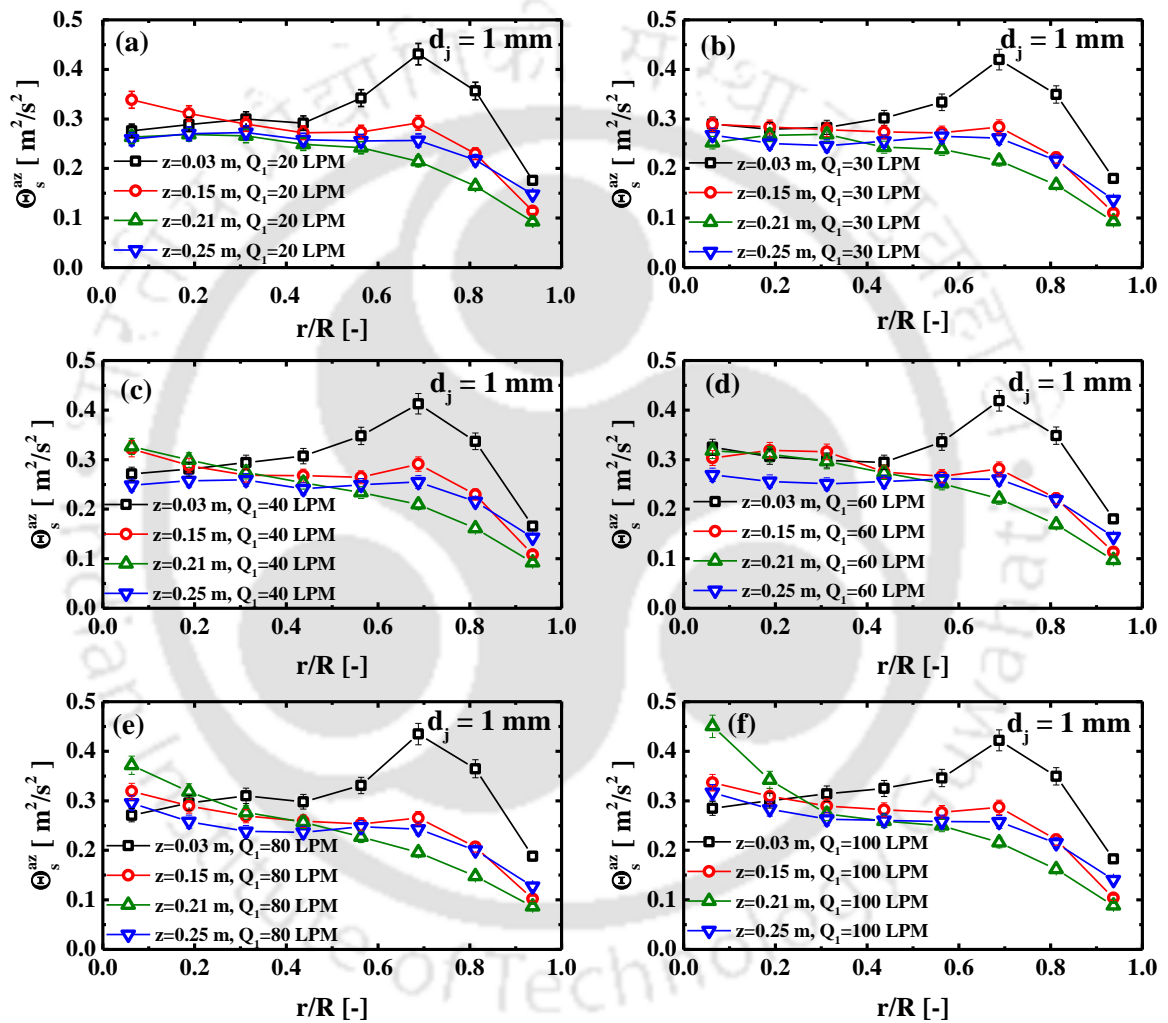


Figure 3.22 Azimuthal averaged granular temperature for different axial planes at fixed Q_1 (a) 20 LPM, (b) 30 LPM, (c) 40 LPM, (d) 60 LPM, (e) 80 LPM and (f) 100 LPM

Axial dispersion coefficients

The axial dispersion coefficient of the solids is also computed for the second case, where RPT is conducted in a bed with a small size nozzle of 1 mm ID. Figure 3.23 presents the distribution of axial dispersion coefficients along the x-axis. For all the injection flowrates (20-100 LPM), the axial dispersion coefficient decreases with bed height.

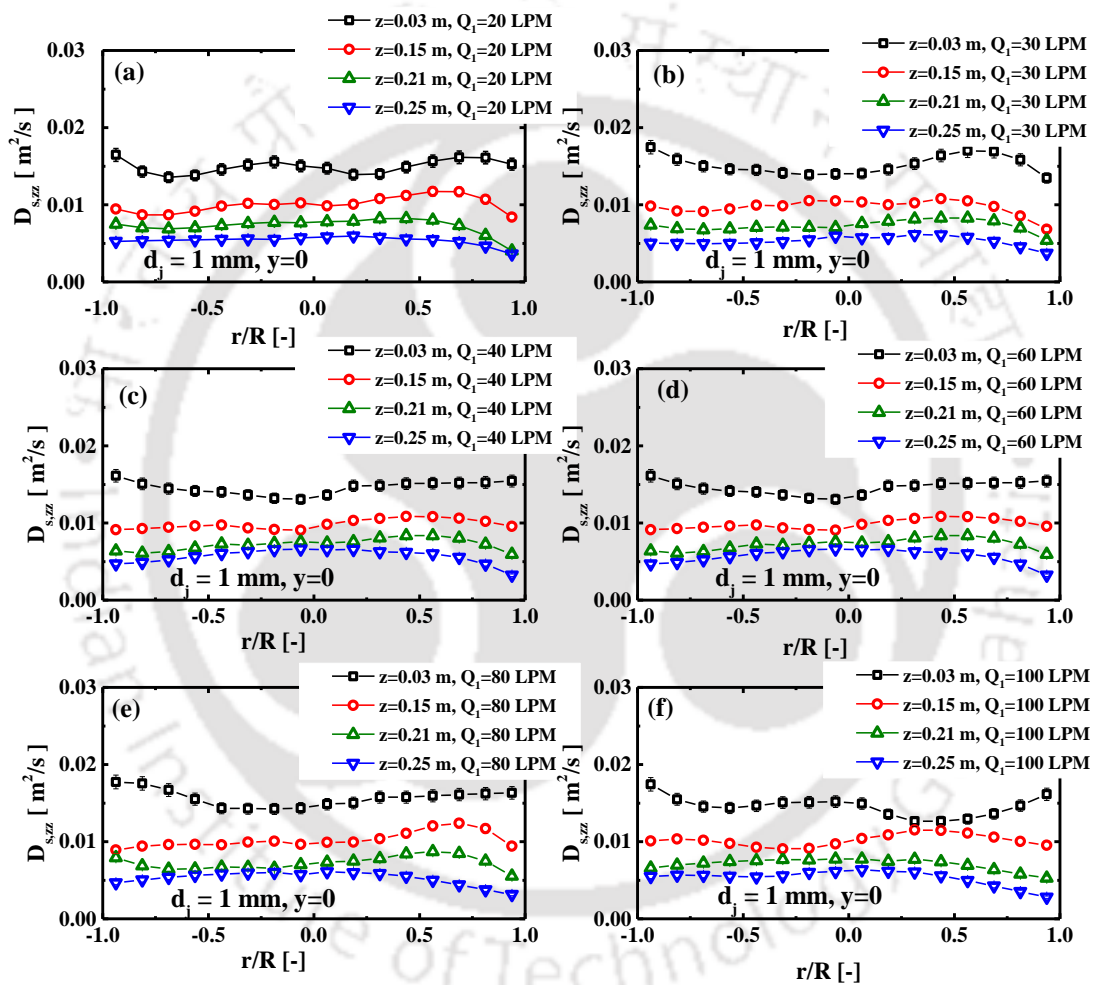


Figure 3.23 Lateral distribution of dispersion coefficient of solids for fixed Q_1 (a) 20 LPM, (b) 30 LPM, (c) 40 LPM, (d) 60 LPM, (e) 80 LPM and (f) 100 LPM

3.3.3. Effect of nozzle diameter

In this section, a comparison between two different size nozzles is presented. RPT allows us to measure the phase distribution locally as well as globally in a multiphase system. Therefore, the cell-wise distribution can be obtained from the Lagrangian data series of instantaneous velocity for the solid phase. The probability distribution function (PDF) of instantaneous solid velocity is obtained with two different diameter nozzles (6 mm and 1 mm ID) at three different Eulerian cells that lie along the x-axis. To find the PDF at a fixed z-plane ($z=15$ cm), three virtual cells are selected along the injection line of nozzle N1. These three cells are located at $r/R=0.94$ (right cell), $r/R=0$ (central cell) and $r/R=-0.94$ (left cell). Among these three cells, the Lagrangian trajectory of the instantaneous position is tracked in the desired cell. Once the particle enters the desired cell, the particle trace is assumed as an independent event. This event is initiated with time zero and the corresponding instantaneous velocity is evaluated for two successive time intervals. This way, the number of visits and the instantaneous velocity are recorded in that cell. The mean and standard deviation are also calculated. Hence, the distribution of solid velocity in r , θ and z -direction are calculated for three different injection flowrates (40, 60 and 100 LPM).

The instantaneous axial velocity

Figure 3.24a, b, c shows the PDF of z -component of the instantaneous velocity of solids for three axial heights: $z=0.15$, 0.21 and 0.25 m respectively, computed at three different cells along the injection line. The PDF is evaluated for three different injection flowrates (40, 60 and 100 LPM) with two different sized nozzles (6 mm and 1 mm ID). For all central cells, the mean axial velocity increases as the secondary injection flowrate increases with larger diameter nozzle. The asymmetric nature of axial velocity distribution is observed with two different diameter of nozzles. The distribution of axial velocity is mostly positive at the central zone as well as around the injection zone for all secondary flowrates. This reveals that local dynamics

of bubbles are similar in both cases. At the opposite wall, the axial velocity is predominantly negative .



(a)

$r / R = 0.94$

$d_j = 6 \text{ mm}$

$d_j = 1 \text{ mm}$

$r / R = 0$

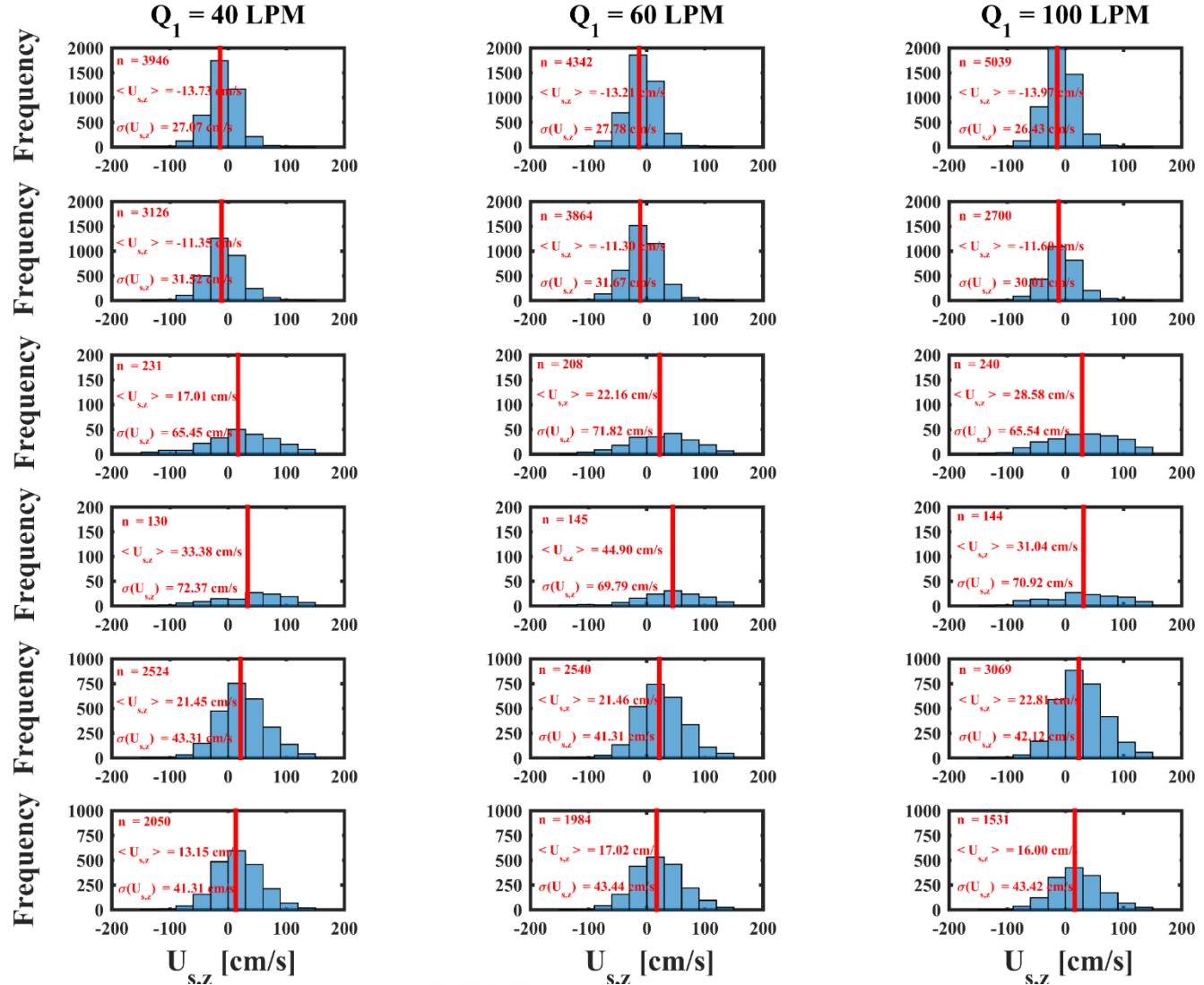
$d_j = 6 \text{ mm}$

$d_j = 1 \text{ mm}$

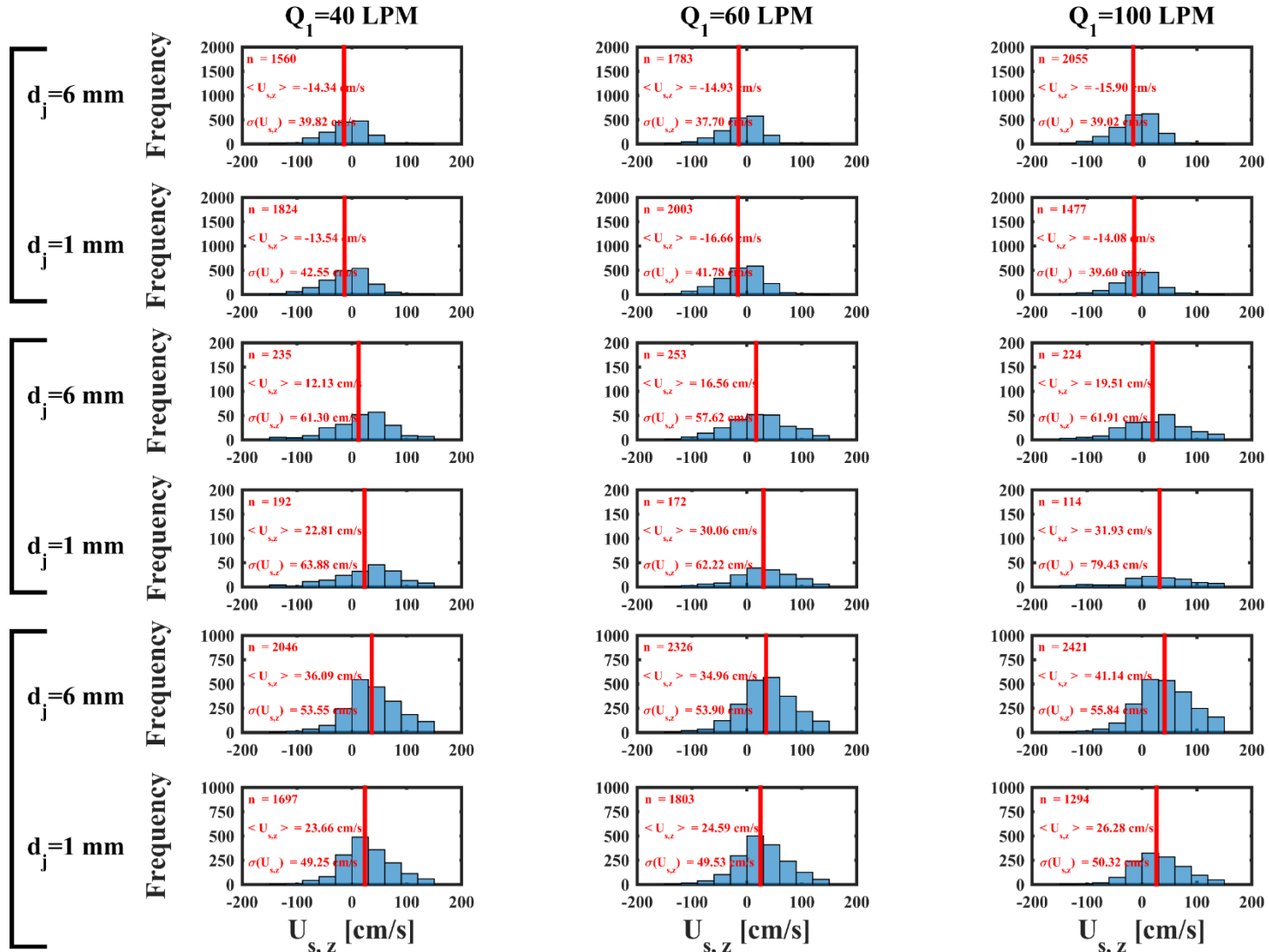
$r / R = -0.94$

$d_j = 6 \text{ mm}$

$d_j = 1 \text{ mm}$



(b)
 $r / R = 0.94$



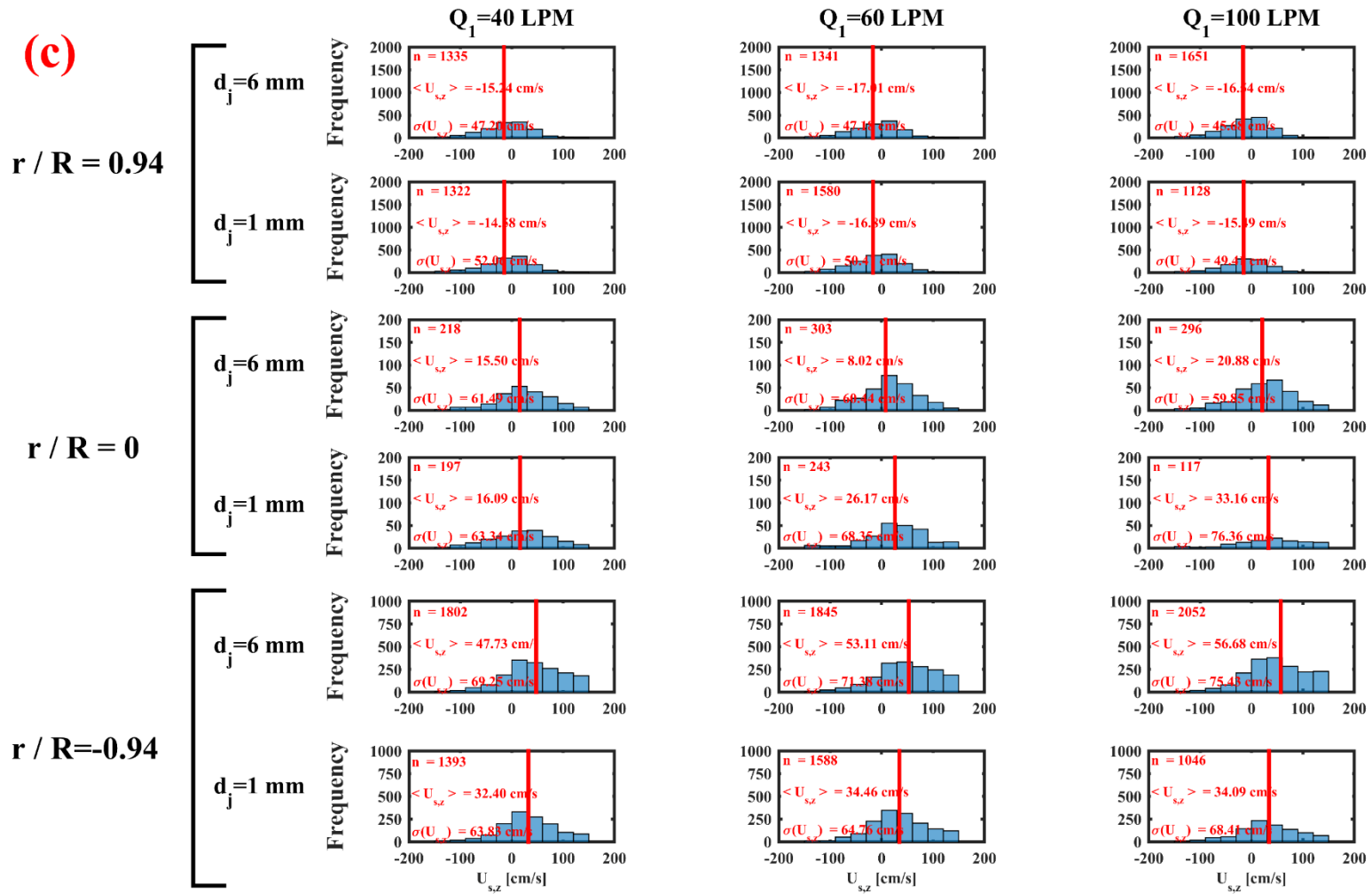


Figure 3.24 PDF of instantaneous velocity at different z -planes (a) $z=0.15$ m, (b) $z=0.21$ m and (c) $z=0.25$ m

The mean and standard deviation are also highlighted for each PDF. For the left cell ($r/R = 0.94$), the mean axial velocity increases with column height until it reaches to the injection plane. At $z=0.21$ m, the maximum axial velocity is observed which further reduces along with the height. The standard deviation values are higher with 6 mm nozzle at three axial position around the injection. Therefore, the injection with large diameter nozzles provides more spreads than smaller diameter nozzles. Meanwhile, the spread of the PDF remains unchanged along the injection line but increases along with the bed height for all cells with two different size nozzle injections.

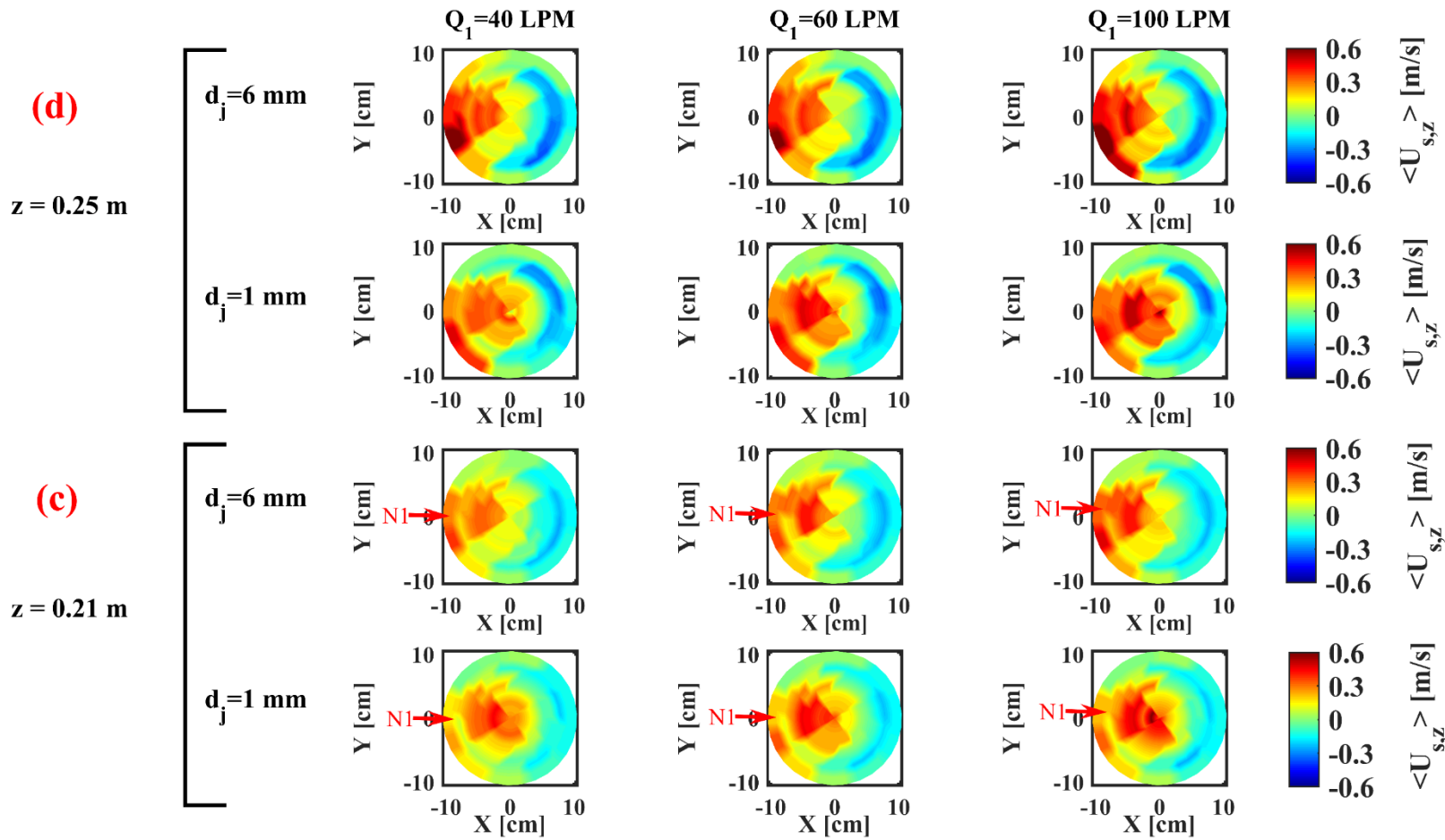
Effect on mean axial velocity

Figure 3.25a-d shows the contour plots of mean axial velocity of solid for 4 different z-planes ($z = 3, 15, 21$ and 25 cm) in both the cases. Figure 3.25a-b displays the mean axial velocity distribution for two lower planes (just below the injection plane) with two different sized nozzles. Similarly, Figure 3.24c-d shows the axial mean velocity distribution on the two upper planes that are located just above the injection plane. The three main observations can be drawn from Figure 3.25. In the first observation, the bubble migration can be easily visualized by observing these contour plots in both the cases. In the gas-fluidized bed, it has been reported that the bubble rises in an upward direction at the core region. Hence, the mean axial velocity of solid has been observed in the central region. In the present study, the bubble dynamics show a different profile along with the height. Figure 3.25 also shows that the red zone (maximum velocity zone) shifts from the center of the bed to the injection wall side. In the second observation, the more spread near the injection wall which can be visible with the large diameter (6 mm ID) nozzle. The third observation shows that the penetration length is higher in the case of a 1 mm nozzle.

Figure 3.26a, b displays the contour of the mean radial velocity of solids at different axial planes for different size nozzle injections, and compare these data for three secondary air

flowrates (40, 60 and 100 LPM). The shape of the boundary between two different zones of dense and less dense in the bed can be inferred from the RPT experiment (Roy et al., 1994). This can be identified by either plotting the radial variation of the ensemble-averaged axial solid velocities at different bed heights or visualizing the contours of mean axial velocity for different z-planes.





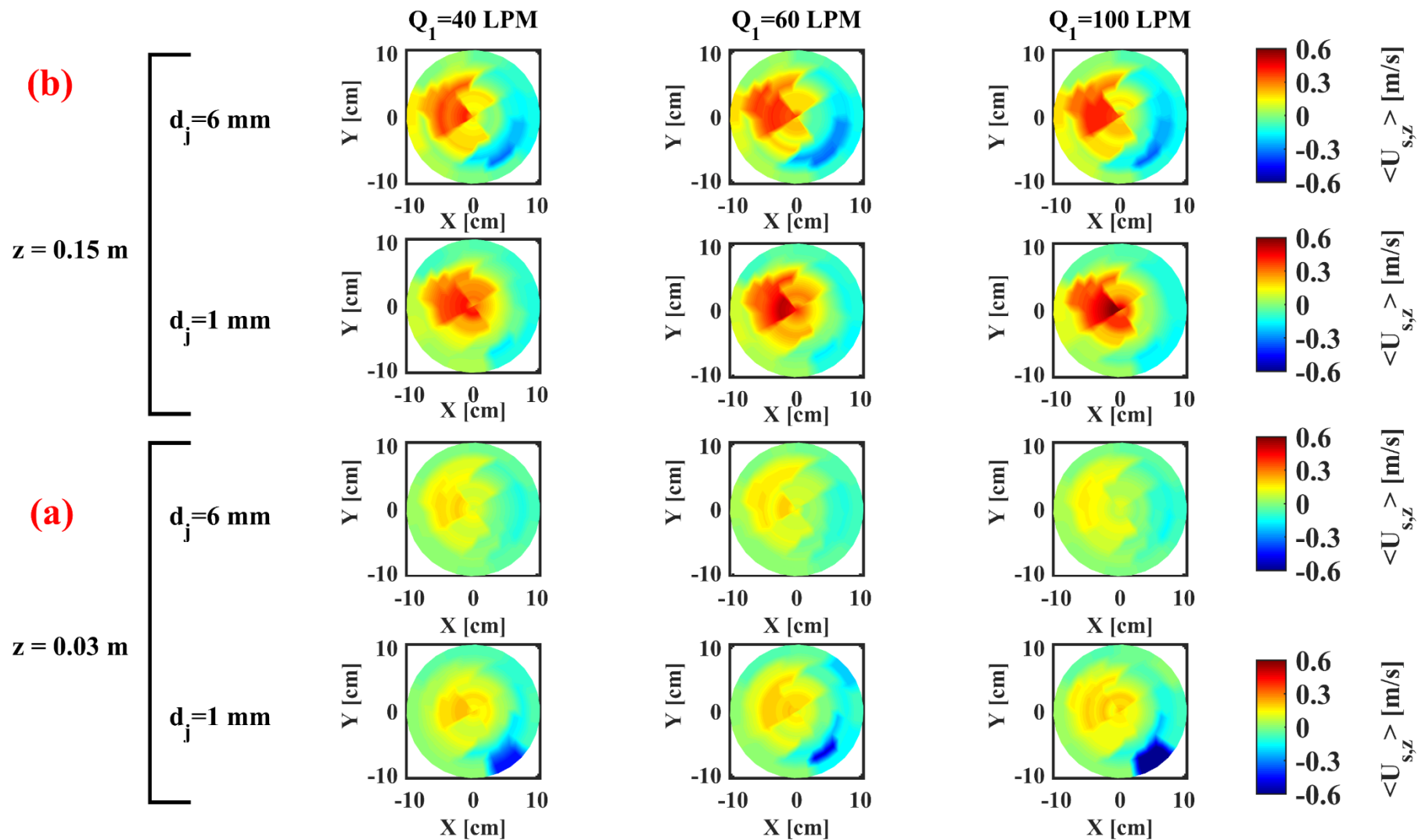
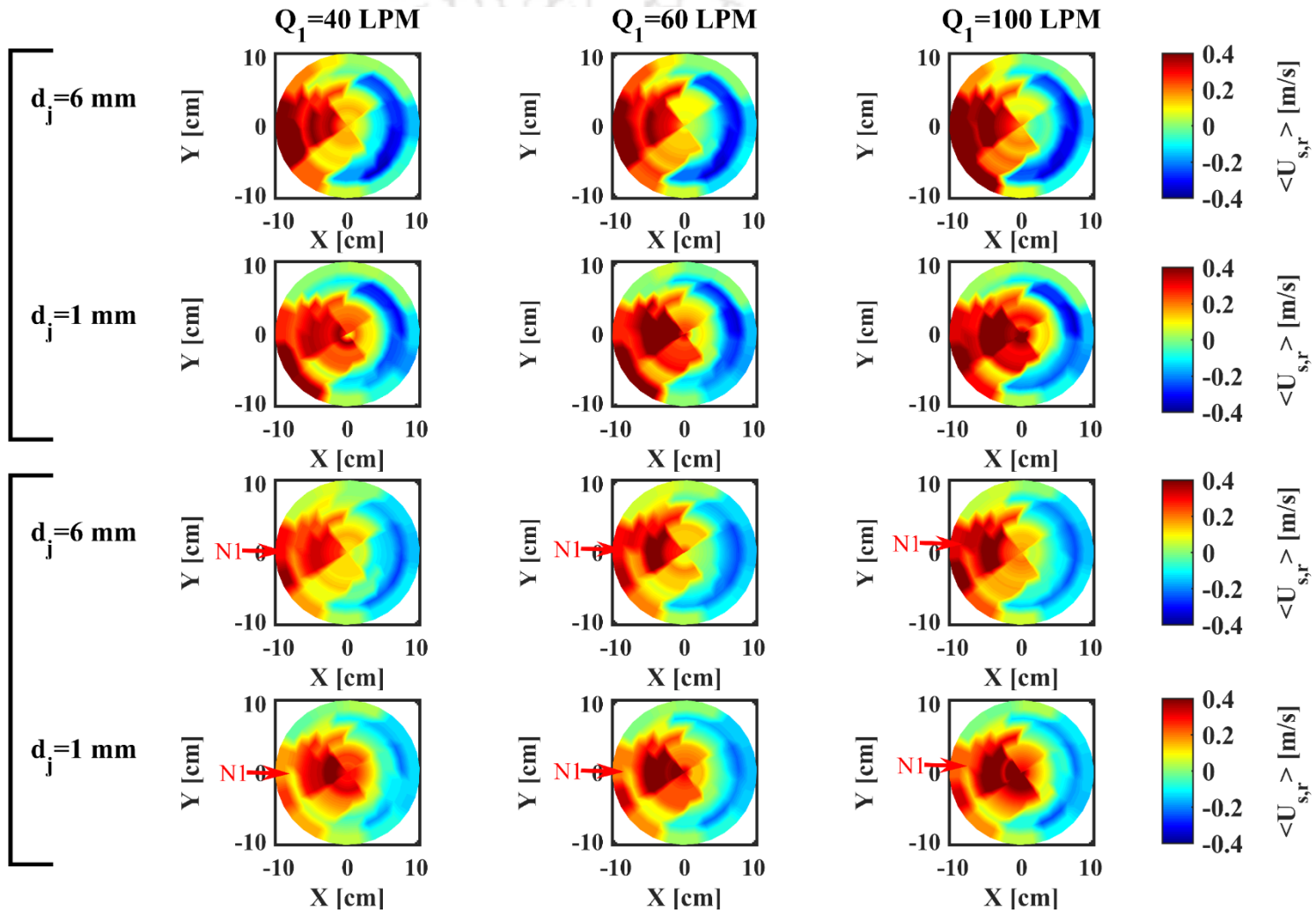


Figure 3.25 Contour of axial mean velocity for different size nozzles at (a) $z = 0.03\text{ m}$, (b) $z = 0.15\text{ m}$, (c) $z = 0.21\text{ m}$, and (d) $z = 0.25$

(d)
 $z = 0.25 \text{ m}$



(c)
 $z = 0.21 \text{ m}$

Figure 3.27 present the comparison of mean axial velocities of solid along the injection line (or x-axis) with two different diameters nozzle i.e. 6 mm and 1 mm ID for three injection flowrates, measured at four different bed heights. It is worth to mention that the small size nozzle injection provides high mean axial solid velocity in the region $x/R > 0$ than the large size nozzle (6 mm ID). The results indicate that it appears farther from the injection location, or from the nozzle for all injection velocities. In both types of nozzle injections, the local maxima shift from the central region to the injection wall.

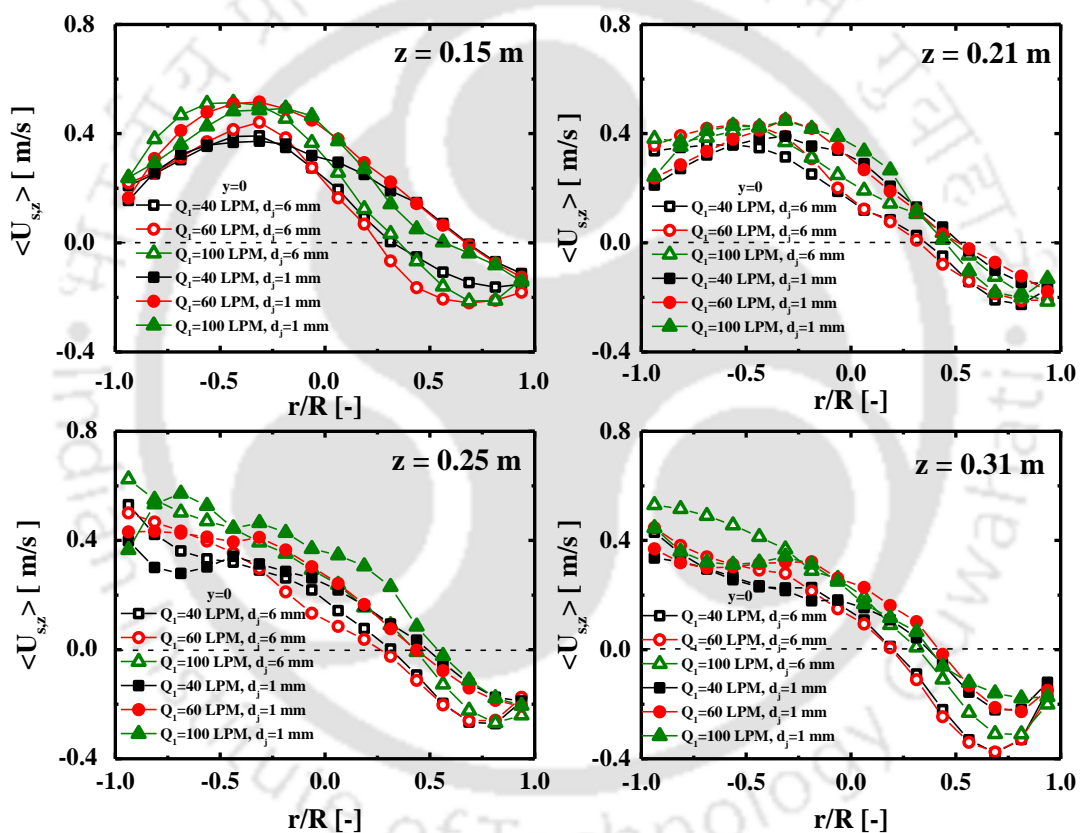


Figure 3.27 Effect of nozzle diameter on the mean axial velocity of solids

Figure 3.28 shows the comparison of azimuthally averaged and time-averaged axial solid velocity profiles, measured with different size nozzles for 4-bed heights at three different value of Q_1 . The positive axial velocities are found at the core region and negative axial velocities are observed near the wall ($r/R=1.0$). The smaller diameter nozzle provides high axial velocity than the large diameter nozzle.

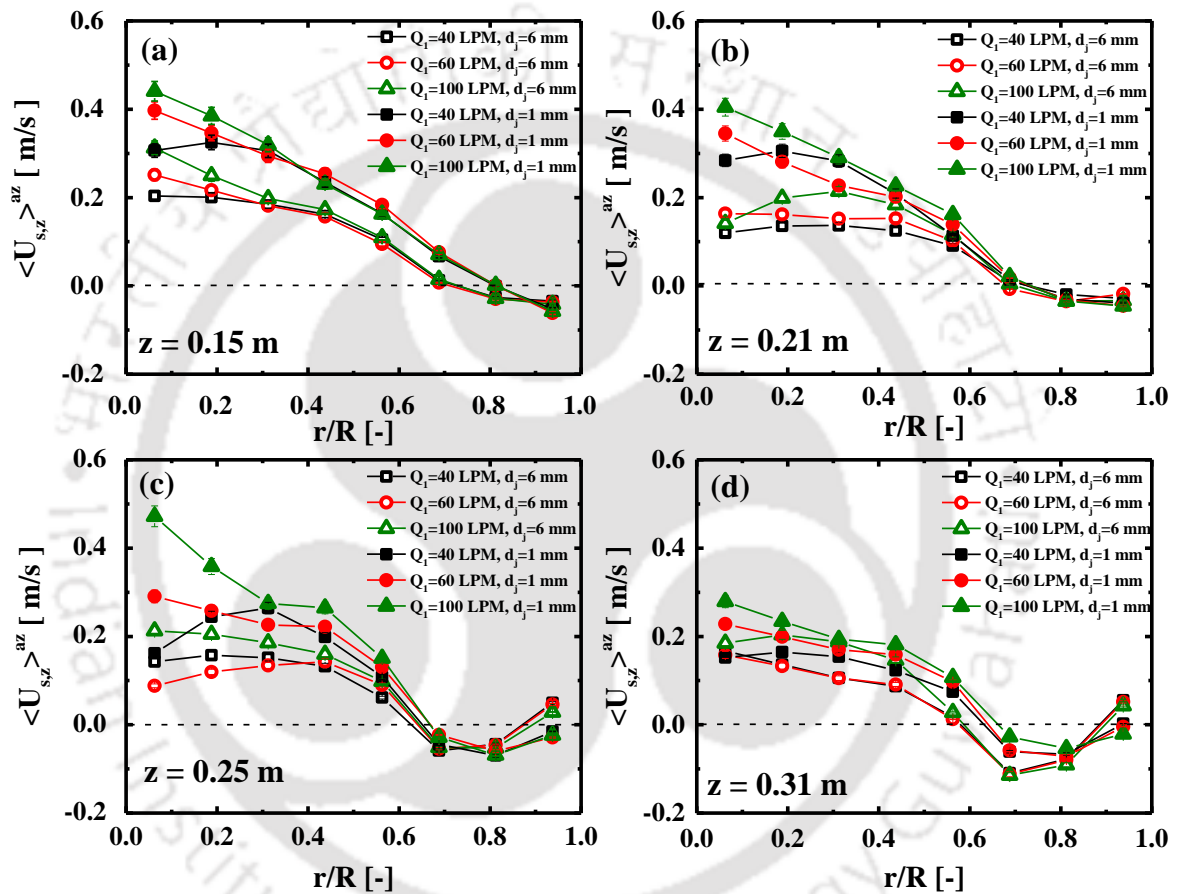


Figure 3.28 Effect of nozzle diameter on the azimuthal averaged axial velocity of solids

Effect on mean radial velocity

Figure 3.29 displays the time-averaged radial velocity distribution along the x-axis, measured at different bed heights for three sets of injection flowrates. The distribution shows similar trends for both types of nozzle injections, with positive mean radial velocities closer to the injection zone and negative velocity nearer to the opposite wall in all the z-planes (Figure 3.29a, c, d) except the injection plane (Figure 3.29b). Similarly, Figure 3.30a, b, c, d present circumferentially averaged mean radial velocity for 4 z-planes. Although, these profiles show that the injection flowrates have no significant impact on the azimuthal averaged mean radial velocity of solids and remain close to zero at each bed height.

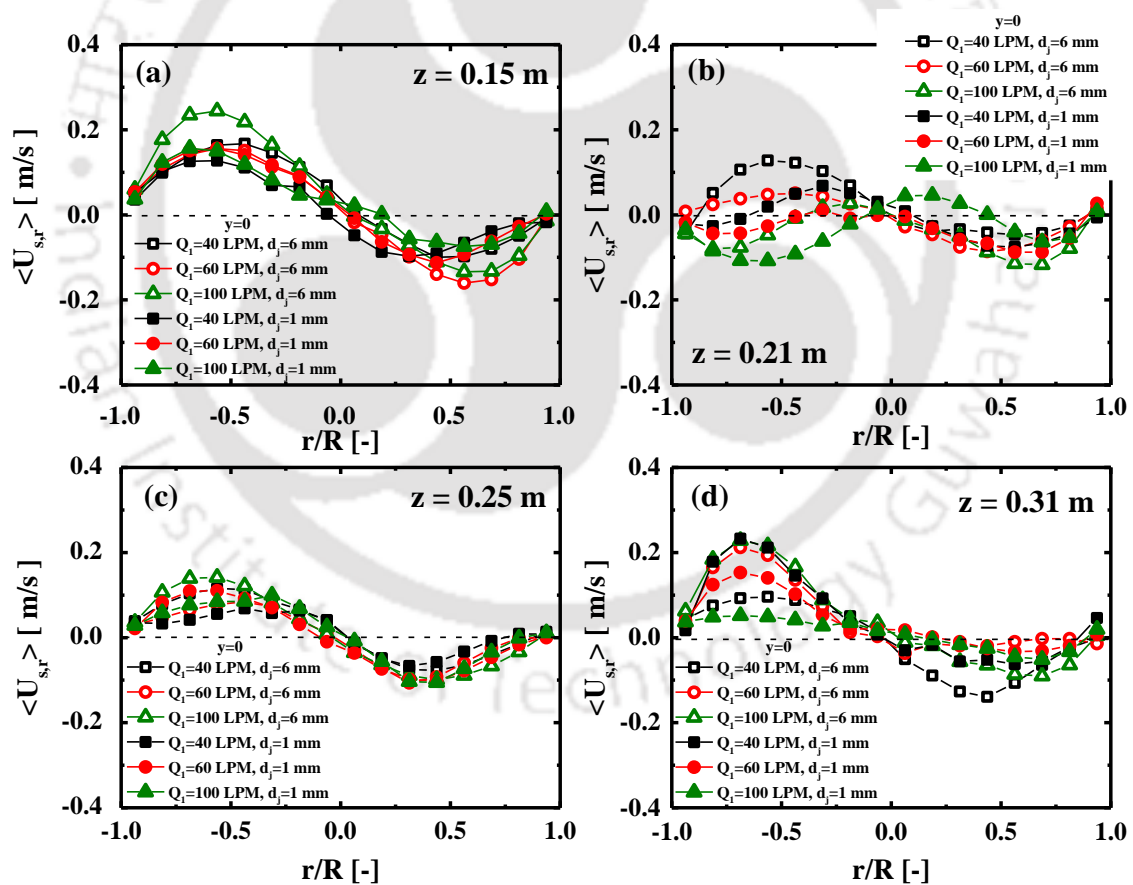


Figure 3.29 Effect of nozzle diameter on the mean radial velocity of solids

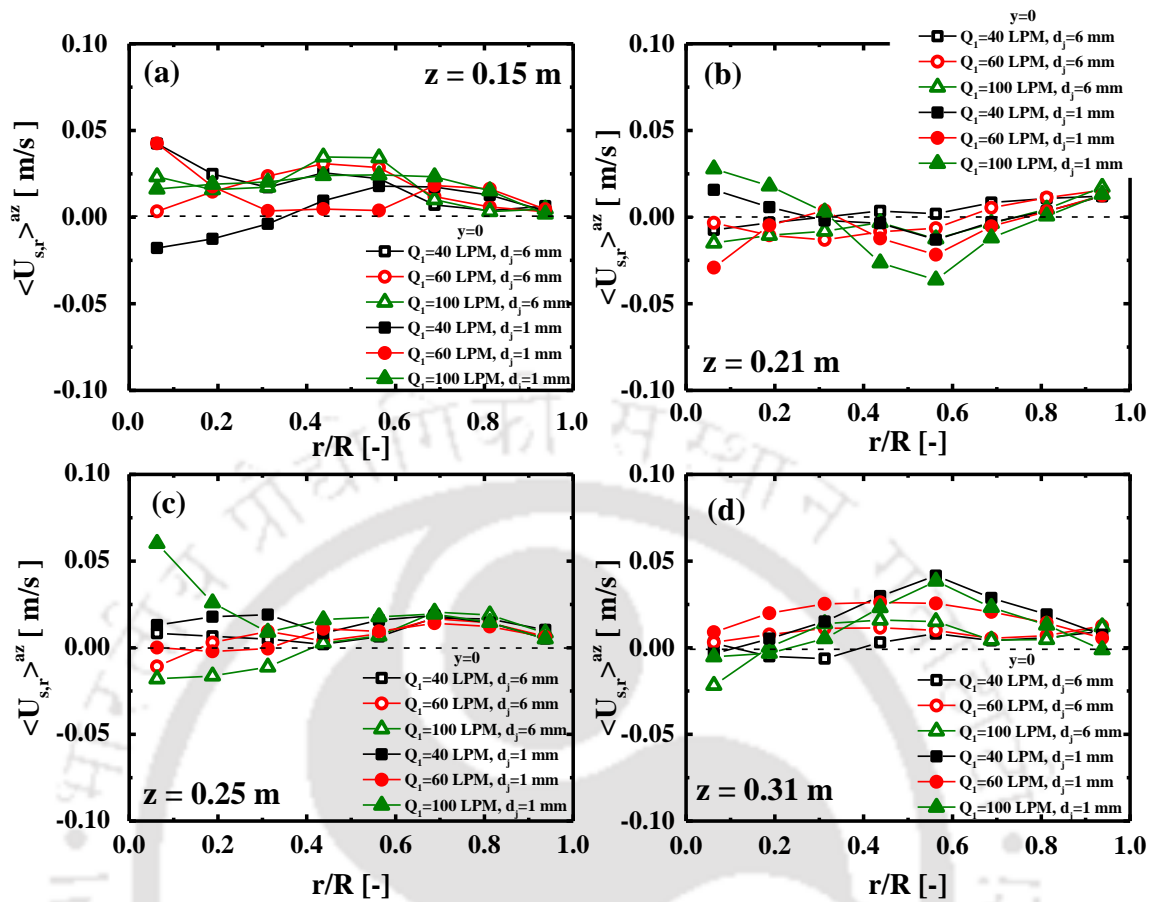


Figure 3.30 Effect of nozzle diameter on azimuthal averaged radial velocity of solids

Effect on axial rms velocity

Figure 3.31a, b, c, d compares the axial rms solid velocities measured for four different z -planes with three injection flow rates. The fluctuations of axial velocity are maximum at the center region and minimum at walls. The fluctuations in axial velocity are higher with small diameter nozzle (Figure 3.31). This may be possible because of the spread of the large size nozzle which causes the accumulation of solids near the opposite wall of the injection site at all heights. Hence, the axial rms values are smaller for 6 mm nozzle at all planes above the

injection plane. Similarly, at the injection plane ($z=0.21$ m), small size nozzle causes the high momentum transfer on the solids present at the same planes. Due to this momentum transfer, the particle moves in the radial direction, and enhances the particle-particle collision. Hence, a significant increment in the axial RMS solid velocity on the injection plane has been observed at $x/R=1.0$. In the case of a 6 mm ID nozzle, the radial motion of solids may not be enough to increase the frequency of particle-particle collision, and hence, the axial RMS decreases on approaching towards $x/R=1$ (Figure 3.31b).

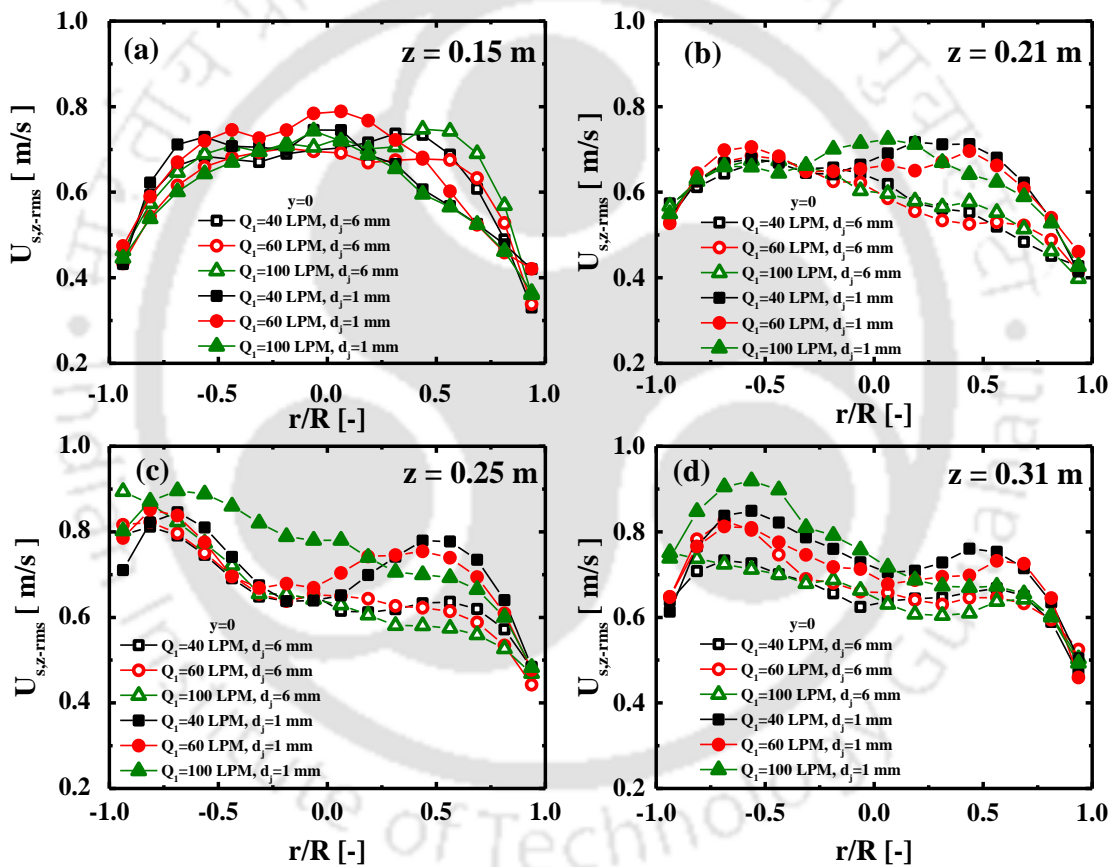


Figure 3.31 Effect of nozzle diameter on the axial rms velocity of solids

At the upper planes (Figure 3.31c, d), the axial rms profiles follow the similar trends with a higher value near to $x/R=-1.0$. These profiles show a continuously decreasing trend on approaching at $x/R=1$. Figure 3.32 shows the azimuthal averaged and time-averaged profiles of axial rms velocity with two different size injections. The azimuthal averaged axial rms remains almost unchanged at the lower planes (Figure 3.32a). except for $z=0.15$ m, the azimuthal averaged axial rms velocity becomes higher in the case of 1 mm ID nozzle at the central region (Figure 3.32b, c, d). It has been noteworthy to say that the axial rms velocity is maximum at the center and minimum closer to the wall ($r/R=1.0$) for all bed heights.

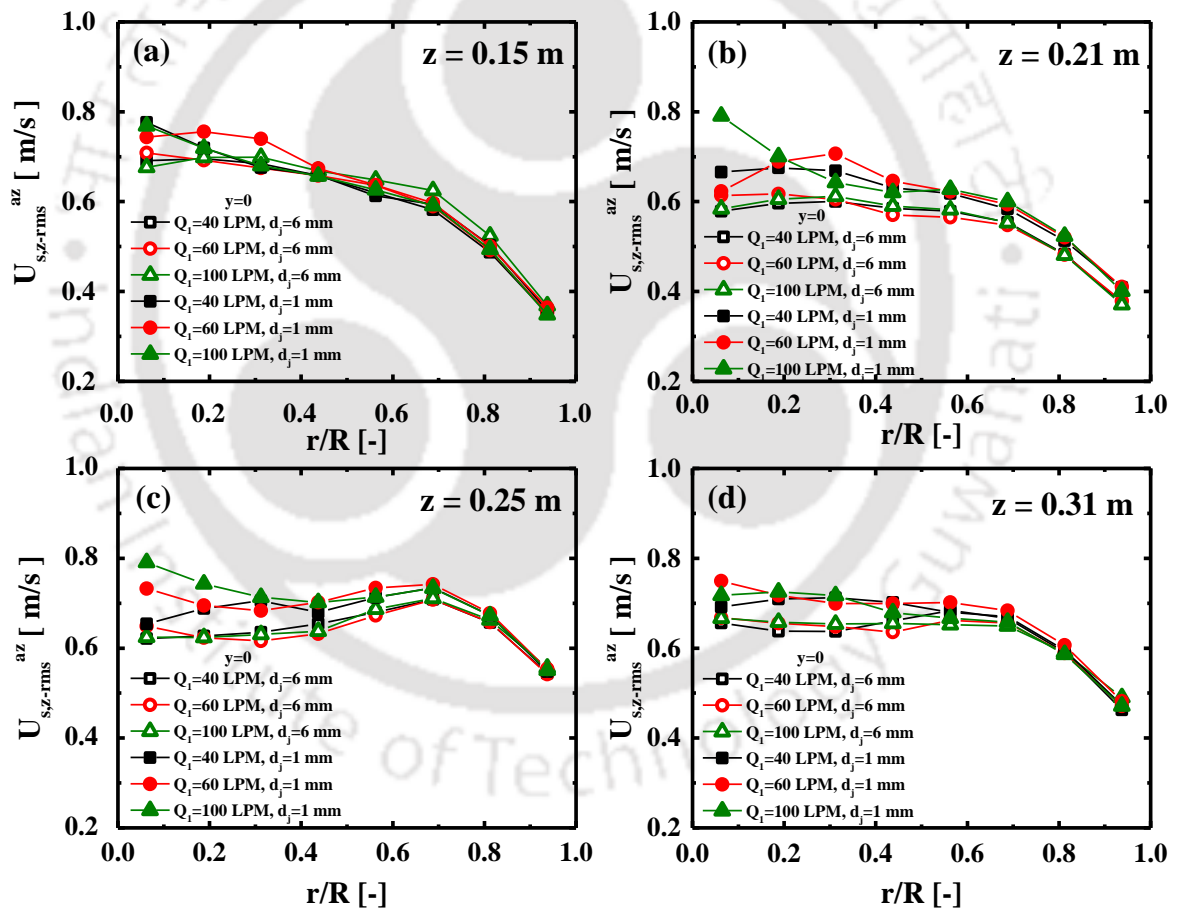


Figure 3.32 Effect of nozzle diameter on azimuthal averaged axial rms velocity of solids

Effect on granular temperature

Figure 3.33 shows the comparison of granular temperature of solid between two nozzle injections of different diameters. The granular temperature, evaluated for three different sets of Q_1 at different axial positions ($z=0.15, 0.21, 0.25$ and 0.31 m), are plotted along the x-axis. The plots show the difference in granular temperatures at lower heights with two nozzles of different diameters. Finally, this difference disappears along the bed heights and the distributions of granular temperature follow the similar trends. The reason is that the bubble dynamics changes upto a certain bed height as the primary air velocity, secondary air velocity and nozzle diameter are changed. Similar trends in granular temperature distribution are observed at $z = 0.15$ m and 0.31 m due to the absence of radial movement of bubbles which is primarily in axial direction (Figure 3.33a, d). The transition between axial motion and radial motion are highly observed in other two planes. Therefore, high values of granular temperature are observed near the injection wall than opposite wall (Figure 3.33b, c).

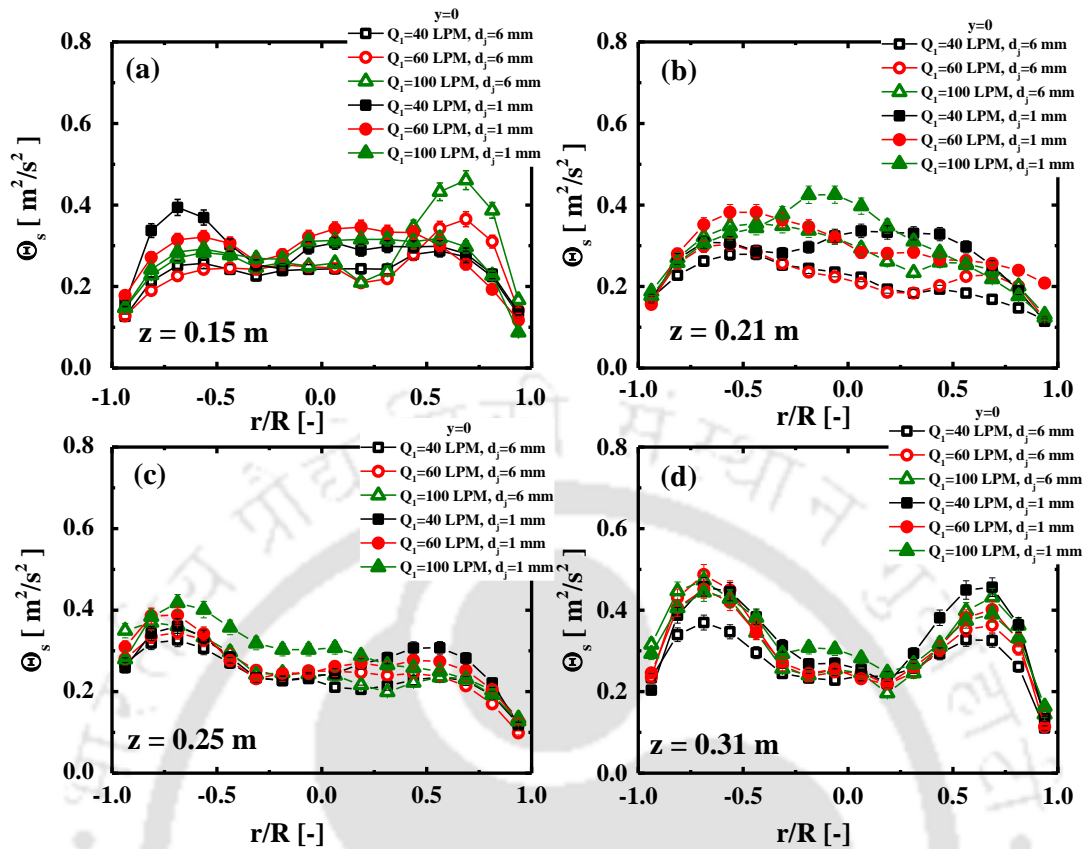


Figure 3.33 Effect of nozzle diameter on the granular temperature of solids

At the injection plane ($z=0.21$ m), the higher granular temperature is obtained with small nozzle injection at the same Q_i . No major impact has been noticed in the upper planes for both types of injections (Figure 3.33c, d). The comparison of azimuthal averaged and time-averaged granular temperature data in Figure 3.34 suggests that no major influence has been observed in the upper planes (Figure 3.34c, d), however, the increment in the granular temperature can be seen at the core region of the bed in the injection plane or at the lower plane (Figure 3.34a, b).

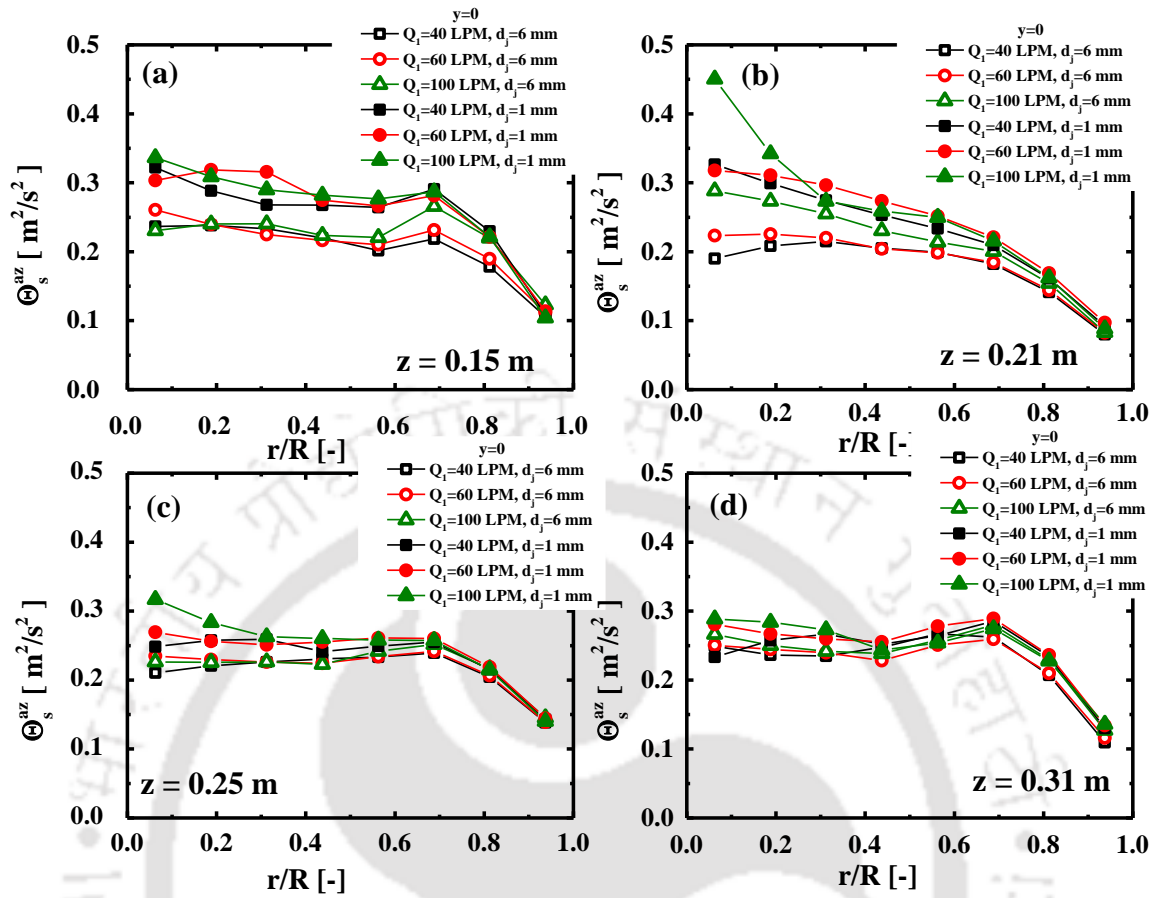


Figure 3.34 Effect of nozzle diameter on the azimuthal averaged granular temperature of solids

Effect on dispersion coefficient

In this section, the local axial dispersion coefficient, $D_{s,zz}$, measured at four bed heights ($z=0.15$, 0.21 , 0.25 and 0.31 m) with three different injection flowrates (40, 60 and 100 LPM), are compared between two nozzle diameters as shown in Figure 3.34. At $z=0.15$ m, the axial dispersion coefficient data shows flat profiles along the injection line for all cases (Figure 3.35a). The maximum value, approximately $0.01 \text{ m}^2/\text{s}$ is obtained at $z=0.15$ m. The average value of $D_{s,zz}$ decreases from $0.01 \text{ m}^2/\text{s}$ to $0.003 \text{ m}^2/\text{s}$ as the bed height increases from $z=0.15$

m to 0.31 m (Figure 3.35a-d). At the upper planes ($z=0.25$ and 0.31 m), higher $D_{s,zz}$ value is observed closer to the injection wall ($x/R=-1.0$) as presented in Figure 3.35c, d. The comparison of azimuthal averaged axial dispersion coefficient data is also displayed in Figure 3.36 for the same. It has been observed that the radial profiles are unchanged under the operated injection flowrates (40-100 LPM)

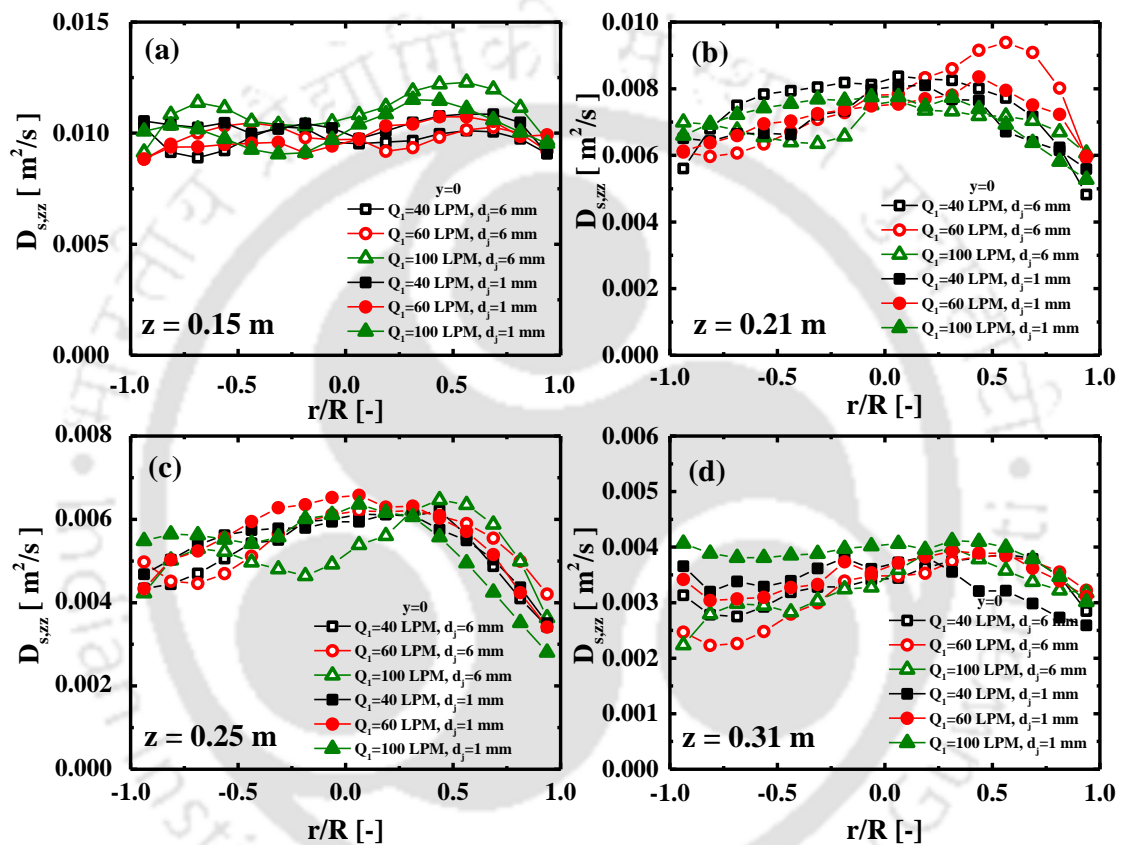


Figure 3.35 Effect of nozzle diameter on the solids dispersion coefficient

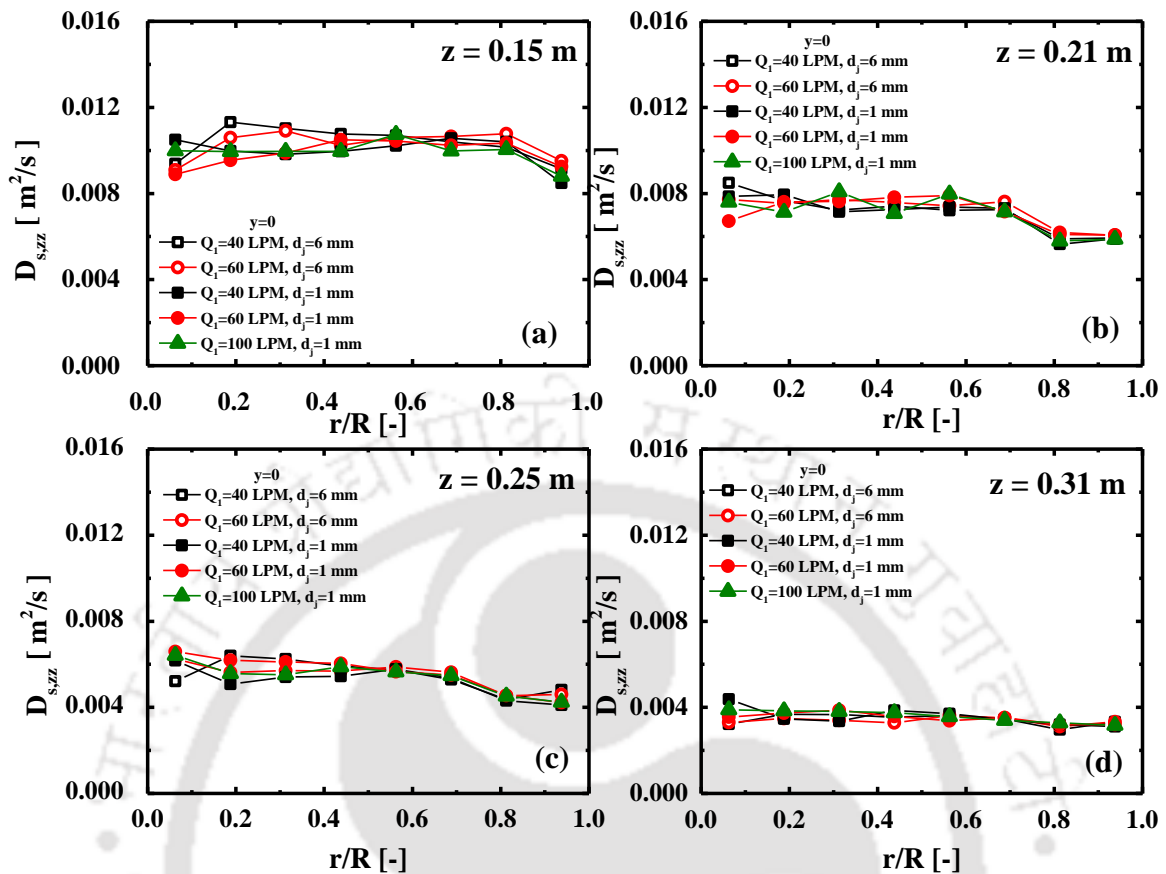


Figure 3.36 Effect of nozzle diameter on azimuthal averaged axial dispersion coefficient of solids

3.3.4. Two sidewall injections operating at same planes ($z=0.20\text{ m}$)

In this section, the time-averaged axial velocity distribution of solids with two sidewall injections, N1 and N2 of 6 mm ID is presented along the x-axis and are compared for different axial heights at a fixed injection flow rates. Figure 3.37a-d display the mean axial velocity of solids at four different injection flowrates through sidewall nozzle keeping the primary gas flow rate same. The mean axial velocity profiles show a similar flow patterns as observed in the case of single nozzle injection. The mean axial velocity of the solids is positive near the

injection wall ($\sim x/R=-1.0$) at all the axial heights under consideration. Similarly, negative mean axial velocity is found at the opposite wall ($x/R=1.0$). A single circulation cell is observed in two sidewall nozzle injection also which is similar to single side wall nozzle injection. It is worth mentioning here that the second nozzle was placed 120° apart from the first nozzle. This may be the primary reason of the single circulation cell observation.

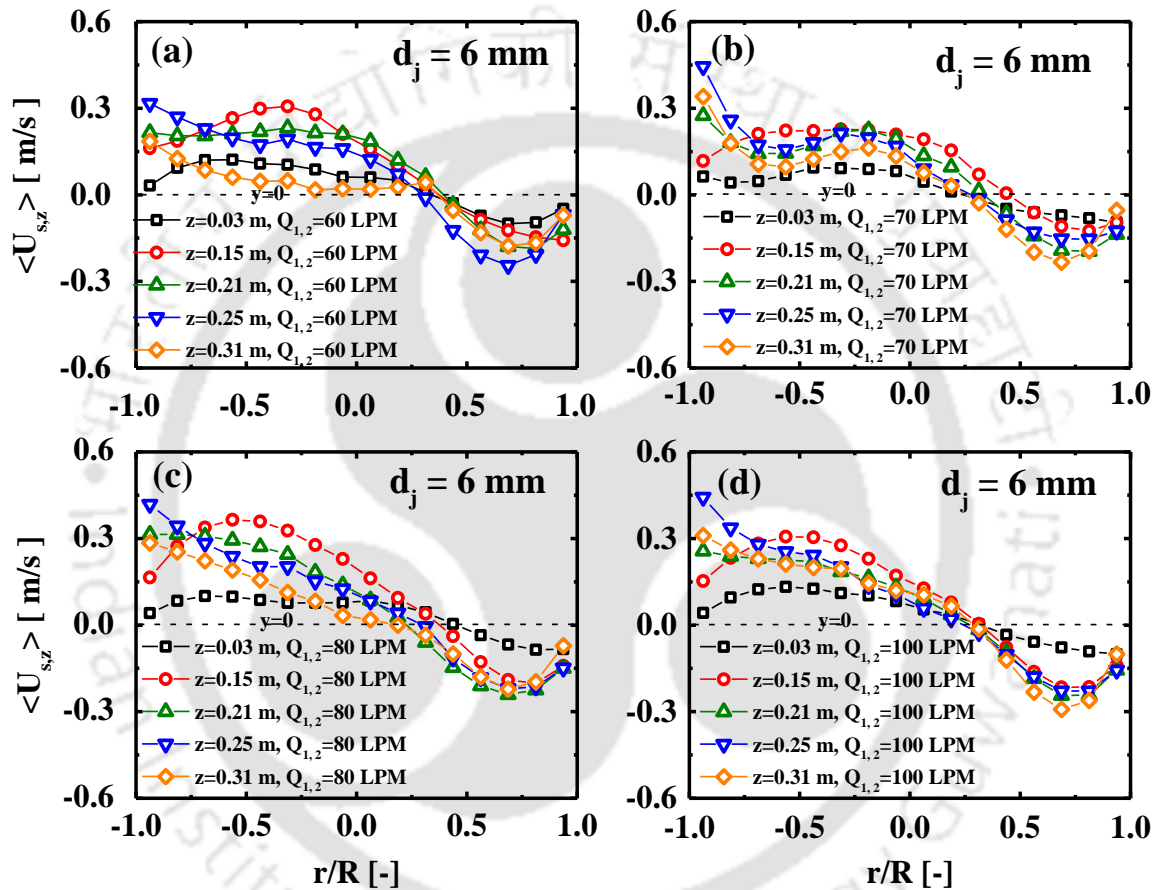


Figure 3.37 Lateral distribution of axial solid velocity for two secondary air flowrates at (a) 60 LPM, (b) 70 LPM, (c) 80 LPM and (d) 100 LPM

Figure 3.38 shows the radial variation of azimuthal averaged axial solid velocities for different injection flowrates of two nozzles operated at the same plane. At all axial heights (z), the solids are moving upward at the centre of the column. Similar observation is made for all the nozzle injection velocity. However, at the wall above the injection plane the azimuthal average solid velocity is also positive for all the injection gas velocity. This shows that with two injections at the same plane the overall profile of the sidewall nozzle injected fluidized bed also differs from conventional fluidized bed, particularly above the nozzle injection points. These results further confirm that primary gas bubbles are migrating towards the injection wall and forming big bubbles. These big bubbles escape the system through the wall itself causing severe bypassing. As in case of two nozzles the wall coverage is higher and hence more gas is migrating towards the wall and changing the overall profile.

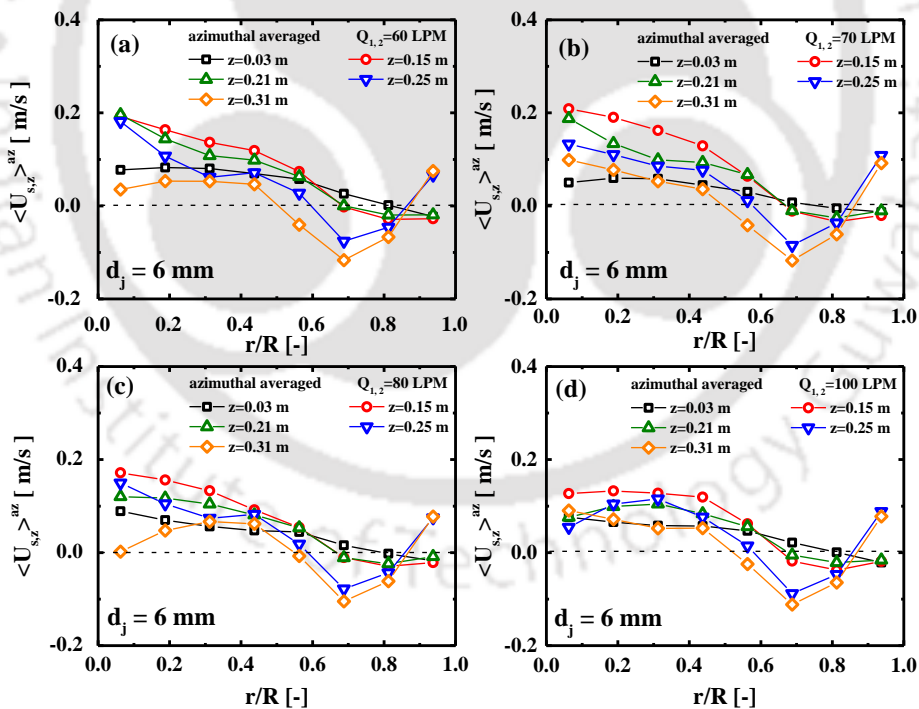


Figure 3.38 Azimuthal averaged and time-averaged axial solid velocity for two secondary air flowrates at (a) 60 LPM, (b) 70 LPM, (c) 80 LPM and (d) 100 LPM

Figure 3.39 shows the axial RMS velocities measured in the lateral direction of injection N1 for different injection flowrates. Results show that axial rms velocity is higher at the center of the column below the nozzle injection plane and profile is almost symmetric. However, at and above the nozzle injection plane the axial rms velocity is higher near the nozzle injection wall compare to the opposite wall. These results further confirms that primary gas is migrating towards the nozzle injection wall and forming the bigger bubbles which results in higher axial rms velocity of the solids. The results also confirms the at the operating condition the sidewall nozzle injected gas and primary gas bubble coalescence occurs at the injection plane. Hence, the axial rms velocity profile becomes asymmetric at and above nozzle injection plane. Further, it is observed that for all the gas velocities, axial rms velocity increases with the height. This shows that larger bubbles are formed with the height due to coalescence which leads to the higher fluctuation velocities.

Figure 3.40 shows the radial variation of azimuthal average axial rms velocity of the solids at different heights for different nozzle injection flowrate. The results show that azimuthal average axial rms velocity is higher at the centre and lower near the wall for all the nozzle injection flowrates. The trend remains same at all the planes, though the azimuthal average solid velocity trend near the wall was different above the nozzle injection plane. The results show that though the solid velocity near the wall is higher above the nozzle injection plane, the fluctuations are lower due to low solid concentration. This shows that in nozzle assisted gas-solid fluidized bed also solid-solid interactions plays an important role. This can be further confirmed with the higher azimuthal average solid axial rms velocity in the core annular region just above the nozzle injection plane. The peaking is observed due to the migration of the solid from nozzle injection plane due to the injection of secondary gas through the nozzles. Further, it is observed that for all the injection velocity azimuthal average axial rms velocity increases with the height. This is mainly due to the formation of bigger bubble with the height due to the

coalescence which results in higher rms velocity. Therefore, it can be concluded that both gas-solid and solid-solid interactions are critical in case of multiple nozzle assisted gas-solid fluidized bed.

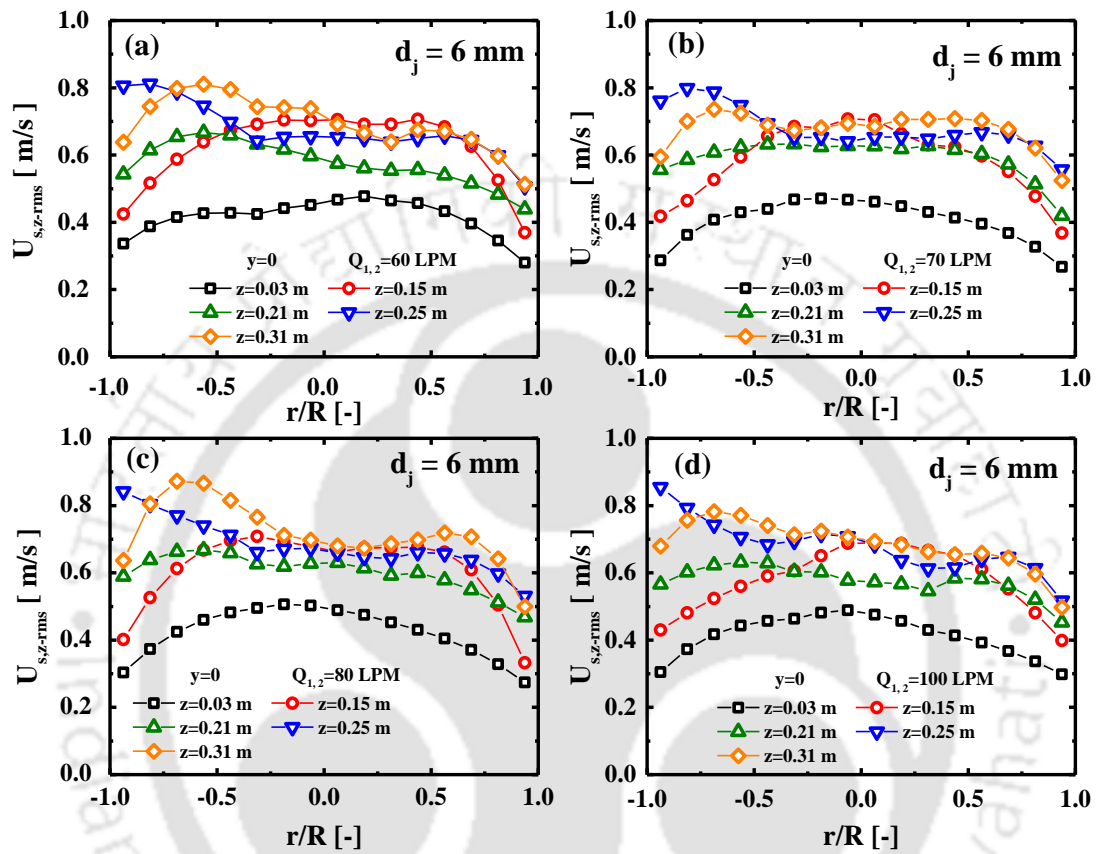


Figure 3.39 Axial RMS solid velocity for two secondary air flowrates at (a) 60 LPM, (b) 70 LPM, (c) 80 LPM and (d) 100 LPM

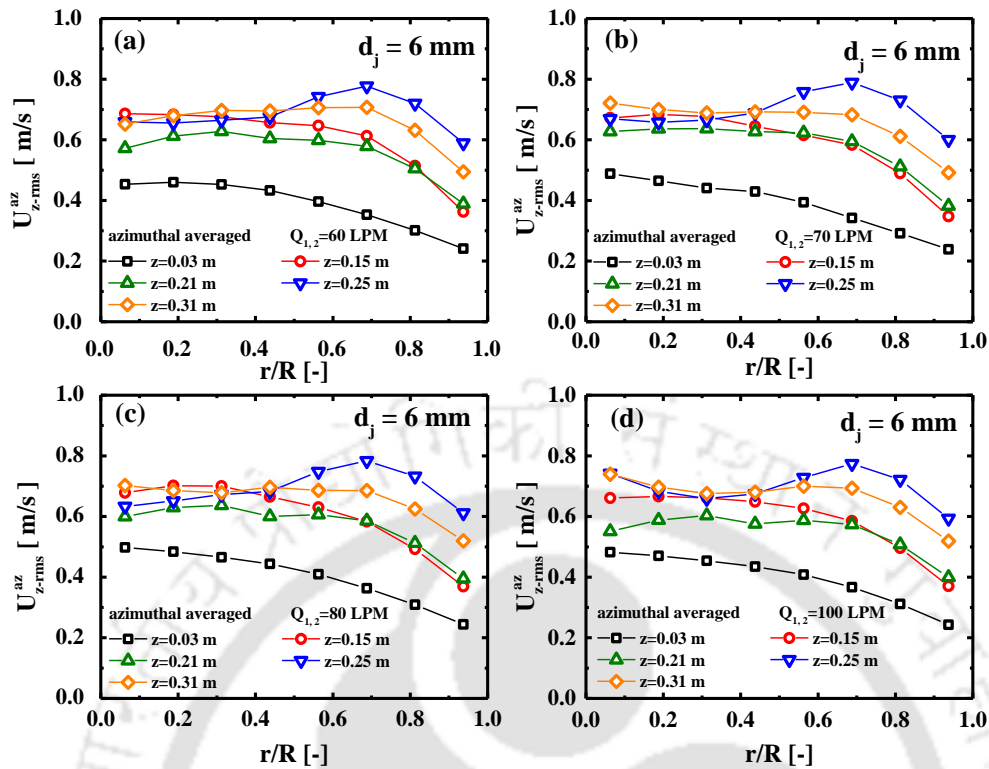


Figure 3.40 Azimuthal averaged axial RMS solid velocity for two secondary air flowrates at (a) 60 LPM, (b) 70 LPM, (c) 80 LPM and (d) 100 LPM

Figure 3.41 shows the comparison of experimentally measured granular temperature of solids at different axial heights (z) from the fluctuation velocities as explained above. The distribution of granular temperature in the lateral direction ($y=0$) highlights the asymmetry in profiles arises due to side injections into beds along the bed height. The profile of granular temperature is similar to the axial rms velocity. This shows that even though the secondary gas is injected through the multiple sidewall nozzles, the flow is primarily in the axial direction. This should be the case as the flows through these nozzles are quite low compared to the primary gas flowrate injected through the bottom of the column.

Figure 3.42 shows the radial variation of azimuthal average granular temperature for all the conditions at different heights. Results show that azimuthal average granular temperature is high at the centre and low near the wall. This shows high fluctuations at the centre compared

to the wall. Further, the profile of azimuthal average granular temperature is similar to the azimuthal average axial rms velocity. This shows that in overall sense the flow is primarily in the axial direction though secondary gas is injected in the perpendicular direction. The granular temperature is high in the core annular region above the nozzle injection plane. This shows that solids are migrated to the upper section due to the side wall nozzle injections. The granular temperature for all the conditions increases with the height shows that the upper section of the bed is more violent due to the formation of bigger bubbles.

Figure 3.43 shows the dispersion coefficient at four axial levels for all injection flowrates. It shows that the variation of injection flow rate does not affect the magnitude of dispersion coefficients. Further, it is noticed that the dispersion coefficient decreases with the bed height.

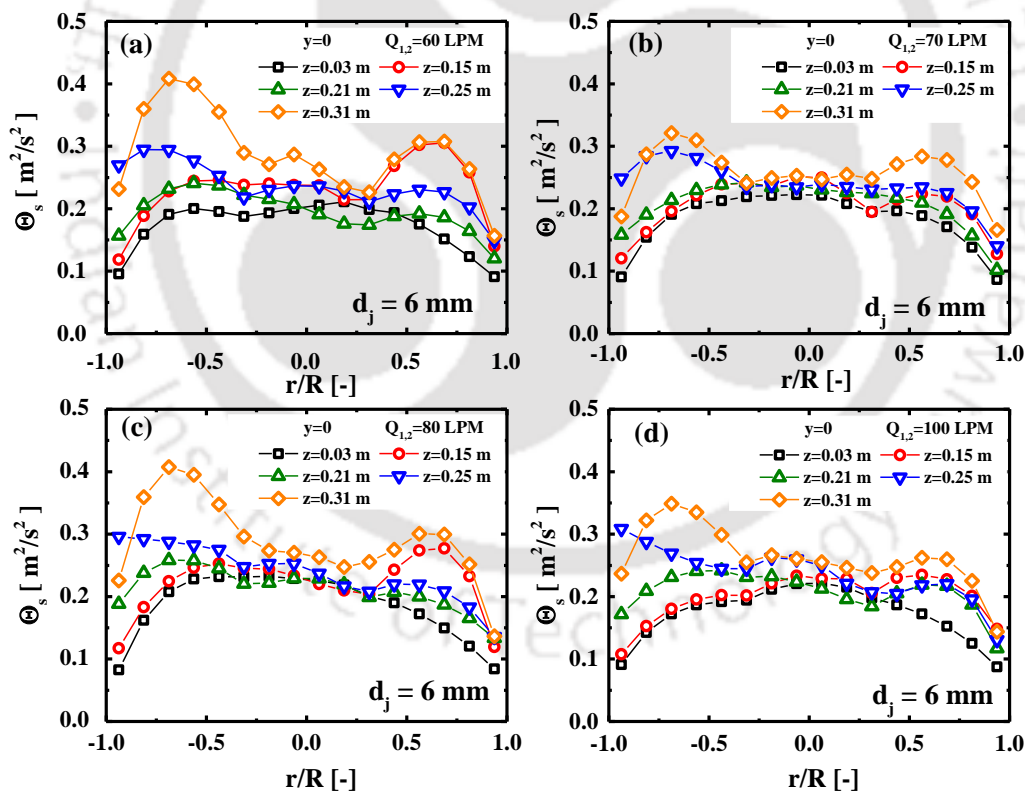


Figure 3.41 Lateral distribution of solid granular temperature for two secondary air flowrates at (a) 60 LPM, (b) 70 LPM, (c) 80 LPM and (d) 100 LPM

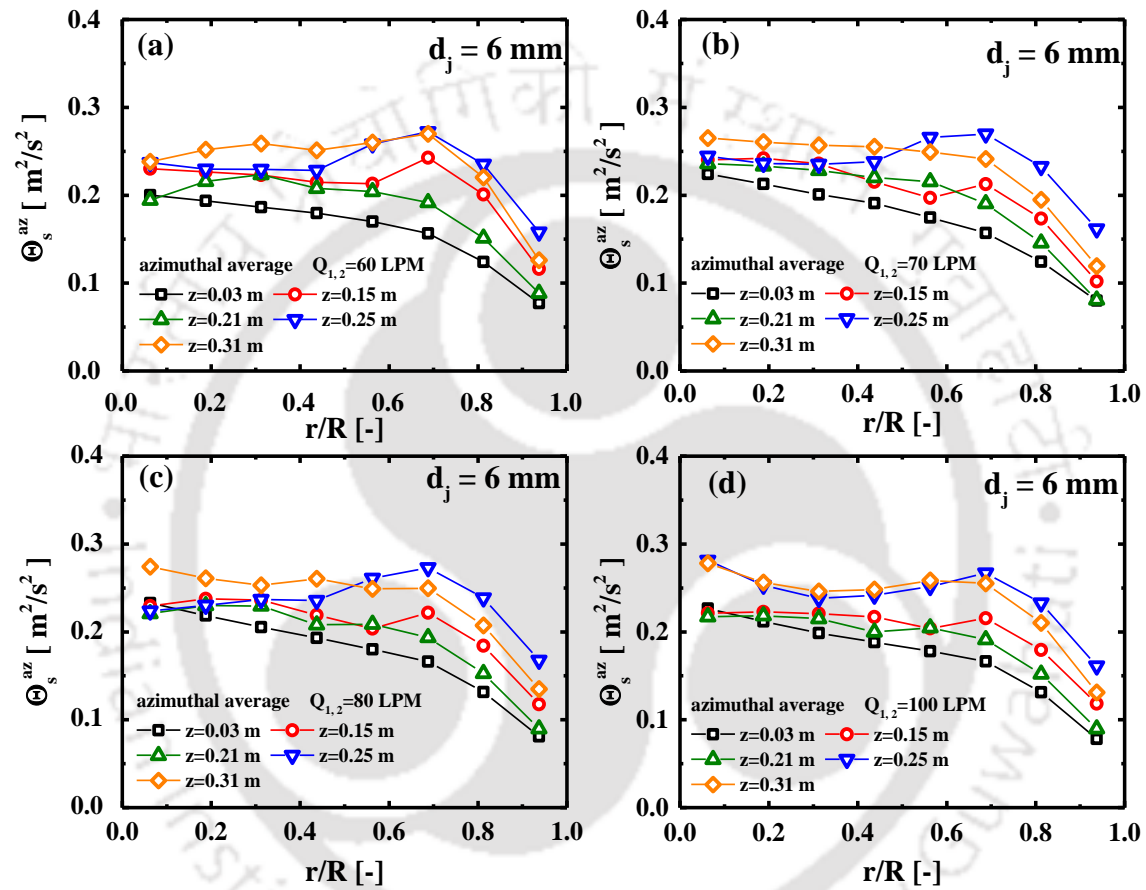


Figure 3.42 Azimuthal averaged and time-averaged solid granular temperature for two secondary air flowrates at (a) 60 LPM, (b) 70 LPM, (c) 80 LPM and (d) 100 LPM

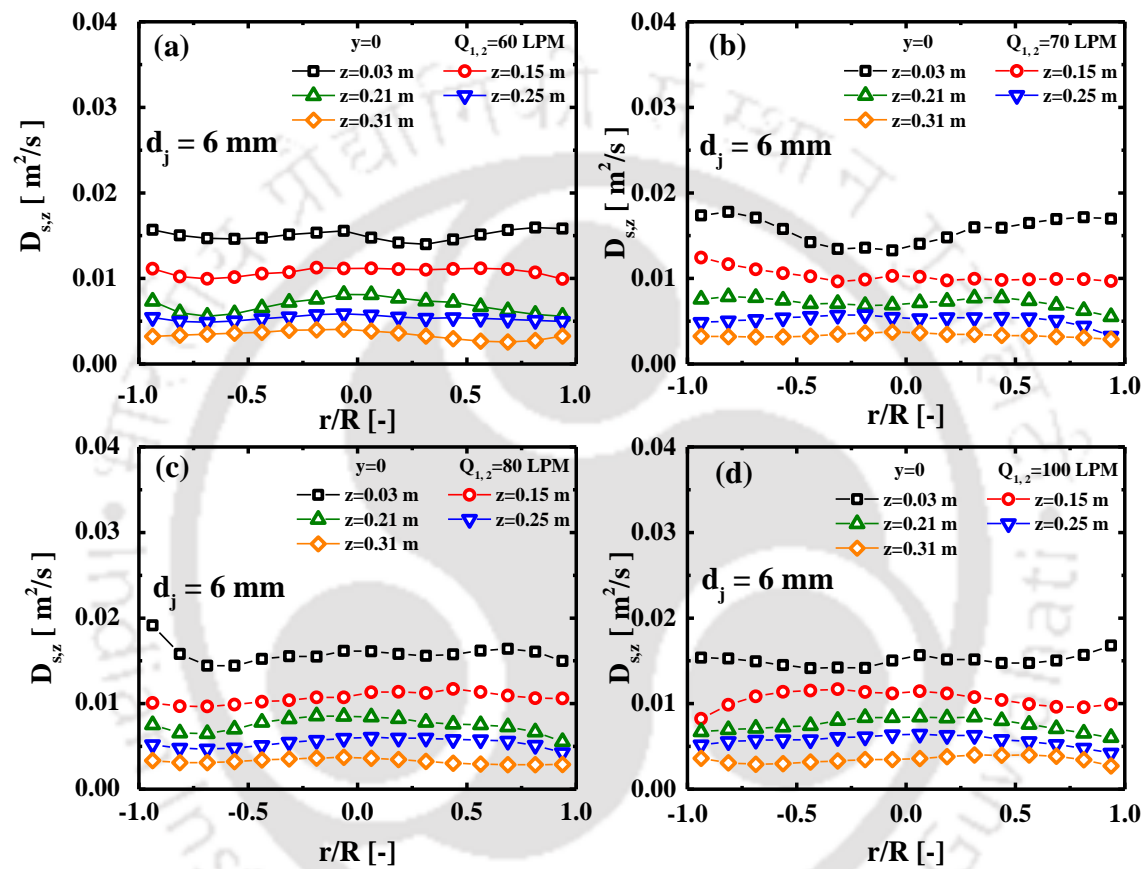


Figure 3.43 Lateral distribution of axial dispersion coefficients of solid for two secondary air flowrates at (a) 60 LPM, (b) 70 LPM, (c) 80 LPM and (d) 100 LPM

3.4. Summary

In the present chapter, the experimental study related to setup the cold flow model of gas-fluidized bed, the geometric configuration of the nozzle setup, and the experimental conditions are reported. The flow dynamics characteristics of solid such as mean axial velocity, mean radial velocity, axial rms velocity, granular temperature, and axial dispersion coefficient have been measured experimentally via RPT. This experiment is performed with low secondary air inlet velocity (< 84 m/s). Finally, the outcome of this chapter provides useful information for further research. The following conclusions are made on the basis of this work.

- For all the cases, the same bubble dynamics can be observed irrespective of size and injection flow rates of nozzles being used. The fluidized bubble rises up along bed height and shifts towards the injection site until reaching the injection plane. Above the injection plane, it tries to move towards the core region.
- The local effect of the side injection can be observed at the neighbour planes in all the directions. This effect strongly depends on the size of the nozzle, injection flowrates, physical properties of the system and operating conditions.
- The upward motion near the injection wall and downward motion along the opposite wall are observed. This can be observed in time-averaged profiles of axial solid velocities at different elevations.
- Only one inversion point has been observed in the time-averaged profile of solid velocity at different bed heights, plotted along the injection path. Hence, a boundary is obtained that separates a high dense zone from the less dense zone present near the injection wall. This provides a clue that shows a distinct characteristic of such types of systems that are completely different from the normal fluidized beds.
- Higher time-averaged axial velocity is obtained with lower diameter nozzle.

- Asymmetric distribution of solid mean and fluctuations (rms) velocities are observed at the upper heights, just above the nozzle injection height.
- The azimuthal averaged rms velocities are higher at the core and low at the wall for all the z-planes, below the injection height. The rise in the azimuthal averaged axial rms velocity can be observed at the upper bed height, above the injection plane, near the wall due to the exchange of high momentum from injected fluid to the solids and frequent collision of particles near the wall. Thus, it can be concluded that rms velocities strongly depends on the geometry of the bed (such as L/D ratio), and flow rates of injected fluid through sidewall nozzle in the gas fluidized bed.
- Relatively higher granular temperature is observed with a 1 mm ID nozzle injection than a 6 mm ID nozzle injection.
- A relatively higher dispersion coefficient is observed at the upper planes neighboring to the injection plane along the injection axis with a small diameter (1 mm ID) nozzle.
- In general, more symmetric arrangements of sidewall injection in a single plane provide a symmetric distribution of ensemble averaged solid velocity, fluctuation velocity and other turbulence parameters.
- The maximum solid velocity in the case of single and two nozzles are observed in the annular region between the injection wall and the central region of bed.
- In case of single and two nozzle injections, the solid motion is predominately in the upward direction at close to injection wall and downward at the opposite wall.
- The local or cross sectional averaged axial velocity of solids is reduced as the number of sidewall injection are increased while operating at the same plane.
- Granular temperature of solids is increased with increasing the number of sidewall injection.

- No significant impact on the axial dispersion coefficient has been observed with increasing the sidewall injection.

Notation

d_j	Nozzle diameter	[m]
d_p	Particle diameter	[μm]
D_t	Bed diameter	[m]
$D_{s,zz}^{az}$	Azimuthal averaged axial dispersion coefficient in z-direction	[m^2/s]
$D_{s,zz}$	Axial dispersion coefficient in z-direction	[$\text{m}^2.\text{s}^{-1}$]
Q_j	Volumetric air-flow rates injected through j-th nozzle	[LPM]
Q_1	Volumetric air-flow rates injected through nozzle N1	[LPM]
$Q_{1,2}$	Volumetric air-flow rates injected through nozzle N1 and N2	[LPM]
r, θ, z	Axes in cylindrical coordinates	[m, degree, m]
Θ_s^{az}	Azimuthally averaged granular temperature of solids per unit density	[$\text{m}^2.\text{s}^{-2}$]
U	Superficial velocity (Q/A_c) of primary air	[LPM]
U_{mf}	Minimum fluidization velocity	[$\text{m}.\text{s}^{-1}$]
$U_{s,z}$	Instantaneous velocity in z-direction	[$\text{m}.\text{s}^{-1}$]
$U_{s,r-rms}$	Radial rms velocity of solid	[$\text{m}.\text{s}^{-1}$]
$U_{s,z-rms}$	Axial rms velocity of solid	[$\text{m}.\text{s}^{-1}$]
$\langle U_{s,r} \rangle^{az}$	Ensemble averaged (time and azimuthal-averaged) radial mean velocity	[m/s]

$\langle U_{s,z} \rangle^{az}$	Ensemble averaged (time and azimuthal averaged) axial mean velocity	
		[m/s]
$U_{s,z-rms}^{az}$	Azimuthal averaged axial rms velocity of solid	[m.s ⁻¹]
W	Solid loading	[kg]
x, y, z	Cartesian coordinates	[m]

Greek Symbols

μ	Attenuation coefficients	[m ⁻¹]
ρ	Density	[kg/m ³]
Θ_s	Granular temperature of solids per unit density	[m ² .s ⁻²]
τ	Delay constant	[s]

Superscript

az azimuthal averaged

Abbreviation

LPM Liter per minute
rms Root Mean Square

References

Anthony, E. J., Lu, D. Y., The fluidized bed combustion of heavy liquid fuels. Sixteenth International Conference on FBC 2001. Paper No. FBC21-0141, May 16-19, Savannah, Georgia, USA.

Bhowmick, S., Rao, H., Sathiyamoorthy, D., 2012. Thermal denitration of ammonium nitrate solution in a fluidized-bed reactor. Ind. Eng. Chem. Res. 51, 8394–8403.

Bhowmick, S., Sharma, V.K., Samantray, J.S., Pant, H.J., Shenoy, K.T., Dash, A., Roy, S.B., 2015. Experimental investigation on the interaction of side gas injection with gas fluidized bed using γ -ray transmission technique. *Ind. Eng. Chem. Res.* 54 (46), 11653-11660.

Bramer, E. A., 1995. Flue gas emission from fluidized bed combustion in atmospheric fluidized bed coal combustion research, *Development and Application* (Ed. M. Valk), *Coal Science and Technology* 22, Elsevier, 51-103.

Bjorklund, W.J., Offutt, G.F., 1973. Fluidized bed denitration of uranyl nitrate. *AIChE Symp.* 69 (128), 123.

Cassanello, M., Larachi, F., Guy, C., Chaouki, J. 1996. Solid mixing in gas-liquid-solid fluidized beds: Experiments and Modelling. *Chem. Eng. Sci.* 51, 2011-2020.

Cavani, F., Triforo, F., 1995. The oxidative dehydrogenation of ethane and propane as an alternative way for the production of light olefins. *Catal. Today*, 24, 307-313.

Choudhary, V. R., Chaudhary, S. T., Rajput, A. M., Rane, V. H., 1989. Beneficial effect of oxygen distribution on methane conversion and C_2 – selectivity in Oxidative coupling of methane to C_2 -Hydrocarbons over Lanthanum-promoted Magnesium oxide. *J. Chem. Soc., Chem. Commun.*, 1526-1527.

Contractor R. M., Sleight, A. W., 1988. Selective oxidation in riser reactor, *Catal. Today* 3, 175-184.

Coronas, J., Menendez, M., Santamaria, J., 1995. Use of a ceramic membrane reactor for the oxidative dehydrogenation of ethane to ethylene and higher hydrocarbons. *Ind. Eng. Res.* 34, 4229-4234.

Degaleesan, S., 1997. Fluid dynamic measurements and modeling of liquid mixing in bubble columns. Ph. D. Thesis, Sever Institute of Technology, Saint Louis, Missouri, USA.

Degaleesan, S., Dudukovic, M. P., Toseland, B. A., Bhatt, B. L., 1997. An improved mixing model for slurry bubble column reactors. *Ind. Eng. Chem. Res.* 36, 11, 4670-4680.

Devanathan, N., Moslemian, D., Dudukovic, M.P., 1990. Flow mapping in bubble columns using CARPT. *Chem. Eng. Sci.* 45, 2281-2291.

Devanathan, N., 1991. Investigation of liquid hydrodynamics in bubble columns via computer automated radioactive particle tracking (CARPT). D. Sc. Thesis. Washington University in St. Louis, USA

Fane, A.G., Charlton, B.G., Alfredson, P.G., 1974. Fluidized bed denitration of uranyl nitrate in a fluidized bed reactor. Technical Report AAEC/E284; Australian Atomic Energy Commission: Lucas Heights, Australia.

Frisch, U., 1995. *Turbulence: The Legacy of A. N. Kolmogorov*, Cambridge University Press.

Geldart, D., 1969. Fluidization Engineering. *Powder Technol.* 3, 255-256.

Gidaspow, D., 1994. Multiphase flow and fluidization, J. non-Newton. *Fluid Mech.* 55, 207-208.

Kalo, L., Pant, H. J., Upadhyay, R. K., 2020. Validation of the Glicksman Scaling Law for Gas-Solid Conical Fluidized Beds Using the Radioactive Particle Tracking Technique. *Ind. Eng. Chem. Res.* **59**, 20943.

Kiared, K., Larachi, F., Cassanello, M., Chaouki, J., 1997. Flow structure of the solids in a three-dimensional liquid fluidized bed. *Ind. Eng. Chem. Res.* 36, 4695-4704.

Koeninger, B., Koegel, T., Hensler, T., Arlt, W., Wirth, K. E., 2018. Solid distribution in fluidized and fixed beds with horizontal high-speed gas jets. *Powder Technol.* 336, 57-69.

Kunii, D., Levenspiel, O., 1991. *Fluidization Engineering*. 2nd Ed., Butterworth-Heinmann, Massachusetts.

Larachi, F., Kennedy, G., Chaouki, J., 1994. A y-ray detection system for 3-D particle tracking in multiphase reactors, *Nucl. Instr. And Meth.* A338, 568-576.

Levenspiel, O. (1999) *Chemical Reaction Engineering*. 3rd Edition. John Wiley & Sons, New York, 54.

Limtrakul, S. 1996. Hydrodynamics of liquid fluidized beds and gas-liquid fluidized beds. D. Sc. Thesis. Washington University, St. Louis, MO, USA.

Massimilla, L., in J. F. Davidson, Clift and D. Harrison (Ed.), 1985. Fluidization 2nd Ed., Academic Press, London, 133.

Monin, A. S., Yaglom, A. M., 1971. In Statistical Fluid Mechanics: Mechanics of Turbulence, Lumley, J. L., Ed., MIT Press: Cambridge, MA, Vol. 1.

Okasha, F., El-Emam, S., Mostafa, H. K. 2003. The fluidized bed combustion of heavy liquid fuel (Mazut). Exp. Therm. Fluid Sci. 27, 473-480.

Rizkalla, A. A., Lefebvre, A. H. 1975. The influence of air and liquid properties on air blast atomization. J. Fluids Eng. 97, 316-320.

Roy, D., Larachi, F., Legros, R. and Chaouki, J., 1994. A study of solid behavior in spouted beds using 3-D particle tracking. Can. J. Chem. Eng., 72, 945-952.

Roy, S. 2000. Quantification of two-phase flow in liquid-solid risers, Ph.D. Thesis, Washington University, Saint Louis, Missouri, USA.

Schmidt, L. D., Huff, M., Bhardwaj, S. S., 1994. Catalytic partial oxidation reaction and reactors. Chem. Eng. Sci. 49, 3981-3994.

Sridhar, T.S., 1986. Performance of a fluidized bed calciner for the calcination of metal nitrate wastes. Nuclear and Chemical Waste Management. 6, 51-60.

Tartan, M. and D. Gidaspow D., 2004. Measurement of granular temperature and stresses in risers, AIChE J. 50, 1760-1775

Tonkovich, A. L. Y, Zilka, J. L., Jimenez, D. M., Roberts, G. L., Cox, J. L., 1996. Experimental investigation of inorganic membrane reactors: A distributed feed approach for the partial oxidation reaction. Chem. Eng. Sci. 51, 789-806.

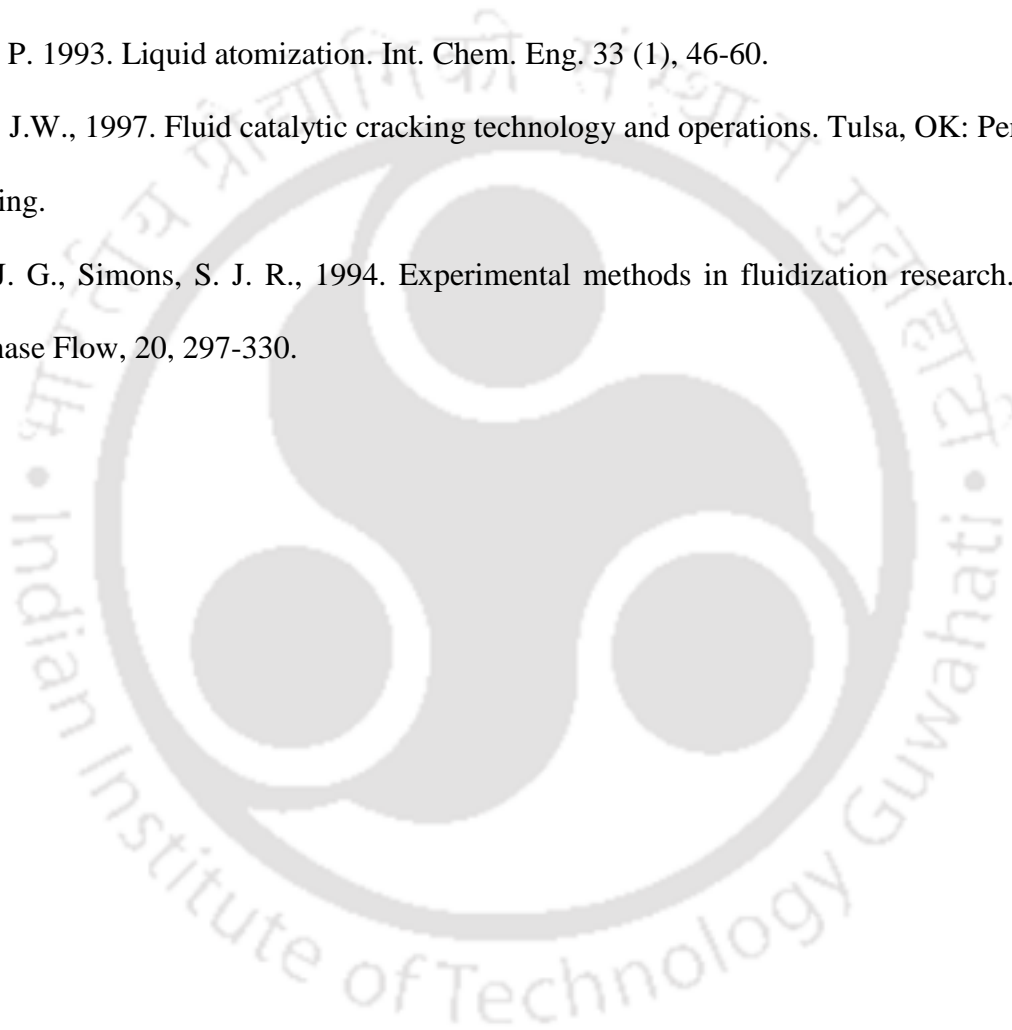
Upadhyay, R.K., Roy, S., 2010. Investigation of the hydrodynamics of binary fluidized beds via radioactive particle tracking and dual -source densitometry. *Can. J. Chem. Eng.* 88, 601–610

Upadhyay, R. K., Pant. H. J., Roy, S., 2019. Experimental validation of design and performance parameters of radioactive particle tracking (RPT) experimentation. *Appl. Radiat. Isot.* 153, 108814

Walzel, P. 1993. Liquid atomization. *Int. Chem. Eng.* 33 (1), 46-60.

Wilson, J.W., 1997. Fluid catalytic cracking technology and operations. Tulsa, OK: PennWell Publishing.

Yates, J. G., Simons, S. J. R., 1994. Experimental methods in fluidization research. *Int. J. Multiphase Flow*, 20, 297-330.



Chapter 4 Solid Holdup Measurements in Gas-Solid Fluidized Bed with Sidewall Injections via GDT Experiment

Scope

In this chapter, the time averaged-chordal averaged volume fraction of solids, $\langle \varepsilon_s \rangle$ in the presence of secondary gas (or air) injection through sidewall nozzles is investigated. Successful implementation of GDT is conducted under different flow conditions and system parameters. The obtained GDT data can be used to scale up such a gas-solid system and can be validated using the CFD tool for further study.

4.1. Introduction

In Chapter 1, detailed features and application of sidewall injection in fluidized bed have already been discussed. In many of these applications, like fluid cooking cracker (Wilson, J.W. 1997), combustion of liquid fuels (Anthony and Lu, 2001; Barker and Beacham, 1980; Okasha et al. 2003), thermal denitration (Bjorklund and Offutt, 1973; Fane et al. 1974), metal nitrate waste (Sridhar, 1986), and coating (Walzel, 1993) etc., reactant/promoters are injected in the bed through pneumatic nozzles placed at sidewall. The injection of this secondary air along with the reactant severely affects the performance of the fluidized bed due to change in the flow field. Since the last many decades, researchers are trying to investigate the effect of nozzle injection on the quality of fluidization. However, large numbers of these studies were focused on finding the penetration depth inside the fluidized bed, which is found to be function of nozzle diameter, injection velocity, particle properties and bottom gas injection velocity (Kozin and Basakov, 1967; Zenz, 1968; Benjelloun et al., 1995).

The hydrodynamic behaviour of horizontal jet in gas-solid fluidized bed were often characterized as jet shape, penetration length, solid distribution and its flow fields. Lummi and Baskakov (1967) conducted an experiment to evaluate CO₂ concentration by injecting air-CO₂ mixture in a fluidized bed. Chen and Weinstein (1993) performed an experiment in a rectangular fluidized bed to observe the influence of injecting air through an X-ray system. Chen and Weinstein (1993) identified three distinct zones near the injection. Chyang et al. (1997) also carried out similar kinds of experiments in a 2-D fluidized bed via videography and drawn a phase diagram (showing bubbling, jetting and transitions regime). Experimental evaluation of void fraction was carried out by Bhowmick et al. (2015) at different axial levels with a single sidewall nozzle injection in a cylindrical bed (ID 250 mm) of the glass beads particles (mean size 385 micron and density 2500 kg/m³). They had performed the experiments for varying nozzle flow rates ($Q_j/Q_{mf} = 0 - 0.4375$ with $Q_{mf} = 400$ SLPM), different bed heights ($h/D_t = 1.6, 2.56$ and 3.16 with $D_t = 0.25$ m) and fluidization ratio ($U/U_{mf} = 1.0, 1.5$ and 2.0 with $U_{mf} = 0.156$ m/s) using gamma-ray transmission technique. The line averaged void fraction data were found under these operating conditions.

Koeninger et al. (2017) obtained the particle velocity and solid concentrations in a fixed/fluidized bed of glass beads (mean size=92 micron and density 2500 kg/m³) with a single horizontally placed sidewall nozzle injection using particle image velocimetry (PIV) and capacitance probe respectively. They had also implemented X-ray based computed tomography to observe the solid dynamics in the jet region without affecting the flow. Further, Koeninger et al. (2018) experimentally analyzed the solid distribution with multiple gas injections for different particle size beds and different injection flow rates. They reported that higher fluidization velocities favor the widening of jet boundary and bending the jet in the upward direction. Though several studies are performed on a gas-solid fluidized bed with sidewall nozzle injection, detailed and systematic investigation of sidewall nozzle injection

fluidized bed is still missing. Further, most of the data are presented for the single sidewall nozzle injection and data for multiple nozzle injection system are not available.

Therefore, in the current thesis work, an extended version of the previous study that had been carried out by Bhowmick et al. (2015) was conducted in a lab-scale setup (gas-solid system) of larger diameter. In the next sections, the detail information of experimental set-up, operating conditions and outcome of flow behavior are presented.

4.2. Experimental setup

The photographs and schematic diagram of the cold flow model of gas-fluidized bed, configured with multiple nozzles at different axial planes, are shown in Figure 4.1 and Figure 4.2, respectively. The experimental setup consists of three different sections: (1) the plenum (conical base at bottom), (2) the bed (a cylindrical shaped middle section of 0.21 m ID and 1.75 m height) and (3) a freeboard (an expanded section of 0.31 m ID and 0.45 m height at the top). The all sections are made of mild steel (MS). A perforated type distributor is fixed between bed and plenum to avoid the particle movement against gravity and to provide uniform flow of primary gas injection. This plate has 120 holes of an opening diameter of 2 mm, giving 30 % of the opening area for gas supply. The bed has multiple ports (of 12 mm ID) located at different axial (or z-) planes. The distance between two successive axial planes is 90 mm. Maximum four ports are made at each plane with angular position of 90°. These ports can be used for pressure measurement and calibration during RPT.

There are three different gas injection levels (plane AA', BB' and CC') along with the column height as shown in Figure 4.1a. The injection planes AA', BB' and CC' are at a height of 20 cm, 40 cm and 60 cm respectively. Each injection plane has three injection orifices spaced at 120° apart from each other on the curved surface wall (Figure 4.1b). At each orifice, a nozzle can be placed in such a way so that it injects the fluid (or air in the present case) at a required angle of α , where α is the angle between the injection line and the perpendicular line to the wall

surface (Figure 4.2c). The details of nozzles were already discussed in the previous chapter. The bed is packed with glass beads (Geldart group B) of 2500 kg/m^3 and mean size of $709 \text{ }\mu\text{m}$ as the solid material. The initial bed height is maintained at 0.75 m from the distributor level. The primary air is supplied to the bed through the distributor (Figure 4.2a). The primary air flow is controlled through air rotameter and valve. Table 4.1 presents the system properties and operating conditions for this experiment.

Two pressure transducers (WIKA Instruments India Pvt. Ltd.; Model S-10; Range 0-2.5 bar; 4-20 mA), located at two different axial locations i.e. $z=2 \text{ cm}$ and $z=56 \text{ cm}$ height, are used to measure the bed pressure at these heights. The pressure transducers give the voltage signal as an output. Thereafter, the signal is converted to the transient data of pressure by using calibration data of individual transducer. The pressure drop across the bed is calculated and plotted against the gas superficial velocity as shown in Figure 4.3. The minimum fluidization velocity is found to be 0.36 m/s .

Table 4.1 Properties and flow conditions of air-glass beads fluidized bed system

Properties	Value	Properties	value
Particle mean diameter, d_p (μm)	709	Initial voidage, ϵ_0	0.40
Particle mean density, ρ_p (kg/m^3)	2500	Solid loading, W_s (kg)	45
Terminal velocity, U_t (m/s)	38.34	Initial bed height, H_0 (m)	0.75
Primary air inlet velocity, U_0 (m/s)	0-0.8	Air viscosity, μ_g (Pa.s)	1.786×10^{-5}
Experimental U_{mf} (m/s)	0.36	Air density, ρ_g (kg/m^3)	1.12
Column diameter, D_t (m)	0.21	Archimedes Number (Ar)	3.344×10^4
Column height, H_c (m)	2.25	Theoretical U_{mf} (m/s)	0.40

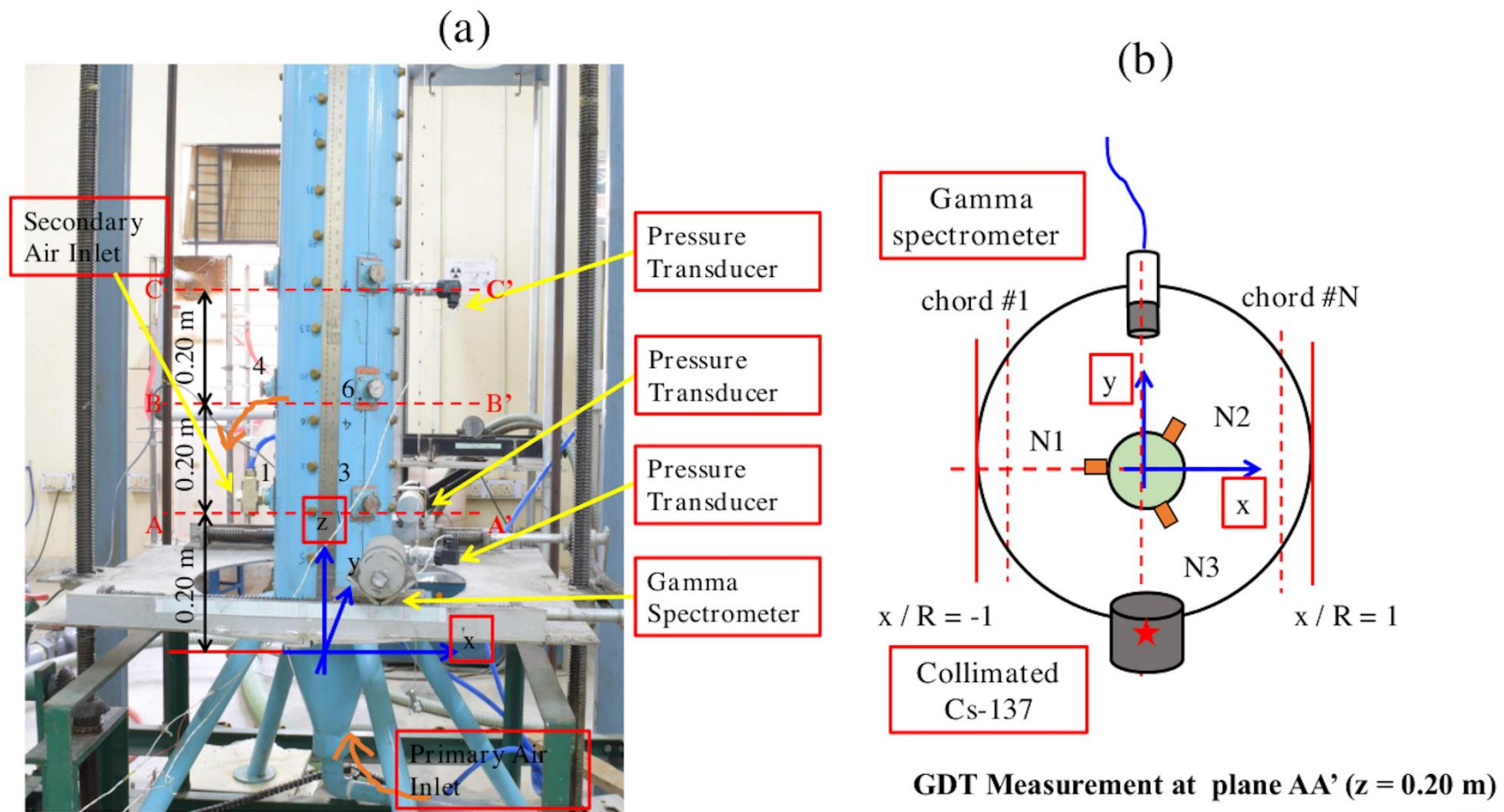


Figure 4.1 GDT setup (a) photographs of cold model setup and (b) top view representation of GDT process at nozzle plane AA'

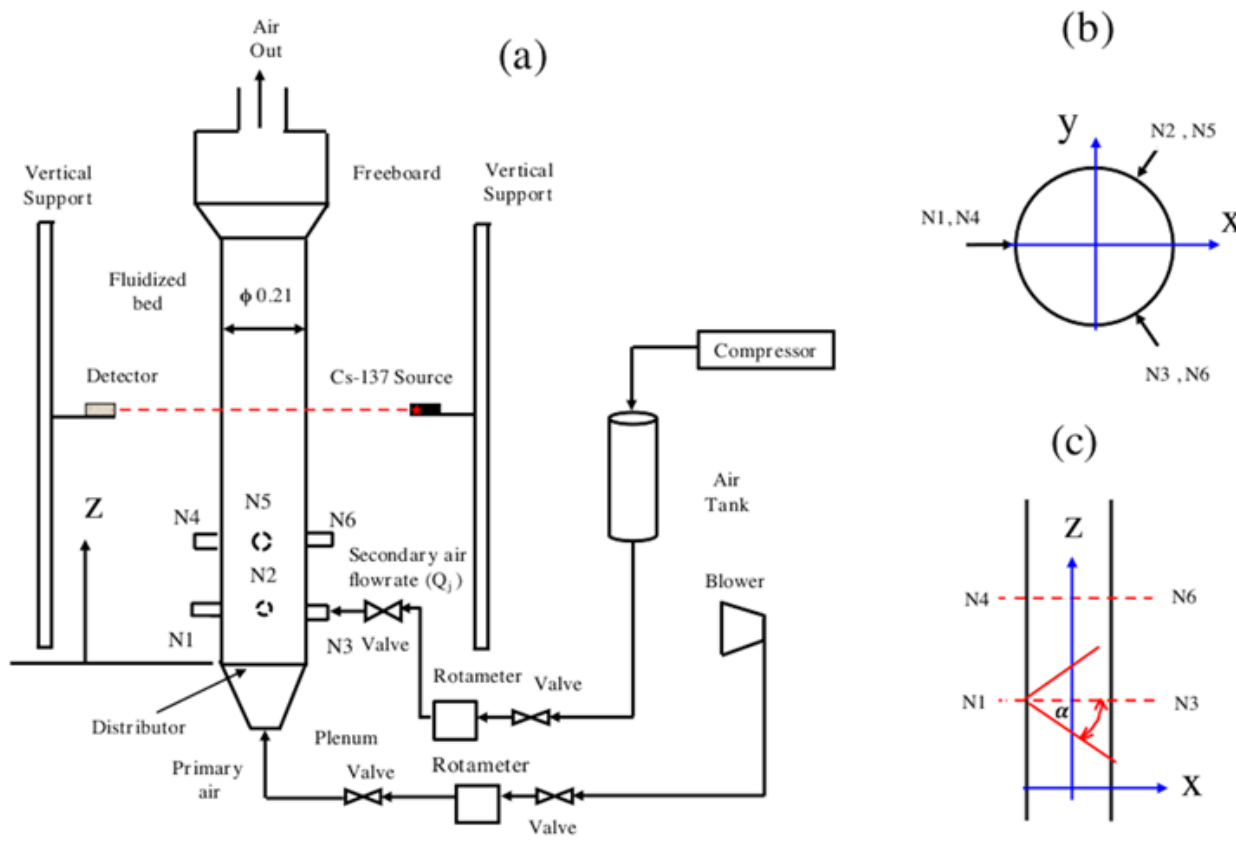


Figure 4.2 Cold flow model (a) schematic of GDT experiment setup, (b) top view of nozzle arrangements and (c) side view of nozzle arrangements.; α is the angle between injection line and x-axis.

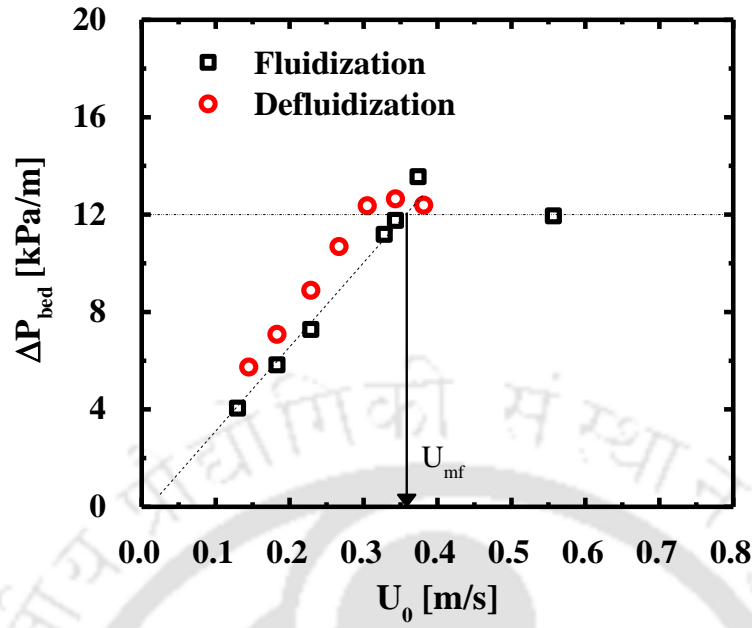


Figure 4.3 Determination of U_{mf} from pressure drop curve

4.3. Result and Discussion

Table 4.2 shows the nozzle configurations and operating flowrates under constant fluidization velocity (1.12 m/s) for 6 mm ID nozzles. GDT experiments were conducted in different cases as described in Table 4.2. As seen in Figure 4.1a, b., the gamma-spectrometer and a radioactive source particle, Cs-137 were aligned along the y-axis which gave the direction of the attenuated beam of γ -ray emitted from Cs-137. A single nozzle (N1) is placed along the x-axis so that the injection line became perpendicular to the y-axis. The detail of GDT implementation and data evaluation has been already discussed in section 2.2. Several chordal scans were performed under the required operating condition as shown in Figure 4.1b. Each chordal scan gave the line averaged volume fraction data for the phase of interest. For example, any chordal Nth scan, the chordal averaged solid volume fraction, $\langle \varepsilon_{S,N} \rangle$ can be evaluated as:

$$\langle \varepsilon_{S,N} \rangle = \varepsilon_{S,static} \frac{\ln I_{GS,N} - \ln I_{G,N}}{\ln I_{S,N} - \ln I_{G,N}} \quad (4.1)$$

where $I_{s,N}$, $I_{G,N}$ and $I_{GS,N}$ are the counts recorded by gamma-spectrometer along the “chord #N” (Figure 4.1b) for three different bed conditions i.e. completely packed bed, empty column and two-phase at “in-situ” condition, respectively; $\bar{\varepsilon}_{s,static}$ is scaling factor, which is used to scale the $\mu_{s,N}$ and can be measured from the solid loading (W_s), static bed height (H_0) and solid density (ρ_p).

Table 4.2 Details nozzle injection flowrates and configuration used for GDT setup ($\alpha=0^\circ$)

Cases	Nozzle ID	d_j [mm]	α [in degree]	Q_j [LPM]
Single nozzle	N1	6, 1	0	80, 100, 120
Two nozzles @ plane AA'	N1, N2	6	0	80, 100, 120
Three nozzles @ plane AA'	N1, N2 & N3	6	0	80, 100
Two nozzles @ plane AA' and BB'	N1, N4	6, 1	0	80, 100, 120
Two nozzles @ plane AA' and BB'	N1, N5	6	0	80, 100, 120
Two nozzles @ plane AA' and BB'	N1, N6	6	0	80, 100, 120
Single nozzle	N1	6	-45°	80, 100, 120

Note: d_j = Nozzle diameter; Q_j = Volumetric flow rate of secondary air;

4.3.1. Without Sidewall Injection

The time-averaged solid volume fractions are measured via GDT for different aspect ratio (or static bed height to column diameter ratio, H/D_t) and fluidization numbers (or U/U_{mf}) in the absence of any side injection. The results are discussed below:

Effect of Fluidization Number

The solid holdup is measured for different gas superficial velocities, varied in the range of $0.45 < U_0 < 1.12$ m/s ($1.88 < U/U_{mf} < 3.12$), at constant solid loading. The solid loading was 39 kg during these sets of experiments. The initial packed bed height, obtained by this amount of solid was 0.65 m ($H/D_t=3.10$). The GDT was applied by scanning the bed at four axial planes ($z=0.15, 0.20, 0.25$ and 0.60 m) and hence, the $\langle \varepsilon_s \rangle$ data were obtained with varying fluidization numbers. These data were compared for different fluidization velocity and plotted at different z-plane as shown in Figure 4.4. The Figure shows that $\langle \varepsilon_s \rangle$ decreases with an increase in axial height (z) at any fluidization velocity (U_0). Similarly, this also indicates that solid holdup reduces significantly as the bottom gas flow rate (or fluidization number) increases. It can also be noted that the solid fraction is higher at the column wall and lower at the center for the high fluidization velocity ($\sim U_{mf}$) as shown in Figure 4.4 except very low gas velocity. This is possible because the up-flow gas velocity is not enough to disperse the packed material inside the bed but can easily pass through the wall. The solid distribution is reversed at high fluidization velocity ($>2 U_{mf}$). These observations are also reported in the literature (Bhowmick et al., 2015). At $U/U_{mf} = 3.12$ (1.12 m/s), the mean solid holdup is 0.47, 0.40, 0.37 and 0.36 for axial height of 0.15, 0.20, 0.25 and 0.25 m respectively.

Effect of Aspect ratio

Figure 4.5 shows the radial profiles of solid distribution at four different axial z-planes ($z=0.15, 0.20, 0.25$ and 0.60 m) for two different solid loadings i.e. 39 kg and 45 kg., thus, initial bed heights were 65 and 75 cm respectively. As observed in Fig. 4.5, the effect seems to be very small, and observed mainly for the higher observation level ($z=0.6$ m). The profiles of $\langle \varepsilon_s \rangle$ are found to be symmetric for every axial plane. The profiles also show that the large fraction of up-flow gas is passed through the core region of bed at higher gas velocity. Therefore, the

solids are found to be in large amounts near the wall and less in the core region as shown in Figure 4.5. The profiles are found bowl-shaped. It was observed that the solid hold-up increases with increase in the height of beds or aspect ratio (AR). Finally, the aspect ratio and fluidization number are set to 3.57 and 1.12 for remaining experiments with different configurations and sizes of nozzles.



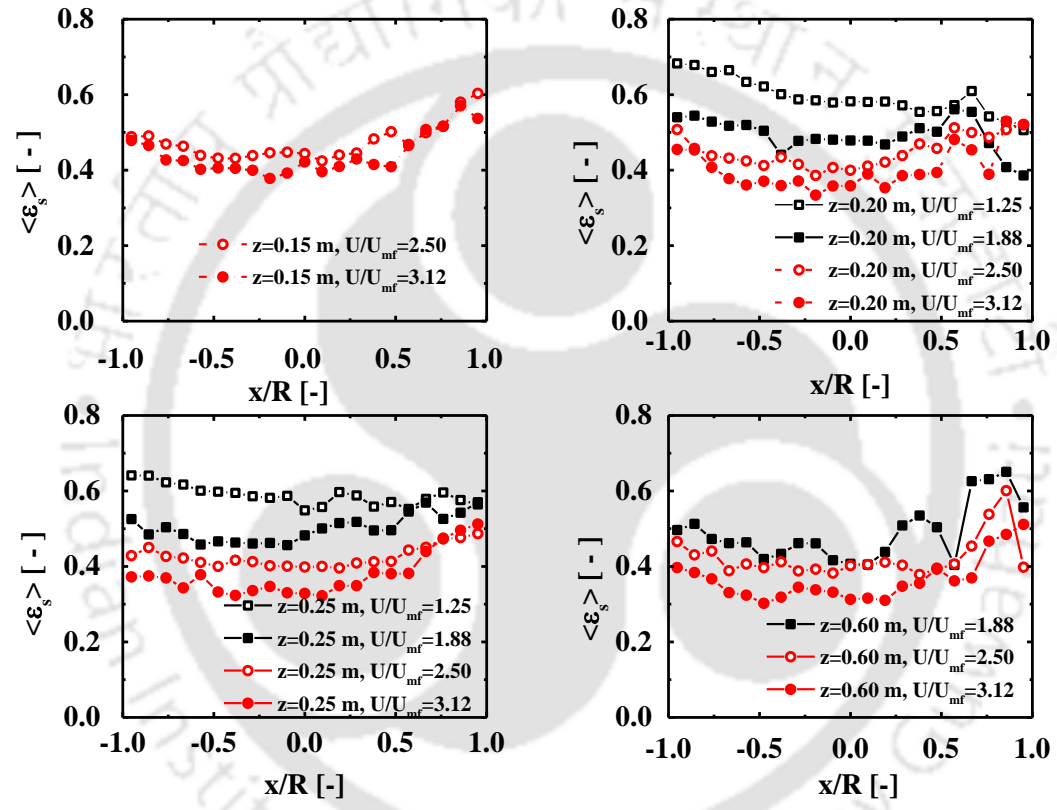


Figure 4.4 Time-averaged profiles of solid hold-up as a function of dimensionless lateral position (x/R) without sidewall injection at $H/D_t=3.10$ for (a) $z = 0.15$ m, (b) $z = 0.20$ m, (c) $z = 0.25$ m and (d) $z = 0.60$ m

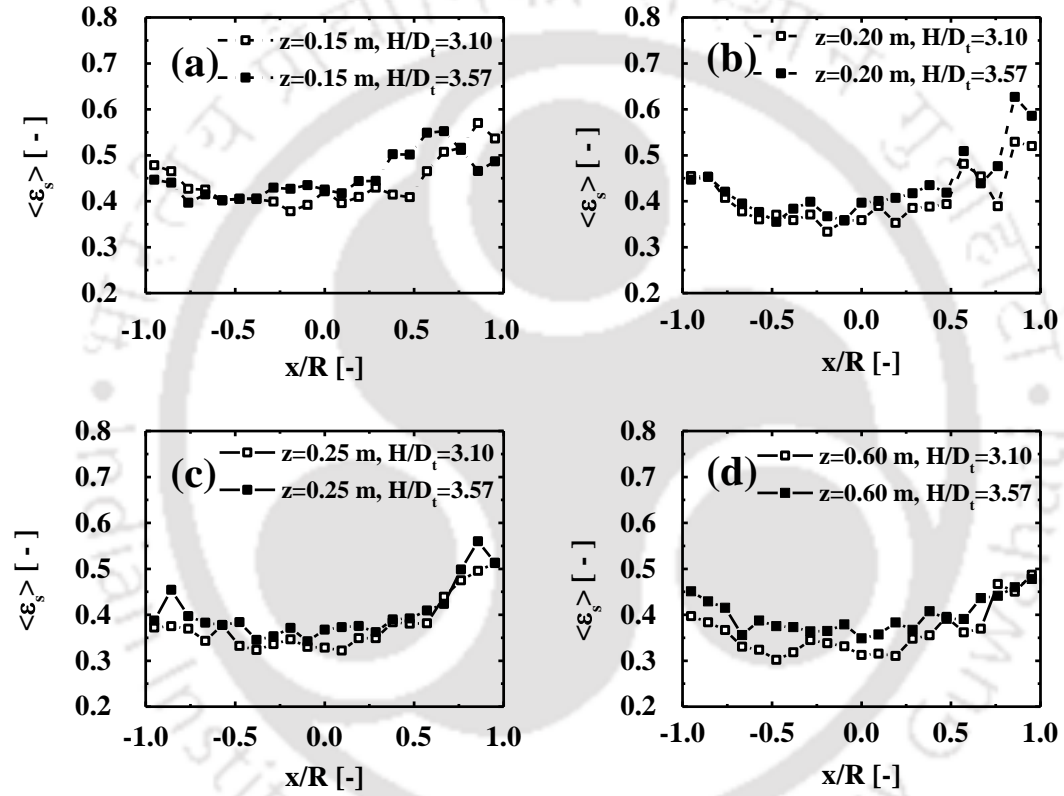


Figure 4.5 Time-averaged profiles of solid hold-up as a function of dimensionless lateral position (x/R) without sidewall injection at $U/U_{mf}=3.12$

for (a) $z = 0.15$ m, (b) $z = 0.20$ m, (c) $z = 0.25$ m and (d) $z = 0.60$ m

4.3.2. Horizontal Sidewall Injection ($\alpha = 0^\circ$) with a Single Nozzle at Plane AA'

A single nozzle, N1 (with $\alpha=0^\circ$) was operated with secondary air injection at three different flow rates (80, 100 and 120 LPM). The primary gas velocity was maintained at $3.12 U_{mf}$. The bed height was also set to 75 cm. Two nozzles with different jet diameter, d_j (6 mm and 1 mm) were utilized for secondary injection. GDT was implemented and the solids holdup were measured in a similar way as discussed earlier. Finally, these results are explained in this section.

GDT Data with 6 mm Nozzle

Figure 4.6 shows the solid holdup profiles as a function of lateral distance (x/R) and compares the data of four different axial planes at a constant secondary injection flow rate (Q_1). The profiles indicate the asymmetric nature of solid distribution along the lateral distance. This behavior of solids distribution has also been noted at both upper axial planes. The less amount of solids is present near the jet injection wall ($x/R = -1.0$) and higher fractions of solids is present on the opposite wall to the injection point (at $x/R = 1.0$).

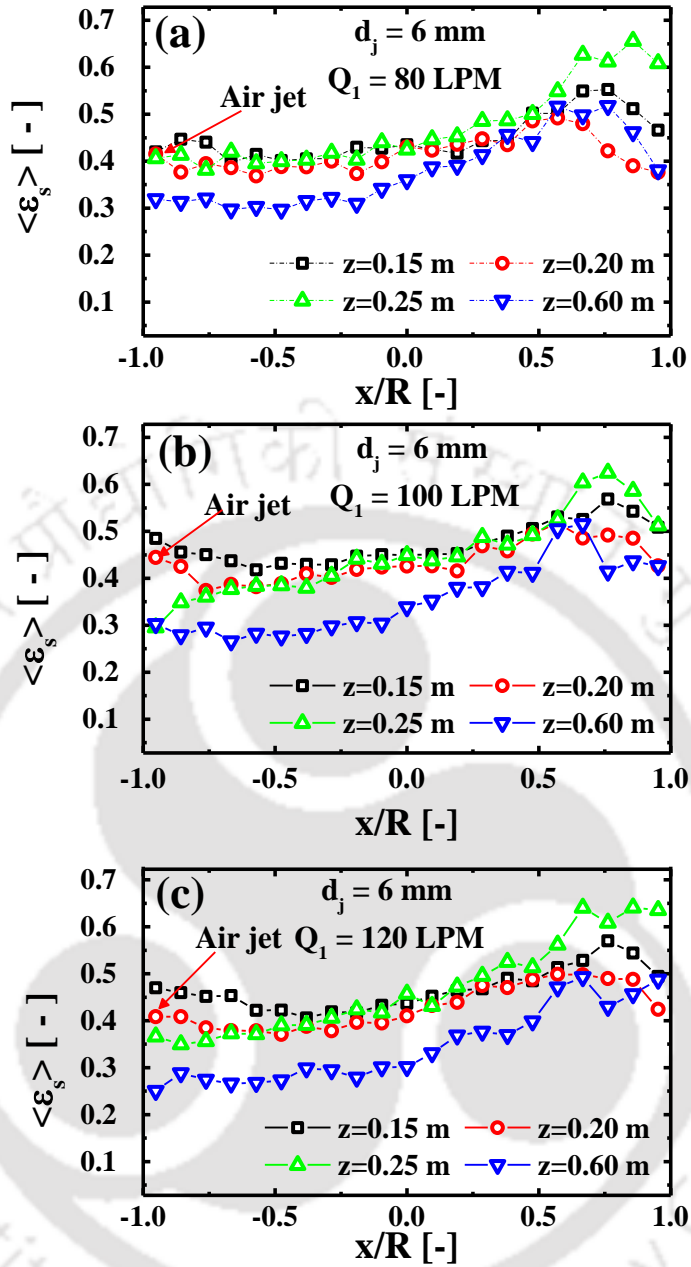


Figure 4.6 Time-averaged profiles of solid hold-up as a function of dimensionless lateral position (x/R) with single nozzle injection (6 mm ID) at different z -planes for (a) $Q_1=80 \text{ LPM}$, (b) $Q_1=100 \text{ LPM}$ and (c) $Q_1=120 \text{ LPM}$ ($H/D_t = 3.57$; $U/U_{mf}=3.12$, $d_p=709 \mu\text{m}$)

In Figure 4.7, the solid hold-up data, obtained for different secondary gas flowrates (Q_1) from GDT experiments are compared and plotted against each flowrate at a fixed z-plane. It has been noted that increasing Q_1 (from 80 LPM to 120 LPM) does not affect solid hold-up at a lower height ($z=0.15$ m). At the lower plane, the change in the solid holdup is insignificant with increasing Q_1 (Figure 4.7a). Results also indicate that the secondary injection has a significant effect on the upper level of the injection plane as shown in Figure 4.7c. Approximately 5-8 % reduction in solid hold up has been observed at $z=0.25$ m in Figure 4.7c. The similar observations have been found on the other planes which are above the plane AA'. This observation was also reported elsewhere in the literature (Bhowmick et al., 2015). They reported that the interaction between the jetting bubble (originating from the secondary injection) and the primary bubble (rising up from the bottom of the bed) played an important role in the solid distribution inside the bed.

The two important operating variables, which can shift the position of interaction plane between a jetting bubble and primary bubble, are the primary gas flow rate at the bottom and secondary gas flow rate at the sidewall. The effect of primary gas flowrates on the position of the interaction plane has been already reported earlier (Bhowmick et al., 2015). The location of the interaction plane is shifted from top to bottom of plane AA', as the U_0 increases from low to high velocity. The effect of injection velocity is now well understood. As the bed is operated under low secondary flowrates (80-120 LPM) through a single nozzle, which is very less compared to primary fluidization flowrates (>3600 LPM), therefore, the interaction between the jetting bubble and primary bubble would occur at the lower axial plane just below the plane AA'. Thus, the interaction plane shifts from a lower plane to the upper plane as the Q_1 is increased.

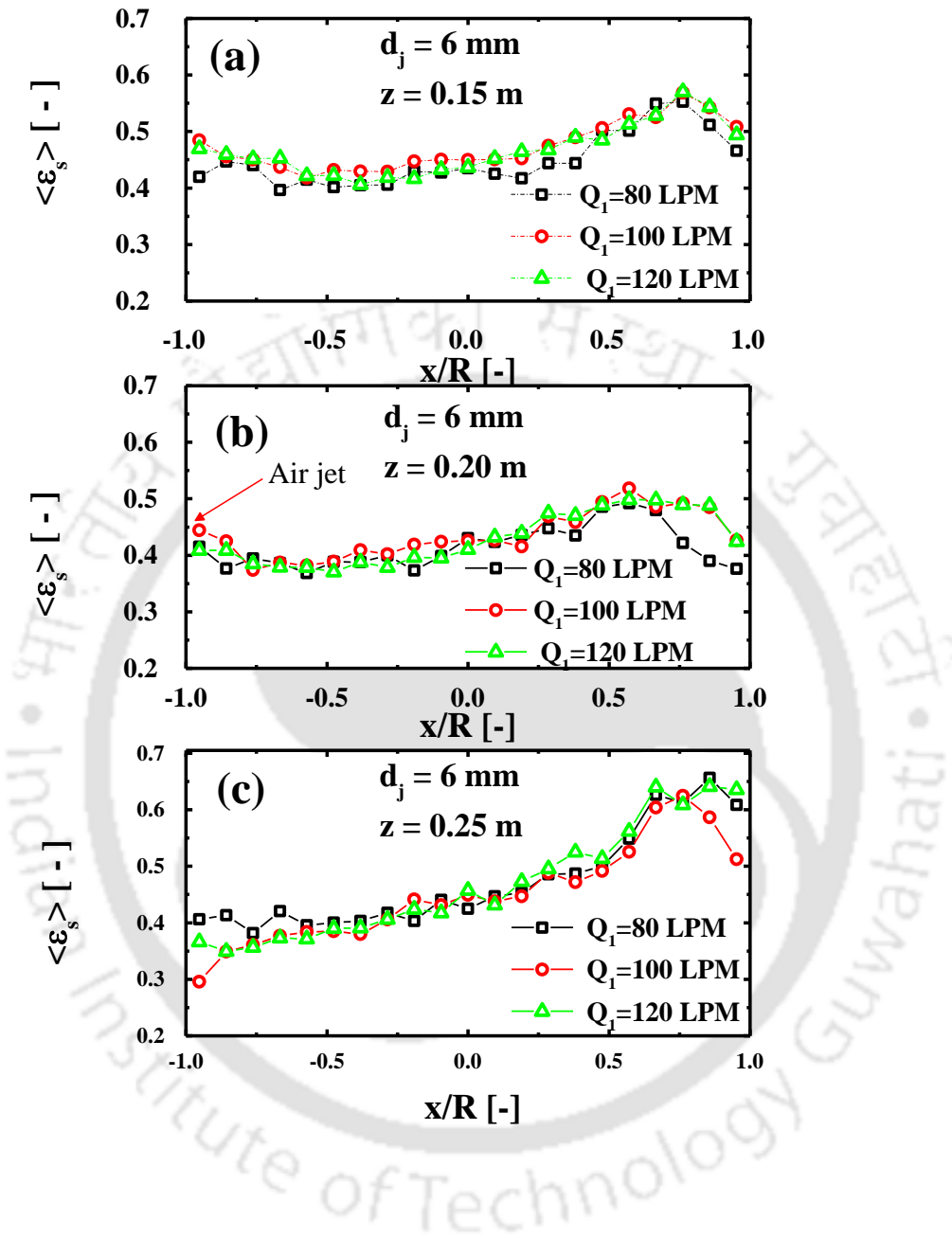


Figure 4.7 Time-averaged profiles of solid hold-up as a function of dimensionless lateral position (x/R) with large diameter (6 mm ID) single nozzle injection at different injection flowrates for (a) $z=0.15$ m, (b) $z = 0.20$ m and (c) $z = 0.25$ m ($H/D_t = 3.57$, $U/U_{mf}=3.12$, $d_p=709$ μ m)

GDT Data with 1 mm Nozzle

The solids holdup data for small size (1 mm ID) nozzle injection are obtained using GDT measurement for Q_1 in the range of 80-120 LPM in a similar way as done with 6 mm nozzle. Thus, the lateral distributions of measured solid fraction at three different heights are shown in Figure 4.8 for a fixed Q_1 . It has been observed that the solid hold up profiles follow the bowl-shaped trends for the nozzle plane/upper axial planes ($z \geq 0.20$ m) except the lower axial plane ($z < 0.20$ m) as shown in Figure 4.8. It is noticed that the solid holdup profile is almost symmetric at the lower height ($z=0.15$ m) for $Q_1=80$. LPM (Figure 4.8a) which becomes asymmetric as the Q_1 increases from 80 to 120 LPM (Figure 4.8c). At the injection plane, the solid holdup is higher at the wall but less in the core region as shown by the red curve.

Effect of the Nozzle Diameter

The GDT data obtained without side injection and a single jet injection through two different sizes of nozzle diameters (6 mm and 1 mm) are compared for different nozzle injection flowrates (80-120 LPM). Figure 4.9 shows the comparison between the solid hold up data obtained at $Q_1 = 80$ LPM. Figure 4.10a shows that the lower plane has a minor effect of side injection of secondary gas through both sizes of nozzles. The average solid holdup value at three different operating conditions: without nozzle, with 6 mm ID nozzle and 1 mm ID nozzle are 0.47, 0.45 and 0.46, respectively. At $z=0.20$ m, the mean solids holdup is 0.43, 0.41 and 0.49 (Figure 4.10b). As the injection flowrates are equal for these two nozzles, therefore, the high jet velocity can be the main reason for the increment of the solid holdup. Further, the mean values are 0.40, 0.47 and 0.49 at the upper plane.

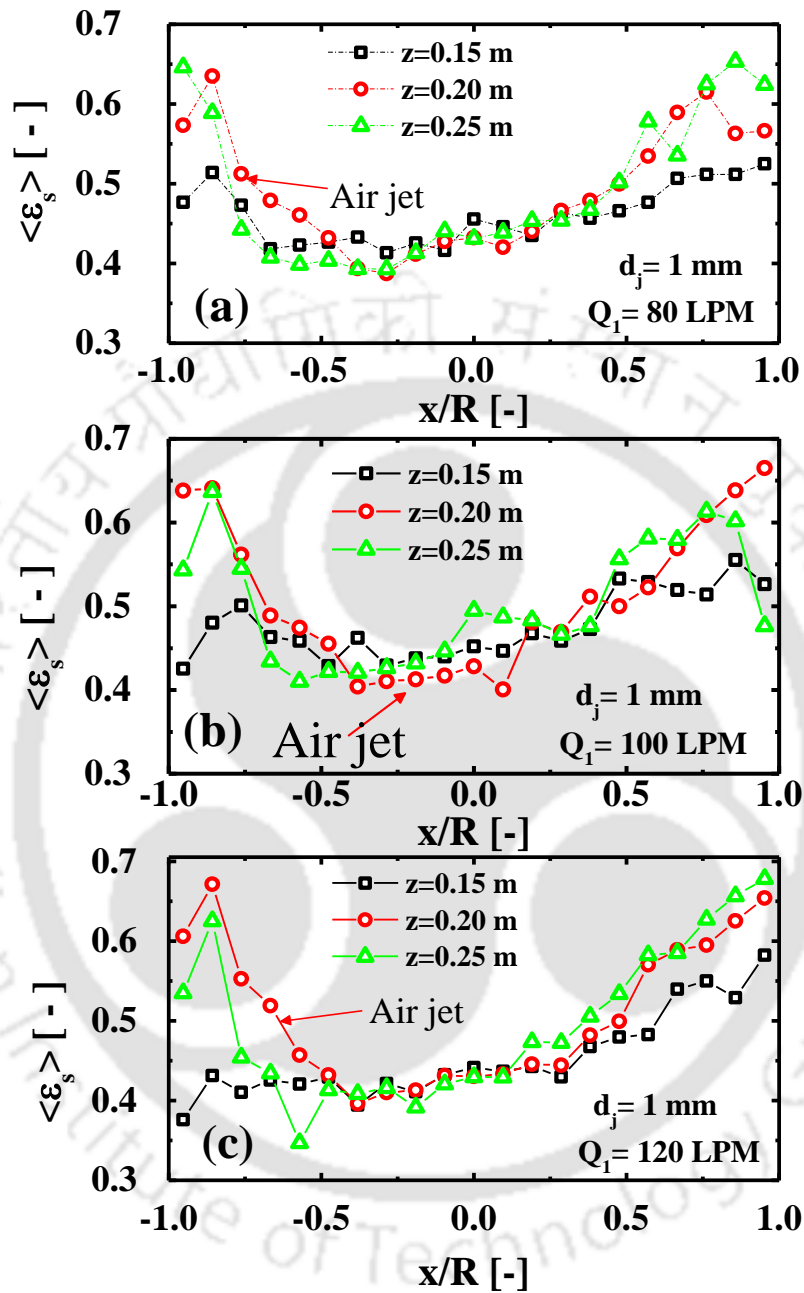


Figure 4.8 Time-averaged profiles of solid hold-up as a function of dimensionless lateral position (x/R) with small diameter (1 mm ID) single nozzle injection at different z -planes for (a) $Q_1=80$ LPM, (b) $Q_1=100$ LPM and (c) $Q_1=120$ LPM ($H/D_t = 3.57$, $U/U_{mf}=3.12$, $d_p=709 \mu m$)

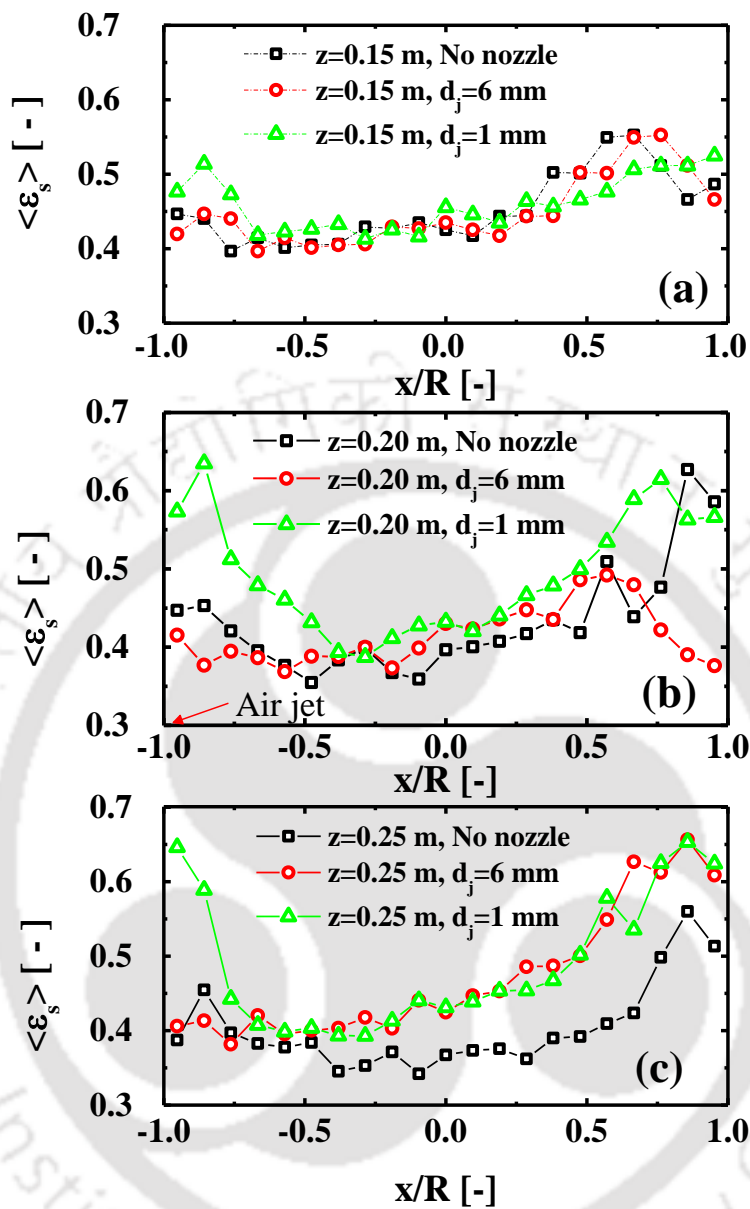


Figure 4.9 Comparison of solids hold-up with single injection of two different size nozzle and in the absence of nozzle at $Q_1 = 80$ LPM for (a) $z=0.15$ m, (b) $z = 0.20$ m and (c) $z = 0.25$ m ($H/D_t = 3.57$, $U/U_{mf}=3.12$, $d_p=709 \mu\text{m}$)

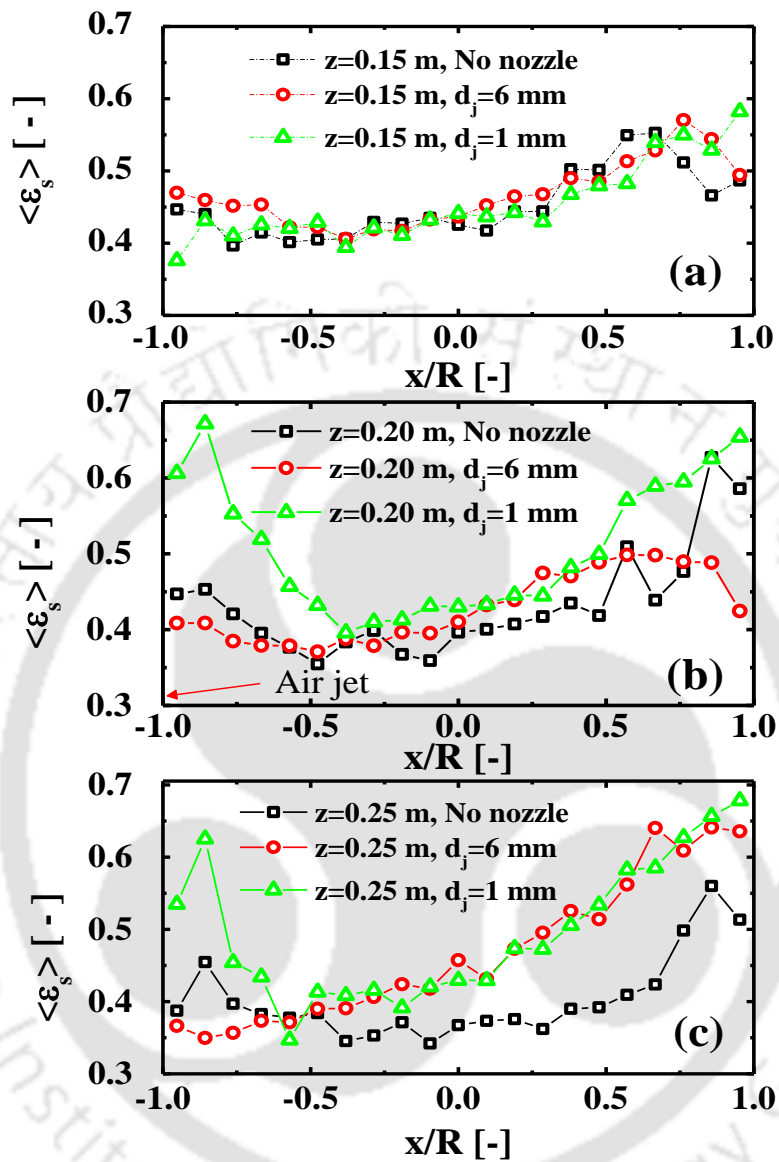


Figure 4.10 Comparison of solids hold-up with single injection of two different size nozzle and in the absence of nozzle at $Q_1 = 120\text{ LPM}$ for (a) $z=0.15\text{ m}$, (b) $z = 0.20\text{ m}$ and (c) $z = 0.25\text{ m}$ ($H/D_t = 3.57$, $U/U_{mf}=3.12$, $d_p=709\text{ }\mu\text{m}$)

4.3.3. Multiple sidewall injections with 6 mm diameter nozzles at the same plane ($z=0.20$ m)

A set of two (N1 & N2) and three nozzles (N1, N2 & N3) of the same size (6 mm ID) were operated at the same flowrates simultaneously, in the range of 80-120 LPM, under constant fluidization velocity of $3.12 U_{mf}$. The GDT was used to measure the solid holdup. These GDT data were compared with the single injection data. The results are discussed in subsequent sections as follows:

Effect of two sidewall injections on the same plane

This section describes the effect of two sidewall injections through the nozzle of the same size ($d_j = 6 \text{ mm}$) operated at the same plane or plane AA' on the solid distribution within the gas-fluidized bed. In this case, N1 and N2 are operated at the equal injection flowrates of 80, 100 and 120 LPM. The GDT data are measured at four different axial planes ($z=0.15 \text{ m}$, 0.20 m , 0.25 m and 0.60 m). Figure 4.11 illustrates the variation of solid volume fraction in the lateral direction, along the injection line of nozzle N1 (or x-axis) in the presence of two nozzles N1 and N2. The plots show similar trends for different operating flow rates, $Q_{1,2}$ at a fixed z-plane as shown in Figure 4.11. It can be noticed that the solid profile at different axial planes for a constant $Q_{1,2}$, is more symmetric than for single sidewall injection (or Q_1).

Effect of three sidewall Injections at the same plane

Figure 4.12 shows the effect of three nozzles (N1, N2, N3) on the solid holdup in the lateral distance along the x-axis for two different flowrates ($Q_{1,2,3}$) under the fixed fluidized condition. The bed is operated with equal side injection flowrates of 80 and 100 LPM as shown in Figure 4.12. The minimum solids holdup can be observed at the lower plane ($z=0.15 \text{ m}$), which is just below the injection plane AA'. At $z=0.15 \text{ m}$, the presence of solids is high near the wall and less at the dimensionless lateral position of $x/R=0.25$ for the secondary injection flow rate of

80 LPM (or $Q_{1,2,3}=80$ LPM). This may be because of the presence of nozzle N2 and N3 (see Figure 4.2). A similar trend has been observed at $z=0.15$ m for $Q_{1,2,3}=100$ LPM, which indicates that the interaction of the jetting bubble and primary bubble does not change the location along the x-axis. For different axial planes, the solid hold up profiles has a local minimum value at the same lateral position (at $x/R=0.25$). This shows the movement of bubble track where the solid hold up is found to be minimum. The profiles are approximately symmetric for all z .



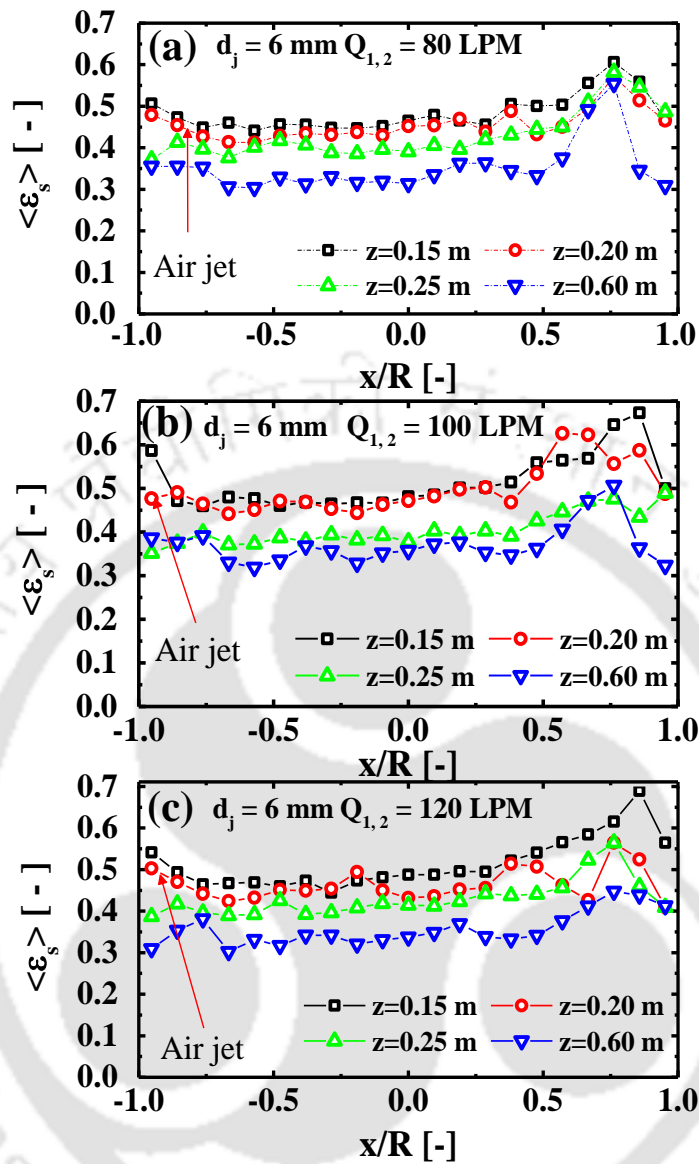


Figure 4.11 Time-averaged profiles of solid hold-up as a function of dimensionless lateral position (x/R) with two nozzle injections (6 mm ID) at different z -planes for (a) $Q_{1,2} = 80 \text{ LPM}$, (b) $Q_{1,2} = 100 \text{ LPM}$ and (c) $Q_{1,2} = 120 \text{ LPM}$ ($H/D_t = 3.57$, $U/U_{mf} = 3.12$, $d_p = 709 \mu\text{m}$)

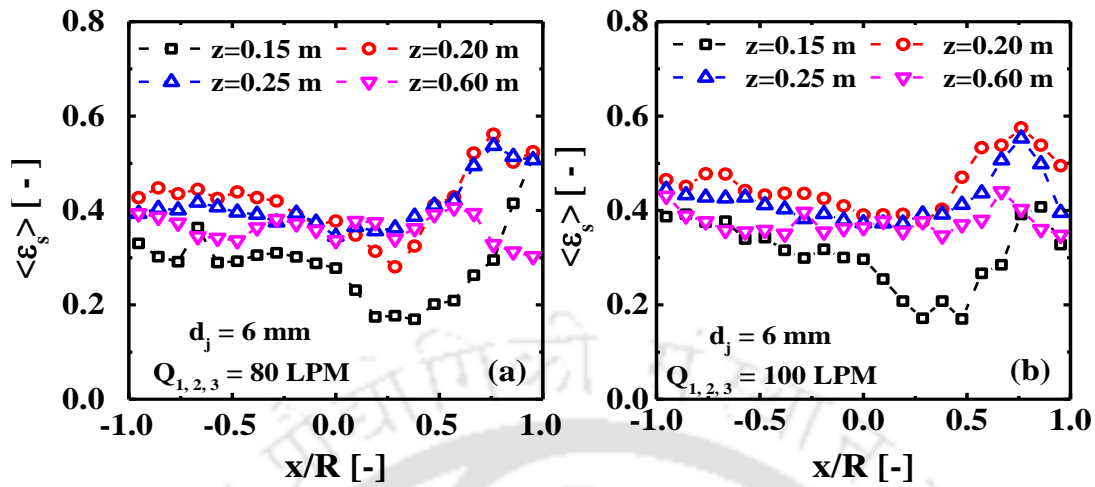


Figure 4.12 Time-averaged profiles of solid hold-up as a function of dimensionless lateral position (x/R) with three nozzle injections (6 mm ID) at different z -planes for (a) $Q_{1,2,3} = 80$ LPM and (b) $Q_{1,2,3} = 100$ LPM ($H/D_t = 3.57$, $U/U_{mf} = 3.12$, $d_p = 709 \mu\text{m}$)

Comparison of solid holdup data with single, two and three sidewall injection(s) through 6 mm ID nozzle(s) at the same plane

The solid holdup data, measured for three different jet configurations operating at the same flowrate 100 LPM, are compared as shown in Figure 4.13. From Figure 4.13a, it has been noticed that the symmetric arrangement of three nozzles provides lowest solids fractions at the lower plane just below the injection plane ($z=0.15$ m). It is worth to say that injection with a single or two nozzle has no significant effect on the solid distribution at $z=0.15$. Figure 4.13b shows the solid distribution at injection planes ($z=0.20$ m). At the wall region, a low fraction of solids is available when two or more sidewall injections work simultaneously as shown in Figure 4.13b. Similarly, the low solid holdup is obtained with two or more side injections at the upper height ($z=0.25$ m).

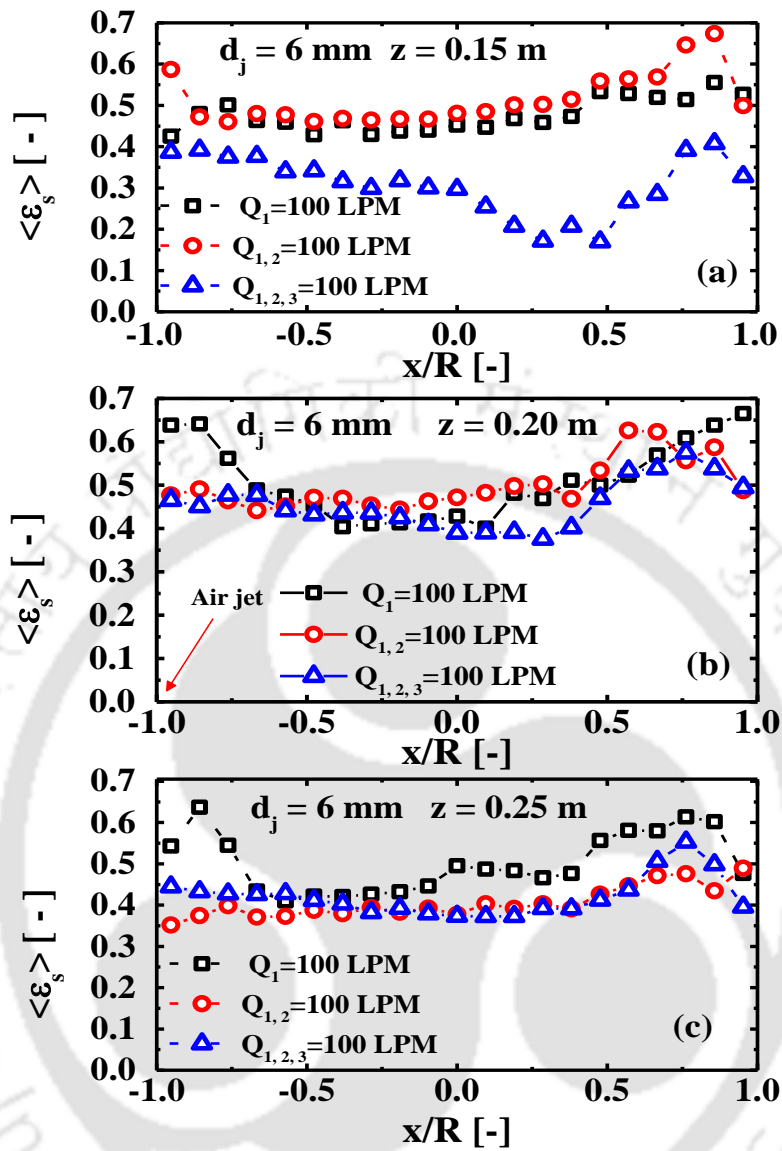


Figure 4.13 Comparison of solid holdup data with sidewall injection(s) operating at (a) $z = 0.15$ m, (b) $z = 0.20$ m, and (c) $z = 0.25$ m ($H/D_t = 3.57$, $U/U_{mf} = 3.12$, $d_p = 709 \mu\text{m}$)

4.3.4. Multiple sidewall injections operating at a different plane

The GDT was performed with a set of two different sets of nozzles such as (N1, N4), (N1, N5) and (N1, N6) as shown in Figure 4.2 with same size (6 mm or 1 mm) for varying injection flowrate in the range of 80-120 LPM. Finally, GDT data are obtained for all these cases. The lateral profiles of GDT data are plotted and discussed as follows:

Solid distribution with two side injection through large diameter nozzles (6 mm ID)

In this section, we present the solid holdup profiles, measured with different nozzle arrangements operated at different axial planes i.e. plane AA' and plane BB' as shown in Figure 4.1., for three different flowrates. For each arrangement such as (N1, N4), the secondary gas flow rate is maintained at a fixed value i.e. 80 LPM for each nozzle. The chordal solid volume fraction is measured at $z=0.15$ m, 0.20 m and 0.25 m. The similar, measurement is repeated for remaining flowrates (100 & 120 LPM). Finally, the GDT data for case (N1, N4) are compared and plotted for different flow rates as shown in Figure 4.14. The solids volume fraction has been reduced near the injection wall ($x/R = -1.0$) as the nozzle flowrates are increased from 80 to 120 LPM. This reduction in the solid fraction is observed with the increasing nozzle flowrates ($Q_{1,4}$). From Figure 4.14a-c, it has been observed that solid holdup is increased with height for a constant $Q_{1,4}$.

The effect of other nozzle configurations such as (N1, N5) and (N1, N6) on solids holdup along the x-axis, are also presented in Figure 4.15 and Figure 4.16, respectively. In both cases, the solid fraction decreases as z increases. The trends are similar in all the cases. The solid holdup becomes higher on moving along the x-axis.

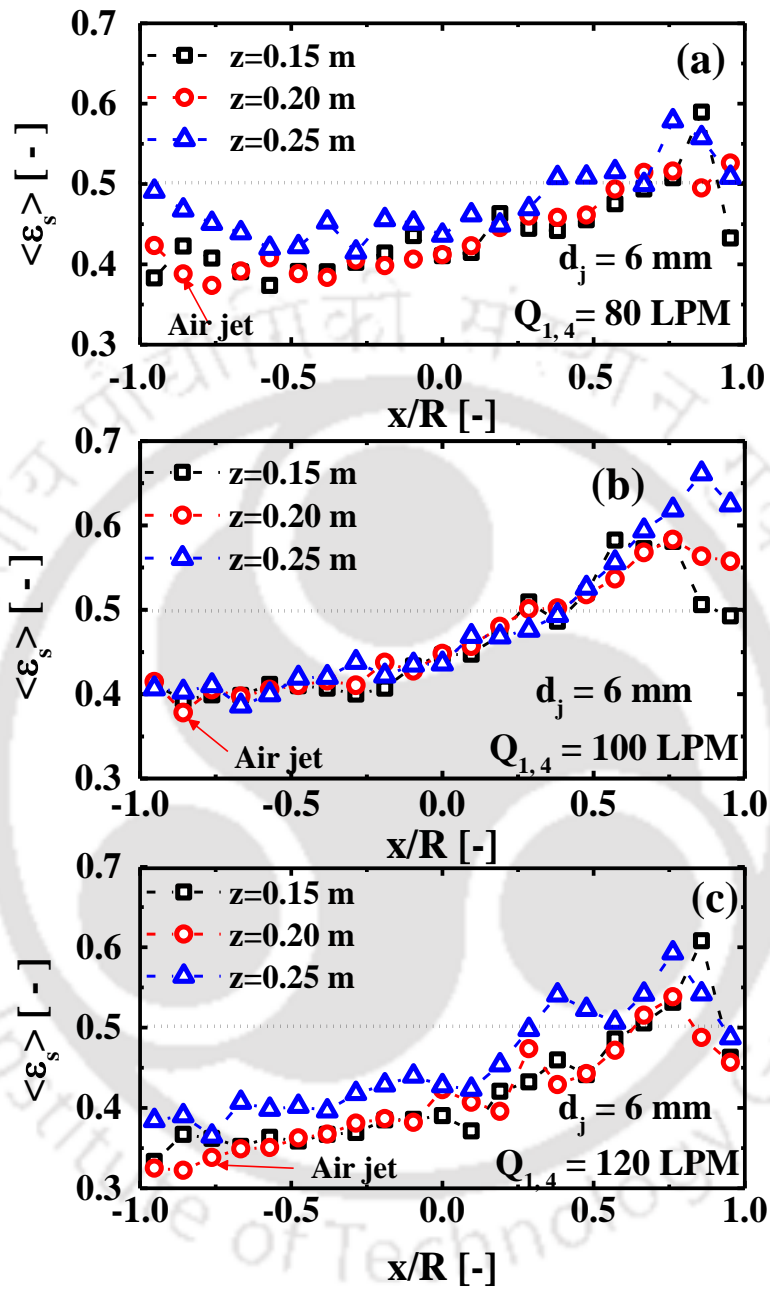


Figure 4.14 GDT data for solids holdup at different axial heights with sidewall injection(s) of large size nozzles, N1 and N4 ($d_j = 6$ mm) operating at (a) $Q_{1,4} = 80$ LPM, (b) $Q_{1,4} = 100$ LPM, and (c) $Q_{1,4} = 120$ LPM ($H/D_t = 3.57$, $U/U_{mf} = 3.12$, $d_p = 709$ μm)

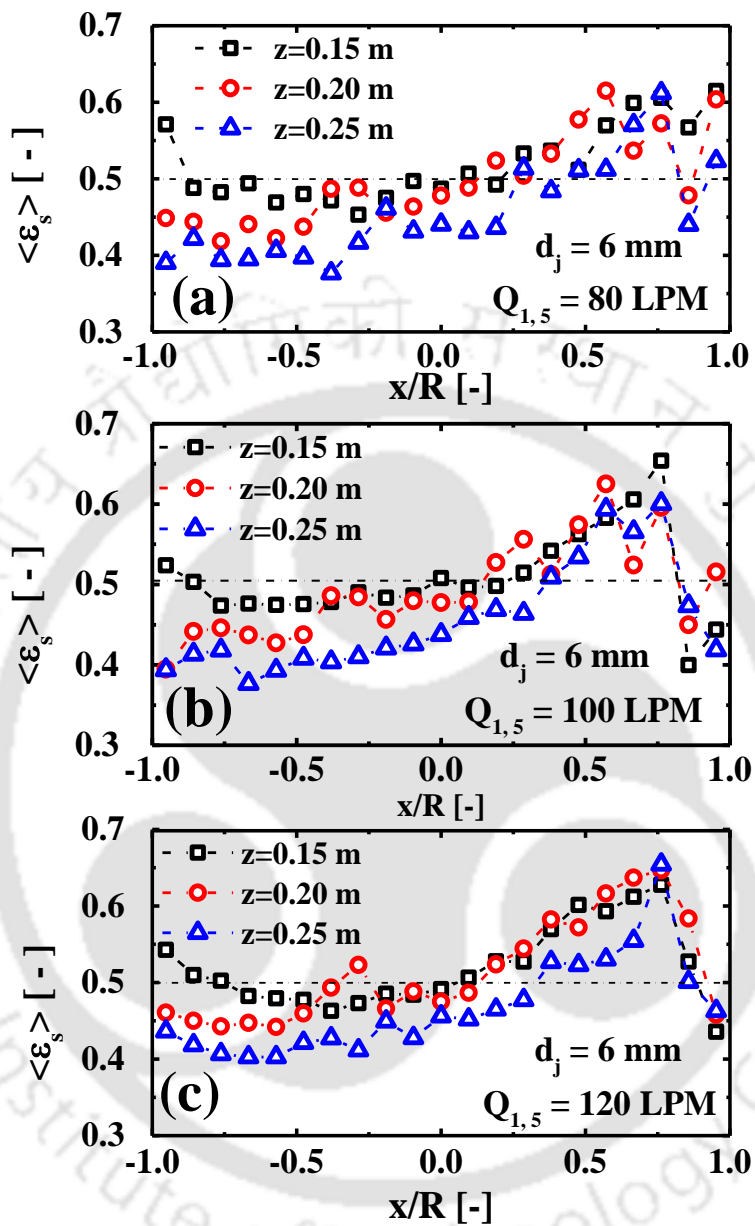


Figure 4.15 GDT data for solids holdup at different axial heights with sidewall injection(s) of large size nozzles, N1 and N5 ($d_j = 6\text{ mm}$) operating at (a) $Q_{1,5} = 80\text{ LPM}$, (b) $Q_{1,5} = 100\text{ LPM}$, and (c) $Q_{1,5} = 120\text{ LPM}$ ($H/D_t = 3.57$, $U/U_{mf} = 3.12$, $d_p = 709\text{ }\mu\text{m}$)

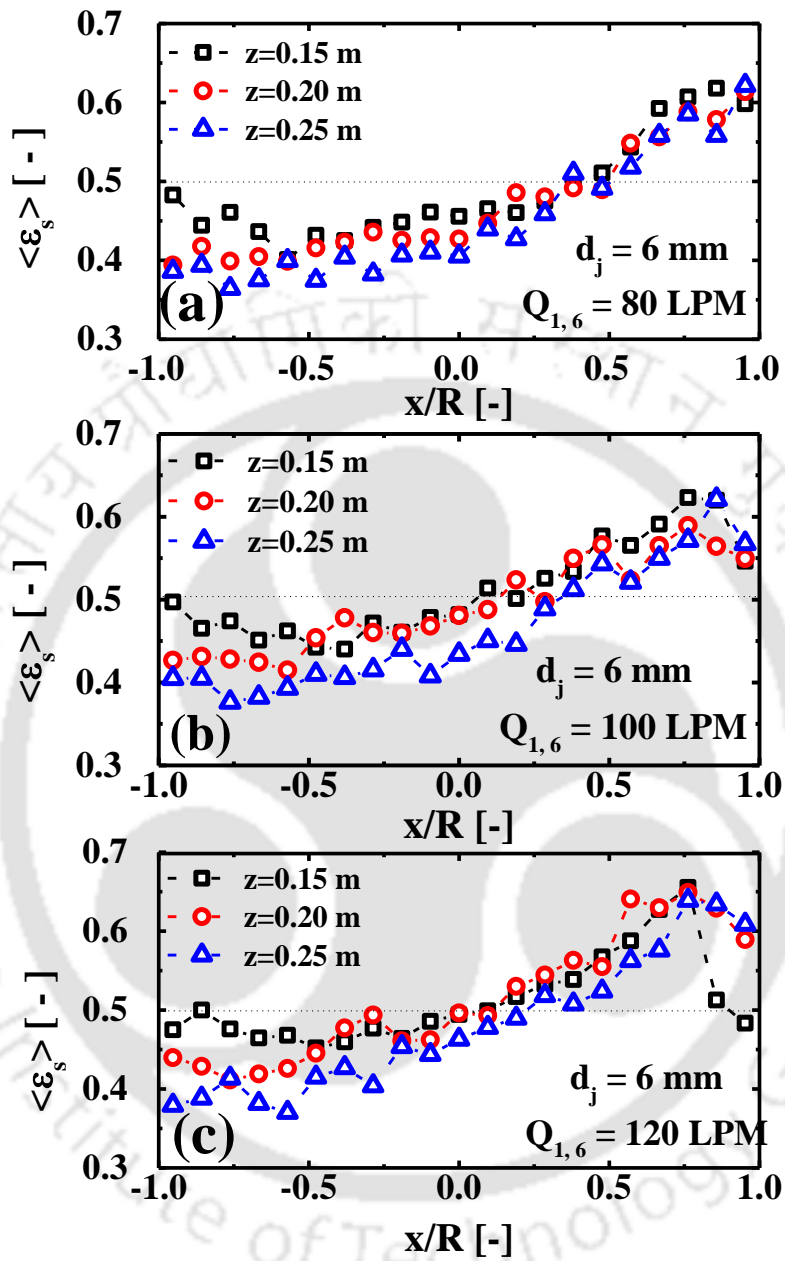


Figure 4.16 GDT data for solids holdup at different axial heights with sidewall injection(s) of large size nozzles, N1 and N6 ($d_j = 6$ mm) operating at (a) $Q_{1,6} = 80$ LPM, (b) $Q_{1,6} = 100$ LPM, and (c) $Q_{1,6} = 120$ LPM ($H/D_t = 3.57$, $U/U_{mf} = 3.12$, $d_p = 709$ μm)

Solid distribution with two side injection through small diameter nozzles (1 mm ID)

In this section, we demonstrated the effect of two small sizes (1 mm ID) nozzles, working at the two different axial positions, on the solid volume fraction. These nozzles are placed at the location N1 and N4. After conducting the GDT experiments, the chordal averaged volume fraction of the solid phase is measured and compared for different z-planes at a fixed secondary gas flowrate as shown in Figure 4.17. These profiles are quite different from the earlier one when the large-diameter nozzles are used in the same position. From Figure 4.17, it has been noticed that solid distribution is not affected significantly at the plane just below the injection plane AA' with a change in the secondary flowrates ($Q_{1,4}$). A similar observation has been noticed in Table 4.4. In addition, the impact of the second injection planes is not seen on the lowest z-plane. At plane AA', the availability of the solids is increased near the wall but remain almost constant at the core region ($x/R=0$) with increasing the secondary gas flowrates, $Q_{1,4}$. This indicates that the primary bubble does not change so much because of the high jet velocity of nozzles (1 mm ID). This also suggests that most of the bubbles rising from the distributor are ascending at the central region of the bed till it reaches to the lower injection plane (or plane AA'). Therefore, the symmetric profiles are found till this height. The interaction between the jet bubble and the primary bubble may occur in the region $0.20 \text{ m} < z < 0.25 \text{ m}$. Hence, the solid holdup moves down near $x/R=-1.0$ for a fixed secondary gas flowrate as shown in Figure 4.17a. As $Q_{1,4}$ increases, the solid fraction also increases which shows that the bubble interaction would take place to the jet for the low $Q_{1,4}$ and at the core region for high $Q_{1,4}$. Overall, all the solid hold up profiles are more symmetric than the previous case (with large diameter nozzles).

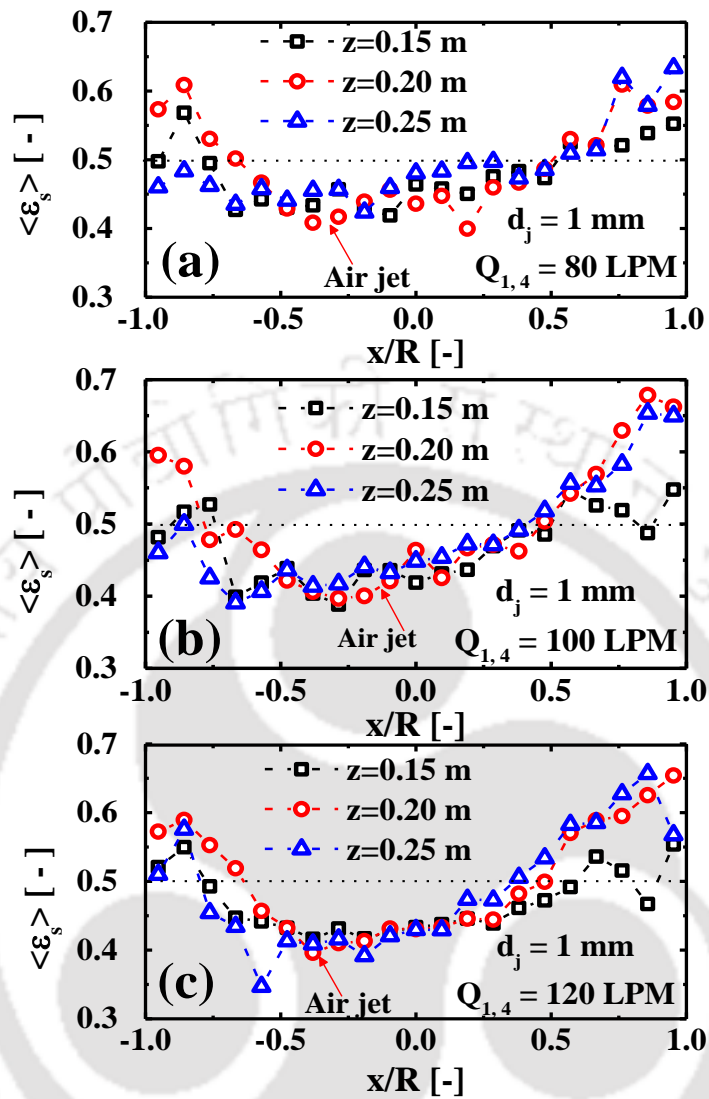


Figure 4.17 GDT data for solids holdup at different axial heights with sidewall injection(s) of small size nozzles ($d_j = 1$ mm) operating at (a) $Q_{1,4} = 80$ LPM, (b) $Q_{1,4} = 100$ LPM, and (c) $Q_{1,4} = 120$ LPM ($H/D_t = 3.57$, $U/U_{mf} = 3.12$, $d_p = 709 \mu\text{m}$)

Comparison between GDT data of same size nozzles injections operating at the different planes

To understand the effect of nozzle diameter, two same size (either 6 mm or 1 mm) nozzles are placed same side at different axial positions (at plane AA' and BB'), and the GDT data are measured at the three different axial height (z) with varying injection flowrate, $Q_{1,4}$. The GDT data is obtained for all three injection flowrates (80, 100 and 120 LPM). Thus, the comparison is shown in Figure 4.18 for $Q_{1,4} = 100$ LPM. These results show the following observations:

- The small diameter nozzle ($d_j = 1$ mm) gives more symmetric distribution than the large-diameter nozzle ($d_j = 6$ mm) below the lower injection plane. The reason for this observation could be the high jet injection velocity and low spray angle of the small size nozzle.
- The small size nozzle provides high solid volume fraction near the wall below the upper injection plane ($z < 0.40$ m or plane BB') as shown in Figure 4.18.

4.3.5. Inclined sidewall injection ($\alpha = -45^\circ$) with a single nozzle at plane AA'

In this section, we investigate the impact of an inclined nozzle, with an angle of -45° to the x-axis, on the solid distribution in the gas fluidized bed. Figure 4.19 shows the solid holdup profiles of chordal averaged data, measured at three different z-planes (0.15, 0.20 and 0.25) of the column with an inclined single sidewall nozzle at $\alpha = -45^\circ$. In this case, the solid holdup reduced from 0.45 to 0.35 at $x/R = -1.0$ as we move up along the height of the bed from a lower plane to the upper plane.

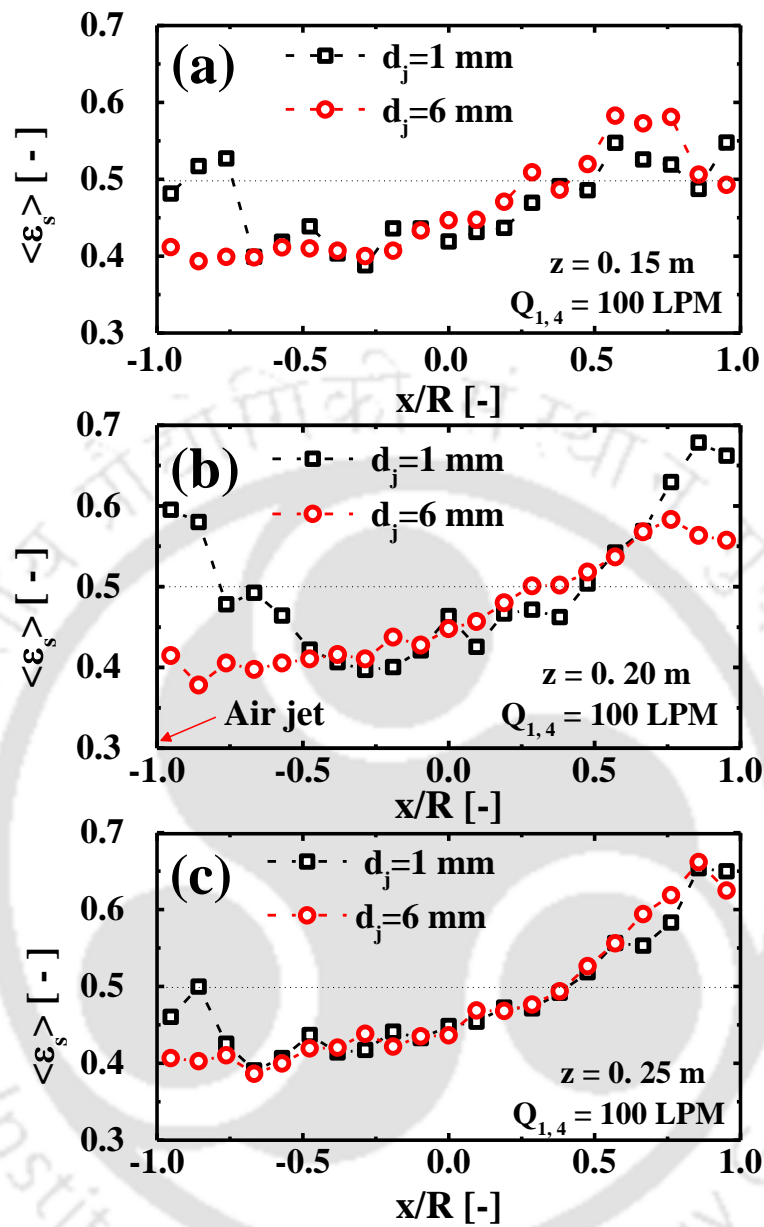


Figure 4.18 Comparison of GDT data for solids holdup for different sizes sidewall injection(s) operating at (a) $z = 0.15\text{ m}$, (b) $z = 0.20\text{ m}$ and (c) $z = 0.25\text{ m}$ ($H/D_t = 3.57$, $U/U_{mf} = 3.12$, $d_p = 709\text{ }\mu\text{m}$)

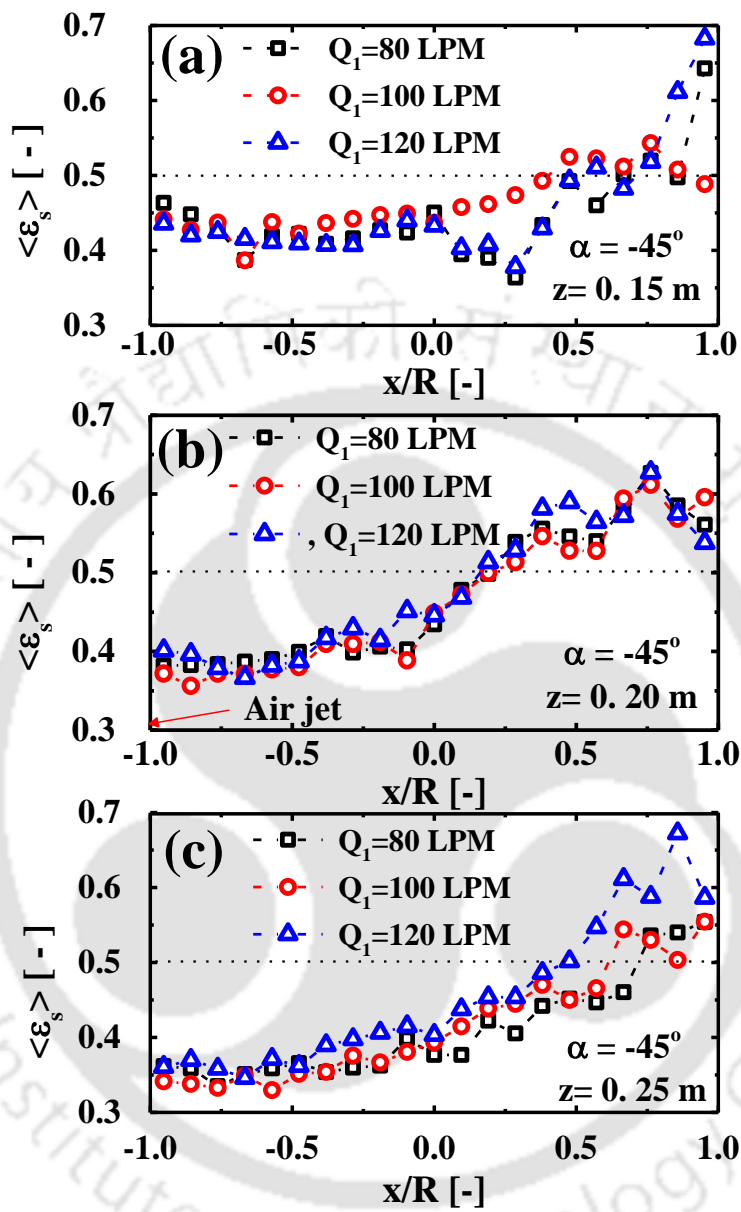


Figure 4.19 GDT data of solids holdup for inclined sidewall injection with single injection operating at (a) $z = 0.15$ m, (b) $z = 0.20$ m and (c) $z = 0.25$ m ($H/D_t = 3.57$, $U/U_{mf} = 3.12$, $d_p = 709 \mu\text{m}$, $d_j = 6$ mm)

Table 4.3 Measured chordal solid holdup with sidewall injection of large size nozzle operated at different flowrates ($H/D_t = 3.57$; $U/U_{mf}=3.12$; $d_p=709 \mu m$)

Experimental Cases	Secondary gas flow rates (LPM)	Chordal Solid Fraction at			
		$z = 0.15 \text{ m}$	$z = 0.20 \text{ m}$	$z = 0.25 \text{ m}$	$z = 0.60 \text{ m}$
No Nozzle	-	0.45	0.43	0.40	0.39
N1 ($d_j = 6 \text{ mm}$)	80	0.45	0.41	0.47	0.37
	100	0.47	0.43	0.45	0.35
	120	0.46	0.43	0.47	0.35
N1, N2 ($d_j = 6 \text{ mm}$)	80	0.48	0.45	0.43	0.35
	100	0.51	0.50	0.40	0.37
	120	0.51	0.46	0.42	0.35
N1, N2, N3 ($d_j = 6 \text{ mm}$)	80	0.29	0.42	0.41	0.36
	100	0.31	0.45	0.42	0.37
	-	-	-	-	-
N1, N4 ($d_j = 6 \text{ mm}$)	80	0.43	0.44	0.47	-
	100	0.46	0.47	0.48	-
	120	0.42	0.41	0.45	-
N1, N5 ($d_j = 6 \text{ mm}$)	80	0.52	0.50	0.45	-
	100	0.51	0.49	0.45	-
	120	0.52	0.51	0.47	-
N1, N6 ($d_j = 6 \text{ mm}$)	80	0.48	0.47	0.45	-
	100	0.51	0.49	0.46	-
	120	0.51	0.51	0.48	-

Table 4.4 Measured chordal solid holdup with sidewall injection of small size nozzle operated at different flowrates ($H/D_t = 3.57$; $U/U_{mf}=3.12$; $d_p=709 \mu m$)

Experimental Cases	Secondary gas flow rates (LPM)	Chordal Solid Fraction at			
		$z = 0.15 \text{ m}$	$z = 0.20 \text{ m}$	$z = 0.25 \text{ m}$	$z = 0.60 \text{ m}$
No Nozzle	-	0.45	0.43	0.40	0.39
N1 ($d_j = 1 \text{ mm}$)	80	0.49	0.49	0.47	-
	100	0.51	0.50	0.45	-
	120	0.51	0.50	0.50	-
N1, N4 ($d_j = 1 \text{ mm}$)	80	0.48	0.49	0.49	-
	100	0.47	0.50	0.48	-
	120	0.46	0.50	0.49	-

Table 4.5 Measured chordal solid holdup with inclined sidewall injection of small size nozzle operated at different flowrates ($H/D_t = 3.57$; $U/U_{mf}=3.12$; $d_p=709 \mu m$)

Experimental Cases	Secondary gas flow rates (LPM)	Chordal Solid Fraction at			
		$z = 0.15 \text{ m}$	$z = 0.20 \text{ m}$	$z = 0.25 \text{ m}$	$z = 0.60 \text{ m}$
No Nozzle	-	0.45	0.43	0.40	0.39
N1 ($d_j = 1 \text{ mm}$)	80	0.45	0.47	0.41	
	100	0.46	0.46	0.42	
	120	0.45	0.48	0.45	

4.4. Summary

The following conclusions are drawn from this work based on horizontal/inclined injections to the fluidized bed through different diameter nozzles:

- In the absence of side injections, the solid distribution profile mainly depends on the fluidization number (U/U_{mf}), aspect ratio (H/D_t) and gas-solid system properties. At a low fluidization number, the radial profile of the solid fraction follows the convex shape. Similarly, at a high fluidization number, the solid fraction distribution gets reversed. Hence, at high fluidization velocity such as (1.12 m/s), all the primary bubble rose up and follow the center zone of the bed.
- The higher solid fraction is observed at a high aspect ratio for the above case.
- In the presence of a single nozzle of large diameter, the solid holdup at $z=0.15$ m is marginally increased by 1-2 % than without nozzle as the secondary gas flowrates are increased in the range of 80-120 LPM. The nozzle plane does not affect in terms of global solid holdup with secondary injection. The solid hold is significantly increased 5-7 % as the Q_1 is increased in the range of 80-120 LPM at $z=0.25$ m. This effect can be seen up to a certain height. Similarly, 2-5 % reduction has been observed at the highest plane (or $z=0.60$ m). Therefore, the secondary gas flowrate Q_1 play a significant role to lower the fluidization quality (Yang et al., 2002; Zhou et al., 2016). Thus it is very important to optimize final product (Wild and Glöckner., 1990).
- In the same case, the solid holdup is increased by 2-6 % at $z=0.15$ m (or lower plane) with operating at the same gas-flow rates through these nozzles (6 mm ID), when operated on the same plane with respect to without side injection. With

increasing z , the solid fraction is still higher than case without nozzle at $z=0.20$ m by 2-7 %. At $z=0.25$ m, the solid availability becomes low than the earlier case with a single nozzle but still high with respect to the. without sidewall injection. Therefore, the high solid fraction at the upper plane (just above the plane AA') is mainly due to the addition of one more side injection, N2 with N1. The introduction of the second nozzle injection may increase the possibility of interaction between the bubbles.

- The solid holdup is increased by 2-6 % at $z=0.15$ m (or lower plane) with operating at the same gas-flow rates through these nozzles (6 mm ID), when operated on the same plane with respect to without side injection. With increasing z , the solid fraction is still higher than without nozzle at $z=0.20$ m by 2-7 %. At $z=0.25$ m, the solid availability becomes low than the earlier case with a single nozzle but still high w. r. t. without sidewall injection. Therefore, the high solid fraction at the upper plane (just above the plane AA') is mainly due to the addition of one more side injection, N2 with N1. The introduction of the second nozzle injection may increase the possibility of interaction between the bubbles.
- The overall solid holdup, measured at the lower plane ($z=0.15$ m) in the presence of three nozzles (6 mm ID), is reduced by an amount of 14-16 % when it is compared with the single nozzle injection (N1). On the other axial planes except for $z=0.15$ m, the overall solid fraction is similar to without sidewall injection
- Among all the cases such as (N1, N4), (N1, N5) and (N1, N6), when two nozzles (6 mm ID) are operated in different planes, case (N1, N4) provides low solid

fraction at the lower planes ($z=0.15$ m, $z=0.20$ m). At the upper height ($z=0.25$ m), a similar solid distribution can be observed.

- Table 4.3 shows that the solid holdup levels off at $z = 0.60$ m for all the cases. With only one injection, the most significant difference is apparent at $z = 0.25$ m; the injected side gas flow rate moves the solid upward close to the injection region and then they levels off. Two injections at the same height increase the solid holdup at the injection plane like hindering the free solid motion above the injection.
- As shown in Table 4.4., single nozzle injection with small diameter nozzle affect the solid distribution significantly and it is increased by 6-9 % at the three different axial planes with respect to without side injection.
- The solid fraction is higher at every axial height of the bed when it is operated with two small size nozzle injections at a different height.
- Table 4.5 shows that the overall solid hold up remains constant at the lower height ($z=0.15$ m) with and without secondary injection for the inclined downward injection ($\alpha = -45^\circ$). At the injection plane, a marginal increment of 3-5 %, has been noticed in the solid holdup compared to the without secondary injection.

Notations

Cs	Cesium -137 radioactive source	
d_j	Nozzle jet diameter	[mm]
d_p	Particle diameter	[μm]
D_t	Bed diameter	[m]
H	Packed bed height	[m]
H_0	Initial packed bed height	[m]
I	Intensity of transmitted gamma ray	[photon. $\text{m}^{-2}\text{s}^{-1}$]
I_1		
N1, N2, N3	ID number of three nozzles placed at plane AA' or $z=0.20$ m	[-]
N4, N5, N6	ID number of three nozzles placed at plane BB' or $z=0.40$ m	[-]
Q_j	Secondary injection flowrate of nozzle with index 'j'	[LPM]
R	Column radius	[m]
U_{mf}	Minimum fluidization velocity	[m s^{-1}]
U, U_0	Fluidization velocity	[m s^{-1}]
W_s	Solid loading	[kg]
x, y, z	Cartesian coordinates	[m]

Greek Symbols

α	Angle between injection line and x-axis	[$^\circ$ or degree]
$\mu_{s,N}$	Linear attenuation coefficient of solid phase along chord N	[m^{-1}]
ρ_p	Particle density	[kg m^{-3}]
ρ_f		

$\bar{\varepsilon}_{s,static}$	Scaling factor	[-]
$\langle \varepsilon_{s,N} \rangle$	Measured chordal averaged solid hold up along chord N	[-]

Subscript

G, S, GS	Gas, solid and gas-solid phase system, respectively
p	Particle phase

Abbreviations

CFD	Computational fluid dynamics
FN	Fluidization number (U/U_{mf})
GDT	Gamma-ray densitometry technique
ID	Internal diameter
LPM	Liter per minute
PP	Perforated plate
RPT	Radioactive particle tracking

References

- Anthony, E. J., Lu, D. Y. 2001. Proc. 16th FBC Conference. FBC01-0093
- Barker, D., Beacham, B. 1980. Proceedings of the Inst. of Fuel Intern. Conf. London p. I.A.-3.
- Benjelloun, F., Liegeois, R., Vanderschuren, J., 1995. Penetration length of horizontal gas jets into atmospheric fluidized beds. In: Large, J.F., Laguerie, C. (Eds.), Fluidization VIII:

- Proceedings of the Eighth Engineering, Foundation Conference on Fluidization, May 14–19, 1995. Tours, France, 239–24
- Bhowmick, S., Sharma, V.K., Samantray, J.S., Pant, H.J., Shenoy, K.T., Dash, A., Roy, S.B., 2015. Experimental Investigation on Interaction of Side Gas Injection with Gas Fluidized Bed Using γ -ray Transmission Technique. *Ind. Eng. Chem. Res.* 54, 11653–11660.
- Bjorklund, W. J., Offutt, G. F., 1973. *AIChE Symp. Ser.* 69(128), 123.
- Chen, L.B., Weinstein, H., 1993. Shape and extent of the void formed by a horizontal jet in a fluidized-bed. *AIChE J.* 39, 1901–1909.
- Chyang, C.S., Chang, C.H., Chang, J.H., 1997. Gas discharge modes at a single horizontal nozzle in a two-dimensional fluidized bed. *Powder Technol.* 90, 71–77.
- Fane, A. G., 1974. The kinetics of hydrogen reduction of UO_3 and U_3O_8 derived from ammonium diuranate. *J Inorg. Nucl. Chem.* 36, 1, 87-92.
- Koeninger, B., Hensler, T., Schug, S., Arlt, W., Wirth, K.E., 2017. Horizontal secondary gas injection in fluidized beds: Solid concentration and velocity in multiphase jets. *Powder Technol.* 316, 49–58.
- Koeninger, B., Koegl, T., Hensler, T., Arlt, W., Wirth, K.E., 2018. Solid distribution in fluidized and fixed beds with horizontal high speed gas jets. *Powder Technol.* 336, 57–69.
- Kunni, D., Levenspiel, O., 1991. *Fluidization Engineering*, 2nd Ed., Butterworth-Heinmann, USA.
- Kozin, V.E., Baskakov, A.P., 1967. *Khim i Tekhnol. Topliv i Masel.* 3, 4.
- Lummi, A.P., Baskakov, A.P., 1967. *Khim. Prom.* 43, 522.

- Okasha, F. M., El-Emam, S. H., Mostafa, H. K., 2003. The fluidized bed combustion of a heavy liquid fuel. *Exp. Therm. Fluid Sci.*, 27 (4), 473-480.
- Sridhar, T. S., 1986. Performance of a fluidized bed calciner for the calcination of metal nitrate wastes. *Nucl. Chem. Waste Man.* 6(1), 51-60.
- Wild, L., Glöckner, G., 1990. Temperature rising elution fractionation. In *Separation techniques thermodynamics liquid crystal polymers*. Springer, 1–47.
- Wilson, J. W. 1997. *Fluid Catalytic Cracking Technology and Operations*. Tulsa, Okla: Penn Well Books.
- Yang, Y. R., Yang, J. Q., Chen, W., Rong, S. X. 2002. Instability analysis of the fluidized bed for ethylene polymerization with condensed mode operation. *Ind. Eng. Chem. Res.*, 41, 2579–2584.
- Zenz, F.A., 1968. Bubble formation and grid design. I. *Chem. E. Symp. Ser.* 30, 136–139.
- Zhou, Y., Shi, Q., Huang, Z., Liao, Z., Wang, J., & Yang, Y. 2016. Realization and control of multiple temperature zones in liquid-containing gas–solid fluidized bed reactor. *AIChE J.*, 62, 1454–1466.

Chapter 5 Conclusions and Future Work

Scope

In all the previous chapters, a detailed summary and research outcomes were presented in respective chapters. In this chapter, the broader concluding remarks of the present thesis and recommendations for future work are highlighted.

5.1. Summary

The overall aim of the current thesis is to understand the solid flow behavior in a sidewall nozzle assisted gas-solid fluidized bed. The work has three different aspects. The first aspect is to implement the radioactive particle tracking technique in a nozzle assisted gas-solid fluidized bed. To the best of my knowledge, no such literature is available which shows the implementation of RPT in such a dynamic and asymmetric reactor configuration. Further, the local velocity at the nozzle injection point in current case is very high which poses the problem in reconstruction of the tracer particle when it is close to the sidewall nozzle injection point. The current work provides the methodology to handle such bed and presented the detailed velocity flow field of the solids in sidewall nozzle assisted gas-solid fluidized bed. To the best this is the first work in which detailed solid flow behavior in a sidewall nozzle assisted gas-solid fluidized bed is studied.

The second aspect of the work is to perform the dRPT experiments in sidewall nozzle injected fluidized bed and decipher the complex flow physics for a single and multiple nozzle injection systems. Being critically important from decades, the detailed characterization of sidewall nozzle assisted fluidized bed is still not achieved and most of

the literature on such fluidized bed presents the data based on time-averaged quantities or develop correlations to predict jet penetration length or distribution of solid in the bed. To the best of my knowledge, this is the first of its kind work where detailed flow behavior of sidewall nozzle assisted fluidized bed is studied with state-of-the-art non-invasive measurement techniques.

The third aspect of the work is to study the solid distribution profile inside the nozzle assisted gas-solid fluidized bed. To the best of my knowledge, only two work are reported in the literature on the solid distribution inside a sidewall nozzle assisted gas-solid fluidized bed. However, these data are for single nozzle injection. This is the first time the solid distribution study is performed for multiple nozzle system. The nozzle in this study are placed at same and different axial plane(s) to show how the secondary injection affect the overall flow field. This data obtained are quite important for scale-up studies and high throughput systems where multiple nozzles at the same and different axial planes will be used. Therefore, the work conducted in the current thesis is quite important and novel. The specific conclusions of each chapter are individually given at the end of the chapter. This chapter is intended to summarize the overall conclusion of the key findings. The broader conclusions of the current thesis are as follows:

- RPT experiments are successfully implemented in a sidewall nozzle assisted gas-solid fluidized bed. For a single nozzle case, it is found that the primary gas injected from the bottom of the column through distributor start migrating towards the nozzle injection wall from the bottom of the column due to the low pressure zone created at the nozzle injection site. This leads to the asymmetric solid velocity fields

in the nozzle injection plane and a single circulation cell is observed. The solids move upward at nozzle injection wall and downwards through the opposite wall.

- The azimuthal average velocity fields shows the two circulation cells as observed in the conventional gas-solid fluidized bed. Hence, it can be stated that the secondary gas injection through sidewall nozzle affects the local dynamics. However, the global dynamics remains unchanged. Hence, for better design and scaleup of such beds, local dynamics should be taken into account as measurement of global flow field may lead to erroneous results.
- It is observed that for single nozzle case solid velocity increases as we move up in the bed, and the lateral profile along the injection path becomes more asymmetric due to the higher velocity at the nozzle injection wall. This suggest the formation of bigger gas bubbles due to the interaction of primary gas bubbles with the nozzle injected gas. This may lead to the severe bypassing. Further, it is observed that for single nozzle case such interaction takes place just below the nozzle injection plane.
- Significant radial solid velocity is observed in case of sidewall nozzle assisted gas-solid fluidized bed which is contrary to the conventional gas-solid fluidized bed. This shows that both axial and radial motion play important role in determining the local hydrodynamics. However, in azimuthal average axial velocity is dominating. This shows motion is primarily in axial direction.
- The effect of nozzle diameter and nozzle injection velocity are also investigated through GDT and RPT measurements. When the injection occurs through a lower diameter nozzle into the fluidized bed, the jet penetrates deep into the bed. Therefore, it brings more solid to the core region and promotes solids circulations.

High injection flowrates and deep penetration depth cause slug motion within the bed which will result in low heat and mass transfer inside the bed.

- The effect of multiple side air injections through a set of nozzles operating on the same plane is studied using RPT and GDT. It is observed that multiple nozzle placed at the same plane worsen the situation. The gases injected through sidewall nozzles interact with the primary gas bubble and forms bigger bubbles which lead to the slug flow. Further, the asymmetric nature of solid flow field is also observed in case of two nozzle injection at the same plane separated by 120° angle. The results of multiple nozzles shows that it is not a 'good' idea to place the multiple nozzle at the same plane; instead the in case of multiple nozzle system the nozzles should be placed at different axial locations. This is established by the GDT experiments.
- It is also shown through GDT experiments that two air injections operating at the different planes at the same azimuthal position (or same side) enhance the bypassing of the injected gas. Hence, two nozzles operating on the two different axial levels with different angular position could be a better option to avoid slug formation and bypassing of injected air.
- The current work shows that sidewall nozzle injection significantly changes the solid flowfield inside the bed even though the nozzle injection flow rate is significantly lower than the primary injected gas flow rate. Further, in case of multiple nozzle system it is found that nozzle should be placed at different axial locations and should be staggered. The 120° staggering is used in this work which shows encouraging results. The nozzle can also be incline at 45° downward to

achieve the better results and avoid the formation of bigger bubbles at nozzle injection plane. However, this may lead to multiple circulation cells in the bed.

5.2. Future Work

The key research topics for future direction on side nozzle injection and bed interactions are as follows:

- In the current work experiments are performed for secondary gas injection through sidewall nozzle(s) with group B particle. It would be interesting to see the effect of sidewall nozzle injection in Group A particles which are more aerable. Further, effect of solid height in the bed, effect of primary gas flowrate and size of the particle can also be studied in future to develop a comprehensive understanding.
- The current experiments are performed in a fixed diameter system. The column diameter will significantly affect the overall dynamics as the penetration depth to column diameter ratio will be higher for smaller column and will be lower for bigger column. Therefore, in future, effect of column diameter on solid flow field can be studied for the sidewall nozzle injection system. Further, such work will also help in developing the scalup methodology for such systems.
- The current work is performed for a mono dispersed bed. However, in practical situation there is always a poly dispersed bed which may have distribution in size and/or density. Therefore, it is critical to estimate the effect of sidewall nozzle injection in a binary/poly dispersed bed.
- In the current work, the impact of nozzle injection(s) on agglomeration and breakage of solids in a fluidized bed are not studied. The agglomeration plays an

important role in many industries including fluid cocking and coating processes. The high injection flowrate generate high shear which can break the bed particle and can also cause agglomeration. Therefore, a study can be performed to find the effect of the same.

- Many industries such as the thermal denitration process involve the phase change during the introduction of nitrate reactant through nozzle injection into the fluid cocker. As soon as the reactant falls over the hot silica catalyst, it starts to vaporize and hence phase change occurs. Therefore, it is important to study the effect of twin fluid injection through the sidewall nozzle in which one phase may change after the injection. This will be quite complex and involved study but the data will be quite useful for the real industrial problem.
- The effect of bed temperature on the sidewall nozzle injection system can also be studied for secondary gas as well as twin fluid nozzle injection system. Further a detailed computational model can be developed for high temperature phase change system.
- In the current work effort is made to develop an Euler-Euler model for the sidewall nozzle injection system which is presented in Appendix A. In the similar line a detailed Euler-Euler model can be developed where effect of different closure models can be studied.
- A detailed Discrete element based computational fluid dynamics model can also be developed for the studied sidewall nozzle injection system. The model data can be validated by the existing results to develop the detailed understanding of the underline flow physics.

Appendix A. CFD Modelling of Gas-Solid Fluidized Beds with Single Side Injection

Scope

Computational fluid dynamics (CFD) modelling of gas-solid fluidized bed with a single nozzle is carried out for the validation of experimental results. The computational fluid dynamics with two-fluid model (TFM) simulation is presented in this appendix. A state of the art available on CFD modelling of fluidized beds with side injection is also introduced. Finally, a 3D model of experimental set up is created, meshed and simulated. The suitability of the numerical model (custom and in-built) depends on several simulation parameters which include grid independency, optimal boundary conditions, suitable viscous model and other interaction parameters (specularity coefficients, restitution coefficients). Hence, an attempt has been made to predict the fluidization behavior and flow information of the solid phase with a single sidewall nozzle injection.

A. 1. Introduction

In gas-solid flow systems, two numerical approaches have been used to predict the flow dynamics in the past for several decades. These are (i) Lagrangian and (ii) Eulerian. The basic concepts of these two approaches have been explained and reviewed by Crowe (1982). In Eulerian approach, both the phases (dispersed and continuous) flow are treated as a continuum, and all the phases are interpenetrating in nature (Crowe, 1982; 1986). It is also reported that the continuum model or two-fluid model (TFM) is applicable to low Stoke numbers and a high loading system (Crowe, 1986). The discrete (or particle) phase

concentration and momentum equations are also governed in a similar manner as the continuous phase. The two-fluid model (TFM) is adopted in the present case, as it requires less computational resources. The system is assumed to be isothermal. The gas phase is treated as an incompressible fluid. The hydrodynamic model equations, governing the conservation of mass for the individual phases: the solid phase and gas phase, are given below:

$$\frac{\partial(\varepsilon_s \rho_s)}{\partial t} + \nabla \cdot (\varepsilon_s \rho_s \vec{U}_s) = S_s \quad (\text{A.1})$$

$$\frac{\partial(\varepsilon_g \rho_g)}{\partial t} + \nabla \cdot (\varepsilon_g \rho_g \vec{U}_g) = S_g \quad (\text{A.2})$$

The subscripts g, s denote gas and solids phases, respectively; ε is volume fraction satisfying the relation: $\varepsilon_g + \varepsilon_s = 1$. The first two terms on the left sides (in Equation A.1 and A.2) are the rate of mass accumulation per unit volume and net rate mass flux due to convection. The only term on the right-hand side is the source term accounting for the mass transfer between the phase due to chemical reaction or phase change, such as condensation and evaporation. In the present case, S_s and S_g both are set to zero.

The conservation of momentum equations for gas and solids phases are represented by the following equations:

$$\frac{\partial(\varepsilon_s \rho_s \vec{U}_s)}{\partial t} + \nabla \cdot (\varepsilon_s \rho_s \vec{U}_s \vec{U}_s) = \nabla \cdot \vec{\sigma}_s - \varepsilon_s \nabla P_s + \varepsilon_s \rho_s \vec{g} + \vec{I}_{gs} \quad (\text{A.3})$$

$$\frac{\partial(\varepsilon_g \rho_g \vec{U}_g)}{\partial t} + \nabla \cdot (\varepsilon_g \rho_g \vec{U}_g \vec{U}_g) = \nabla \cdot \vec{\tau}_g - \varepsilon_g \nabla P_g + \varepsilon_g \rho_g \vec{g} + \vec{I}_{sg} \quad (\text{A.4})$$

Where, P_g is gas-phase pressure; \vec{g} is the acceleration due to gravity; \vec{I}_{sg} is the momentum transfer due to interphase forces e.g. drag force; $\vec{\sigma}_s$ and $\vec{\tau}_g$ are the stress tensor of the solid and gas phases respectively.

A.1.1. Constitutive Equations

Interphase-Momentum Transfer

The interphase momentum exchange \vec{I}_{sg} term in equation (A.3) and (A.4) account for the effects of drag, Saffmann lift, virtual mass, Basset force and Magnus force etc. (Fan and Zhu, 1998). For dense gas-solid flows ($\rho_s / \rho_g \gg 1$), the drag force has a dominant effect on the flow behavior. The interphase momentum exchange is represented by β_{gs} times the slip velocity $(\vec{U}_g - \vec{U}_s)$ between the phases and given by the following equation:

$$I_{gs} = -I_{sg} = \beta_{gs}(\vec{U}_g - \vec{U}_s) \quad (\text{A.5})$$

where β_{gs} is the coefficient of interphase momentum transfer. The Gidaspow drag model which is widely used in most CFD simulations of the gas-solid system is given by Gidaspow (1994) as follows:

$$\beta_{gs} = \begin{cases} 150 \frac{\varepsilon_s(1-\varepsilon_g)\mu_g}{\varepsilon_g d_s^2} + 1.75 \frac{\varepsilon_s \varepsilon_g \rho_g |\vec{U}_s - \vec{U}_g|}{d_s} & \varepsilon_g < 0.8 \\ \frac{3}{4} C_D \varepsilon_g^{-2.65} \frac{\varepsilon_s \varepsilon_g \rho_g |\vec{U}_s - \vec{U}_g|}{d_s} & \varepsilon_g > 0.8 \end{cases} \quad (\text{A.6})$$

Where,

$$C_D = \begin{cases} \frac{24}{\text{Re}_s} (1 + 0.15 \cdot \text{Re}^{0.687}) & \text{Re} < 1000 \\ 0.44 & \text{Re} > 1000 \end{cases} \quad (\text{A.7})$$

$$\text{Re} = \frac{\varepsilon_g \rho_g |\vec{U}_s - \vec{U}_g| d_s}{\mu_g} \quad (\text{A.8})$$

In the literature, several drag models have been developed to evaluate the interphase momentum exchange coefficients (Wen and Yu, 1966; Syamlal et al., 1993; Gidaspow, 1994; Gibilaro, 2001; Hill et al., 2001; Benyahia et al., 2006), and some of them are listed in Table A.1.

Table A-1 Summary of the models used in the gas-solid fluidized bed

Wen and Yu (1966):

$$\beta_{gs} = \frac{3}{4} C_D \varepsilon_g^{-2.65} \frac{\varepsilon_s \varepsilon_g \rho_g |\vec{U}_s - \vec{U}_g|}{d_s}$$

$$C_D = \begin{cases} \frac{24}{\text{Re}_s} (1 + 0.15 \cdot \text{Re}^{0.687}) & \text{Re} < 1000 \\ 0.44 & \text{Re} > 1000 \end{cases}$$

Gidaspow (1994):

$$\beta_{gs} = \begin{cases} 150 \frac{\varepsilon_s (1 - \varepsilon_g) \mu_g}{\varepsilon_g d_s^2} + 1.75 \frac{\varepsilon_s \varepsilon_g \rho_g |\vec{U}_s - \vec{U}_g|}{d_s} & \varepsilon_g < 0.8 \\ \frac{3}{4} C_D \varepsilon_g^{-2.65} \frac{\varepsilon_s \varepsilon_g \rho_g |\vec{U}_s - \vec{U}_g|}{d_s} & \varepsilon_g > 0.8 \end{cases}$$

$$C_D = \begin{cases} \frac{24}{\text{Re}_s} (1 + 0.15 \cdot \text{Re}^{0.687}) & \text{Re} < 1000 \\ 0.44 & \text{Re} > 1000 \end{cases}$$

$$\text{Re} = \frac{\varepsilon_g \rho_g |\vec{U}_s - \vec{U}_g| d_s}{\mu_g}$$

Hulin and Gidaspow (2003):

$$\beta_{gs} = \omega \left(150 \frac{\varepsilon_s (1 - \varepsilon_g) \mu_g}{\varepsilon_g d_s^2} + 1.75 \frac{\varepsilon_s \varepsilon_g \rho_g |\vec{U}_s - \vec{U}_g|}{d_s} \right) + (1 - \omega) \left(\frac{3}{4} C_D \varepsilon_g^{-2.65} \frac{\varepsilon_s \varepsilon_g \rho_g |\vec{U}_s - \vec{U}_g|}{d_s} \right)$$

$$\omega = \frac{1}{2} + \frac{\tan^{-1}[262.5(\varepsilon_s - 0.2)]}{\pi}$$

Syamlal and O'Brien (1989):

$$\beta_{gs} = \frac{3}{4} C_D \frac{\varepsilon_s \varepsilon_g \rho_g |\vec{U}_s - \vec{U}_g|}{d_s V_r^2}$$

$$C_D = \left(0.63 + 4.8 \sqrt{\frac{V_r}{\text{Re}}} \right)^2$$

$$V_r = 0.5 \left[a - 0.06 \text{Re} + \sqrt{(0.06 \text{Re})^2 + 0.12 \text{Re}(2b - a) + a^2} \right]$$

$$a = \varepsilon_g^{4.14}$$

$$b = \begin{cases} P \varepsilon_g^{1.28} & \varepsilon_g \leq 0.85 \\ \varepsilon_g^Q & \varepsilon_g > 0.85 \end{cases}$$

$$P = 0.8 \text{ and } Q = 2.65$$

Gibilaro (2001):

$$\beta_{gs} = \left(\frac{17.3}{\text{Re}} + 0.336 \right) \frac{\rho_g |\vec{U}_s - \vec{U}_g|}{d_s} \varepsilon_s \varepsilon_g^{-1.8}$$

Modified Hill-Koch-Ladd drag model (Benyahia et al., 2006):

$$\beta_{gs} = 18 \mu_g (1 - \varepsilon_s)^2 \varepsilon_s \frac{F}{d_s^2}$$

$$F = \begin{cases} 1 + 0.375 \text{Re}' & \varepsilon_s \leq 0.01; \text{Re}' \leq \frac{F_2 - 1}{0.375 - F_3} \\ F_0 + F_1 (\text{Re}')^2 & \varepsilon_s > 0.01; \text{Re}' \leq \frac{F_3 + \sqrt{F_3^2 - 4F_1(F_0 - F_2)}}{2F_1} \\ F_2 + F_3 \text{Re}' & \begin{cases} \varepsilon_s \leq 0.01; \text{Re}' > \frac{F_2 - 1}{0.375 - F_3} \\ \varepsilon_s > 0.01; \text{Re}' > \frac{F_3 + \sqrt{F_3^2 - 4F_1(F_0 - F_2)}}{2F_1} \end{cases} \end{cases}$$

$$F_0 = \begin{cases} (1-w) \frac{1 + 3\sqrt{0.5\varepsilon_s} + 2.11\varepsilon_s \ln(\varepsilon_s) + 17.14\varepsilon_s}{1 + 0.681\varepsilon_s - 8.48\varepsilon_s^2 + 8.1\varepsilon_s^3} + w \frac{10\varepsilon_s}{\varepsilon_g^3} & 0.01 < \varepsilon_s < 0.4 \\ \frac{10\varepsilon_s}{\varepsilon_g^3} & \varepsilon_s \geq 0.4 \end{cases}$$

$$F_1 = \begin{cases} \frac{\sqrt{0.5\varepsilon_s}}{40} & 0.01 \leq \varepsilon_s \leq 0.1 \\ 0.11 + 0.00051 \exp(11.6\varepsilon_s) & \varepsilon_s > 0.1 \end{cases}$$

$$F_2 = \begin{cases} (1-w) \frac{1 + 3\sqrt{0.5\varepsilon_s} + 2.11\varepsilon_s \ln(\varepsilon_s) + 17.89\varepsilon_s}{1 + 0.681\varepsilon_s - 11.03\varepsilon_s^2 + 15.41\varepsilon_s^3} + w \frac{10\varepsilon_s}{\varepsilon_g^3} & \varepsilon_s < 0.4 \\ \frac{10\varepsilon_s}{\varepsilon_g^3} & \varepsilon_s \geq 0.4 \end{cases}$$

$$F_3 = \begin{cases} 0.935\varepsilon_s + 0.03667 & \varepsilon_s < 0.0953 \\ 0.0673 + 0.212\varepsilon_s + \frac{0.0232}{\varepsilon_g^5} & \varepsilon_s \geq 0.0953 \end{cases}$$

$$w = e^{\frac{-10(0.4 - \varepsilon_s)}{\varepsilon_s}}$$

$$\text{Re}' = \frac{\varepsilon_g \rho_g |\vec{U}_s - \vec{U}_g| d_s}{2\mu_g}$$

Viscous Model

In a two-phase flow, the nature of flow in the system determines the applicability of different viscous models (laminar or turbulent) available in commercial CFD software. In multiple applications such as bubbling fluidized bed, the gas-solid flow is dense flow by nature. In such a flow, the particle-particle collision becomes more important (Crowe et al., 1996). Hence, the particle-particle collision can be modeled as the kinetic theory of granular flow or KTGF (Gidaspow, 1994). It has been reported that dense particles minimize the effect of turbulence of the continuous phase due to its inertial effect, and can be ignored in such flow system (Enwald et al., 1996; Portela and Oliemans, 2006). In dilute gas-solid flow, the fluid-solid interaction becomes important. Therefore, the turbulence effect of the continuous phase cannot be ignored (Reeks, 1991; Xu and Subramaniam, 2006). In this chapter, the laminar model is used.

Particle-Particle Interaction Model

The granular temperature of solids as discussed in chapters 3, is derived from the KTGF model (Gidaspow, 1994) that is analogous to the kinetic theory of gases. The governing equation of granular temperature is as follows:

$$\frac{3}{2} \left[\frac{\partial(\epsilon_s \rho_s \Theta_s)}{\partial t} + \nabla \cdot (\epsilon_s \rho_s \vec{U}_s \Theta_s) \right] = \left(-\mathbf{P}_{s,vis} \bar{\mathbf{I}} + \bar{\boldsymbol{\tau}}_{p,vis} \right) : \nabla \vec{U}_s + \nabla \cdot (k_s \nabla \Theta_s) - \gamma_\Theta + \phi_{gs} \quad (\text{A.9})$$

The right-hand side term of equation (A.9) consists of four different terms: first term is for generation of granular energy; the second term represents the diffusion; the third term is accounted for dissipation energy and the fourth term is accounted for energy exchange between the gas and solid phase. The equation (A.9) is a partial differential equation and it requires high computational resource to solve. Therefore, the convection and diffusion

terms were neglected with no energy exchange between gas and solid phase and proposed into the following equation as:

$$(-P_{S,vis} \bar{I} + \bar{\tau}_{P,vis}) : \nabla \bar{U}_S - \gamma_{\Theta} = 0 \quad (\text{A.10})$$

Further, it is simplified into an algebraic equation (Syamlal et al.,1993) as given below:

$$\Theta_s = \left[\frac{-(K_1 \varepsilon_s + \rho_s) Tr(\bar{D}_s)}{2K_4 \varepsilon_s} + \frac{\sqrt{(K_1 \varepsilon_s + \rho_s)^2 Tr^2(\bar{D}_s) + 4K_4 \varepsilon_s [2K_3 Tr(\bar{D}_s^2) + K_2 Tr^2(\bar{D}_s)]}}{2K_4 \varepsilon_s} \right]^2 \quad (\text{A.11})$$

Where, \bar{D}_s = deformation tensor

$$K_1 = 2(1 - e_s) \rho_s g_{0,s} \quad (\text{A.12})$$

$$K_2 = \frac{4}{3\sqrt{\pi}} d_s \rho_s (1 + e_s) g_{0,s} \varepsilon_s - \frac{2}{3} K_3 \quad (\text{A.13})$$

$$K_3 = \frac{d_s \rho_s}{2} \left[\frac{\sqrt{\pi}}{3(3 - e_s)} \left\{ 1 + \frac{2}{5} (1 + e_s) (3e_s - 1) g_{0,s} \varepsilon_s \right\} + \frac{8\varepsilon_s}{5\sqrt{\pi}} g_{0,s} (1 + e_s) \right] \quad (\text{A.14})$$

$$K_4 = \frac{12(1 - e_s^2) \rho_s g_{0,s}}{d_s \sqrt{\pi}} \quad (\text{A.15})$$

Solid Stress

For gas-solid flow with high solid concentrations $\varepsilon_s > 0.5$, the surface friction becomes more important. Limited theoretical models are available to represent the frictional flow regime which is in between two limiting flow regimes: rapid flow regime and quasi-static flow regime. Savage (1983) presented the expression for the total solid stress $\bar{\sigma}_s$ as follows:

$$\bar{\sigma}_s = \bar{\sigma}_{S,vis} + \bar{\sigma}_{S,fric} \quad (\text{A.16})$$

Where, $\bar{\sigma}_S$, $\bar{\sigma}_{S,vis}$ and $\bar{\sigma}_{S,fric}$ are the total solid stress, viscous stress from the kinetic model of granular flow and frictional stress, respectively. The constitutive equations to model $\bar{\sigma}_{S,vis}$ and $\bar{\sigma}_{S,fric}$ are presented in Table A.2.



Table A-2 Constitutive equations used in momentum equations

Solid Pressure

Anderson and Jackson (1969):

$$P_{s,vis} = \varepsilon_s \rho_s \Theta_s (1 + 2\varepsilon_s g_{0,s} (1 + e_s))$$

Gidaspow (1994):

$$g_{0,s} = \frac{3}{5} \left[1 - \left(\frac{\varepsilon_s}{\varepsilon_{s,max}} \right)^{\frac{1}{3}} \right]^{-1}$$

Lun and Savage (1985):

$$g_{0,s} = \left[1 - \left(\frac{\varepsilon_s}{\varepsilon_{s,max}} \right)^{\frac{1}{3}} \right]^{-1}$$

Solid stress: Kinetic model

$$\overline{\sigma}_{s,vis} = -\overline{P}_{s,vis} \overline{I} + \overline{\tau}_{s,vis}$$

$$\overline{\tau}_{s,vis} = \mu_s \left[\nabla \overline{U}_s + (\nabla \overline{U}_s)^T \right] + \left(\lambda_s - \frac{2}{3} \mu_s \right) \overline{I} \cdot \nabla \cdot \overline{U}_s$$

Gidaspow (1994):

$$\mu_s = \frac{4}{5} \varepsilon_s^2 \rho_s d_s g_{0,s} (1 + e_s) \sqrt{\frac{\Theta_s}{\pi}} + \frac{5\sqrt{\pi}}{48} \rho_s d_s \sqrt{\Theta_s} \left[1 + \frac{4}{5} g_{0,s} \varepsilon_s (1 + e_s) \right]^2$$

Lun et al. (1984):

$$\lambda_s = \frac{4}{3} \varepsilon_s^2 \rho_s d_s g_{0,s} (1 + e_s) \sqrt{\frac{\Theta_s}{\pi}}$$

Solid stress: Frictional model

Schaeffer (1987):

$$\bar{\sigma}_{S,fric} = -P_{S,fric} \left(\bar{I} - \frac{\sin \phi}{\sqrt{I_{2D}}} \bar{D}_S \right)$$

$$\bar{D}_S = \frac{1}{2} \left(\nabla \vec{U}_S + (\nabla \vec{U}_S)^T \right)$$

$$I_{2D} = \frac{1}{6} \left[(D_{S,11} - D_{S,22})^2 + (D_{S,22} - D_{S,33})^2 + (D_{S,33} - D_{S,11})^2 + D_{S,12}^2 + D_{S,23}^2 + D_{S,31}^2 \right]$$

$$\mu_{fric} = \frac{P_{S,fric} \sin \phi}{\sqrt{I_{2D}}}$$

Johnson et al. (1990):

$$P_{S,fric} = \begin{cases} 0 & \varepsilon_S < \varepsilon_{S,min} \\ Fr \frac{(\varepsilon_S - \varepsilon_{S,min})^n}{(\varepsilon_{S,max} - \varepsilon_S)^p} & \varepsilon_S \geq \varepsilon_{S,min} \end{cases} ;$$

Fr=0.005, n=2, p=5 and $\varepsilon_{S,min} = 0$

Diffusion Coefficients

Gidaspow (1994):

$$k_{s,\Theta} = \frac{150\rho_S d_S \sqrt{\Theta_S \pi}}{384(1+e_S)g_{0,S}} \left[1 + \frac{6}{5} \varepsilon_S g_{0,S} (1+e_S) \right]^2 + 2\rho_S g_{0,S} (1+e_S) \sqrt{\frac{\Theta_S}{\pi}}$$

Dissipation of granular energy

Lun et al. (1984)

$$\lambda_S = \frac{12(1-e_S^2)g_{0,S}}{d_S \sqrt{\pi}} \rho_S \varepsilon_S^2 \Theta_S^{\frac{3}{2}}$$

Energy exchange between phase

Gidaspow (1994):

$$\phi_{gs} = -3\beta_{gs}\Theta_s$$

In the present case, the simplified version of equation (A.10) i.e. algebraic equation is used which retains only generation (first term of RHS) and dissipation (third term of RHS) terms and neglecting all other terms. Finally, the constitutive equation for solid pressure, solid stresses are highlighted in Table A.3. The algebraic equation for granular temperature is given as follows (Syamlal et al., 1993):

Modelling of dense particle-flows in gas-fluidized bed with single sidewall injection is a main research area of industrial applications. It has been observed that the Eulerian approach is most popular and efficient with low computational resource. Therefore, it is significantly used in the industrial scale. It has been used by other researchers in gas-fluidized beds as presented in Table A.3. In this chapter, Eulerian-Eulerian (EE) models as described above are used in simulating gas-fluidized bed with single nozzle injection. The predictions are further used for validating the experimental data as obtained from GDT and RPT measurements.

Table A.3 Summary of literature available on horizontal nozzle injection in the gas-solid fluidized bed

Investigators	System Details	CFD Application Used	Investigated parameters	Conclusive Remarks
Li et al. (2010b)	Commercial-scale gasifier in 2D; $D_c = 1.6$ m; $L_c = 50$ m;	MFIX (2.4 million cells); EE model	Coal jet penetration was investigated using the contour plots of gas volume fraction at three different axial heights	The effect of grid size and numerical discretization scheme on flow behavior were studied and the following conclusions are observed. <ul style="list-style-type: none"> ▪ The higher-order scheme is desired in such an application. ▪ Depending on computational capabilities, the medium grid can be used rather than the fine grid.
Gerber et al. (2010)	$D_{\text{bubbling-bed}} = 95$ mm; $D_{\text{free-board}} = 134$ mm; $H_{\text{char}} = 30-40$ cm; $D_{\text{fuel-inlet}} = 50$ mm	MFIX-TFM (2D setup with $\Delta x = 0.7$ & $\Delta y = 0.71$ cm)	EE simulation of wood pyrolysis and char gasification were performed and compared with experimental data (product gas concentration & temperature).	This study had shown that bed temperature is a very critical and influential parameter. The packed bed height and throughput have minimum influence on product gas concentration.

Pannala et al. (2006, 2007)	Spouted beds	2D & 3D MFIx-TFM	The key experimental observations such as solids circulation and spout formation were also captured by simulation.	The performance of four different designs of coaters was evaluated with the help of discriminating characteristics by Pannala et al. (2006). Cardioid chalice with the multi-port design was reported as best design for making nuclear fuel particles (or TRISO particles)
Li (2009)	Fluidized Beds; $D_{bb} = 0.152$ m; $L_{bb} = 2.056$ m; $D_{fb} = 0.229$ m; $L_{fb} = 0.315$ m; $H_{FCC} = 1.15$ m;	NA	The predicted jet penetrations into FBs from simulation were compared with Al-Sherehy's experiments ^{1,2} . FBs was fluidized with a superficial air velocity of 5.1 mm/s along with the secondary gas injection at three different velocities (50, 78.5 & 156 m/s) through a nozzle (ID=4.3 mm) mounted on the wall (560 mm above distributor).	A comparison of experimental data (penetration length and jet angle) was made with the predicted data for different jet velocities by scaled Gibilaro's drag model & Gidaspow's drag model. It was reported that variable-scaled Gibilaro's drag law model gave a better prediction with the experimental data.

Li (2009)	DTSB ^{3,4} ; D _{column} = 0.229 m; D _{draft-tube} = 0.102 m; S.L.=700 g of glass beads	FLUENT 6.3 (frictional & liquid spray model were used with user-defined functions)	The simulation was performed with gas spray in DTSB and flow patterns was measured. The solids velocity and solids volume fraction were compared with Saadevandi and Turton's (2004) experiments. Three different frictional models (Schaeffer, Darteville, & Srivastava and Sundaresan) were validated.	The increase in spray velocity increases the solids circulation rates. The parametric studies of the restitution coefficient showed that solid concentration became higher inside the draft tube with higher restitution coefficients. Although, no effect was observed in maximum spouted height with RCs. Among different frictional models, Schaeffer model showed better prediction over experimental results
Li (2009)	Rectangular FB; L= 0.1 m;W=0.1 m; H=0.65 m; H _{FCC} =0.4 m; d _p =150 μm; ρ _p =1400 kg/m ³ ;	MFIX-TFM	A 3D-model with 139000 cells of a constant grid size of 5 mm was used in the simulations. The secondary injection velocities were varied in the range of 25-175 m/s and 50-100 m/s for single and multiple injections respectively.	The following conclusions were reported: <ul style="list-style-type: none"> ▪ Gas back mixing decreases with increasing the secondary gas velocity ▪ Jet penetrations length increases as the secondary injection velocity increases ▪ Hydrodynamics is strongly influenced by secondary injections at the upper plane than the lower plane

	Four side injection from four sides;			
Wang et al. (2015)	Same model as used by Li (2009) and similar to the cold model setup of Al-Sherehy's experiments ^{1,2} in 3D domain	MFIX-TFM (MFIX 2012-1)	A 3D-model with 45830, 74690 and 98450 cells were used in the simulations. The solid volume fraction, solid velocity and penetration length of the jet were determined using an in-house filtered fluid model.	The following conclusions were reported: <ul style="list-style-type: none"> ▪ The predicted jet penetration length and expansion jet angle was consistent with the experiments ▪ The upward motion of solids at the injection sidewall and downward motion at the opposite wall of the injection were reported.

ϵ_g : Gas voidage; D_c : Column diameter; L_c : Column height; d_p : Particle diameter; ρ_p : Particle density; MFIX: Multiphase Flow with Interphase eXchanges (open source available at <https://mfix.netl.doe.gov/>); TFM: Two Fluid Model; TRISO: TRistructural ISOtropic; bb: bubbling bed; fb: free board; 1= Al-Sherehy (2002), 2= Al-Sherehy et al. (2004); 3=Saadevandi (1996); 4=Saadevandi and Turton (2004); DTSB: Spouted Bed with Draft Tube; S.L.= Solid Loading; RC: Restitution Coefficients

A. 2. Case Set Up

The experimental results (from RPT), obtained in the chapter 3 are compared with the CFD simulation data. In the simulation, 3-D model with a cylindrical bottom section as a bed and a tapered section as a freeboard is generated using the workbench component of a commercial software code ANSYS 14.5® as shown in Figure A.1b. A single nozzle with a diameter of 6 mm is used for secondary air inlet (Figure A.1a to c). The nozzle is placed on the wall at $z = 0.20$ m from the distributor level ($z=0$). The uniform structured mesh is generated in the upper section of the nozzle level of the geometry while a non-uniform unstructured mesh is used for the lower part of the 3D model (Figure A.1b). The simulation is performed in ANSYS Fluent 14.5 platform using the system parameters highlighted in Table A.4. In this chapter these parameters are constant until specified.

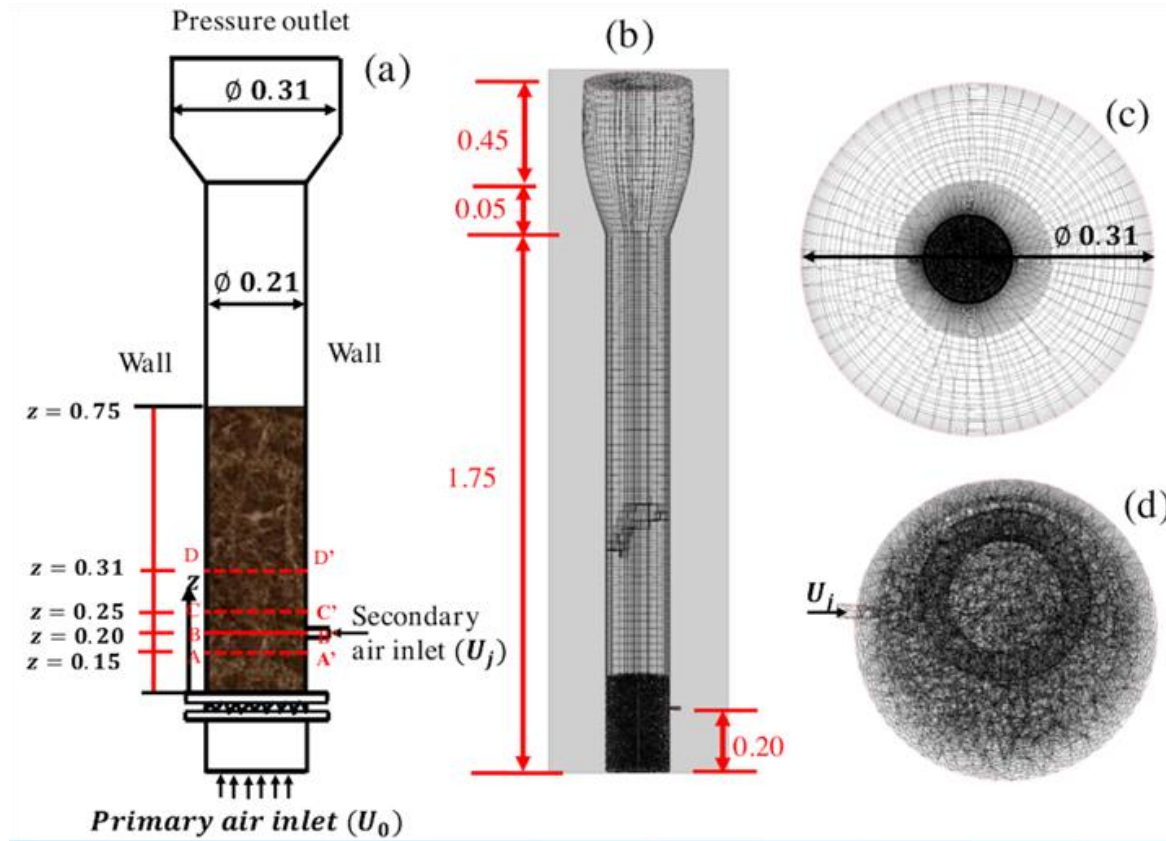


Figure A.1 Schematic of 3-D simulation model (a) fluidized bed geometry, (b) side view, (c) top view and (d) bottom section of fluidized bed system

Table A.4 Summary of properties and parameters used in simulation of fluidized bed

Properties	Value/input
Column diameter D_t [m]	0.21
Column height H_c [m]	2.25
Particle mean diameter d_p [μm]	0.709
Particle mean density ρ_p [kg/m^3]	2500
Primary air inlet velocity U_0 [m/s]	1.12
Air viscosity μ_g [Pa.s]	1.786×10^{-5}
Air density ρ_g [kg/m^3]	1.225
Initial voidage ϵ_0	0.6
Initial bed height H [m]	0.75
Nozzle diameter d_j [mm]	6
Secondary air injection velocity U_j [m/s]	72
Specularity coefficients ϕ	0-1
Restitution coefficients e	0.9 – 0.99
Time step [s]	1.0×10^{-4}
Transient formulation	First order implicit
Pressure velocity coupling	SIMPLE
Momentum formulation	First order implicit
Volume fraction formulation	QUICK

ANSYS Fluent 14.5 utilizes control volume methods to solve the PDEs governing the flow of two phases: air and glass beads. The Euler-Euler model (or TFM) is used to describe the motion of both the phases (air and glass beads), where these are assumed to be interpenetrating continuum phases. Initially, the static bed height is fixed at 0.75 m from the distributor level with the volume fraction of 0.6. The boundary conditions used in the simulations are shown in Figure A.1a. The bottom z-plane is set up as a velocity inlet (Figure A.1a, d). Similarly, the boundary condition for the nozzle is also set to be velocity inlet. The wall boundary condition is set to the curve surface of the 3-D model and top surface is treated as pressure outlet. In the first stage, the fluidization of the bed is achieved by supplying primary air through the bottom distributor at 1.12 m/s. In the second stage, when the bed is reached to a fully developed state, the secondary air is injected through a side nozzle at a jet velocity 72 (or $Q_1 = 120$ LPM). The time-averaged data are saved as soon as the bed reaches a steady-state. Most of the simulations are carried out using parallel computation with 2 CPUs.

A. 3. Results and Discussion

A.1.1. Grid Independency Test

To understand the insight of a gas-solid fluidized bed system with a single sidewall injection, an attempt has been made using the commercial simulation software package FLUENT®. The prediction of the simulation is compared with the RPT data as discussed in previous chapters. The solid flow-field information have been predicted with four different 3D-simulation cases and the grid convergence is achieved (Table A.5). The Hulin-Gidaspow drag (Hulin and Gidaspow., 2003) is used to perform the grid convergence test. The coarse structured mesh is used in the upper region of the beds while the fine

unstructured hexahedral mesh is applied to the bottom region of the bed including the injection zone as shown in Figure A.1.

Table A.5 Details of grids used for CFD-TFM simulation

Cases	No of cells
TFM1C	25984
TFM2C	53275
TFM3C	75301
TFM4C	101938

Figure A.2 shows the contour plots of predicted time-averaged solid distribution for different grid sizes in xz-plane. It is noteworthy to mention that the predicted expanded bed height is maximum by the coarser grid (TFM1C) and minimum with the fine grid (TFM4C). It is also noticed that the last two cases with a fine grid, have predicted equal expanded bed height. Further, the time-averaged volume fraction and axial velocity of solid are extracted at different z-planes ($z=0.03, 0.15, 0.20$ and 0.25 m) in x-direction. Figure A.3 shows the comparison of radial profiles of time-averaged axial velocities of solid predicted at the mentioned vertical locations for different simulation cases with the finite number of cells. It is observed that the axial velocities of solid are higher at the central region for all axial levels. The maximum value of axial velocity of solid at the central region increases with the fine grid. The fine grid increases the maximum axial velocity of the solid at the core region for all axial levels as shown in Figure A.3. No significant difference were observed in the results predicted by the TFM1C and TFM2C cases. There was no discernible difference between the velocities anticipated by the TFM1C and TFM2C cases. As the grid becomes finer, the prediction are noticeable .

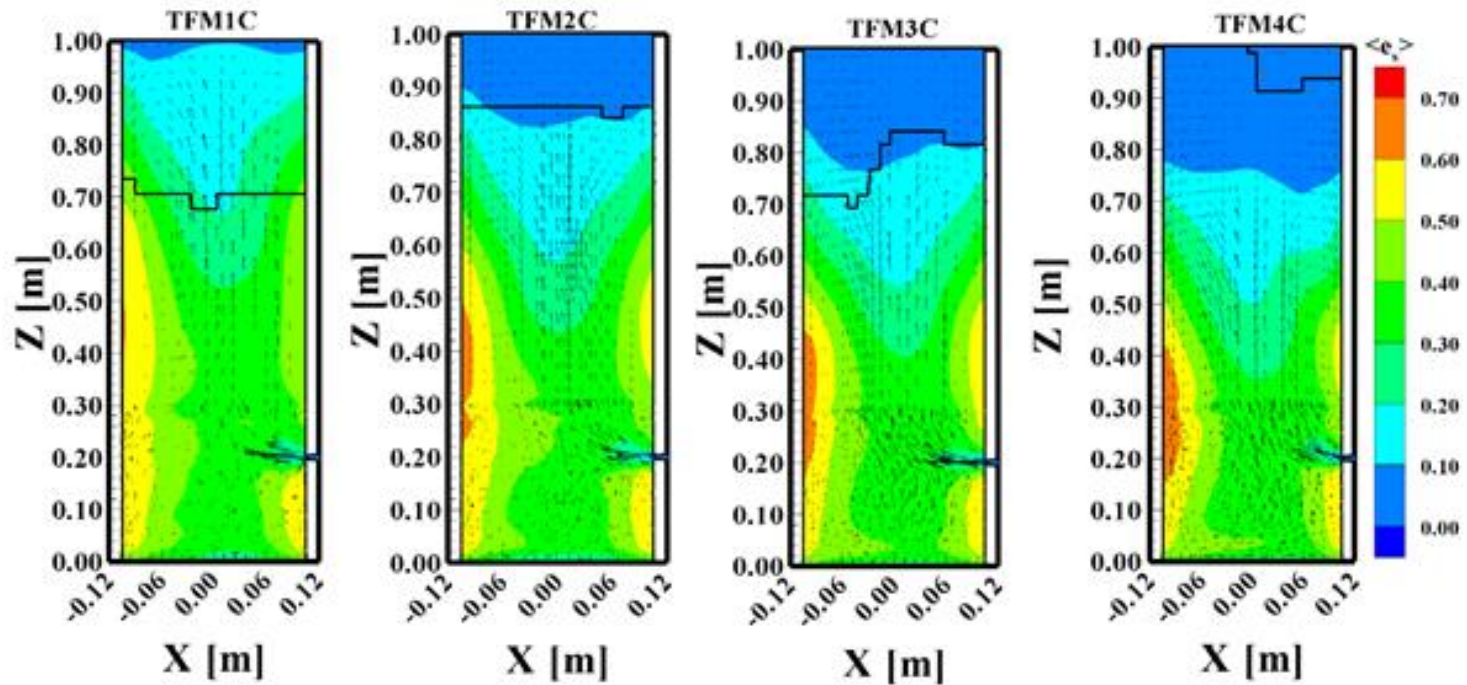


Figure A.2 Effect of grid size on the time-averaged solid volume fraction (*Drag model=Hulin Gidaspow, $H/D_t=3.57$, $U/U_{mf}=3.12$, $U_{mf}=0.36$ m/s, $d_p=709$ μ m; $\phi = 0.003$, $e = 0.95$, $u_j = 72$ m/s*)

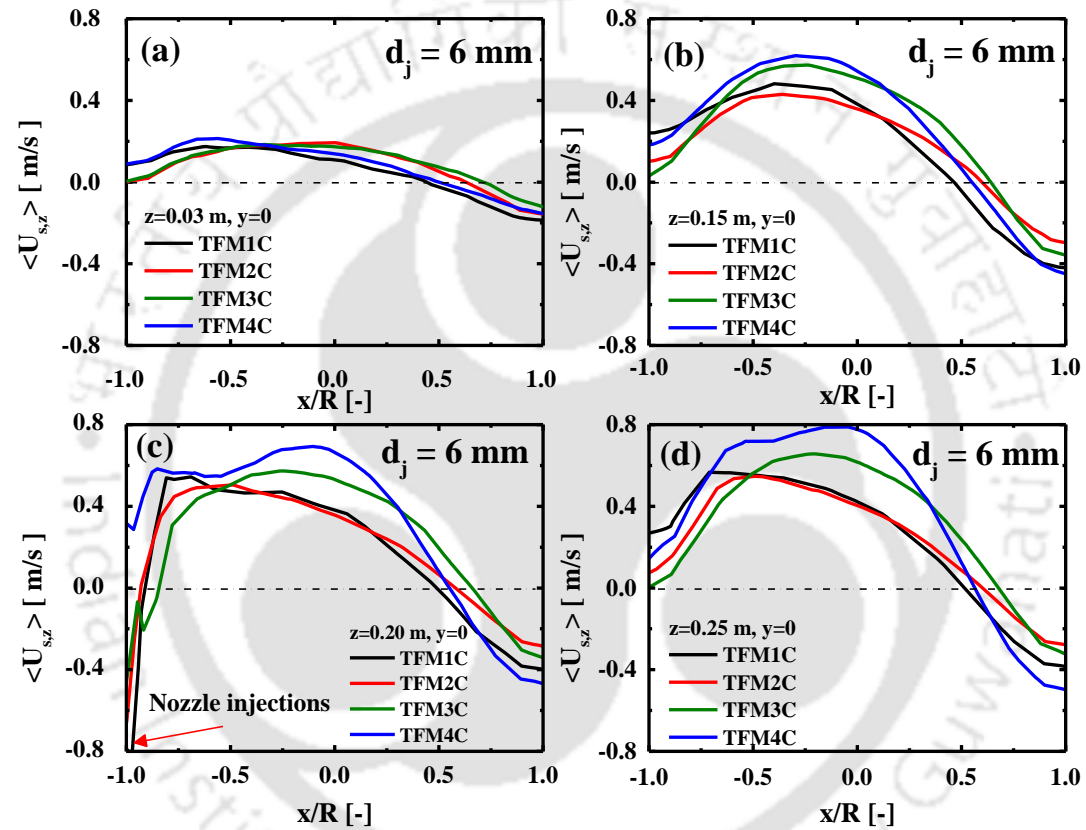
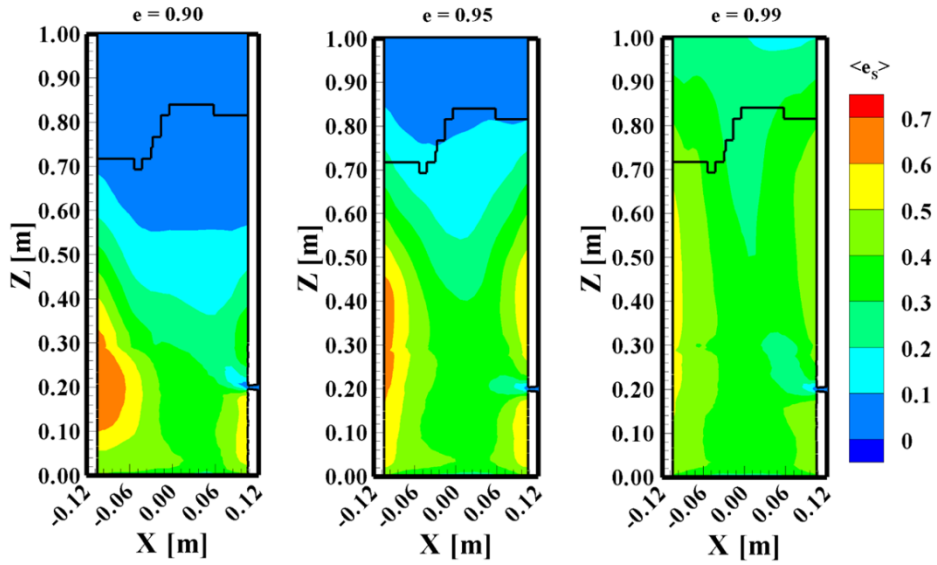


Figure A.3 Solid velocity for different grids used in TFM simulations (*Drag model=Hulin Gidaspow, $H/D_t=3.57, U/U_{mf}=3.12, U_{mf}=0.36$ m/s, $d_p=709\text{ }\mu\text{m}; \phi = 0.003, e = 0.95, u_j = 72\text{ m/s}$*)

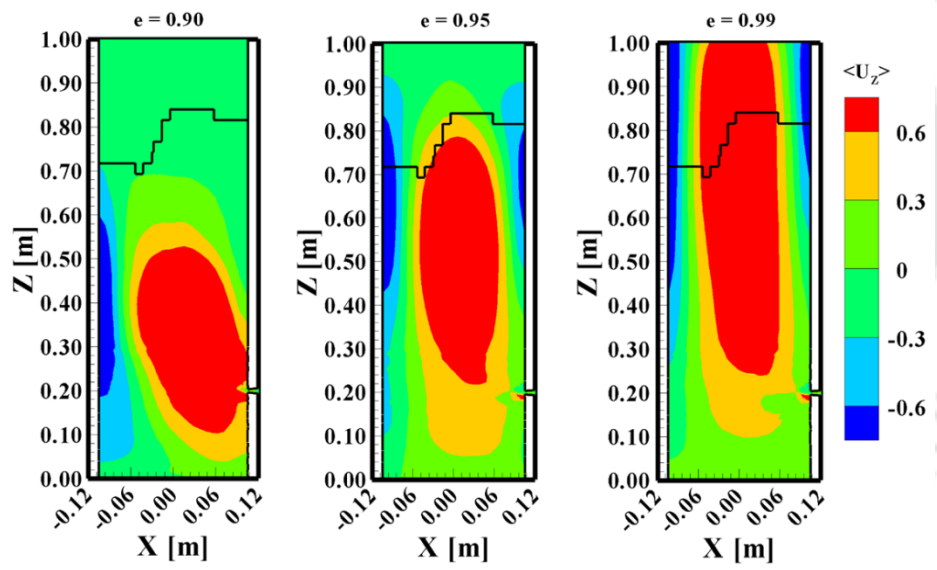
A.1.2. Effect of Restitution Coefficients

Figure A.4 (a) shows the contour plots solid volume fraction in the vertical plane aligned with the nozzle injection for three different values of restitution coefficients. It is notable that the initial static bed height (H) is 0.75 m. The e value of 0.99 overpredicts the expanded bed height. Similarly, the e value of 0.9 also underpredicts the bed heights which is not realistic. Therefore, the value of $e = 0.95$ is chosen for the rest of simulations. Figure A.4 (b) presents the contours of solid mean axial velocity at the same vertical plane as mentioned above. It is noticed that the solid mean axial velocity distribution is asymmetric for all three different values of ' e ' ($0.9 < e < 0.99$). The value of $e = 1$ is always avoidable as it requires high computational power as well as it is unrealistic.

Figure A.5 shows the comparison of mean axial velocity of solids obtained with RPT and the simulation data with single nozzle injection for three different values of restitution coefficients. These data are compared for 4-different heights ($z = 0.03$ m, 0.15 m, 0.21 m and 0.25 m) at a vertical plane parallel along the nozzle injection. Figure A.5 shows that the predicted data are much higher than the measured values from RPT experiments for all the three different values of restitution coefficients. However, the lower value of restitution coefficient ($e = 0.90$) predict the highest values near the injection wall ($r/R = -1.0$) while lowest at the opposite wall ($r/R = 1.0$). Thus, the lower value can not be used for the simulation and the medium value ($e = 0.95$) is used for other simulation as it requires less computational resource than the highest restitution coefficient value. Figure A.6 presents the axial rms velocities at the same 4-different heights. It suggest that the prediction are lower at lower than the experimental values for all heights. The prediction are much closer for the upper heights. Thus, the value of 0.95 is used for further study.



(a)



(b)

Figure A.4 Contour of (a) solid volume fractions and (b) time-averaged solid axial velocity

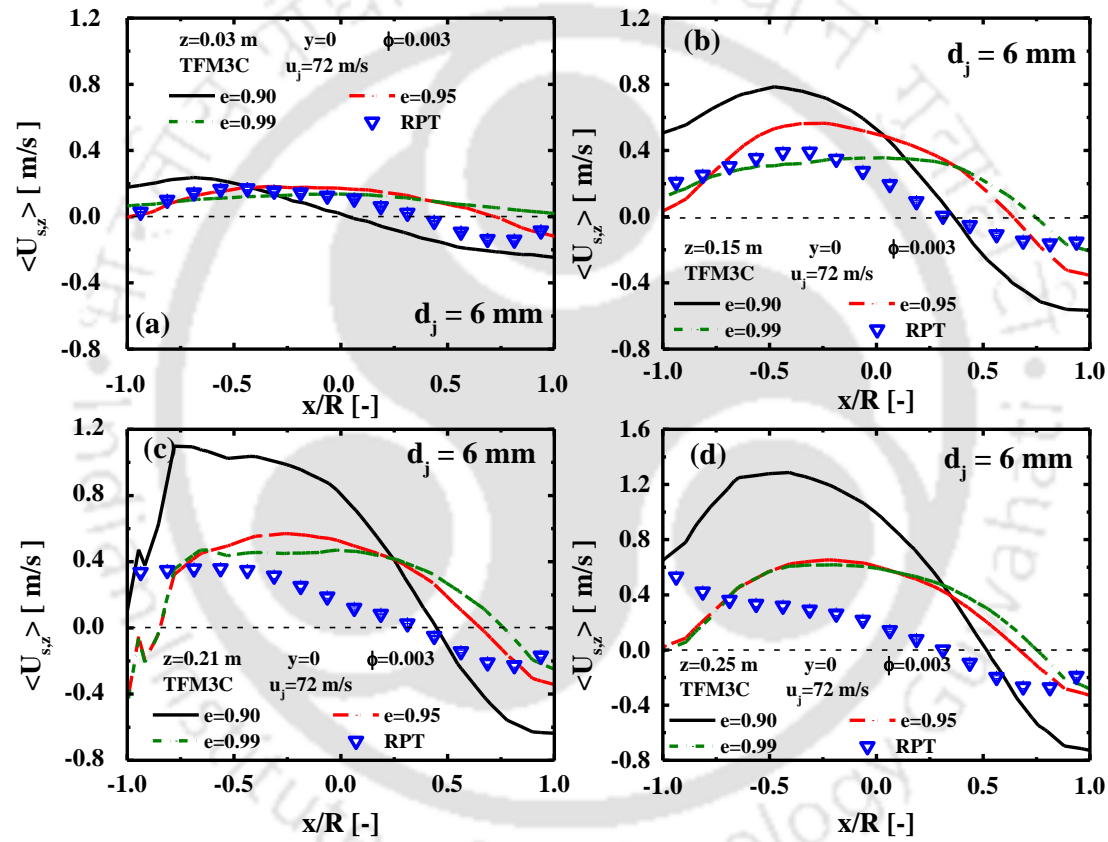


Figure A.5 Effect of restitution coefficient on time-averaged solid axial velocity

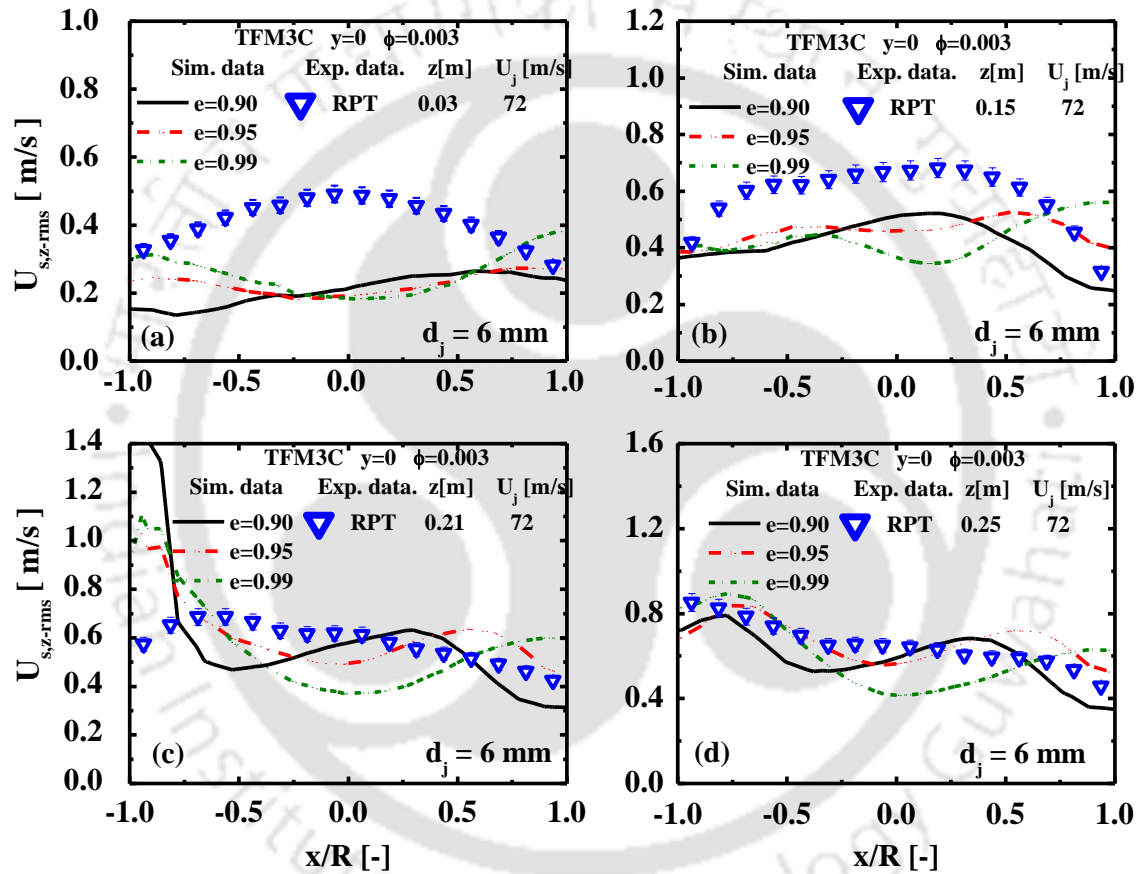


Figure A.6 Effect of restitution coefficient on time-averaged solid axial RMS velocity

A.1.3. Effect of Specularity Coefficients

The specularity coefficient is an important parameter that evaluates the frictional viscosity to compute the solid stress (Table A.2). Figure A.7 shows the plots of mean axial velocity of solids, obtained with four different values of specularity coefficients against the RPT data. It is noticed that the prediction are higher than experimental data for all conditions except 0.25.

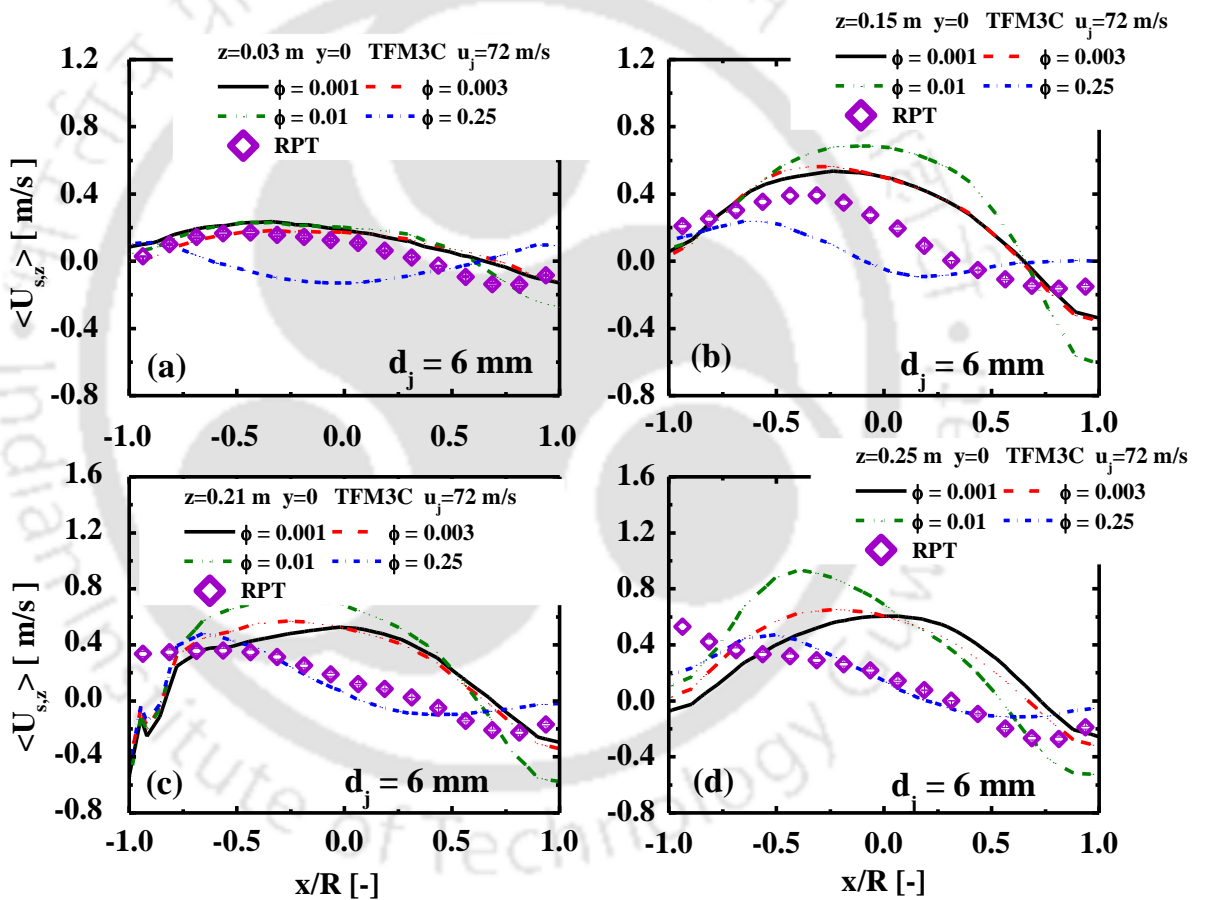


Figure A.7 Effect of specularity coefficient on time-averaged solid axial

A.1.4. Effect of Drag Models

The time-averaged axial velocities of solid measured through RPT experiments and predicted from the CFD simulation are plotted in Figure A.8. The predicted data are obtained with five different drag models such as Gibilaro (GIB), Gidaspow (GID), Shyamlal (SYAM), Hullin Gidaspow (HG) and Hill-Koch-Ladd (HKL) as shown in Figure A.8. It may be noted that GIB and HKL drag models are able to predict the RPT data qualitatively. The prediction are closer at lower heights as shown in Figure A.8(a) and A.8(b). In addition, CFD simulation over predicts the experimental data of the axial mean velocity at above the nozzle plane (Figure A.8c, d). A similar flow patterns of particle motion with side injection in the gas-solid fluidized bed has been reported by Wang et al. (2015) using a filtered drag model.

The contour of the time-averaged axial solid velocities predicted at four distinct cross sections of the column from the CFD simulations for the various drag models discussed earlier is depicted in Figure A.9a–d. Figure A.9e shows the time-averaged axial velocities of solids inferred from RPT for the same z-planes as those previously indicated in simulation. The contour and vector plots at $y=0$ plane were illustrated in Figure A.10. The figure shows that the axial velocities of solid in this kind of fluidized bed with single nozzle injection may be qualitatively predicted using the GIB and HKL models.

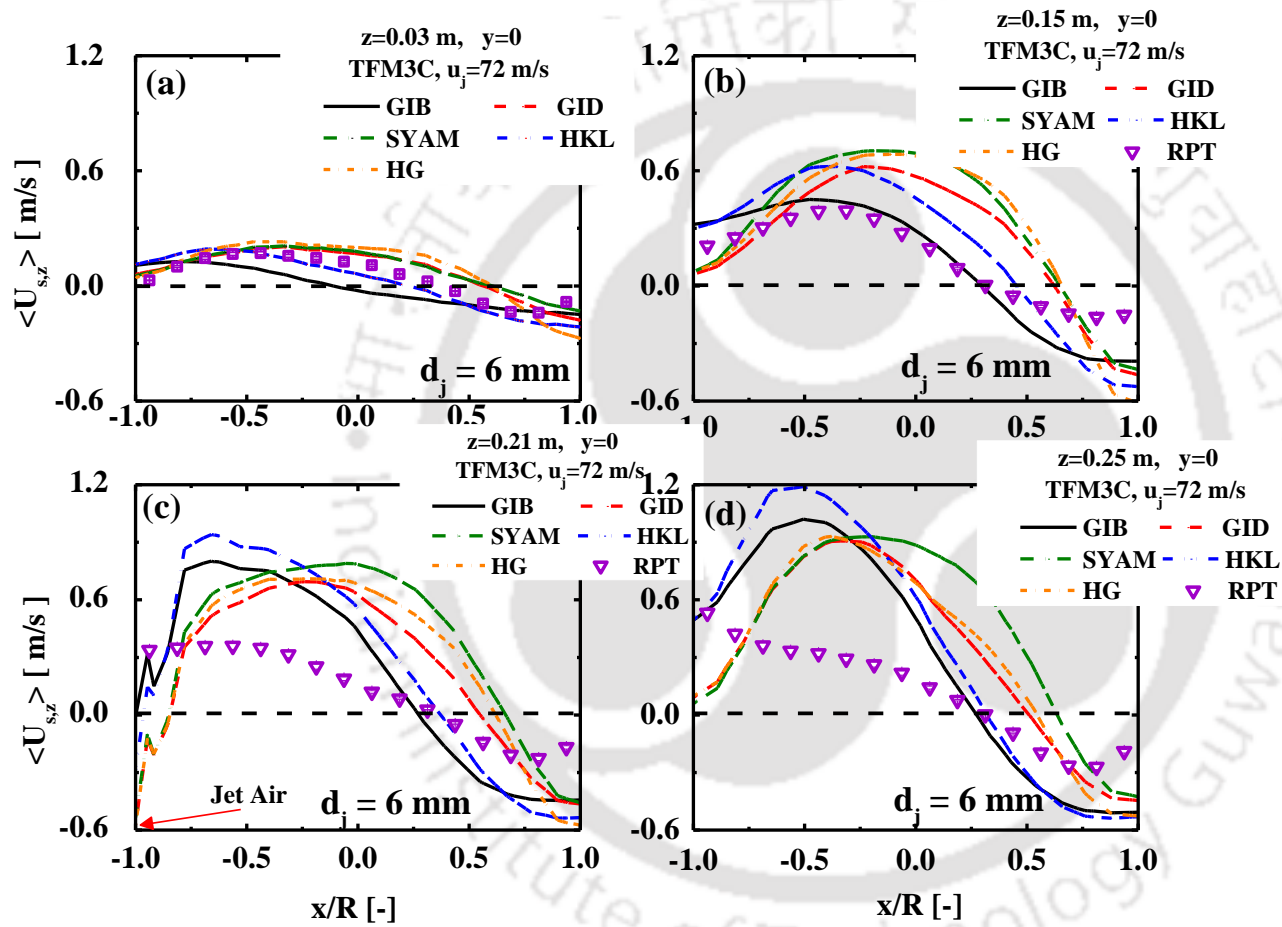
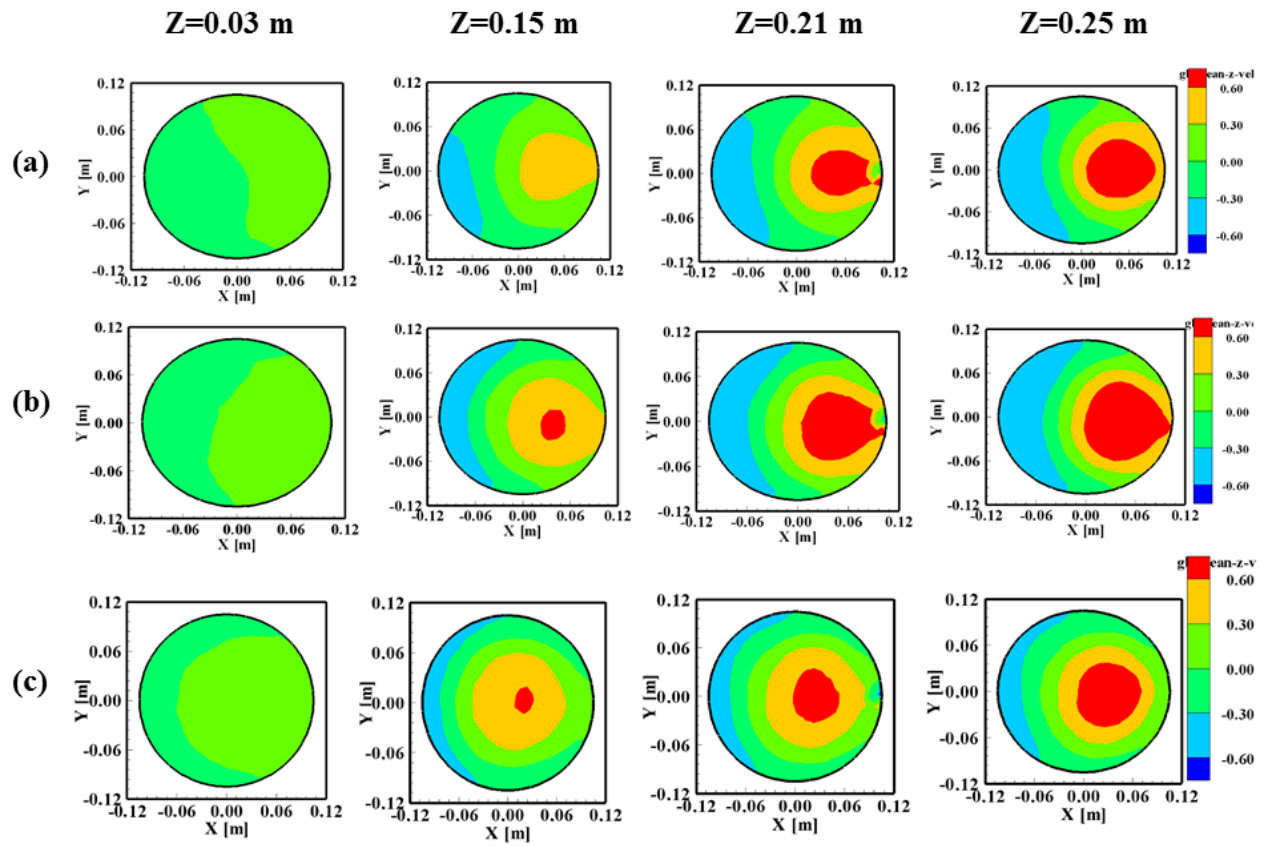


Figure A.8 Comparison of mean axial velocity of solids obtained from RPT and CFD simulation with different drag models



Institute of Technology

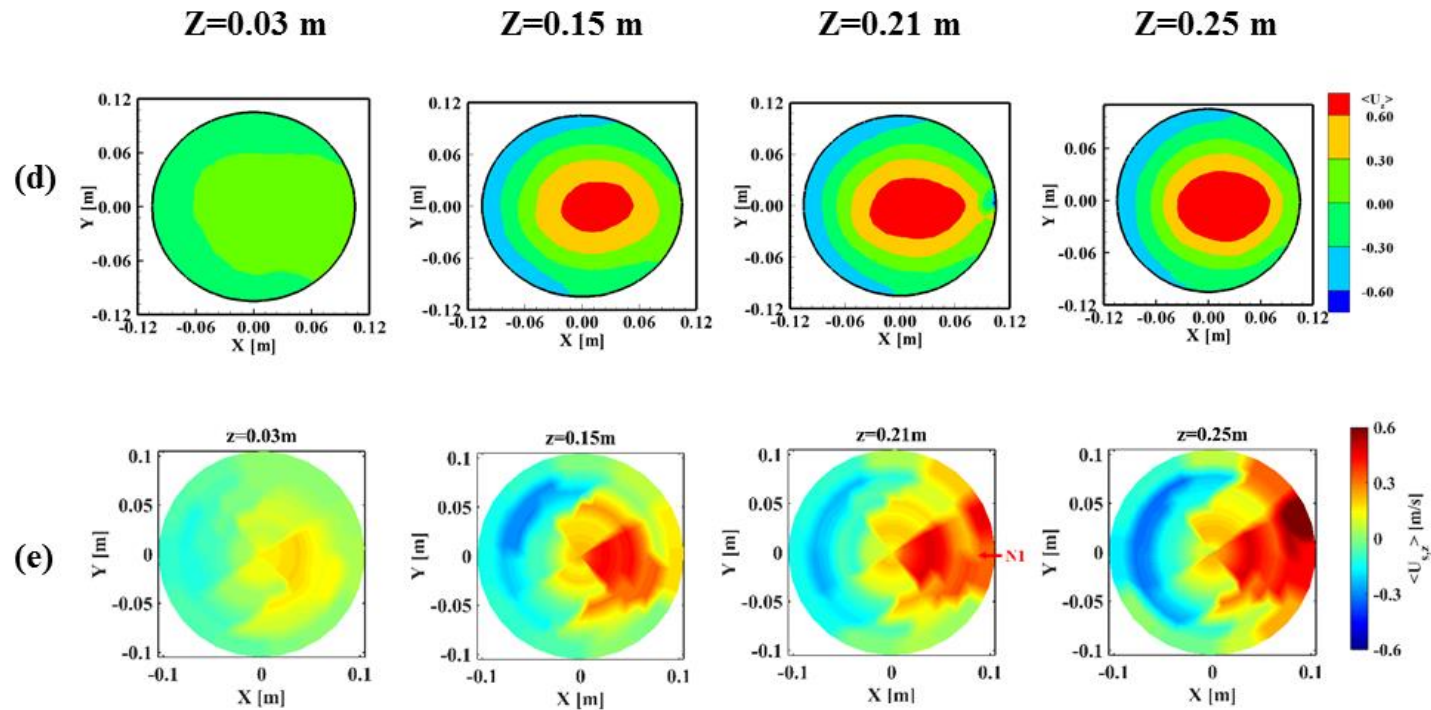


Figure A.9 Contour of mean axial velocity of solids obtained through CFD simulation with different drag models (a) Gibilaro model, (b) Hill-Koch-Ladd model and (c) Gidaspow (d) Syamlal and (e) RPT experiment for fixed operating condition ($H/D_t=3.57$, $U/U_{mf}=3.12$, $U_{mf}=0.36\text{ m/s}$, $d_p=709\text{ }\mu\text{m}$; $\phi = 0.01$, $e = 0.95$, $u_j = 72\text{ m/s}$)

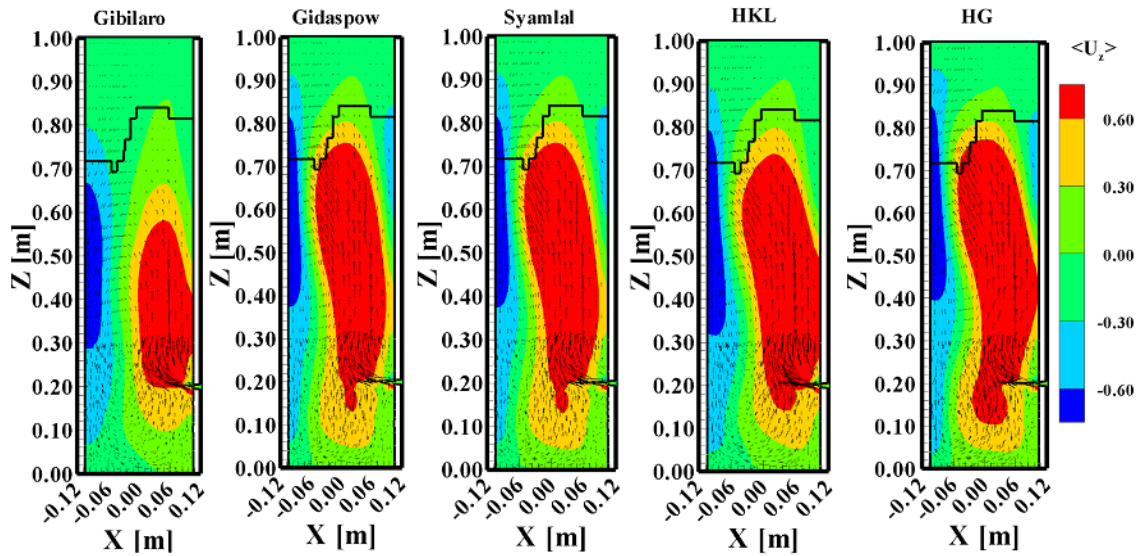


Figure A.10 Contours of time-averaged axial velocity of solids on xz-plane for fixed operating condition ($H/D_t=3.57$, $U/U_{mf}=3.12$, $U_{mf}=0.36$ m/s, $d_p=709$ μm ; $\phi = 0.01$, $e = 0.95$, $u_j = 72$ m/s)

A. 4. Summary

The effect of a single gas injection at the sidewall as a secondary inlet to the gas-solid fluidized bed has been investigated via CFD simulation. The simulations are performed with the Euler-Euler approach at fixed fluidization conditions as used in an experimental study ($H/D_t=3.57$, $U/U_{mf}=3.12$, $U_{mf}=0.36$ m/s, $d_p=709$ μm). The simulations highlight the optimal selection of different simulation parameters that do affect the local and overall flow patterns of the solid motion inside the fluidized bed. Hence, the outcome of this chapter provides a suitable approach to set up a base case for further study (i.e. the effect of primary/secondary injection velocity, multiple arrangements of nozzle injections at different axial locations or planes etc.).

The following conclusions can be summarised on the basis of the simulation study:

- The selection of the drag model plays an important role in predicting the accurate hydrodynamic flow behavior of solids in gas-solid fluidized beds with side injection. It has been demonstrated the feasibility of integrating the HKL drag model (Benyahia et al., 2006) using user define function (UDF) with the two-fluid CFD model. It is observed that Gibilaro and HKL are able to predict the flow field closely (Gibilaro., 2001; Benyahia et al., 2006).
- The selection of a grid near the injection zone is equally important for a similar setup. The overall computational cells also affect the flow behavior of solid in such a system.
- The recommended range of restitution coefficient for better prediction is 0.95-1. The recommended range of specularly coefficient for better prediction is 0.01-0.25

Notations

d_p	Particle diameter	[μm]
D_t	Colum diameter	[m]
$\overline{\overline{D_s}}$	Rate of deformation tensor	[-]
e	Restitution coefficient	[-]
e_p	Internal energy of particles	[$\text{kg.m}^2.\text{s}^{-2}$]
\vec{F}_{body}	Body force of particles	[kg.m.s^{-2}]
$\vec{F}_{collision}$	Collision forces of particles	[kg.m.s^{-2}]
$\vec{F}_{surface}$	Surface forces of particles	[kg.m.s^{-2}]
g	Gravitational field	[m.s^{-2}]
I_{2D}	Second invariant of $\overline{\overline{D_s}}$	[-]
I_{gS}	Interface momentum exchange coefficients	[]

m_p	Mass of particle	[m]
\dot{m}_p	Rate of change of mass of particle	[kg.s ⁻¹]
P_g, P_s	Gas and solid pressure	[Pa]
Q_1	Injection flow rate of air	[LPM]
\vec{U}_s, \vec{U}_g	Velocity of solids and gas respectively	[m.s ⁻¹]
$\langle U_{s,z} \rangle$	Ensemble averaged axial mean velocity	[m.s ⁻¹]
$U_{s,z-rms}$	Axial RMS velocity	[m.s ⁻¹]
V_p	Volume of particle	[m ³]
\vec{V}_p	Velocity fields vector of particles	[m.s ⁻¹]
\vec{X}_p	Position vector of particles	[m]
t	Time	[s]

Greek Symbols

∇	Gradient	[m]
$\varepsilon_s, \varepsilon_g$	Volume fraction of solid and gas respectively	[-]
$\langle \varepsilon_s \rangle$	Chordal averaged of solid volume fraction	[-]
ϕ	Internal angle of friction	[degree]
ρ_s, ρ_g	Density of solid and gas respectively	[kg.m ⁻³ .]
σ_s	Solid stress	[Pa]

Subscript

s, g	solid and gas respectively	[-]
------	----------------------------	-----

Abbreviation

CFD	Computational fluid dynamics
GDT	Gamma ray densitometry technique
GIB	Gibilaro
GID	Gidaspow
HG	Hullin Gidaspow
HKL	Hill-Koch-Ladd
MFIX	Multiphase Flow with Interphase eXchange
RPT	Radioactive particle technique
SYAM	Syamlal

References

- Al-Sherehy, F., 2002. Distributed addition of gaseous reactants in fluidized beds. PhD. Thesis. University of British Columbia, Vancouver.
- Al-Sherehy, F., Grace, J.R., Adris, A.E., 2004. Gas mixing and modelling of secondary gas distribution in a bench-scale fluidized bed. *AIChE Journal*. 50 (5), 922-936.
- Anderson, T. B., Jackson, R., 1967. A fluid mechanical description of fluidized beds-comparison of theory and experiment. *Ind. Eng. Chem. Fund.* 8 (1), 137-144.
- Benyahia, S., Syamlal, M., O'Brien, T. J., 2006. Extension of Hill-Koch-Ladd drag correlation over all ranges of Reynolds number and solids volume fraction. *Powder Technol.* 162 (2), 166-174.
- Crowe, C. T., 1982. Review: Numerical models for dilute gas-particle flows. *J. Fluid Eng.* 104 (3), 297-303.
- Crowe, C.T., 1986. Two fluid versus trajectory models: range of applicability. *Gas-solid flows-1986 ASME FED*, 35, 91-96.
- Crowe, C. T., Troutt, T. R., Chung, J. N. 1996. Numerical models for two-phase turbulent flows. *Annual Review of Fluid Mechanics*. 28, 11-43.

- Enwald, H., Peirano, E., Almstedt, A. E., 1996. Eulerian two-phase flow theory applied to fluidization. *Int. J. Multiphas. Flow.* 22, 21-66.
- Fan, L. S., Zhu, C., 1998. Principles of gas-solid flows. Cambridge, New York: Cambridge University Press, 557.
- Gerber, S., Behrendt, F., Overmann, M., 2010. An Eulerian modelling approach of wood gasification in a bubbling fluidized bed reactor using char as bed material. *Fuel.* 89 (10), 2903-2917.
- Gibilaro, L. G., 2001. Fluidization-dynamics: the formulation and applications of predictive theory for the fluidized state. Boston: Butterworth-Heinemann, 232.
- Gidaspow, D., 1994. Multiphase flow and fluidization: continuum and kinetic theory descriptions. Boston: Academic Press. 467.
- Gronli, M. G., 1996. A theoretical and experimental study of the thermal degradation of biomass. PhD Thesis. NTNU Trondheim, Norway, Europe.
- Hill, R. J., Koch, D. L., Ladd, A. J. C. 2001. The first effects of fluids inertia on flows in ordered and random arrays of spheres. *J. Fluid Mech.* 448, 213-241.
- Huilin, L., Gidaspow, D., 2003. Hydrodynamic simulations of gas-solid flow in a rise. *Ind. Eng. Chem. Res.* 42, 2390-2398.
- Johnson, P. C., Nott, P., Jackson, R., 1990. Frictional collisional equations of motion for particulate flows and their application to chutes. *J. Fluid Mech* 210, 501-535.
- Li, T. 2009. Numerical investigation of the gas/spray jet interaction with fluidized beds. PhD. Thesis. The University of British Columbia, Vancouver.
- Li, T., Gel, A., Syamlal, M., Guenther, C., Pannala, S., 2010b. High resolution simulation of coal injection in a gasifiers. *Ind. Eng. Chem. Res.* 49, 10767-10779.
- Lun, C.K.K., Savage, S.B., 1986. The effects of an impact velocity dependent coefficient of restitution on stresses developed by sheared granular materials. *Acta. Mechanica.* 63, 15-44.

Lun, C.K.K., Savage, S.B., Jeffrey, D.J., Chepuruiy, N., 1984. Kinetic theories for granular flow-inelastic particles in coquette flow and slightly inelastic particles in a general flow field. *J. Fluid Mech.* 140, 223-256.

Patankar, S. V., 1980. *Numerical Heat Transfer and Fluid Flow*, Hemisphere Publishing Corporation, New York.

Pennala, S., Daw, C. S., Boyalakuntla, D., Finney, C.E.A., 2006. Process modelling phase I summary report for the advance gas reactor fuel development and quantification program. ORNL/TM-2006/520, March, 2006.

Pennala, S., Daw, C. S., Finney, C.E.A, Boyalakuntla, D., Syamlal, M., O'Brien, T. J., 2007. Simulating the dynamics of spouted-bed nuclear fuel coaters. *Chem. Vapor. Depos.*, 13, 481-490.

Portela, L. M., Oliemans, R. V. A., 2006. Possibilities and limitations of computer simulations of industrial turbulent dispersed multiphase flows. *Flow Turbul. Combust.* 77 (1-4), 381-403.

Pougatch, K., 2005. Equation for the Eulerian multiphase model. Personal Communication.

Versteeg, H. K., Malalasekera, W., 1995. *An Introduction to Computational Fluid Dynamics*. Pearson-Prentice Hall.

Reeks, M. W., 1991. On a kinetic-equation for the transport of particles in turbulent flows. *Phys. Fluids A-Fluid Dynamics* 3 (3), 446-456.

Savage, S. B., 1983. Granular flows down rough inclines-review and extension. In: *Mechanics of granular materials: New model and constitutive relations*. 261-282

Schaeffer, D. G., 1987. Instability in the evolution-equations describing incompressible antigranulocytes flow. *J. Differ. Equations.* 66(1), 19-50.

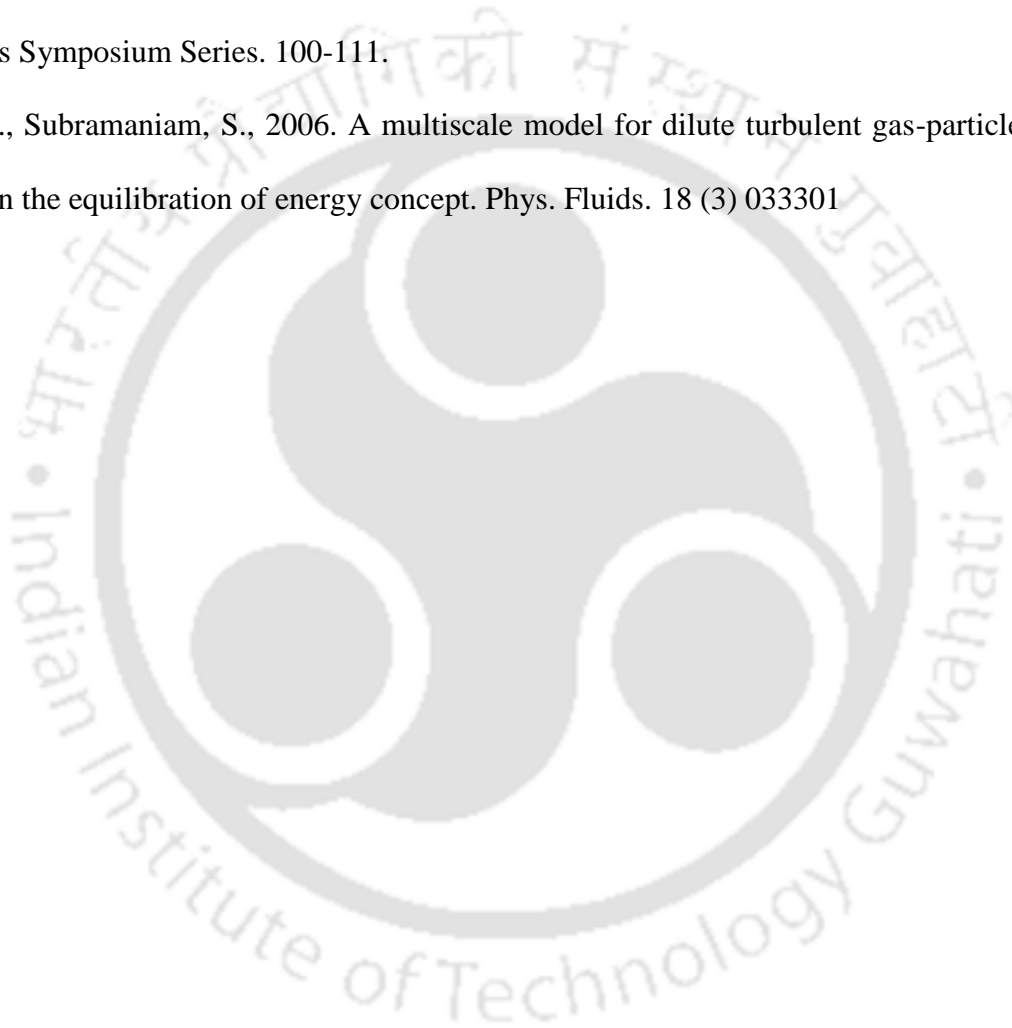
Syamlal, M., Rogers, W., Brien, T. J. O., 1993. MFIx documentation: Theory guide, U. S. Department of Energy (DOE), Morgantown Energy Technology Center. Morgantown. West Virginia.

Syamlal, M., O'Brien, T. J. 1989. Computer simulation of bubbles in a fluidized bed. AIChE Symposium Series. 85, 22-31.

Wang, S., Yang, Q., Shao, B., Zhao, J., Liu, L., Liu, Y., 2015. Numerical simulation of horizontal jet penetration using filtered fluid model in gas-solid fluidized bed. Powder Technol. 276, 1-9.

Wen, C. Y., Yu, Y. H., 1966. Mechanics of fluidization. Presented at Chemical Engineering Progress Symposium Series. 100-111.

Xu, Yu., Subramaniam, S., 2006. A multiscale model for dilute turbulent gas-particle flows based on the equilibration of energy concept. Phys. Fluids. 18 (3) 033301



BIO-DATA

Jitendra Singh Rawat

Place of Birth Pauri Garhwal, Uttarakhand, India

Degree B. Tech., BTKIT-Dwarahat,
Almora-India
M. Tech., Indian Institute of Technology-Karnataka,
Surathkal, India.
Ph. D., Chemical Engineering
Indian Institute of Technology-Guwahati,
India

Awards

Excellent Poster Award presented on the topic entitled “CFD Simulation of Nozzle Assisted Gas-Solids Fluidized Bed with Experimental Validation” in CAMURE-10 & ISMR-9 symposium, Qingdao, China, July 2017

Publications

Jitendra S. Rawat, Rajesh K. Upadhyay and Pankaj Tiwari, “Effect of Horizontal Side Injection on Solid Motion in Gas –Solid Fluidized Bed System via Radioactive Particle Tracking (RPT)” (to be submitted)

Jitendra S. Rawat, Rajesh K. Upadhyay and Pankaj Tiwari, “Effect of Multiple Nozzle injection through Sidewall on Flow Field of Gas-Solid Fluidized Beds” (to be submitted)

International Conferences

Jitendra S. Rawat, Rajesh K. Upadhyay and Pankaj Tiwari, “Effect of Single/Multiple Nozzle Injection Through Sidewall on Flow Field of Gas-Solids Fluidized Bed”, **Poster Presentation, ISCRE -25**, Florence, Italy, May 20-23, 2018.

Jitendra S. Rawat, Rajesh K. Upadhyay and Pankaj Tiwari, “CFD Simulation of Nozzle Assisted Gas-Solids Fluidized Bed with Experimental Validation”, **Poster presentation, CAMURE-10 & ISMR-9 symposium**, Qingdao, China, July 2017.

Jitendra S. Rawat, Rajesh K. Upadhyay and Pankaj Tiwari, “Experimental Investigation of Nozzle Assisted Gas-Solid Fluidized Bed Using Gamma-ray Densitometry and Radioactive Particle Tracking Technique”, **Oral presentation, CAMURE-10 & ISMR-9 symposium**, Qingdao, China, July 2017.

Jitendra S. Rawat, Rajesh K. Upadhyay, H. J. Pant and Pankaj Tiwari, “Investigation of the Multiple Side Injections on Hydrodynamics of the Gas-Solids Fluidized Bed Using Radiotracer Based Techniques”, **Oral presentation, ICARST**, Vienna, Austria, April 2017.

Jitendra S. Rawat, Rajesh K. Upadhyay and Pankaj Tiwari, “Investigation of Gas-Solids Fluidized System with Side Injections using Non-invasive based Techniques and CFD simulations”, **Oral presentation, CHISA & PRES**, Prague, Czech Republic, August 2016.

Jitendra S. Rawat, Rajesh K. Upadhyay and Pankaj Tiwari, “Investigation of Nozzle Assisted Gas-Solids Fluidized Bed: Experimental and Numerical Studies”, **Poster presentation, 3rd Indo-German Workshop**, IIT Guwahati, India, February 2016.

Jitendra S. Rawat, S. K. Baheshwar, Pankaj Tiwari and Rajesh K. Upadhyay, “Experimental and Numerical Investigation of Gas-Solid Fluidized Bed with Nozzle Spray from the Side Wall”, **Oral presentation, CAMURE-9 & ISMR-8 symposium**, Lyon, France, December 2014.

National Conferences

Jitendra S. Rawat, Pankaj Tiwari and Rajesh K. Upadhyay, “Comparison of Spatial Distribution of Solid in Nozzle Assisted Gas Solid Fluidized Bed”, **Oral presentation, CHEMCON**, IIT Guwahati, Assam, India, December 2015.

Jitendra S. Rawat, Pankaj Tiwari and Rajesh K. Upadhyay, “Investigation of the Material Distribution of Solids in Gas-Solid Fluidized Bed Column with Side Wall Nozzle Assembly”, **Oral presentation, CHEMCON**, Chandigarh, India, December 2014.

Workshops and Training

Attended a training course on “**Research Aspects in Research Applications of Ionizing Radiations**” organized by “**Indian Association for Radiation Protection in collaboration with Radiological Physics & Advisory Division, Bhabha Atomic Research Centre**”, CT&CRS, Anushaktinagar, Mumbai-400094, India, December 2013